Wireless communication for hearing aid system

Nour, Baqer; Breinbjerg, Olav; Sigmund, Ole

Publication date:
2012

Document Version
Publisher's PDF, also known as Version of record

Wireless communication for hearing aid system

Ph.D. Thesis

Baqer Nour

March 2012

Supervisors:

Olav Breinbjerg, Professor, Ph.D.
Department of Electrical Engineering, Technical University of Denmark

Ole Sigmund, Professor, Ph.D.
Department of Mechanical Engineering, Technical University of Denmark

Niels Asger Mortensen, Professor, Ph.D.
Department of Photonics Engineering, Technical University of Denmark

Abstract

This thesis focuses on the wireless coupling between hearing aids close to a human head. Hearing aids constitute devices with advanced technology and the wireless communication enables the introduction of a range of completely new functionalities. Such devices are small and the available power is limited, it is therefore important to characterize the wireless link-budget and to understand the mechanisms that control propagation of waves inside and outside the head. For this purpose, different approaches have been used.

There are two objectives for this thesis. The first objective is to characterize the ear-to-ear wireless communication channel by understanding the mechanisms that control the propagations of the signals and the losses. The second objective is to investigate the properties of magneto-dielectric materials and their potential in antenna miniaturization.

There are three approaches to study the ear-to-ear wireless communication link; a theoretical approach models the human head as a sphere that has the electrical properties of the head, a numerical approach implements a more realistic geometry of the head, and an experimental approach measures directly the coupling between the antennas near a real persons or a phantom head imitating the human head's electrical properties. Each approach has advantages and disadvantages; the analytical approach gives accurate results and is very fast, though it does not treat complex structures. The numerical approach can treat complex structures but is limited by the electrical size of the structures and requires large memory and long processing time. The experimental approach yields accurate coupling between the antennas but does not provides detailed information about the field distribution. Therefore, we combine all these three approaches to gain some understanding of the ear-to-ear wireless communication channel.

A circular patch antenna was used to study the properties of the magneto-dielectric materials. In the thesis, we focused on three properties; efficiency, quality factor and bandwidth of the antenna. An analytical method is used to calculate the properties of a low-loss circular patch antenna, while a numerical method was used to analyze a high-loss circular patch antenna. The low-loss magneto-dielectric materials can potentially be used to miniaturize the size of the antennas, offering higher efficiency and wider bandwidth than the dielectric materials.

Resumé

Denne afhandling fokuserer på den trådløse kobling mellem høreapparater tæt på et menneskeligt hoved. Høreapparater udgør enheder med avanceret teknologi og den trådløse kommunikation giver mulighed for indførelse af en række helt nye funktionaliteter. Sådanne enheder er små og de tilgængelige virkning er begrænset, er det derfor vigtigt at karakterisere det trådløse link-budget, og at forstå de mekanismer, der styrer udbredelsen af bølger inden i og uden for hovedet. Til dette formål har forskellige tilgange været anvendt.

Der er to formål for denne afhandling. Det første mål er at karakterisere øre til øre trådløse kommunikationskanal ved at forstå de mekanismer, der styrer udbredelser af signalerne og tab. Det andet mål er at undersøge egenskaberne af magneto-dielektriske materialer og deres potentiale i antenne miniaturisering.

Der er tre metoder til at studere øre til øre trådløs kommunikation kanal; en teoretisk tilgang modeller det menneskelige hoved som en sfære, der har de elektriske egenskaber af hovedet, en numerisk metode implementerer en mere realistisk geometri af hovedet, og en eksperimentel tilgang måler direkte kobling mellem antennerne i nærheden af en virkelige personer eller et fantom hoved efterligner det menneskelige hoved elektriske egenskaber. Hver metode har fordele og ulemper, den analytiske tilgang giver nøjagtige resultater og er meget hurtigt, selvom det ikke behandler komplekse strukturer. Den numeriske metode kan behandle komplekse strukturer, men er begrænset af den elektriske størrelsen af de strukturer og kræver stor hukommelse og lang behandlingstid. Den eksperimenterende tilgang giver nøjagtig kobling mellem antennerne, men ikke indeholder detaljerede oplysninger om feltet distribution. Derfor kombinerer vi alle disse tre tilgange til at opnå en vis forståelse for øre-til-øre trådløs kommunikationskanal.

En cirkulær patch antenne blev brugt til at studere egenskaberne for magneto-dielektriske materialer. I afhandlingen fokuserede vi på tre ejendomme, effektivitet, kvalitet faktor og båndbredde af antennen. En analytisk metode bruges til beregning af egenskaber ved et lavt tab cirkulær patch antenne, mens en numerisk metode blev anvendt til at analysere en høj-tab cirkulær patch antenne. Den lave-tab magneto-dielektriske materialer kan potentielt anvendes til at miniature-udgave af størrelsen af antenner, der tilbyder højere effektivitet og større båndbredde end den dielektriske materialer.

Preface

This thesis is submitted in partial fulfillment of the requirements for obtaining the degree of Ph.D. in the electrical engineering at the Technical University of Denmark (DTU). The Ph.D. project is part of a major project “Wireless Coupling in Small Autonomous Apparatus” carried out from 2007-2011 in a cooperation between the Technical University of Denmark, Danish Technological Institute and Widex with financial support from the Danish National Advanced Technology Foundation.

There are several people who encouraged me and assisted me in these three years, and I would like to thank them all. First and foremost my supervisors, Professor Ph.D. Olav Breinbjerg (DTU Electrical Engineering), Professor Dr.techn. Ole Sigmund (DTU Mechanical Engineering) and Professor Dr.techn. Niels Asger Mortensen (DTU Fotonik). I am very grateful to them and specially to Professor Breinbjerg for always taking his time to discuss the work and the results during the project.

I would also like to express my gratitude to the partners from the joint research group “Wireless Coupling in Small Autonomous Apparatus” for the successful collaboration.

I am deeply grateful to my colleagues from the EMI section for technical support, discussion and advices.

Finally, I would like to thank my family for inspiration, support, and encouragement.

Technical University of Denmark, March, 2012.

Baqer Nour

Publications

The following publications are part of the thesis

[1] B. Nour and O. Breinbjerg, “Investigation of Bandwidth, Efficiency, and Quality Factor for Circular Patch Antennas with Magneto-Dielectric Substrate,” *Electromagnetics in Advanced Applications ICEAA 2011*, Torino, pp. 815 – 818, 12 September 2011.

[2] B. Nour and O. Breinbjerg, “Measurement and Characterization of the Path Loss for Ear-to-Ear Wireless Communication,” *Proceeding of the 5th European Conference on Antennas and Propagation EUCAP 2011*, Rome, pp. 1621 – 1625, 11 April 2011.

[3] B. Nour and O. Breinbjerg, “Electromagnetic Power Flow between Opposite Sides of a Lossy Dielectric Sphere Using Spherical Vector Wave Expansion,” *Proceeding of the 5th European Conference on Antennas and Propagation EUCAP 2010*, Barcelona, Spain, pp. 1 – 5, 12 April 2010.

Contents

1. Introduction

Hearing-aids already constitute an advanced technology and wireless coupling to hearing-aids will open for a range of completely new functionalities. Recent years tremendous development of wireless communication, involving ever smaller terminals, such as mobile phones, GPS receivers, headsets, etc., has caused a significant research interest in antenna miniaturization. The challenge is not just to develop geometrically small antennas but electrically small antennas that are less than half a wavelength of the RF signal – the traditional minimum length of resonant antennas. This recent research on antenna miniaturization has spawned many new results on fundamental properties and new design technologies involving high-permittivity ceramics, structural optimization, and novel materials. Indeed, while an antenna size of the order of one-tenth of a wavelength is realistic at present, it is necessary to further pursue these miniaturization techniques since hearing-aids antennas must be even smaller.

This Ph.D. project comprises 3 major areas of investigation for the antennas of wireless communication systems with hearing-aids. The first area is theoretical analysis of the ear-to-ear communication channel for communication directly between hearing-aids. This communication channel has received none to very little attention in the scientific literature and there are many aspects to be investigated. The second area concerns the development of an experimental setup for testing of ear-to-ear communications; again this is new ground with no established testing procedure and there are many aspects to be investigated. The third area concerns antenna miniaturization using magneto-dielectric materials. It is expected that these materials can outperform purely dielectric materials in terms of both impedance matching and bandwidth.

Ear-to-ear communication describes the situation where the left and the right hearing-aids communicate with each other using a wireless channel. Low data rate channels, 315 bit per second, have been introduced in the industry, which is used to synchronization of left and right volume controls and a few other basic functions [1]. The data rate of the ear-to-ear communication should be increased into tens of thousands of bits per second to transfer audio data between them. This will help in speech understanding by using beamforming techniques [1]. Most hearing-aids require less than 1 mW of power in total, adding wireless communication would increase the power consumption and reduce the battery life of the hearing-aid. Therefore, it is very important to design a very efficient wireless communication system. There are several aspects that regular the efficiency, such as the electrical length, the orientation, the location and the type of the antennas.

In wireless communication the concept of a link-budget is commonly used to characterize the performance of a communication system. The link-budget includes all the losses of the system, from the transmitter to the receiver. It is relatively simple to calculate the link-budget in free-space, where the path-loss of the free-space is well defined, while there is no general rule to characterize the path-loss near and around a human head. Most research on on-body communication [2]-[8], deal with path-loss for the case of a transmitter and a receiver are positioned at different locations on a human body, but do not consider the path-loss for ear-to-ear link.

Several treatments of the interaction of electromagnetic waves with the human head help us in understanding some of the problems that are related to ear-to-ear communication. In [8] and [10], the head is modeled by a multilayered sphere, which is subject to an incoming plane-wave. In [9], the distribution of the heating potential inside a lossy sphere having the same electrical characteristics as those of brain tissue was investigated. The heat was calculated from the magnitude of the electrical field. It was found that hot spots appear inside spheres with radii < 8 cm and only in the frequency range 300 MHz to 12 GHz. In [10], seven layers have been used to model the tissues of the head and the radius of the outer sphere is larger than the used radius in [9]. It is found that all objects exhibit a resonant behavior, where the absorbed energy increases significantly. For electrically small and medium-sized object, hot spot effects are significant over the frequency range for which resonance absorption occurs. The higher the frequency the poorer is the energy penetration. In [11], the specific absorption rate (SAR) was measured in models of a human head exposed to hand-held radios at 800 MHz. The SARs were calculated from internal electric field which is measured by isotropic implantable electric field probe. The magnitudes and the distributions of the SAR, affected by antenna position relative to the head, type of the antenna and location of its feed-point More realistic and detailed numerical models for the human head are presented in [12]-[14]. In [12], the head was exposed to a plane-wave from the front and the side, where the SAR values were calculated using a finite-difference time-domain (FDTD) method. Local maxima take form at the centre of the brain in the region of the eyes, and as the frequency increases the absorption becomes superficial (concentrated on the surface). Antenna implantation and communication link were studied in [13]. A multilayered spherical head was used beside a realistic head model. A spherical dyadic Green's function expansion was applied to analyze the electromagnetic characteristics of a dipole antennas implanted in the human head. The method is used to calculate the pattern of the implanted antenna and the maximum coupled power to an exterior half-wavelength dipole. As the distance between the implanted and the exterior antennas increases from 1 and 5 m, the maximum available power from the exterior decreases from -40 dB to -53 dB for 402 MHz. This level is more than 20 dB below the available power in free-space. In [14], the effect of ring jewelry was investigated on the energy absorbed in a head when illuminated by a 1.8 GHz dipole and a monopole on a conducting box.

There are three major approaches to analyze the ear-to-ear communication link; a) an analytical approach where the head is modeled as a homogenous sphere, and the electrical properties of the sphere are adjusted to emulate the properties of a real head, b) an experimental approach where direct measurements on the transmission properties (S_{21}) between two antennas are used to characterize the communication link, and c) a numerical approach with a head model having a realistic properties. The analytical approach gives accurate solutions and much faster than the numerical approach, but uses simple antennas. Both the analytical and the numerical solutions provide information about the coupling, the distribution of the fields inside and outside the head as well as the losses in the head. The experimental approach gives the actual values for the coupling between the antennas, while it is difficult to measure the fields inside and outside the head without interfering the fields. Since small antennas were used for the measurements,

it was necessary to design several antennas to carry out measurements at different frequency bands.

The thesis consists of six chapters; chapter 2 treats the theoretical approach for the ear-to-ear wireless communication. In this chapter the spherical vector wave expansion will be introduced and we will derive the fields of dipole antennas. Four different dipole antenna models will simulate transmitting and receiving antennas of different types and different orientations. The scattering and the total fields will be calculated and then validated. The spherical vector wave expansion involves series of an infinite number of terms. The numerical implementation of the spherical vector wave expansion truncates the series to a finite number of terms. The truncation produces error in the value of the field; this error is known as the truncation error. Depending on the truncation number, the truncation error can be very small. The truncation number will be discussed under the section of the convergence. The objective of the theoretical investigation is to provide a qualitative understanding of the propagation mechanisms.

Chapter 3 presents the experimental and the numerical approaches. The measurement setups consist of a network analyzer, a phantom head filled with material with similar electrical properties as a human head over a wide band, two identical antennas and a mechanical setup for aligning the head and the antennas. We designed the antennas and the mechanical setup, and they were built in-house. A set of antennas were designed to operate at different frequency bands. The structures and the measured performances of the antennas are given in this chapter. All the designed antennas are balanced, therefore it was necessary to design baluns which also work as transformers that match the antennas to the 50 Ω coaxial cables of the network analyzer. Two different baluns have been used; one is made of a quarter wavelength coaxial line and the second is made of lumped elements. Equivalent circuit of the lumped balun is presented together with a brief explanation about its properties and performance. Two parameters, including the distance of the antennas from the head and the positions of the antennas with respect to the head, will be investigated.

In chapter 4, we present the results of the theoretical model and the measurements. For the theoretical study, several parameters, like the operating frequency, the dimension of the sphere, the distance of the antennas and the electrical properties, will be investigated. Numerical approach simulates the ideal measurement setups, which includes the phantom head and the antennas without the presence of the mechanical setup, the room or the cables. The numerical model is implemented in HFSS [15], which is a commercial simulation program based on finite element method. The numerical approach provides us the fields' distributions inside and outside the phantom head. This phantom head has same electrical properties as the real phantom head which is used in the measurements. The electrical properties of real phantom head were provided by the factory [16].

In chapter 5, we investigate properties of the magneto-dielectric antenna. The antenna is a circular patch on top of a magneto-dielectric substrate. The properties of the antenna including the efficiency, the bandwidth, the quality factor and the dimensions of the antenna will be calculated analytically.

2. Ear-to-ear communication – Theoretical approach

2.1 Introduction

In this chapter, the theoretical formulation of the ear-to-ear communication will be presented by using spherical vector wave expansions (SWE). First, the spherical vector wave functions will be introduced as a solution for the electromagnetic wave equation. Then general formulas will be derived to calculate the power that is dissipated in a dielectric sphere, which represent a human head, and that is accepted by the antenna. The antennas are modeled by dipoles, and therefore we will derive the spherical vector wave expansion of a z-oriented electric dipole antenna, whereas the expansions of the remaining antennas will be given in appendix B "Source coefficients". Later, general formulas will be derived for the scattering and total coefficients. Rotation and translation algorithms will be presented and they will be used to calculate the S-parameters. At last, truncation numbers of the SWE will be estimated.

2.2 Spherical vector wave expansion

The spherical vector wave expansion expresses the electromagnetic field as an infinite series of spherical vector wave functions weighted by spherical coefficients. Spherical wave functions were introduced by W. W. Hansen [17], then a detailed formulation and derivation was given by Stratton [18]. In relation to the spherical near-field antenna measurements, J. E. Hansen [19] gives a more detailed formulation of the spherical vector wave expansion and the scattering matrix description of an antenna; his notation is used in this thesis.

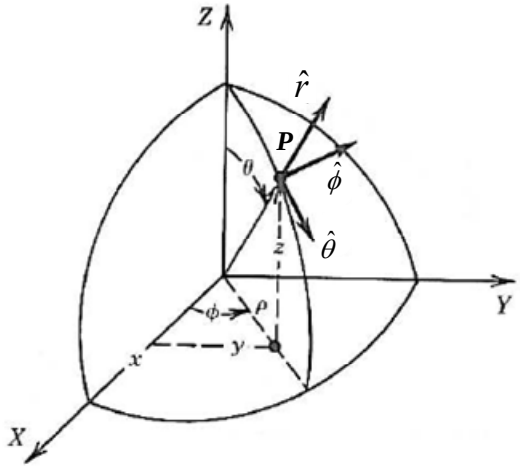

Fig. 2.1: Rectangular and spherical coordinate systems. The figure is copied from [20].

A point P at the coordinates (x, y, z) in Fig. 2.1 can also be described by the spherical coordinate (r, θ, ϕ), which is more appropriate for a spherical object. The expressions of the SWE in a source-free region can be derived by solving the wave equation (2.1) [18, eq. (7.2)] of the electric field $\vec{E}$ in a spherical coordinate system, which is shown in Fig. 2.1

$$\nabla^2 \vec{E} + k^2 \vec{E} = 0 \tag{2.1}$$

where $k = \omega\sqrt{\varepsilon\mu}$ is the wave number, with ε and μ being the permittivity and the permeability of the medium, respectively. To solve this equation, let a scalar function ψ be a solution to the scalar wave function,

$$\nabla^2 \psi + k^2 \psi = 0 \tag{2.2}$$

where ψ is called the generating function. It is possible to construct two vectors $\vec{F}_1$ and $\vec{F}_2$ from the function ψ, that are solutions to (2.1),

$$\vec{F}_1 = \nabla\psi \times \hat{r} \tag{2.3a}$$

$$\vec{F}_2 = k^{-1}\nabla \times \vec{F}_1 \tag{2.3a}$$

where $\vec{F}_1$ and $\vec{F}_2$ correspond to the $\vec{M}$ and $\vec{N}$ vector wave functions in Stratton's notation respectively. By utilizing the method of separation of variables, it is possible to obtain the expression of the generating function. The generating function ψ can be written as a product of independent terms,

$$\psi(r,\theta,\phi) = \psi_1(r)\psi_2(\theta)\psi_3(\phi) \tag{2.4}$$

and solving (2.2) by separation of variables gives

$$\psi_{mn}^{(c)}(r,\theta,\phi) = \frac{1}{\sqrt{2\pi}} \frac{1}{\sqrt{n(n+1)}} \left(-\frac{m}{|m|}\right)^m z_n^{(c)}(kr)\overline{P}_n^{|m|}(\cos\theta)e^{jm\phi} \tag{2.5}$$

according to [19, eq. (2.18)], with n = 1, 2, 3, …, m = -n, -n + 1, … , n – 1, n, $\overline{P}_n^{|m|}$ is the normalized associated Legendre function of first kind of the degree n and the order $|m|$, which is related to the Legendre function by the relation,

$$\overline{P}_n^{|m|}(\cos\theta) = \sqrt{\frac{2n+1}{2}\frac{(n-|m|)!}{(n+|m|)!}} P_n^{|m|}(\cos\theta) \tag{2.6}$$

Time factor exp(-$j\omega t$) is used in this thesis, where $j = \sqrt{-1}$, $\omega = 2\pi f$ is the radian frequency and t is the time factor. The radial function $z_n^{(c)}$ is specified by an upper index c as one of the functions

$$z_n^{(1)} = j_n(kr) \quad \text{(spherical Bessel function)} \tag{2.7a}$$

$$z_n^{(2)} = n_n(kr) \quad \text{(spherical Neumann function)} \tag{2.7b}$$

$$z_n^{(3)} = h_n^{(1)}(kr) = j_n(kr) - jn_n(kr) \quad \text{(spherical Hankel function of the first kind)} \tag{2.7c}$$

$$z_n^{(4)} = h_n^{(2)}(kr) = j_n(kr) + jn_n(kr) \quad \text{(spherical Hankel function of the second kind)} \tag{2.7d}$$

where c = 1 and 2 indicate standing waves, while c = 3 represents an outward propagation wave and c = 4 an inward propagation wave. From (2.3) and (2.5), the spherical wave functions defined by [19, eq. (2.20) and (2.21)], are also introduced here:

$$\vec{F}_{1nm}^{(c)}(r,\theta,\phi)=\frac{1}{\sqrt{2\pi}}\frac{1}{\sqrt{n(n+1)}}\left(-\frac{m}{|m|}\right)^{m}e^{jm\phi}\cdot$$
$$R_{1n}^{(c)}(kr)\left\{\hat{\theta}\frac{jm\overline{P}_n^{|m|}(\cos\theta)}{\sin\theta}-\hat{\phi}\frac{\mathrm{d}\overline{P}_n^{|m|}(\cos\theta)}{\mathrm{d}\theta}\right\} \tag{2.8}$$

and,

$$\vec{F}_{2nm}^{(c)}(r,\theta,\phi)=\frac{1}{\sqrt{2\pi}}\frac{1}{\sqrt{n(n+1)}}\left(-\frac{m}{|m|}\right)^{m}\mathrm{e}^{jm\phi}\cdot$$
$$\left\{\hat{r}\frac{n(n+1)}{kr}R_{1n}^{(c)}(kr)\overline{P}_n^{|m|}(\cos\theta)+R_{2n}^{(c)}(kr)\left(\hat{\theta}\frac{\mathrm{d}\overline{P}_n^{|m|}(\cos\theta)}{\mathrm{d}\theta}+\hat{\phi}\frac{jm\overline{P}_n^{|m|}(\cos\theta)}{\sin\theta}\right)\right\} \tag{2.9}$$

where

$$R_{sn}^{(c)}(kr)=\begin{cases}z_n^{(c)}(kr); & s=1\\ \dfrac{1}{kr}\dfrac{\mathrm{d}}{\mathrm{d}(z_n^{(c)}(kr))}\left\{krz_n^{(c)}(kr)\right\}; & s=2\end{cases} \tag{2.10}$$

The electric and the magnetic fields in a source-free region can be written as [19, eq. (2.22) and (2.23)],

$$\vec{E}(r,\theta,\phi)=\frac{k}{\sqrt{\eta}}\sum_{csmn}Q_{smn}^{(c)}\vec{F}_{smn}^{(c)}(r,\theta,\phi) \tag{2.11}$$

$$\vec{H}(r,\theta,\phi)=-jk\sqrt{\eta}\sum_{csmn}Q_{smn}^{(c)}\vec{F}_{3-s,m,n}^{(c)}(r,\theta,\phi) \tag{2.12}$$

with s = 1, 2, $\eta=\sqrt{\varepsilon/\mu}$ being the intrinsic admittance of the medium and $Q_{smn}^{(c)}$ being the spherical coefficient. The index, c, is chosen depending on the location of the region in Fig. 2.2; c = 1 in region 1, while in region 2 there are two options either c = 1 and 2 or 3 and 4, and c = 3 in region 3.

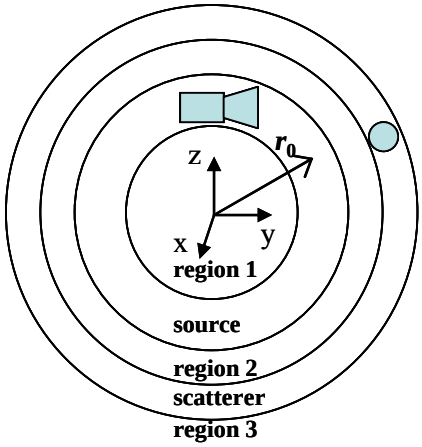

Fig. 2.2: Source-free regions 1, 2 and 3, where the SWE is valid.

2.3 Power computation

In this section, the derivation of a general formula will be introduced to compute the power dissipated within a spherical volume. Bringing a lossy dielectric sphere near a dipole antenna causes some power loss within the sphere, while the remaining is lost by radiation. The dissipated power within the sphere is the net power that flows into the sphere, so it becomes [21, eq. (2.59a)],

$$P_{\text{dis}} = \text{Re}\frac{1}{2}\oint_S \vec{E}\times\vec{H}^* \cdot\left(-d\vec{S}\right) \tag{2.13a}$$

$$P_{\text{dis}} = \frac{\omega}{2}\int_V \varepsilon_0\varepsilon_r''\vec{E}\cdot\vec{E}^* dV + \frac{1}{2}\int_V \sigma\vec{E}\cdot\vec{E}^* dV + \frac{\omega}{2}\int_V \mu_0\mu_r''\vec{H}\cdot\vec{H}^* dV \tag{2.13b}$$

where (*) denotes the complex conjugate, $\varepsilon_r = \varepsilon_r' + j\varepsilon_r''$ is the relative permittivity, $\mu_r = \mu_r' + j\mu_r''$ is the relative permeability (the imaginary parts are positive because the used time factor is exp(-$j\omega t$)), σ is the conductivity and V is the volume of the sphere and S is the surface of the sphere. The first and the third terms in eq. (2.13b) are the losses resulting from polarization damping force, and the second term is the loss produced by conduction current $\sigma\vec{E}$ resulting in Joule heating [21, pp. 37].

The dissipated power in a dielectric sphere, as depicted in Fig. 2.2, can either be found from (2.13a) or (2.13b). Here (2.13a) is used to find the lost power, and the closed surface integral is taken on the dielectric sphere with radius a. Inside the sphere, the field is represented by spherical standing waves of type c = 1,

$$\vec{E}_1(r,\theta,\phi) = \frac{k_1}{\sqrt{\eta_1}}\sum_{smn} Q_{smn}^{t(1)}\vec{F}_{smn}^{(1)}(r,\theta,\phi) \tag{2.14}$$

$$\vec{H}_1(r,\theta,\phi) = -jk_1\sqrt{\eta_1}\sum_{smn} Q_{smn}^{t(1)}\vec{F}_{3-s,m,n}^{(1)}(r,\theta,\phi) \tag{2.15}$$

The superscript t indicates the total field inside the dielectric sphere, $k_1 = k_0\sqrt{\varepsilon_r}$ and $\eta_1 = \eta_0\sqrt{\varepsilon_r}$, where k_0 and η_0 are respectively the free-space wave number and the intrinsic admittance. Though the Bessel function is a real function, the fields will be complex since both k_1 and η_1 are complex numbers. By inserting (2.14) and (2.15) into (2.13a) and integrating over the surface of the dielectric sphere, the dissipation in the sphere becomes,

$$P_{\text{dis}} = \text{Re}\left\{ j\frac{|k_1|^2\left(\sqrt{\eta_1}\right)^*}{2\sqrt{\eta_1}}\sum_{smn}\sum_{\sigma\mu\upsilon}\int_0^{2\pi}\int_0^{\pi} Q_{smn}^{t(1)}\vec{F}_{smn}^{(1)}(a,\theta,\phi)\times Q_{\sigma\mu\upsilon}^{t(1)*}\vec{F}_{\sigma\mu\upsilon}^{(1)*}(a,\theta,\phi)\cdot\left(-\hat{r}\right)a^2\sin\theta d\theta d\phi \right\}$$

and utilizing the orthogonality property, Eq. (A.4) in appendix A, yields,

$$P_{\text{dis}} = \text{Re}\left\{ j\frac{|k_1|^2\left(\sqrt{\eta_1}\right)^*}{2\sqrt{\eta_1}}\sum_{smn}\left|Q_{smn}^{t(1)}\right|^2\int_0^{2\pi}\int_0^{\pi} \vec{F}_{smn}^{(1)}(a,\theta,\phi)\times\vec{F}_{3-s,mn}^{(1)*}(a,\theta,\phi)\cdot\left(-\hat{r}\right)a^2\sin\theta d\theta d\phi \right\}$$

and it becomes,

$$P_{\text{dis}} = \text{Re}\left\{ ja^2 \frac{|k_1|^2 \left(\sqrt{\eta_1}\right)^*}{2\sqrt{\eta_1}} \sum_{smn} \left|Q_{smn}^{t(1)}\right|^2 (-1)^s R_{sn}^{(1)}(k_1 a) R_{3-s,n}^{(1)*}(k_1 a) \right\} \tag{2.16}$$

The radiated power P_{rad} is the power radiates to the far-field. The outgoing field will be represented by spherical wave functions of type $c = 3$,

$$\vec{E}_3(r,\theta,\phi) = \frac{k_0}{\sqrt{\eta_0}} \sum_{smn} \left(Q_{smn}^{i(3)} + Q_{smn}^{s(3)}\right) \vec{F}_{smn}^{(3)}(r,\theta,\phi) \tag{2.17}$$

$$\vec{H}_3(r,\theta,\phi) = -jk_0\sqrt{\eta_0} \sum_{smn} \left(Q_{smn}^{i(3)} + Q_{smn}^{s(3)}\right) \vec{F}_{3-s,m,n}^{(3)}(r,\theta,\phi) \tag{2.18}$$

with superscripts i and s indicating the incident (fixed dipole moment, see section 2.4) and the scattered fields, respectively. The radiated power P_{rad} can be calculated over a sphere that has a radius that tends to infinity, as follows,

$$P_{\text{rad}} = \text{Re}\frac{1}{2}\oint_S \vec{E} \times \vec{H}^* \cdot d\vec{S}$$

$$\Downarrow$$

$$P_{\text{rad}} = \text{Re}\left\{ \frac{1}{2} \sum_{smn} \left|Q_{smn}^{i(3)} + Q_{smn}^{s(3)}\right|^2 \lim_{r\to\infty} \left\{ jk_0^2 \oint_S \vec{F}_{smn}^{(3)}(r,\theta,\phi) \times \vec{F}_{3-s,mn}^{(3)*}(r,\theta,\phi) \cdot d\vec{S} \right\} \right\} \tag{2.19}$$

where the integral part is given in [19, sec. (2.24)]. This yields

$$P_{\text{rad}} = \frac{1}{2} \sum_{smn} \left|Q_{smn}^{i(3)} + Q_{smn}^{s(3)}\right|^2 \tag{2.20}$$

In presence of the lossy dielectric sphere, the radiated power from the antenna P_{source} is the sum of the dissipated and the far-field radiation powers,

$$P_{\text{source}} = P_{\text{rad}} + P_{\text{dis}} \tag{2.21}$$

2.4 Excitation

The configuration of interest is depicted in Fig. 2.3. A sphere (region 1) of radius a is illuminated by either an electric hertzian dipole antenna (EHD) or a magnetic hertzian dipole antenna (MHD). Both the EHD and the MHD are good candidates to model electrically small antennas which represent a transmitting antenna (Tx) and a receiving antenna (Rx). Two orientations with respect to the sphere have been considered; orthogonal and tangential. In the figure, the red arrow represents an orthogonal oriented dipole antenna and the green arrow a tangential oriented dipole antenna. The dipoles can be either EHD or MHD in both orientations. The hertzian dipole antenna has a simple current distribution, which is given by the formula,

$$\vec{J}_{e,m} = \hat{p} d_{e,m} \delta(\vec{r} - \vec{r}') = \hat{p} d_{e,m} \frac{\delta(r - r_0)\delta(\theta - \pi)\delta(\phi)}{r^2 \sin\theta} \tag{2.21}$$

with $\hat{p}$ being a unit vector indicating the orientation, $d_{e,m}$ is the dipole moment, e denotes an electric dipole, m a magnetic dipole and δ is the Dirac delta function. The electric field generated by the hertzian dipole antenna in a free-space can be expressed in terms of the SWE as:

$$\vec{E}^{i}_{e,m}(r,\theta,\phi) = \frac{k_0}{\sqrt{\eta_0}} \sum_{smn} Q^{i(c)}_{smn} \vec{F}^{(c)}_{smn}(r,\theta,\phi) \tag{2.22}$$

$$\vec{H}^{i}_{e,m}(r,\theta,\phi) = -jk_0\sqrt{\eta_0} \sum_{smn} Q^{i(c)}_{smn} \vec{F}^{(c)}_{3-s,m,n}(r,\theta,\phi) \tag{2.23}$$

In order to determine the spherical coefficients of the antenna, the reciprocity theorem in [19, pp. 332] was applied. In the case of a z-oriented EHD (EHDz), the coefficients can be found by utilizing [3, eq. (A1.78)],

$$Q^{i(c)}_{smn} = (-1)^{m+1} \int_V \left(\frac{k}{\sqrt{\eta}} \vec{F}^{(4-c)}_{s,-m,n} \cdot \vec{J}_e + jk\sqrt{\eta} \vec{F}^{(4-c)}_{3-s,-m,n} \cdot \vec{J}_m \right) \mathrm{d}V \tag{2.24}$$

$$Q^{i(c)}_{smn} = (-1)^{m+1} \int_0^{2\pi} \int_0^{\pi} \int_0^{\infty} \frac{k}{\sqrt{\eta}} \vec{F}^{(4-c)}_{s,-m,n}(r,\theta,\phi) \cdot \hat{z} d_e \delta(r - r_0)\delta(\theta - \pi)\delta(\phi) \mathrm{d}r \mathrm{d}\theta \mathrm{d}\phi$$

the unit vector, $\hat{z}$, is expressed in terms of the spherical components at $r = r_0$, $\theta = \pi$ and $\phi = 0$, so the $Q^{i(c)}_{smn}$ becomes,

$$Q^{(c)}_{smn} = (-1)^{m+1} d_e \frac{k}{\sqrt{\eta}} \vec{F}^{(4-c)}_{s,-m,n}(r_0, \pi, 0) \cdot (-\hat{r}) \tag{2.25}$$

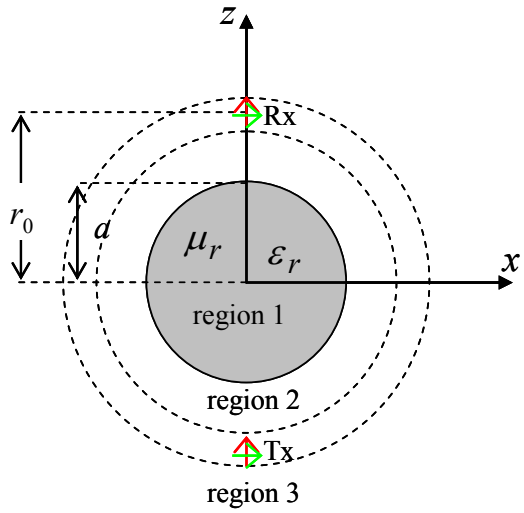

Fig. 2.3: The dipole antennas near the dielectric sphere.

From the special values in [19, pp. 325-327], it is found that the only non-zero solutions are related to the modes with $s = 2$ and $m = 0$ while n can have any integer value between 1 and ∞, i.e.

$$Q_{20n}^{i(c)} = d_e \frac{k_0}{\sqrt{\eta_0}} (-1)^n \sqrt{\frac{n(n+1)(2n+1)}{4\pi}} \frac{z_n^{(4-c)}(k_0 r_0)}{k_0 r_0} \tag{2.26}$$

where $c = 3$ for $r > r_0$ and $c = 1$ for $r < r_0$. The coefficients will be re-written in terms of Q_{201} which is the coefficient of the EHDz in the origin of the coordinate system [19, eq. (2.117)]:

$$Q_{20n}^{i(c)} = Q_{201} C_{20n}^{21(c)}(k_0 r_0) \tag{2.27}$$

and inserting

$$C_{20n}^{21(c)}(k_0 r_0) = (-1)^{n+1} \sqrt{\frac{3}{2}} \sqrt{n(n+1)(2n+1)} \frac{z_n^{(4-c)}(k_0 r_0)}{k_0 r_0} \tag{2.28}$$

$$Q_{201} = -d_e \frac{1}{\sqrt{6\pi}} \frac{k_0}{\sqrt{\eta_0}} \tag{2.29}$$

where $C_{20n}^{21(c)}(k_0 r_0)$ is the translation coefficient that is given in [19, eq. (A3.18)] with some modifications where the number that describes the mode type c in (2.27) and (2.28) has different meaning from the used one in [19]. For the translation coefficients $c = 1$ is used for $r < r_0$ and $c = 3$ for $r > r_0$. By utilizing the symmetry property [19, eq. (A3.10)], it is possible to derive the translation coefficient in [19, eq. (A3.18)]. The generated electric and magnetic fields by the EHDz are,

$$\vec{E}_e^{z,i}(r,\theta,\phi) = \frac{k_0}{\sqrt{\eta_0}} \sum_{n=1}^{\infty} Q_{201} C_{20n}^{21(1)}(k_0 r_0) \vec{F}_{20n}^{(1)}(r,\theta,\phi) \tag{2.30}$$

and

$$\vec{H}_e^{z,i}(r,\theta,\phi) = -jk_0 \sqrt{\eta_0} \sum_{n=1}^{\infty} Q_{201} C_{20n}^{21(1)}(k_0 r_0) \vec{F}_{10n}^{(1)}(r,\theta,\phi) \tag{2.31}$$

Similar procedures can be used to calculate the fields for the EHDx, the MHDz and EHDx. Without showing the derivation steps, the fields of the MHDz are,

$$\vec{E}_m^{z,i}(r,\theta,\phi) = \frac{k_0}{\sqrt{\eta_0}} \sum_{n=1}^{\infty} Q_{101} C_{10n}^{11(1)}(k_0 r_0) \vec{F}_{10n}^{(1)}(r,\theta,\phi) \tag{2.32}$$

and

$$\vec{H}_m^{z,i}(r,\theta,\phi) = -jk_0 \sqrt{\eta_0} \sum_{n=1}^{\infty} Q_{101} C_{10n}^{11(1)}(k_0 r_0) \vec{F}_{20n}^{(1)}(r,\theta,\phi) \tag{2.33}$$

and

$$Q_{10n}^{i(c)} = Q_{101} C_{10n}^{11(c)}(k_0 r_0) \tag{2.34q}$$

$$C_{10n}^{11(c)} = C_{20n}^{21(c)} \tag{2.34b}$$

$$Q_{101} = -d_m \frac{j}{\sqrt{6\pi}} k_0 \sqrt{\eta_0} \tag{2.34c}$$

with Q_{101} being the coefficient of the MHDz at the origin of the coordinate system. The MHDz and the EHDz are dual sources where their fields are interrelated by $\vec{E}_m^{zi} = \vec{H}_e^{zi} / \eta_0$ and $\vec{H}_m^{zi} = -\eta_0 \vec{E}_e^{zi}$. The fields of the MHDz can be also found by utilizing duality principle, since EHDz and MHDz are dual sources. The fields and the coefficients of the *x*-oriented electric and magnetic dipoles are given in appendix B.

2.5 Scattered and total fields

In order to calculate the *Q*-coefficient for the SWEs of the scattered and total fields, the fields must satisfy the boundary conditions on the surface of the sphere. The boundary conditions require that the tangential components of the electric and the magnetic fields shall be continuous across the surface. Equations (2.14) and (2.15) describe the electric and the magnetic fields inside the dielectric sphere, while the total field outside the sphere (but inside the radius of the antenna) is described by the following equations,

$$\vec{E}_2(r,\theta,\phi) = \frac{k_0}{\sqrt{\eta_0}} \sum_{smn} \left(Q_{smn}^{i(1)} \vec{F}_{smn}^{(1)}(r,\theta,\phi) + Q_{smn}^{s(3)} \vec{F}_{smn}^{(3)}(r,\theta,\phi) \right) \tag{2.35}$$

$$\vec{H}_2(r,\theta,\phi) = -jk_0 \sqrt{\eta_0} \sum_{smn} \left(Q_{smn}^{i(1)} \vec{F}_{3-s,m,n}^{(1)}(r,\theta,\phi) + Q_{smn}^{s(3)} \vec{F}_{3-s,m,n}^{(3)}(r,\theta,\phi) \right) \tag{2.36}$$

The boundary conditions $\hat{r} \times \vec{E}_2 = \hat{r} \times \vec{E}_1$ and $\hat{r} \times \vec{H}_2 = \hat{r} \times \vec{H}_1$ construct a system of equations which are used to find the *Q*-coefficients. The spherical modes will be decoupled by using the products of tangential components property [19, Eq. (A1.69)]. This yields the following equations

$$\frac{k_0}{\sqrt{\eta_0}} \left[Q_{smn}^{i(1)} R_{sn}^{(1)}(k_0 a) + Q_{smn}^{s(3)} R_{sn}^{(3)}(k_0 a) \right] = \frac{k_1}{\sqrt{\eta_1}} \left[Q_{smn}^{t(1)} R_{sn}^{(1)}(k_1 a) \right] \tag{2.37a}$$

$$k_0 \sqrt{\eta_0} \left[Q_{smn}^{i(1)} R_{3-s,n}^{(1)}(k_0 a) + Q_{smn}^{s(3)} R_{3-s,n}^{(3)}(k_0 a) \right] = k_1 \sqrt{\eta_1} \left[Q_{smn}^{t(1)} R_{3-s,n}^{(1)}(k_1 a) \right] \tag{2.37b}$$

The scattering and the total spherical coefficients are then found to be

$$Q_{smn}^{s(3)} = Q_{smn}^{i(1)} \frac{\sqrt{\mu_r} R_{sn}^{(1)}(k_1 a) R_{3-s,n}^{(1)}(k_0 a) - \sqrt{\varepsilon_r} R_{3-s,n}^{(1)}(k_1 a) R_{sn}^{(1)}(k_0 a)}{\sqrt{\varepsilon_r} R_{3-s,n}^{(1)}(k_1 a) R_{sn}^{(3)}(k_0 a) - \sqrt{\mu_r} R_{sn}^{(1)}(k_1 a) R_{3-s,n}^{(3)}(k_0 a)} \tag{2.38a}$$

$$\alpha_{smn} = \frac{Q_{smn}^{s(3)}}{Q_{smn}^{i(1)}} = \frac{\sqrt{\mu_r} R_{sn}^{(1)}(k_1 a) R_{3-s,n}^{(1)}(k_0 a) - \sqrt{\varepsilon_r} R_{3-s,n}^{(1)}(k_1 a) R_{sn}^{(1)}(k_0 a)}{\sqrt{\varepsilon_r} R_{3-s,n}^{(1)}(k_1 a) R_{sn}^{(3)}(k_0 a) - \sqrt{\mu_r} R_{sn}^{(1)}(k_1 a) R_{3-s,n}^{(3)}(k_0 a)} \tag{2.38b}$$

$$Q_{smn}^{t(1)} = Q_{smn}^{i(1)} (-1)^{s+1} \frac{1}{(k_0 a)^2} \frac{j}{\mu_r R_{sn}^{(1)}(k_1 a) R_{3-s,n}^{(3)}(k_0 a) - \sqrt{\varepsilon_r \mu_r} R_{3-s,n}^{(1)}(k_1 a) R_{sn}^{(3)}(k_0 a)} \tag{2.39a}$$

$$\beta_{smn} = \frac{Q_{smn}^{t(1)}}{Q_{smn}^{i(1)}} = (-1)^{s+1} \frac{1}{(k_0 a)^2} \frac{j}{\mu_r R_{sn}^{(1)}(k_1 a) R_{3-s,n}^{(3)}(k_0 a) - \sqrt{\varepsilon_r \mu_r} R_{3-s,n}^{(1)}(k_1 a) R_{sn}^{(3)}(k_0 a)} \tag{2.39b}$$

where Wronskian's relation [19, eq. (A1.11)] was used to reduce the nominator of $Q_{smn}^{t(1)}$. The coefficients of the scattering and the total fields in (2.38) and (2.39) represent general solutions for any incident field on a magneto-dielectric sphere ($k_1 = k_0\sqrt{\varepsilon_r \mu_r}$). For example Stratton [18, sec. 9.25] solved the problem of a plane-wave scattered by a dielectric sphere, where the plane-wave is *x*-polarized and propagates in the positive *z*-direction. The coefficients of the scattered field are here denoted a_n^r and b_n^r, which correspond to the normalized spherical wave functions of TE (s = 1) and TM (s = 2) modes. By using equations (2.38b) and (2.39b), and by substituting the variables, k_0, k_1 and a by $\rho = k_0 a$ and $N\rho = k_1 a$, it is possible to derive a_n^r and b_n^r. The derivation is given in appendix B.

An EHDz antenna, located on the *z*-axis at 1 m distance from the origin, illuminates a dielectric sphere of a radius a = 7 cm and having a dielectric constant $\varepsilon_1 = \varepsilon_r$ = 10. The centre of the sphere is located at the origin of the coordinate system. The components of the electric and the magnetic fields were calculated at observation points on lines that extended from the origin and made θ_0 angles with the *z*-axis.

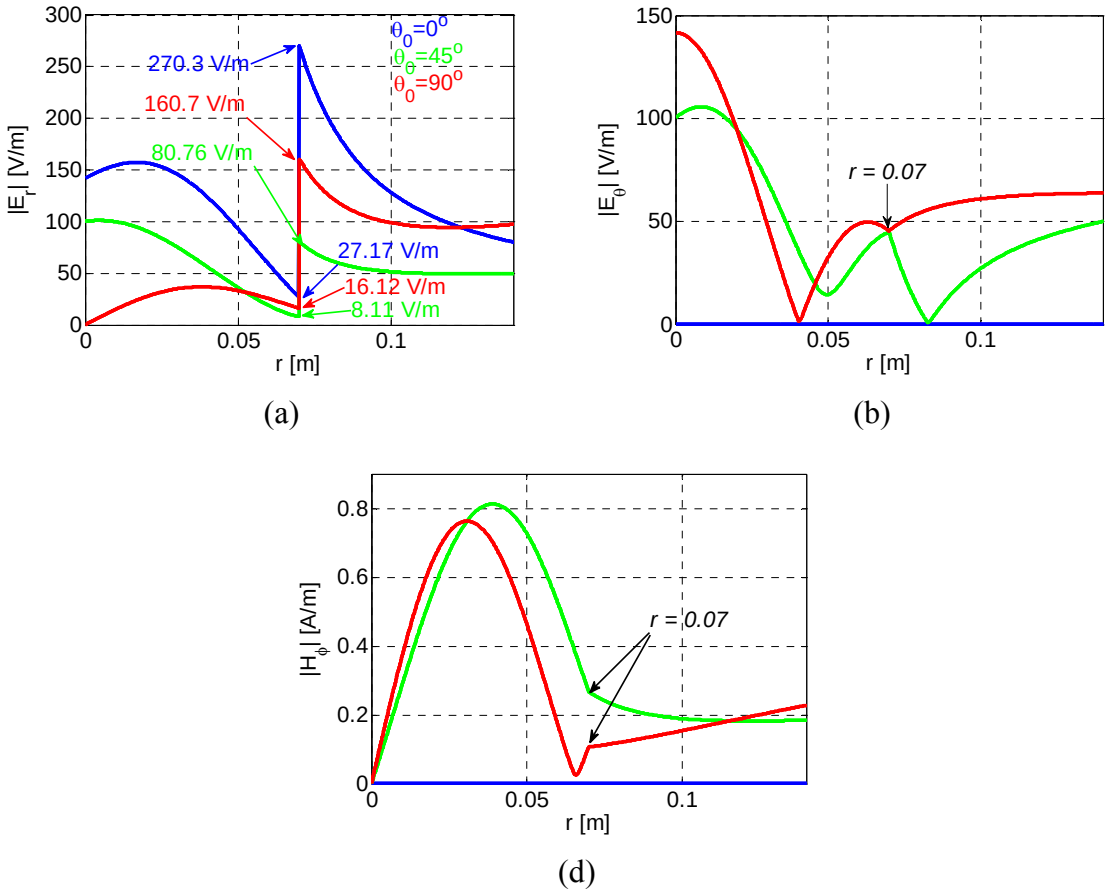

Fig. 2.4: The electric and the magnetic field components for a *z*-oriented electric dipole near a dielectric sphere, that has a radius a = 7 cm and a dielectric constant ε_r = 10. The dipole is positioned at (x, y, z) = (0, 0, -1) m and operates at 1 GHz.

All the lines are situated in the *xz*-plane. In Fig. 2.4, the blue lines represent the field components on the line that has $\theta_0 = 0^o$, while for the red and the green lines $\theta_0 = 45^o$ and 90^o, respectively. These plots are generated by using Matlab, which is a programming environment for algorithm development, data analysis, visualization, and numerical computation [22]. Both the electric and the magnetic fields must satisfy the conditions,

$$\hat{r}\cdot\left(\varepsilon_2\vec{E}_2-\varepsilon_1\vec{E}_1\right)=0\Rightarrow\frac{E_{2,r}}{E_{1,r}}=\frac{\varepsilon_1}{\varepsilon_2}=10 \tag{2.40a}$$

$$\hat{r}\times\vec{E}_1=\hat{r}\times\vec{E}_2\quad,\quad\hat{r}\times\vec{H}_1=\hat{r}\times\vec{H}_2 \tag{2.40b}$$

where subscript 1 and 2 indicate the fields inside and outside the sphere. The ratios of the radial components of the electric fields are not exactly 10, but they are 9.95, 9.97 and 9.96, as seen in Fig. 2.4a, for the blue, the red and the green lines, respectively. The errors are very small and can be reduced further by calculating the fields as close as possible to the surface of the sphere. The tangential components, in Fig. 2.4b and 2.4c, of the electric and the magnetic fields are continues on the surface of the sphere. The boundary conditions are thus satisfied which is validated by the computations.

2.6 Rotation and translation algorithms

It is a straightforward to calculate the coefficients of the EHDz, situated on the *z*-axis, by using the reciprocity theory. For other orientations or different positions, the calculations of the coefficients become more complicated. Therefore, the rotation and the translation coefficients need to elaborate on the sequence. The sequences of the rotation and the translation are shown in Fig 2.5. The original coordinate system is (*x*, *y*, *z*) and the new coordinate system is (x'', y'', z''). During the rotation and the translation sequences auxiliary coordinate systems will be used and they will have the same notations of Fig. 2.5.

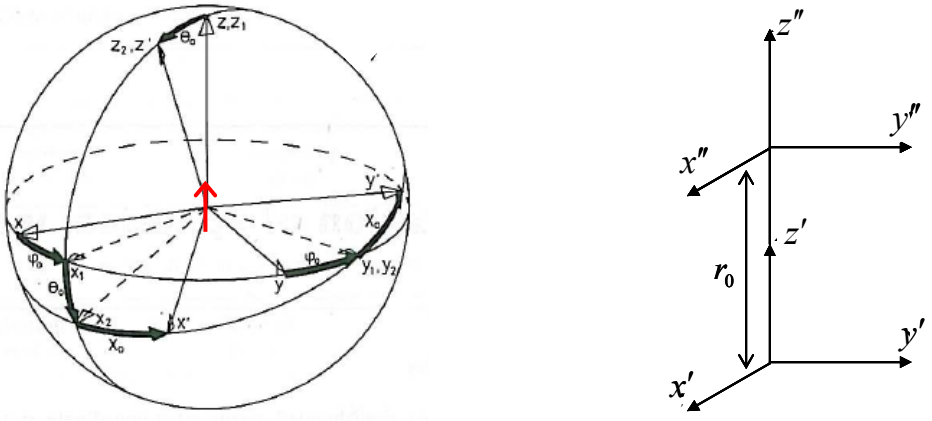

(a) (b)

Fig. 2.5: The rotation (left figure) and translation (right figure) of the primed coordinate system relative to the unprimed. Fig.2.5a is copied from [19].

The sequence of rotations and translation are as following, first an auxiliary coordinate system (x_1, y_1, z_1) lays on the (x, y, z) rotates an angle φ_0 around the z-axis, then a new auxiliary coordinate system (x_2, y_2, z_2) lays on (x_1, y_1, z_1) rotates an angle θ_0 around the y_1-axis as it is seen in Fig. 2.5a, then the coordinate system (x', y', z') which lays on (x_2, y_2, z_2) rotates an angle χ_0 around the z_2-axis, and the last step is to translate the coordinate system (x'', y'', z'') which lays on the (x', y', z') a distance r_0 on the z'-axis as it is seen in Fig. 2.5b.

A spherical vector wave function $\vec{F}^{(c)}_{smn}(r,\theta,\phi)$ in one coordinate system (x, y, z) can be expanded in terms of a combination of spherical wave functions $\vec{F}^{(c)}_{smn}(r',\theta',\phi')$ in other coordinate system (x', y', z') using the equation in [19, eq. (A2.2)],

$$\vec{F}^{(c)}_{smn}(r,\theta,\phi) = \sum_{\mu=-n}^{n} e^{jm\phi_0} d^{n}_{\mu m}(\theta_0) e^{j\mu\chi_0} \vec{F}^{(c)}_{s\mu n}(r',\theta',\phi') \qquad \text{s(2.41)}$$

where $\phi_0 = \varphi_0$. The χ_0- and ϕ_0-rotations give rise to phase shifts only, the θ_0-rotation also gives rise to the rotation coefficient $d^{n}_{\mu m}(\theta_0)$. Computation of $d^{n}_{\mu m}(\theta_0)$ is described by the following equation [19, eq. (A2.3)],

$$d^{n}_{\mu m}(\theta_0) = \sqrt{\frac{(n+\mu)!(n-\mu)!}{(n+m)!(n-m)!}} \sum_{\substack{\zeta=-\mu-m \\ \zeta\geq 0}}^{\zeta=n-m} \left\{ \binom{n+m}{n-\mu-\zeta} \binom{n-m}{\zeta} (-1)^{n-\mu-\zeta} \cdot \left(\cos\frac{\theta_0}{2}\right)^{2\zeta+\mu+m} \left(\sin\frac{\theta_0}{2}\right)^{2n-2\zeta-\mu-m} \right\} \qquad (2.42)$$

where the binomial coefficient is defined as,

$$\binom{n}{m} = \frac{n!}{(n-m)!m!}$$

The limits for the $\zeta-$summation are not given in [19], but it is a simple matter to find them. From the first binomial coefficient, ζ should satisfy the condition $n+m \geq n-\mu-\zeta \Rightarrow \zeta \geq -\mu-m$ and from the second binomial coefficient $\zeta \leq n-m$. The rotation coefficient $d^{n}_{\mu m}(\theta_0)$ may also be calculated using special cases [19, eq. (A2.17)-(A2.19)] and the recurrence relation [19, eq. (A2.14)], or by using Fourier series [19, eq. (A2.11)]. In this thesis, the rotation coefficients are calculated by using the equation (2.42).

The translation is always along the positive z-direction, see Fig. 2.5b. In reference to Fig. 2.5b, the spherical vector function $\vec{F}^{(c)}_{smn}(r,\theta,\phi)$ shall be expressed as a combination of spherical vector waves defined in the primed coordinate system [19, eq. (A3.1) and (A3.2)],

$$\vec{F}_{s\mu n}^{(c)}(r',\theta',\phi') = \sum_{\sigma=1}^{2}\sum_{\substack{\nu=|\mu|\\ \nu\neq 0}}^{\infty} C_{\sigma\mu\nu}^{sn(c)}(kr_0)\vec{F}_{\sigma\mu\nu}^{(1)}(r'',\theta'',\phi'') \qquad r'' < |r_0| \tag{2.43a}$$

$$\vec{F}_{s\mu n}^{(c)}(r',\theta',\phi') = \sum_{\sigma=1}^{2}\sum_{\substack{\nu=|\mu|\\ \nu\neq 0}}^{\infty} C_{\sigma\mu\nu}^{sn(1)}(kr_0)\vec{F}_{\sigma\mu\nu}^{(c)}(r'',\theta'',\phi'') \qquad r'' > |r_0| \tag{2.43b}$$

where $C_{\sigma\mu\nu}^{sn(c)}(kr_0)$ is the translation coefficient [19, eq. (A3.3)]. Since the azimuthal index μ involved on both sides of (2.43), the $\phi-$dependence of the wave function is preserved under *z*-translation. The calculation of the translation coefficient involves linearization coefficients that are known as Gaunt coefficients [23]. The computation method that calculates Gaunt coefficients in [19, Eq. (A3.6)] is slow and inefficient. There is another method [23] and [24] that utilizes recurrence formulas to calculate Gaunt coefficients. The method in [24] reduces the computation time to ~ 1%, compared to the method in [19]. The method in [24] was implemented in Matlab, and was validated against the special coefficients [19, eq. (A3.20)].

The rotation and the translation algorithms were validated by visual inspection of the radiation patterns of a dipole antenna at the origin and the radiation patterns after a sequence of rotations and translations. Fig 2.6 shows the real values of the electric field (at time t = 0) that is generated by the EHDz in the origin and after the translation and rotation of the coordinate system, where r_0 = 10 cm and θ_0 = 45 degree. The dipole operates in the free-space at 1 GHz. The color scale is the magnitude of the real values of the electric field in V/m and the arrows indicate the polarizations of fields in the *xz*-plane, where the horizontal axis is the *x*-axis and the vertical axis is *z*-axis. By comparing the color patterns and the courses of the arrows, it is concluded that the rotation and the translation algorithms produce correct results. This is also built on several plots with different rotation angles and different distances are generated, where they are not shown here.

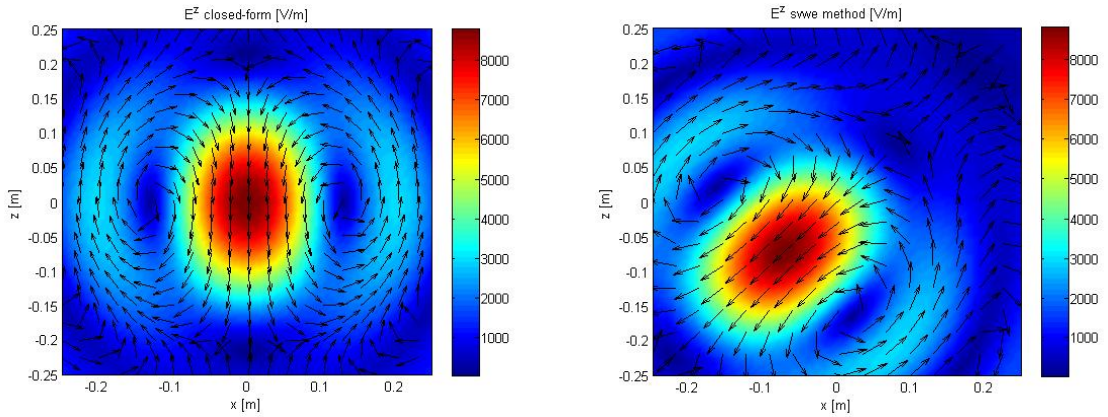

(a) (b)

Fig. 2.6: The electric fields distribution for an electric dipole antenna before and after the translation and rotation of the coordinate system.

2.7 Computation of S_{21} and S_{11}

The transmission coefficient S_{21}, which is the ratio of the received power to the transmitted power, represents a path-loss for an ideal case where both the transmitting and the receiving antennas are lossless. Here the steps to derive the transmission coefficient between two orthogonal EHD antennas near the dielectric sphere, where one antenna is transmitting (on the negative z-axis) and the second antenna is receiving are shown. The electric field generated by the transmitting antenna is described by (2.35), but in the present case the receiving antenna is located at $r_1 > r_0$ and therefore the terms of the incident field should be of type $c = 3$,

$$\vec{E}_2(r,\theta,\phi) = \frac{k_0}{\sqrt{\eta_0}} Q_{201} \sum_{n=1}^{N_1} C_{20n}^{21(3)}(k_0 r_0)\left(1+\alpha_{20n}\right)\vec{F}_{20n}^{(3)}(r,\theta,\phi) \tag{2.44}$$

with $C_{20n}^{21(3)}(k_0 r_0)$, Q_{201} and α_{20n} defined by (2.28), (2.29) and (2.38a), respectively, and N_1 is the number of modes. The first step is to rotate the coordinate system through the angles $(\theta_0, \phi_0, \chi_0)$, so the electric field becomes,

$$\vec{E}_2(r,\theta,\phi) = \frac{k_0}{\sqrt{\eta_0}} Q_{201} \sum_{n=1}^{N_1} C_{20n}^{21(3)}(k_0 r_0)\left(1+\alpha_{20n}\right)\sum_{\mu=-n}^{n} d_{\mu 0}^{n}(\theta_0) e^{j\mu\chi_0} \vec{F}_{2\mu m}^{(3)}(r',\theta',\phi') \tag{2.45}$$

The origin of the coordinate system is then translated to the position of the receiving antenna $r_1 > r_0$,

$$\vec{E}_2(r,\theta,\phi) = \frac{k_0}{\sqrt{\eta_0}} Q_{201} \sum_{n=1}^{N_1} C_{20n}^{21(3)}(k_0 r_0)\left(1+\alpha_{20n}\right)\cdot$$
$$\sum_{\mu=-n}^{n}\sum_{\sigma=1}^{2}\sum_{\substack{\nu=|\mu| \\ \nu\neq 0}}^{N_2} d_{\mu 0}^{n}(\theta_0) e^{j\mu\chi_0} C_{\sigma\mu\nu}^{2n(1)}(k_0 r_1)\vec{F}_{\sigma\mu\nu}^{(1)}(r'',\theta'',\phi''), \qquad r'' < |r_1| \tag{2.46}$$

The double primed variables are the parameters of the new coordinate system. The standing vector wave function $\vec{F}_{\sigma\mu\nu}^{(1)}$ may be written as a sum of incoming and outgoing waves, each of amplitude 0.5,

$$\vec{F}_{\sigma\mu\nu}^{(1)} = \frac{1}{2}\left(\vec{F}_{\sigma\mu\nu}^{(3)} + \vec{F}_{\sigma\mu\nu}^{(4)}\right) \tag{2.47}$$

Equation (2.46) then becomes,

$$\vec{E}_2(r,\theta,\phi) = \frac{1}{2}\frac{k_0}{\sqrt{\eta_0}} Q_{201} \sum_{n=1}^{N_1} C_{20n}^{21(3)}(k_0 r_0)\left(1+\alpha_{20n}\right)\cdot$$
$$\sum_{\mu=-n}^{n}\sum_{\sigma=1}^{2}\sum_{\substack{\nu=|\mu| \\ \nu\neq 0}}^{N_2} d_{\mu 0}^{n}(\theta_0) e^{j\mu\chi_0} C_{\sigma\mu\nu}^{2n(1)}(k_0 r_1)\left(\vec{F}_{\sigma\mu\nu}^{(3)}(r'',\theta'',\phi'') + \vec{F}_{\sigma\mu\nu}^{(4)}(r'',\theta'',\phi'')\right) \quad , r'' < |r_1| \tag{2.48}$$

The incident waves have amplitudes $a_{\sigma\mu\nu}$ which, according to (2.48) are,

$$a_{\sigma\mu\nu} = \frac{1}{2} Q_{201} \sum_{n=1}^{N_1} e^{j\mu\chi_0} d_{\mu 0}^{n}(\theta_0) C_{\sigma\mu\nu}^{2n(1)}(k_0 r_1) C_{20n}^{21(3)}(k_0 r_0)\left(1+\alpha_{20n}\right) \tag{2.49}$$

According to [19, eq. (3.8)], the signal received by the receiving antenna (EHDz″) in the origin of the (x'', y'', z'') coordinate system is,

$$w^{z,e} = R_{201}^{z,e} a_{201} \tag{2.50a}$$

$$w^{z,e} = \frac{v^{z,e}}{2} T_{201}^{z,e} \sum_{n=1}^{N_1} d_{00}^{n}(\theta_0) C_{201}^{2n(1)}(k_0 r_1) C_{20n}^{21(3)}(k_0 r_0)\left(1+\alpha_{20n}\right) R_{201}^{z,e} \tag{2.50b}$$

where $R_{201}^{z,e}$ is the receiving coefficient of the EHDz″ antenna which has a single mode (σ, μ, ν) = (2, 0, 1) and $v^{z,e} T_{201}^{z,e} = Q_{201}$. $v^{z,e}$ and $T_{201}^{z,e}$ are the excitation amplitude and EHDz antenna transmission coefficients. The transmitting and the receiving coefficients of the EHDz antenna are $T_{201} = R_{201} = 1$ [19, Eq. (2.148)]. The transmission coefficient S_{21} is then,

$$S_{21}^{z,e} = \frac{w^{z,e}}{v^{z,e}} = \frac{1}{2} \sum_{n=1}^{N_1} d_{00}^{n}(\theta_0) C_{201}^{2n(1)}(k_0 r_1) C_{20n}^{21(3)}(k_0 r_0)\left(1+\alpha_{20n}\right) \tag{2.51}$$

Some of the incident field will be reflected back toward the transmitting antenna, generating a receiving signal in the EHDz. This signal is represented by S_{11}. In order to calculate S_{11}, the origin of the (x, y, z) coordinate system will be translated to the EHDz location and, according to (2.44), the scattered field at the original coordinate system is given as

$$\vec{E}^{s}(r,\theta,\phi) = \frac{k_0}{\sqrt{\eta_0}} Q_{201} \sum_{n=1}^{N_1} C_{20n}^{21(3)}(k_0 r_0) \alpha_{20n} \vec{F}_{20n}^{(3)}(r,\theta,\phi) \tag{2.52}$$

Here there is no need to rotate the coordinate system, but the translation is along the negative direction of the z-axis. This results in

$$\vec{E}^{s}(r,\theta,\phi) = \frac{k_0}{\sqrt{\eta_0}} Q_{201} \sum_{n=1}^{N_1} C_{20n}^{21(3)}(k_0 r_0) \alpha_{20n} \sum_{\sigma=1}^{2} \sum_{\nu=1}^{N_2} C_{\sigma 0\nu}^{21(1)}(-k_0 r_0) \vec{F}_{\sigma 0\nu}^{(1)}(r'', \theta'', \phi'') \tag{2.53}$$

and by using the similar steps that have been used to calculate S_{21}, the S_{11} on EHDz becomes,

$$S_{11}^{z,e} = \frac{\varpi^{z,e}}{v^{z,e}} = \frac{1}{2} \sum_{n=1}^{N_1} (-1)^{n+1} \alpha_{20n} C_{201}^{2n(3)}(k_0 r_0) C_{20n}^{21(1)}(k_0 r_0) \tag{2.54}$$

where $\varpi^{z,e}$ is the receiving signal by the EHDz . [19, Eq. (A3.13)] is used to get rid of the negative argument. The S-parameters for the other antennas are given in appendix B without derivation.

2.8 Truncation number

The series in eq. (2.11) and (2.12) are infinite in the N index. For practical purpose, i.e. numerical implementation, the series can be truncated, so m will run between -M and M and n from 1 to N. The truncation of the series produces truncation error in the computations.

In spherical wave theory the space is interpreted as a spherical waveguide [19] and [25]. Hence many concepts such as orthogonal modes, cut-off, propagation and evanescence are common features. The orthogonality property of the modes leads to the conclusion that each mode carries part of the accepted power. Therefore, the convergence of the accepted power shall be used to test the convergence of the series. This method ensures that the eliminated modes do not affect the accepted power. The new convergence criterion was inspired by [26] and will be used to evaluate the relative amount of the truncation power $\xi_P^{N_t}$:

$$\xi_P^{N_t} = \frac{P_{acc}^{N_t+1} - P_{acc}^{N_t}}{P_{acc}^{N_t}} \tag{2.55}$$

where P_{acc}^{N} is accepted power at $N = N_t$, and N_t is the truncation number. N_t increases until the truncation power $\xi_P^{N_t}$ is below α, which is the maximum relative error that can be accepted.

In this section we studied the truncation number (order) in terms of different parameters, including frequency, the distance of the transmitting antenna and the radius of the sphere. Fig. 2.7 shows the truncation number as a function of the operating frequencies (400 MHz – 4 GHz), where the maximum relative error was chosen to be α = -80 dB. The radius of the sphere is a = 8.5 cm, and the transmitting dipole antennas were positioned at r_0 = 9.3 cm, while the receiving dipole antenna were positioned at 10 cm. The electrical properties of the sphere are modeling the properties of a real human head. The color of the lines are in the following sequence; blue, red, green and black lines represent the truncation numbers of the EHDz, MHDz, EHDx and MHDx calculations. From 400 MHz to around 1.7 GHz, the truncation number decreases as the frequency increase, and then from 1.7 GHz to 3.1 GHz it remains constant. In general the difference is not large, while the truncation number is large with respect to the electric dimension of the structure.

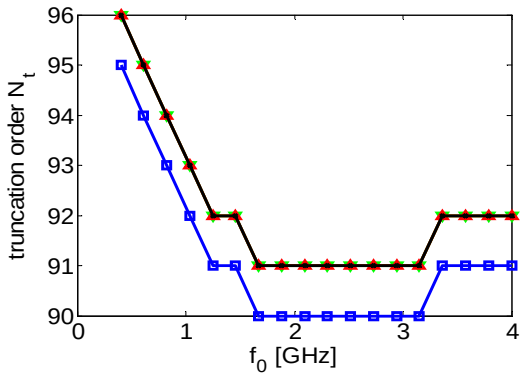

Fig. 2.7: The truncation number (order) and the relative errors for the EHdz, MHDz, EHDx and MHDx as functions of the operating frequencies.

In the following, the truncation number is studied as function of the radius of the sphere and the distance of the transmitting antenna, as seen in Fig. 2.8a and 2.8b, respectively. For the radius analysis, the position of the transmitting antenna from the surface of the sphere was kept constant $r_0 - a = 7$ mm. The radius of the sphere was then kept constant $a = 8.5$ cm while the distance r_0 was increased. Since all the antennas have almost similar truncation numbers, the convergence was calculated for the EHDz antenna. In Fig. 2.8 the blue, green and red lines correspond to the frequencies 400 MHz, 1 GHz and 2.45 GHz, respectively. From Fig. 2.8a it is seen that there is a linear relation between the truncation number and the radius of the sphere. For example, at 1 GHz the truncation number can be described by the following relation:

$$N_t = 48.2k_0a + 6.2 \tag{2.56}$$

where k_0 is the free-space wave-number. The equation (2.56) shows that the truncation number is proportional to the radius of the sphere a, while the wave-number is constant. For 1 GHz the truncation number decreases as the distance of the antenna increases, and the truncation number can be described as,

$$N_t = \frac{17}{k_0 r_0 - 1.7} \tag{2.57}$$

Here the truncation number is inverse proportional to the distance r_0, while the wave-number k_0 is constant. This illustrates that the convergence does not depend only on the distance of the antenna, but also on the radius of the sphere.

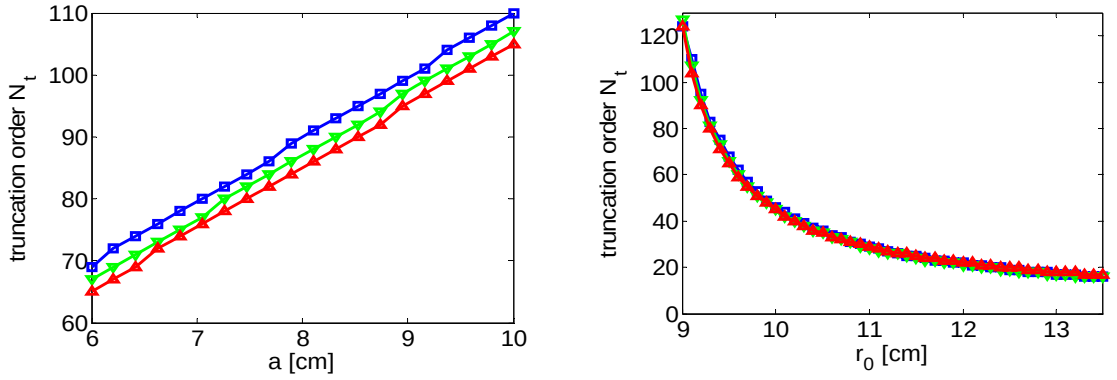

(a) (b)

Fig. 2.8: The left figure shows the truncation orders as a function of the sphere radius and the right figure shows the truncation orders as functions of the dipole antenna distance. For the left figure the distance of the dipole antenna is kept constant, while the radius of the sphere is kept constant in the right figure.

2.9 Matlab programs

All the fields and the scattering coefficients are calculated by algorithms that are programmed using Matlab. The algorithms are written as scripts in appendix G, where each script represents a function that uses variables as input. Script 1 is a function that

calculates the spherical function and the scripts from 2 to 6 are the functions that calculate the components of the spherical wave functions. Script 7 and 8 calculate the rotation and the translation coefficients. Each script from 1 to 8 can be used independently from each other.

Script 9 is a program that uses the functions in scripts 1 to 6 to calculate electric field, magnetic field and power density for a EHDz antenna near a dielectric sphere. The fields are plotted over a region that can be decided by the user. This program requires short processing time, which usually depends on the number of points and the number of modes. For example to calculate the fields over a region which consists of 100 x 100 points and $N = 95$ modes the program requires 162.4 seconds. The processing takes place on a laptop. The translation and the rotation algorithms are used in script 13, where a EHDz is translated and rotated as Fig. 2.6b shows.

3. Ear-to-ear communication – Experimental approach

3.1 Introduction

The objective of the experimental approach is to evaluate the path-loss for different frequencies and at different positions of the antennas near the head. The measurements covered bands of frequencies around; 920 MHz, 1.5 GHz, 2.45 GHz and 3.23 GHz and for each frequency the proximity effect on the path-loss was studied. The proximity effect is the effect of the antenna distance from the surface of the head on the path-loss. At small distances and in proximity of an object, it is impossible to utilize Friis equation to calculate the path-loss. Therefore, the path-loss will be defined in terms of S-parameters, which can be measured by a network analyzer. Usually for such measurements, a measurement system will constitute two antennas, a network analyzer, head model, absorbers, two long coaxial cables and calibration kits.

A port is defined as the location where the antenna and the coaxial cable are connected. A power transmit from port 1 to port 2 is $P_{inc}\left|S_{21}\right|^2$, where P_{inc} is the incident power on port 1. The transmitted power includes all losses of the path between port 1 and 2, including the antennas, and to compensate for such losses, the efficiencies of the antennas should be included in the path-loss definition. In addition to the antennas losses, part of the incident power reflects back so the transmitting antenna will accept a power $P_{inc}\left(1-\left|S_{11}\right|^2\right)$. The path-loss PL will be defined as

$$PL = 10\log_{10}\frac{\left|S_{21}\right|^2}{1-\left|S_{11}\right|^2} - 2\times 10\log_{10}\varepsilon_{rad} \tag{3.1}$$

where ε_{rad} is the radiation efficiency of the antenna. This definition will give negative values. Here, it is assumed that the transmitting and the receiving antennas are identical, wherefore the radiation efficiency term is multiplied by 2. The reflection part $(1-\left|S_{11}\right|^2)$ becomes insignificant for a well matched antenna, and thus it can be neglected. Using highly efficient antennas minimizes the second part in (3.1). Therefore, many researchers use the S_{21} as the value of the path-loss. But by bringing the antenna close to the head may affect the efficiency either in positive or negative ways. Hence this adds to the uncertainty about the measured path-loss, and therefore a number was added to account for that uncertainty. The number depends on the efficiency of the antenna in free-space; for example if the efficiency was ε_{rad} = 90 % in free-space and it changes to 80 % when the antenna brought close to the head the difference will be ~ 1 dB, while if ε_{rad} was 24 % and then it becomes 20 % near the head the deference will be ~ 1.6 dB. So to account for worst cases, we add ± 3 dB to the path-loss formula, therefore the uncertainity in the path-loss is 3 dB. The path-loss for well matched antennas (S_{11} < -10 dB) becomes:

$$PL = 20\log_{10}\left|S_{21}\right| - 20\log_{10}\varepsilon_{rad} \pm 3\,\text{dB} \tag{3.2}$$

3.2 Setup

A standard head phantom SAM (Specific Anthropomorphic Mannequin) that was used in the measurements, as seen in Fig. 3.1, is filled with material with similar electrical properties as human head. The electrical properties of the head phantom are given chapter 4. The figure also shows the mechanical setup, which is made of low-loss materials except for the absorber, see Tab. 3.1. The antennas were mounted with baluns in order to prevent the feed cables from radiating. A HP8753D vector network analyzer performed a running average of 16 samples at 201 frequency points in different ranges in order to get stable S-parameter measurements. Two 1.5 m RG-58 coaxial cables that were used to extend the cables of the vector network analyzer. For some of the measurements, the antennas were held in place with ordinary household tape. Evaluating of the measured S_{21} indicates that some reflections occurred during the measurements. The reflected parts of the measured S_{21} were identified and they were removed by time-gating as in [27] and [28], where a hamming window was used.

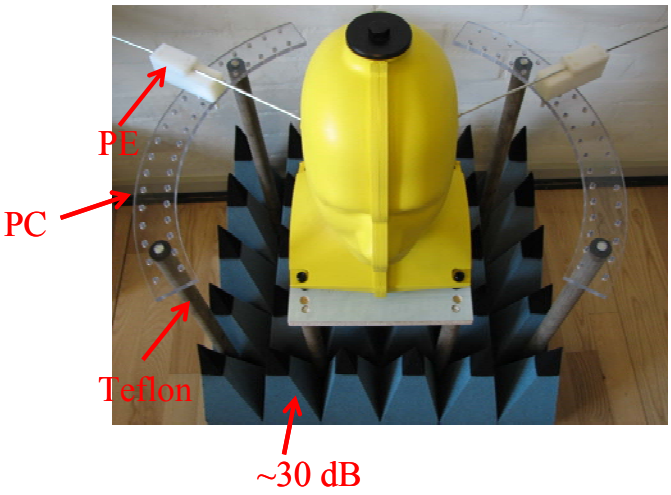

Fig. 3.1: A standard SAM head phantom was used in the measurements. The dipole antennas were mounted with lumped baluns, in order to reduce the radiation from the cables.

Tab. 3.1: Electrical properties of the mechanical setup

	ε_r	tanδ
Polyethylene (PE)	2.25	0.001
Polycarbonate (PC)	2.95	0.01
Teflon	2.1	0.001

3.2.1 Antennas for the measurements

In order to characterize the path-loss for ear-to-ear communication, a set of simple dipole antennas were designed. The dipole antennas are characterized by omni-directional pattern and they are linearly polarized. The dipole antenna may not be a good candidate for ear-to-ear communication, but we chose it to compare the measured path-loss with the results of the spherical model. All the antennas are very small in comparison

with the head. Some of the antennas may not be electrically small but they are small with respect to the head, which shadows the radiation of the antennas. Electrically small antennas usually have low input resistance, high input reactance, low efficiencies and low directivity [29].

Fig. 3.2 shows the antennas that were used in the measurements. All the used antennas are dipoles except for Ant. 5 which does not has a dipole pattern. Ant. 2 is a simple dipole antenna that is made of two small wires of 1 mm in diameter and 4 cm in length, where they are mounted directly on a balun.

Ant. 1 is a simple dipole antenna that operates near 1 GHz, and it is mounted with a baluns that is made of lumped components, the balun is used also as a transformer that match the impedance of the antenna $(5.76 - j343.0)\ \Omega$ to a feed line with 50 ohms. The dipole is printed on RF-4 substrate with thickness of 1.5 mm. The antenna is electrically small, whereas the maximum length of the antenna is $0.133\lambda_0$, where λ_0 is the free-space wave length. While Ant. 2 to Ant. 4 have electrical dimensions of $\lambda_0/2$ lengths, therefore they can not be interpreted as small antennas. Ant. 5 is an electrically small antenna that is resonant at 1 GHz.

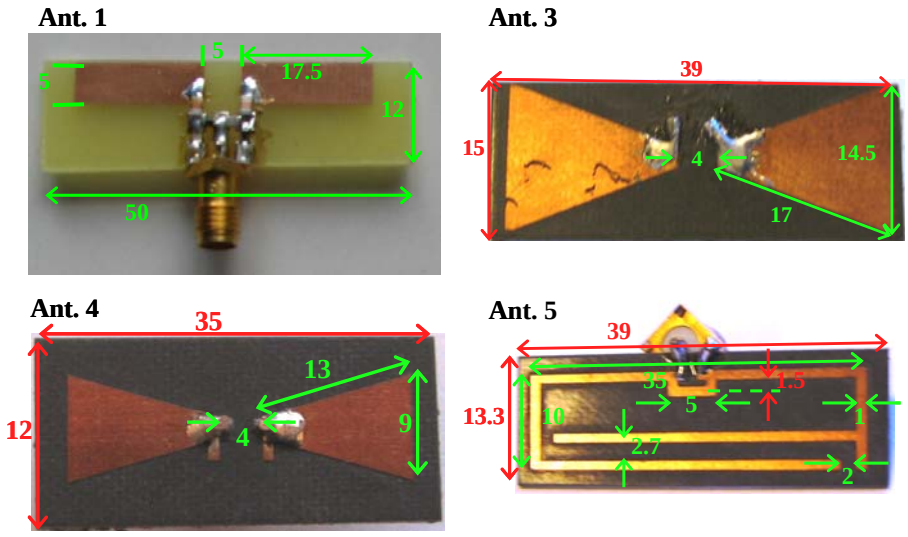

Fig. 3.2: Some of the antennas that had been used in the measurements.

3.2.2 Baluns

One problem with all the designed antennas is that they are balanced while the coaxial feeding lines are unbalanced. Therefore it is necessary to use baluns to avoid surface currents which may run on the cables. Depending on the magnitudes and the orientations of the surface currents, the measurements of the S_{21} can be higher than the actual values, resulting in small path-loss. There are several kinds of baluns which may also work as transformers, in [30, sec. 9.8.6] some of the well known baluns are described, like Bazooka balun, λ/4-coaxial balun and coaxial balun, all these baluns have impedance relation (1:1), some baluns like the λ/2-coaxial balun and the ferrite core transformer have impedance relation (4:1) or (1:4). In [31], a quarter-wave transmission line was

employed to design a wideband balun that matches 50 Ω unbalanced line to a balanced antenna with input impedance of 70 Ω. The balun and the steps to construct it are depicted in Fig. 3.3. It can be used to match larger impedance than 70 Ω [32].

Lumped element circuits were used to design a broad-band balun in [33] and [34], where the designs and the analysis were inspired from [35]. The distributed transmission lines can be replaced by low-pass and high-pass ladder networks [35]. By equating the ABCD matrix of the transmission line and the ABCD matrix of the lumped element networks at the design frequency, it is possible to calculate the values of the lumped elements. In [33], the impedance relation is (1:1) and the balun is a second-order lattice, while in [34] an extended analysis of the lumped balun was given in [33] and the balun has inherent impedance transformation.

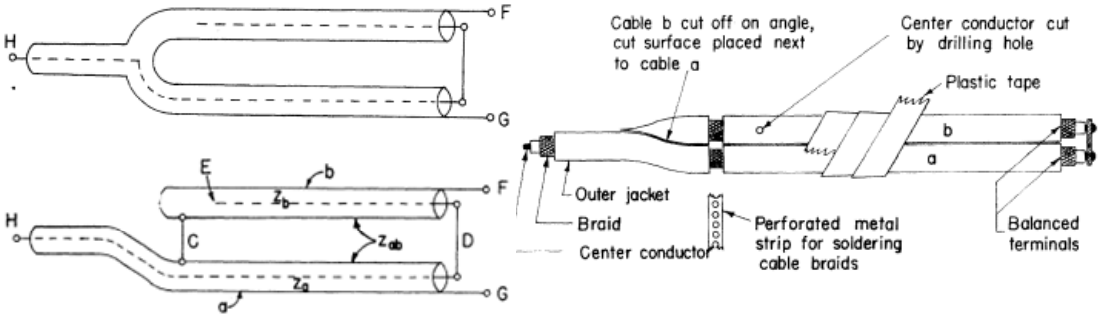

Fig. 3.3: The quarter wave coaxial balun is copied from [31], where Z_b and Z_a are the impedances of the coaxial cable, Z_{ab} is the impedance of the two lines transmission line.

A first order lattice balun with inherent transformation was used, the design and the derivations of the components values were inspired by the work in [34] and [35]. The ABCD matrix for a λ/4 transmission line is:

$$\begin{bmatrix} A & B \\ C & D \end{bmatrix} = \begin{bmatrix} 0 & jZ \\ jY & 0 \end{bmatrix} \tag{3.3}$$

with Z and Y being the characteristic impedance and admittance of the transmission line #1 (see Fig. 3.4a) which has λ/4 length, respectively. A low-pass network models the transmission line segment is shown in Fig. 3.4b. where X and B in Fig. 3.4 are the reactance and the susceptance,respectively. The ABCD matrix that represents the low-pass filter can be calculated using the table on front cover of the book [36]:

$$\begin{bmatrix} A & B \\ C & D \end{bmatrix} = \begin{bmatrix} 1 & jX_L \\ 0 & 1 \end{bmatrix} \begin{bmatrix} 1 & 0 \\ jB_C & 1 \end{bmatrix} \begin{bmatrix} 1 & jX_L \\ 0 & 1 \end{bmatrix} = \begin{bmatrix} 1 - X_L B_C & jX_L(2 - X_L B_L) \\ jB_C & 1 - X_L B_C \end{bmatrix} \tag{3.4}$$

where all the values are defined in Fig. 3.4. Equating (3.3) and (3.4) yields the following results:

$$X_L B_C = 1 \tag{3.5a}$$
$$B_C = Y \tag{3.5b}$$

While the transmission line #2 has a length of 270 degree and it will be modeled by a high-pass filter, which is shown in Fig. 3.4c and its ABCD matrix is given in [35].

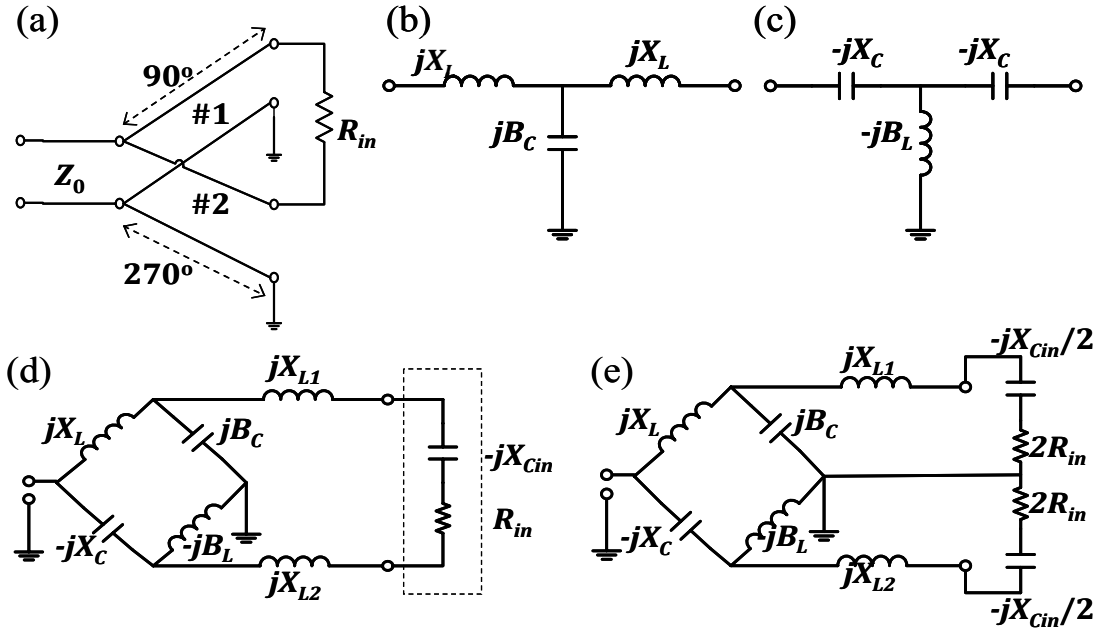

Fig. 3.4: Transmission line balun (a), low pass filter (b), high pass filter (c), first order lattice balun (d) connects small electric dipole antenna, which is modeled by the network in the box and (e) is the equivalent circuit for the circuit in (d). The dashed rectangle in (d) represents an antenna.

Equating the matrices of the transmission line and the high-pass network yields the following results:

$$B_L X_C = 1 \tag{3.6a}$$

$$B_L = Y \tag{3.6b}$$

The capacitances and the inductors in the low-pass filter equal the capacitances and the inductors in the high-pass filter, therefore we used variables of identical notation in (3.5) and (3.6). The characteristic impedance Z of the $\lambda/4$ transmission line is given as:

$$Z = \sqrt{2R_{in}Z_0} \tag{3.7}$$

where Z_0 usually is 50 Ω for the coaxial cable. The apparent load for the low/high pass filters is 2 times the input resistance of the antenna R_{in} and therefore input resistance is multiplied by 2. While the apparent capacitance for the low/high pass filters is half the C_{in}, which is the equivalent input capacitance of the antenna. The circuit in Fig. 3.4e is the equivalent for the circuit in Fig. 3.4d. The values of the components can be calculated either by using (3.5) or (3.6),

$$L = \frac{Z}{2\pi f_0} \tag{3.8}$$

$$C = \frac{1}{2\pi f_0 Z} \tag{3.9}$$

where f_0 is the resonance frequency of the antenna. The reactance X_{L1}, which is used to cancel out the reactance of the antenna $X_{in}/2$, includes X_L and the reactance X_{L2} includes X_C. So the values of the inductors L_1 and L_2 can be calculated as following:

$$L_1 = \frac{X_{Cin}/2 - X_L}{2\pi f_0} \tag{3.10}$$

$$L_2 = \frac{X_{Cin}/2 + X_C}{2\pi f_0} \tag{3.11}$$

From (3.5b) and (3.5e) it is found that $X_L = X_C = Z$. Equations (3.10) and (3.11) become

$$L_1 = \frac{X_{Cin}/2 - Z}{2\pi f_0} \tag{3.12}$$

$$L_2 = \frac{X_{Cin}/2 + Z}{2\pi f_0} \tag{2.13}$$

For a loop antenna the input impedance can be modeled as a resistance in series with an inductor, therefore the inductances L_1 and L_2 will be replaced by capacitors C_1 and C_2. The apparent inductor for the low/high pass filters will be 2 times the input inductor, so the values of the capacitors C_1 and C_2 become:

$$C_1 = \frac{1}{2\pi f_0 (2X_{in} + Z)} \tag{3.14}$$

$$C_2 = \frac{1}{2\pi f_0 (2X_{in} - Z)} \tag{3.15}$$

3.2.3 Performances of the antennas and the baluns

Some of the performances can be easily measured by a network analyzer like the resonance frequency and the S-parameters, while other performances like the efficiency and the patterns can not be measured directly by the network analyzer. The efficiency enters in the path-loss formula, and the pattern is used to ensure no leakage currents that run on the feeding cable. Therefore, Ant. 1 and Ant. 4 were measured in DTU-ESA facility [38], where the patterns and the efficiency were measured. Ant. 4 was chosen, because it used similar balun as Ant. 2 and 3, while it is resonant at higher frequency range than the other two antennas, so it is more sensitive to deformations. For the remaining antennas, the reflection coefficients were measured by the network analyzer, but the efficiencies were estimated by simulating the designs in HFSS. Tab. 3.2 includes some of the measured and simulated data in free-space. Only the marked efficiencies with the superscript (+) were measured. The resonance frequencies may shift near the head.

Tab. 3.2: The data for the antennas.

	Ant. 1	Ant. 2	Ant. 3	Ant. 4	Ant. 5
Freq. [GHz]	0.945	1.5	2.45	3.325	1.008
l [mm]	41.8	85	41.8	37	41.8
l / λ_0	0.133	0.425	0.368	0.411	0.133
ε_{rad} %	24.3^+	93	93	91.2^+	10

where l is the maximum length of the antenna. The simulated reflection coefficient of Ant. 5, which is the black line in Fig. 3.5a, proves that the antenna work properly, where the difference between the measured and the simulated resonance frequencies is less than 1%. To see the effect of the surface currents (on the coaxial cables) on the reflection coefficient, Ant. 3 was simulated with and without a cable. The red line in Fig. 3.5b is the reflection coefficient for the case where Ant. 3 was fed without a cable, and the green line corresponds to the case where Ant. 3 was fed through a coaxial cable. This shows the effect of the surface currents on the reflection coefficient response. Since the current on the cable will run on long road, then the resonance shall be lower than the ideal case which is represented by the green line. This is a simple explanation, but the antenna affects the reflection in complex manner. In some cases, the measurements of the reflection coefficient help to find if surface currents exist or not. It is clear from the structure of Ant. 5 in Fig. 3.5a that Ant. 5 is not a balanced antenna, and this may explain the well behaved reflection coefficient of the antenna. The measured S_{11} for the remaining antennas are given in appendix F. The measurements of the radiation patterns of Ant. 1 and Ant. 4, as seen in Fig. 3.6a and 3.6b respectively, show that the antennas work properly, where they have dipole patterns. The blue line is the field in the *E*-plane and the red dashed line is the field in the *H*-plane. The sizes of the antennas are very small in comparison with the tower, which is shown in Fig. 3.7, and that explains the drop in the values of the radiation patterns. The ripples in the fields appear because the origin of the measurement coordinate system is not centered on the antenna, but it shifted a little bit either in the positive or in the negative z-direction. The measurement of the radiation pattern utilizes the theory that is represented in chapter 2. Therefore when the antenna is shifted from the center, its pattern can not be represented by a single mode but with multi-modes, in reality few modes are used while high order modes are not used, therefore the ripples appear.

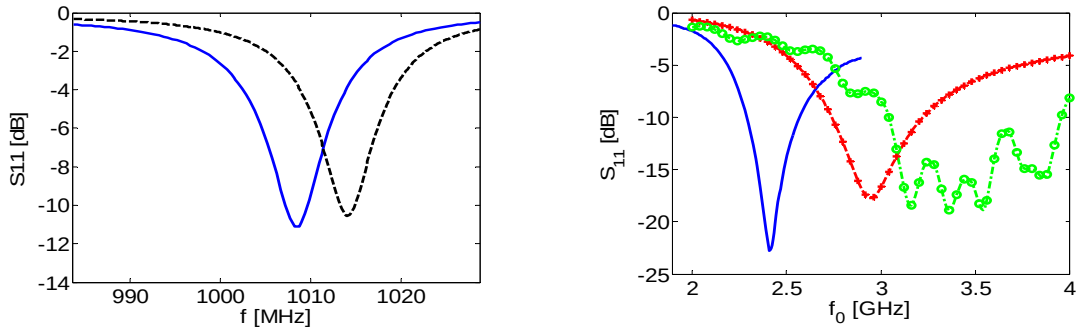

(a) (b)

Fig. 3.5: The measured and the simulated S_{11} of Ant. 5 (a) and Ant. 3 (b). The blue lines are the measurements values, the black and the red lines are the simulated S_{11} for the antenna fed without a cable, while the green line corresponds to the antenna fed by a cable.

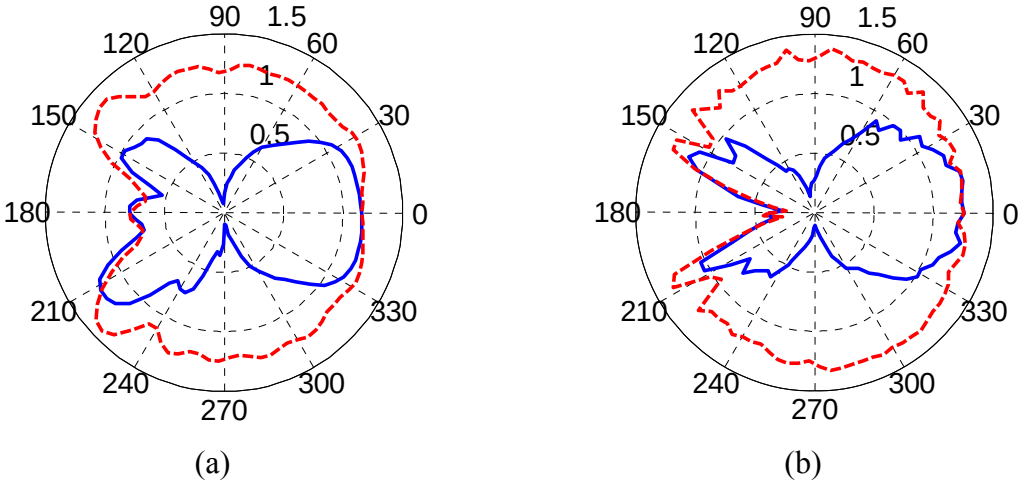

Fig. 3.6: Far-field patterns of the Ant. 1 (a) and Ant. 4 (b). The blue lines are the fields in the E-plane and the red dashed lines are the fields in the H-plane. The E-plane in the *xz*-plane and the H-plane is in the *yz*-plane.

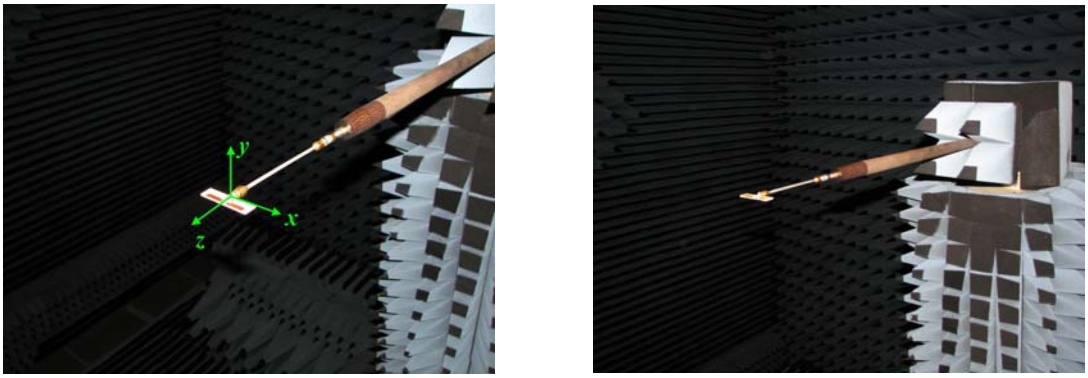

Fig. 3.7: Ant. 1 on the tower model in DTU-ESA facility.

3.3 Precision evaluation

Accuracy is the quality that characterizes the capacity of a measuring instrument for giving results close to the true value of the measured quantity, while the precision is the quality that characterizes the capability of a measuring instrument of giving the same reading when repetitively measuring the same quantity under the same prescribed conditions (environmental, operator, etc.), without regard for coincidence or discrepancy between the result and the true value [37, pp. 13-14]. For each measurement, the network analyzer was calibrated to ensure the accuracy of measurements. The precision was ensured by repeating the measurements at different periods, where the setup had been preserved. The precision can be affected by several factors, such as:

1) The environment that surrounds the measurement setup,
2) the dynamic range of the network analyzer,
3) and the mechanical alignments of the antennas with respect to the head.

The mechanical alignments include the distances of the antennas from the head, the distances of the antennas from the ground and the alignment of the antennas with respect

to each other. The accuracy of the distance is around 1 mm, and the horizontal alignments of the antennas with respect to the ground plane can be an accuracy of 2 degree, where a light weight level instrument was used to check the alignments.

The precision of the experiments was evaluated for two different antennas; Ant. 1 and Ant. 4. The measurements of the S-parameters for the antennas are repeated at different times and each time the network analyzer was calibrated using a full 2-port calibration procedure. A set of precision SOLT (Short-Open-Load-Through) standards were attached to the network analyzer ports to perform the calibration. The mimium value (noise floor) that the network analyzer can measure is around -70 dB.

Tab. 3.3: The precision of the measurements vs. the distance from the head.

Distance [mm]	Uncertainity [dB]	
	Ant. 1	Ant. 4
0	1.5	2
2	0.2	1
4	0.5	2
8	0.25	1
10	0.2	1
20	0.1	0.5
30	0.5	0.25
40	0.1	0.25

During the evaluation, the effect of the distance on the path-loss was tested, where each measurement was repeated three times at different periods. The distance that separates the antenna from the head was limited between 0 and 40 mm. Tab. 3.3 includes the uncertainity values for each distance. The uncertainity was calculated by dividing the maximum difference between the measured S_{21} for same distances by 2. The precision improves as the distance increases and it is high for the low frequency antenna. Since Ant. 4 works at the highest frequency among the other antennas, therefore we expect the other antennas to have better precision, where the uncertainity is less than the 2 dB. The resonance frequency of Ant. 1 shifts to 920 MHz near the head and the measured S_{21} are shown in Fig. 3.8a, where the antennas are kept at distances of 2 mm and 40 mm from the head. Each color represents a measurement at a certain time.

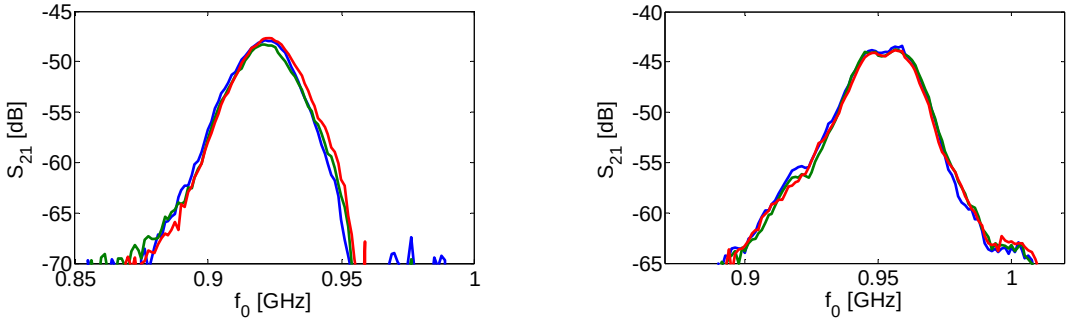

(a) (b)

Fig. 3.8: Measurements of S_{21} by Ant. 1 at distances of 2 mm (a) and 40 mm (b). The measurements take place at different periods, so each color represents a different time.

4 Ear-to-ear communication – results and discussions

4.1 Introduction

Electrical properties of the human tissues will be presented and these properties will be used to carry out the investigations. In order to understand the mechanisms involved in the ear-to-ear wireless communication, the electric and magnetic fields will be plotted inside and outside the sphere. The path-loss will also be computed as a function of the frequency, the radius of the sphere, and the distances of the antennas from the sphere. Influence of the electrical properties on the path-loss will be studied for four different antennas. In addition to the theoretical results, the measurements of the path-loss will also be presented.

4.2 Electrical properties of the tissues

Many experimental and theoretical studies were carried out in the literature to estimate the electrical properties of the different tissues of the human body. The question of whether radio frequency (RF) radiation might have harmful effects on people, have motivated many researchers to study the electrical properties which include both the relative permittivity and the conductivity of the tissues. In [39], the electrical properties of the muscles, skin, fat and the bones were measured and it was found that their properties can be described in terms of Debye dispersion equations with a single relaxation time. The electrical properties were measured using the method in [40], where the specimen fills a short length of a waveguide or a coaxial line that is terminated by a short circuit. Measurements on a standing wave set up in the guide or line section preceding the specimen then enable the complex dielectric constant to be evaluated. In [41] a comparison between the behavior of the blood and the water at microwave frequencies has been done based on the measurement data. More tissues have been studied in [42] for the frequency band 10 MHz – 1 GHz, where the permittivity was measured based on the input reflection coefficient of an open-end coaxial line placed against the test tissue. Electrical properties of white and grey matter of the brain were measured in [43] for the frequency band 10 MHz and 10 GHz, the measurements were based on the method of [40]. Other works state the electrical properties for several tissues but over wider frequency bands, like in [44] where the frequency range was between 10 Hz and 20 GHz and in [45] where the frequency range was between 1 MHz and 20 GHz. Most of the mentioned works use the Cole-Cole equation [46] to describe the frequency dependence of the electrical properties of the tissues. Coefficients of the Cole-Cole equation were given in [45], such that the electrical properties for bone (cortex), lens, brain (grey and white matters), and many other tissues can be determined. The coefficients where found by data-fitting of the experimental results to the Cole-Cole equation. In Fig. 4.1, the values of the permittivity and the conductivity of the white and the grey maters are shown over the frequency range between 10 MHz and 10 GHz according to the Cole-Cole method and by using the coefficients in [45]. As the frequency increases the permittivity decreases and the conductivity increases. The electrical properties depend on the temperature and the concentration of water in the tissues; this may explain the difference in the values of the electrical properties that are given in different works. Those works estimate the electrical properties of some tissues not the whole head. Since in the experimental part of this thesis, the measurements were

made on a standard SAM phantom head [16], we therefore used the data provided by [16] in the theoretical investigation to compare the measurement and theoretical results. Fig. 4.2 shows the electrical properties of SAM phantom head according to [16]. Unless otherwise stated, the electrical properties are defined in Fig. 4.2. Since the conductivity and the relative permittiviy were known then the real and the imaginary values of the permittiviy can be calculated as:

$$\varepsilon = j\omega\varepsilon_0\left(\varepsilon_r' - j\frac{\sigma}{\omega\varepsilon_0}\right) \tag{4.1a}$$

or,

$$\varepsilon = j\omega\varepsilon_0\left(\varepsilon_r' + j\frac{\sigma}{\omega\varepsilon_0}\right) \tag{4.1b}$$

where $\omega = 2\pi f$ and f is the operating frequency. The equation (4.1a) shall be used with the time factor $\exp(j\omega t)$ and the equation (4.1b) with time factor $\exp(-j\omega t)$.

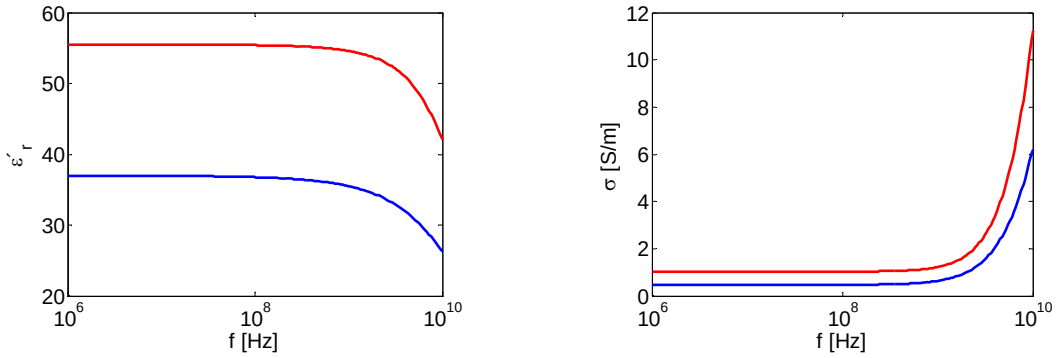

(a) (b)

Fig. 4.1: The permittivity (a) and the conductivity (b) of the white (blue line) and the grey (red line) matters of a brain.

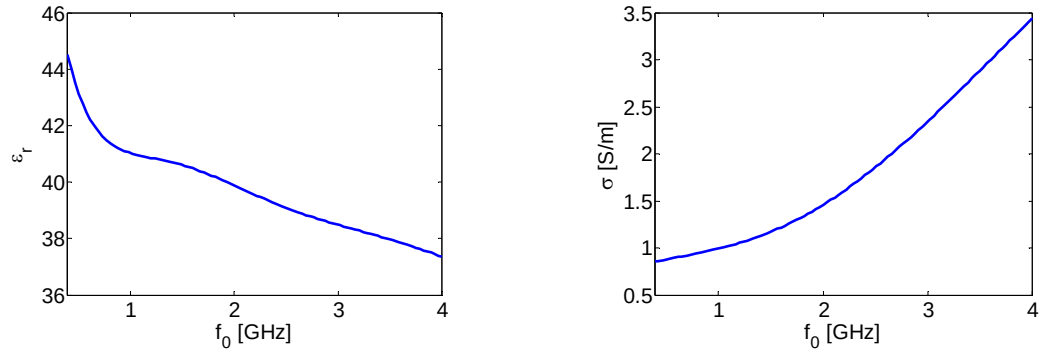

(a) (b)

Fig. 4.2: The relative permittivity (a) and the conductivity (b) of the SAM phantom head.

4.3 Theoretical investigations

4.3.1 Field distribution of EHDz

Field plots help to visualize the communication channels; therefore the electric and magnetic fields, as well as the power flow density, have been computed at 400 MHz, 1 GHz and 2.45 GHz, whereas the radius of the sphere and the distance of the antenna remain constant a = 8.5 cm and r_0 = 9.2 cm. Fig. 4.3 shows the fields generated by the EHDz, while the fields of the remaining antennas are given in appendix D. The magnetic fields in rows 2 and 4 are continuous through the surface of the sphere, and thus satisfy the boundary conditions. Electromagnetic waves propagate through and around the sphere, as seen in rows 1 and 2 in the figure. The waves move toward focal regions inside the sphere, and their magnitudes decay while they propagate. The focal region is a concentration region of wave fronts. It is very clear in Fig. 4.3 in row 1 and column C, where the focal region is close to the centre of the sphere.

The decay depends on the attenuation constant of the medium. For example, the magnitude of a plane-wave that propagates a distance $2a$ = 17 cm inside a medium that has the same electrical properties (ε_r = 41.0 +j17.8 at 1 GHz) as the sphere will decay by -42 dB. Therefore, the attenuation is expected to be high inside the sphere.

Outside the sphere, the waves that propagate along the surface of the spheres constitute surface-bound waves. The polarizations of the surface-bound waves are orthogonal to the surface, which helps to make a good coupling with the receiving antenna, which is EHDz. The generated surface waves that propagate in the clockwise and counterclockwise directions interact constructively or destructively and this results in standing waves outside the sphere. The standing waves appear clearly in Fig. 4.3-B3 and -C3, which corresponds to 1 GHz and 2.45 GHz, while at 400 MHz there is standing wave neither inside nor outside the sphere. At 1 GHz there are two minima which occur at $\theta \cong 45$ and -45, and a maximum at $\theta \cong 0$, while at 2.45 GHz there are more than 2 minima.

Power flow density plots emphasize the high attenuation that exists inside the spheres, where the colors rapidly changes to the dark blue. In addition to that, the directions of arrows inside the spheres point toward the focal regions, whereas outside the sphere they point in tangential directions with respect to the surface. The attenuation of the power flow density outside the sphere is lower than the attenuation inside it.

From the discussion, it is clear that power propagation take place around the sphere and not through it. The surface-bound waves are the main mechanism for the communication, and these waves have orthogonal polarizations with the surface. Because of this polarization which agrees with the polarization of the receiving antenna, the coupling will be high and that leads to low path-loss as we shall see later.

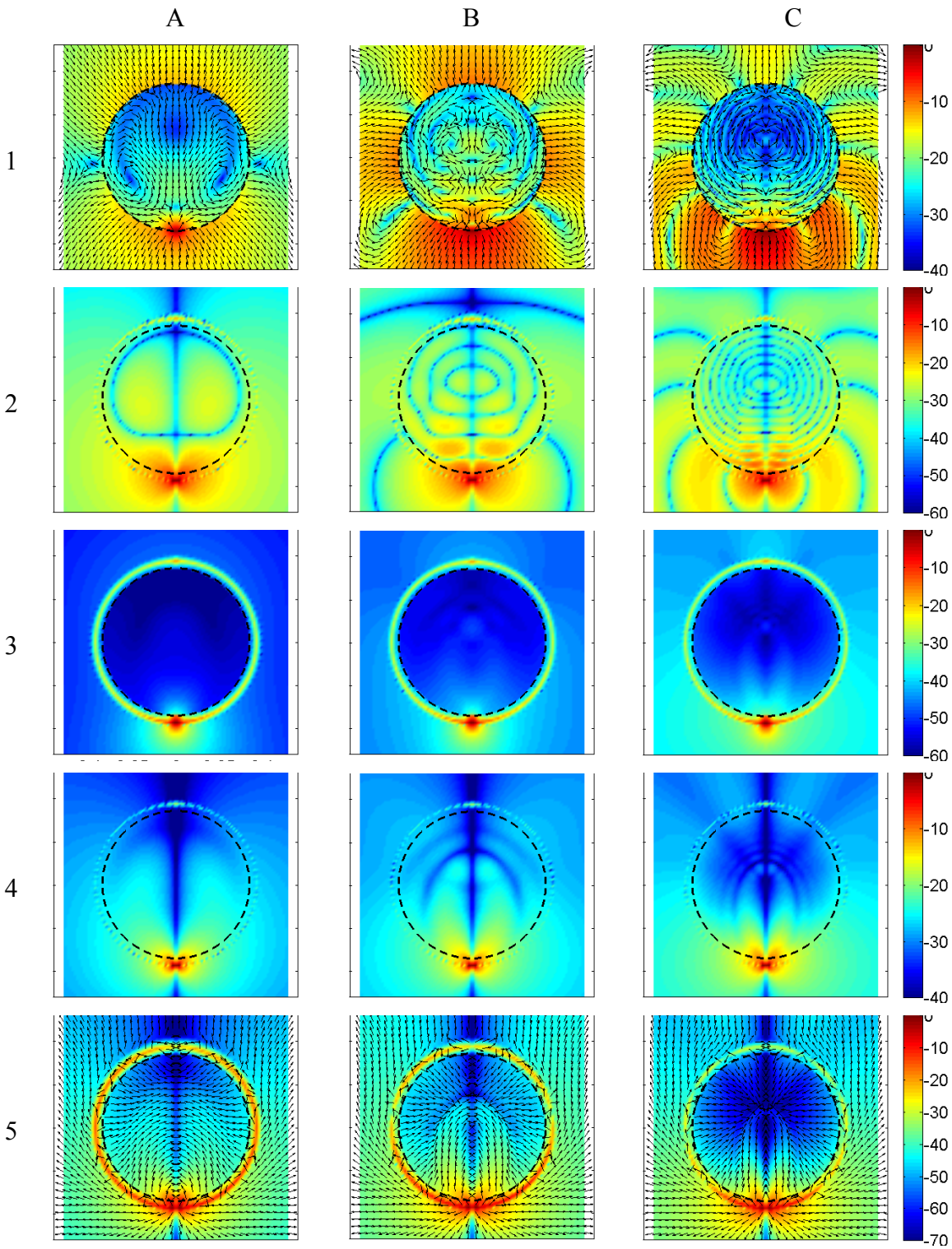

Fig. 4.3: The computed electric fields, magnetic fields and power densities of an orthogonal oriented EHD, where the EHD is located below the dielectric sphere, which is bounded by dashed circle. The plots in rows 1 and 2 show the amplitudes of the real values of the electric and magnetic fields, $|\mathrm{Re}\{\boldsymbol{E}\}|$ and $|\mathrm{Re}\{\boldsymbol{H}\}|$, while rows 3 and 4 show the magnitudes of the electric and magnetic fields, $|\boldsymbol{E}|$ and $|\boldsymbol{H}|$, and row 5 shows the magnitude of the associated power flow densities $|\boldsymbol{P}|$. The bold letters here represent vector quantities. Column A, B and C in sequence correspond to 400 MHz, 1 GHz and 2.45

GHz. The colors are the logarithmic scalar values in dB of the fields normalized to the maximum values, whereas the arrows in rows 1 and 2 represent the polarization of the fields, and in row 5 represent the directions of the power density in the *xz*-plane.

4.3.2 Field distribution of EHDx, MHDz and MHDx

The fields plots generated by the EHDx antenna are shown in Fig. D.2 and D.3 in appendix D, where Fig. D.2 shows the fields in the *xz*-plane (E-plane) and Fig. D.3 shows the fields in the *yz*-plane (H-plane). The electromagnetic waves propagate through and around the sphere. The waves that propagate through the sphere move all the way from the transmitting antenna side toward the opposite side. Except for the case where the frequency is 2.45 GHz, where the waves moves toward the focal regions inside the sphere. These waves have the same polarization as the transmitting antenna in both of the planes. Outside the spheres the propagation takes place through surface-bound waves, which have orthogonal polarizations to the surface of the spheres in the E-plane and parallel polarizations in the H-plane. Some of the surface-bound waves couple to the receiving antenna and some do not. Therefore, not all the power that is carried by the surface-bound waves will be received by the antenna. The standing waves appear both inside and outside the spheres, where the locations of the nulls depend on the frequency and the size of the sphere. Power flow density plots show that most of the power is concentrated close to the transmitting antennas while very small amount is transmitted to the other sides. The attenuation of the fields is high both inside and outside the sphere.

For the MHDz, the electromagnetic waves propagate through and around the spheres. The waves that propagate through the sphere move all the way from the transmitting antenna side toward the opposite side. For the magnetic dipoles, we use the polarization term to refer for the polarization of the magnetic field and not the electric field. The surface-bound waves have complex polarizations, where the polarizations look like they move in vortex over the surface of the sphere. Therefore, the coupling between the receiving antenna and the surface-bound waves will be low. The attenuation of the power density is high and small part of the power gets transmitted toward the receiving side.

The MHDx generates electromagnetic waves that propagate through and around the sphere. The waves that propagate through the sphere move toward the focal regions inside the sphere. Outside the sphere, the surface-bound waves propagate along the surface of the spheres and they have tangential polarizations in the E- and the H-planes, as seen in Fig. D.4 and D.5. Therefore the coupling between the receiving antenna and the surface-bound waves will be high. In consequence of the surface-bound waves and the standing waves appear for all the three frequencies. The attenuation of the power flow density is higher inside the sphere than outside it.

In summary, both the EHDz and the MHDx generate surface-bound waves that have the same polarization as the receiving antenna. The waves that propagated through the sphere do not contribute to the communication, since they propagated toward the focal regions inside the sphere. Thus, the communication for those antennas is carried out by the surface-bound waves. The EHDx and the MHDz generated surface-bound waves that had

mixed polarizations, which depended on the location and the propagation directions near the sphere. The waves that propagated through the sphere contributed to the communication, but most of the power was concentrated around the transmitting area while small amount propagated to the receiving area.

4.3.3 Effects of antennas locations and frequency on S_{21}

In the previous section, the field plots showed the distributions of the fields near the sphere. There is a relation between the field components and the S_{21}. It is reported in [19, pp. 77] that a received signal by a Hertzian dipole is proportional to the field component that is parallel to the dipole orientation. There is proportionality between the field components and the S_{21} values, as seen in Fig. 4.4. Therefore, the field distribution plots can be used to estimate the location where the maximum coupling can be achieved, such that the S_{21} becomes high. The results in Fig. 4.4 show that the S_{21} depends not just on the frequency, but also on the type and the orientation of the receiving antenna.

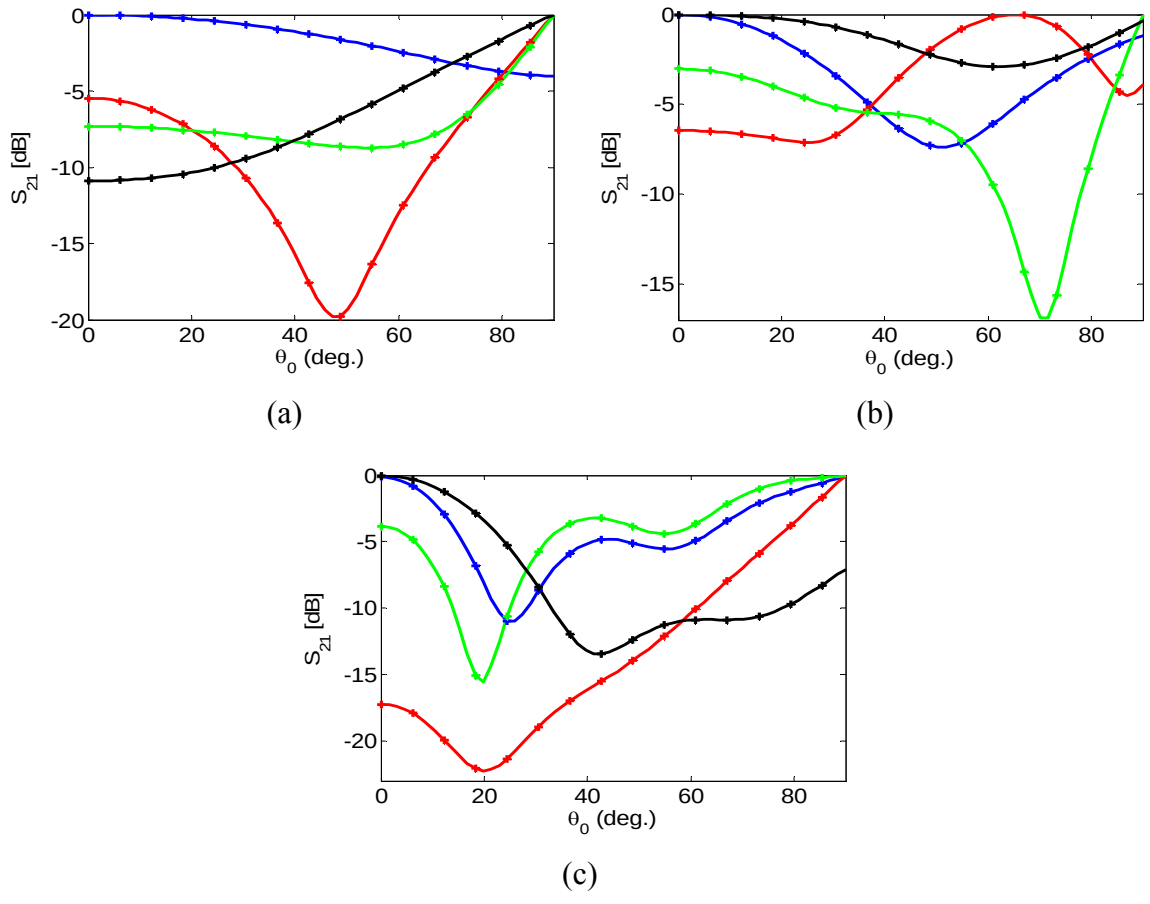

Fig. 4.4: The normalized S_{21} as a function of the position angle θ_0 at 400 MHz (a), 1 GHz (b) and 2.45 GHz (c). The color of the lines in the following sequence; blue, green, red and black correspond to the normalized $|E_r|$ of the EHDz, the normalized $|E_\theta|$ of the EHDx, the normalized $|H_r|$ of the MHDz and the normalized $|H_\theta|$ of the MHDx. The crosses correspond to the S_{21}.

First the effect of the frequency on the S_{21} values will be studied. The S_{21} is the value of the path-loss in the theoretical investigation. The antennas will remain at constant locations whereas the frequency varies between 400 MHz to 4 GHz. This investigation tests the effect of the frequency on the S_{21} for the four antennas, as seen in Fig. 4.5a. The use of the EHDz provides the highest coupling where the S_{21} is around -2 dB at 400 MHz then it decreases as the frequency increases to -10 dB at 1 GHz, and -24 dB at 2.45 GHz. The MHDx provides the next best coupling, where the S_{21} is around -20 dB at 400 MHz; it decays as the frequency increases to -27 dB at 1 GHz and -30 dB at 2.45 GHz. The EHDx and MHDz provide low S_{21} values in comparison to the EHDz and MHDx. In addition, their S_{21} oscillates while they decay as the frequency increase. The S_{21} for the EHDx is around -43 dB at 400 MHz, -50 dB at 1 GHz and -57 dB at 2.45 GHz, while for the MHDz the S_{21} is around -30 dB at 400 MHz, -65 dB at 1 GHz and -74 dB at 2.45 GHz. There is a relation between the S_{21} and the dissipated power, where the dissipated power is very high for the EHDx and MHDz, as seen in Fig. 4.5b, whereas it is low for the EHDz and MHDx. The dissipated power at 1 GHz is around 36 % for the EHDz and 96 % for the EHDx.

Notice that the EHDz and the MHDx are the antennas that provide the best coupling to the surface-bound waves, whereas the coupling of the MHDz and the EHDx to the surface-bound waves is not as good.

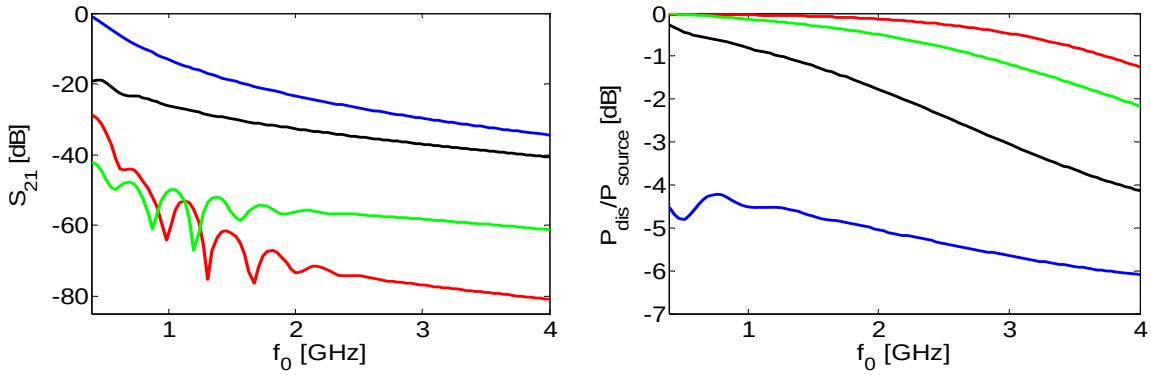

(a) (b)

Fig. 4.5: S_{21} (a) and the normalized dissipated power (b) vs. the frequency at $\theta = 0$, where the color of the lines in sequence are blue, green, red and black represent the S_{21} for the EHDz, EHDx, MHDz,and MHDx.

4.3.4 Effect of the sphere radius on S_{21}

The size of heads varies among people, and that will have an impact on the S_{21}. Therefore in this section, the radius of the sphere takes values between 6 cm to 10 cm, while the frequency and the distance of the antenna remains constants. Fig. 4.6a shows S_{21} as a function of the radius at 1 GHz. For all four antennas, the S_{21} values decrease as the radius increases.

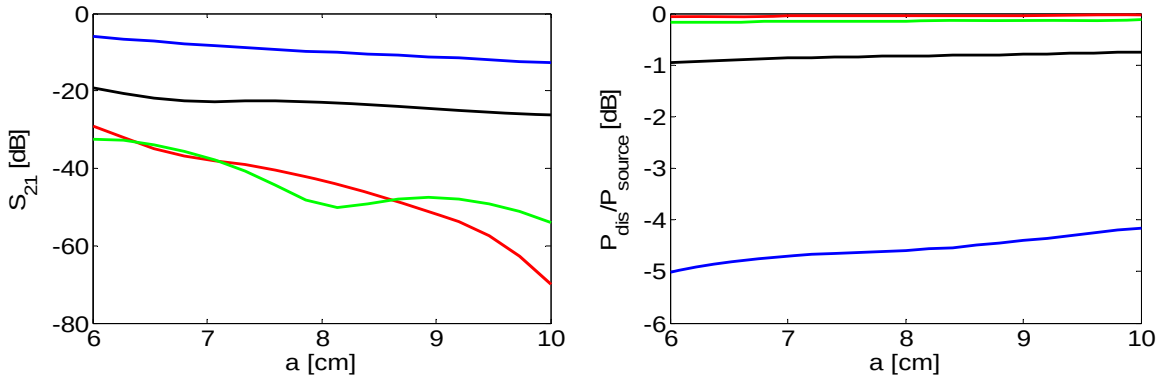

(a) (b)

Fig. 4.6: S_{21} (a) and the normalized dissipated power (b) vs. the radius of the dielectric sphere, where the color of the lines in sequence are blue, red, green and black represent the S_{21} for the EHDz, MHDz, EHDx and MHDx antennas.

The response of the S_{21} depends on the antenna, where the change can be at least 7 dB for the EHDz and the MHDx, whereas for the EHDx and the MHDz, the change can be even 20 dB. Therefore the S_{21} for EHDz and MHDx are less sensitive to change in the radius than the EHDx and MHDz. The significant changes in the S_{21} can not be explained by the dissipated power, which is seen in Fig. 4.6b, where the increases of the dissipated powers are very small especially for the EHDx and the MHDz. Therefore, the increase or decrease of the S_{21} is related more to the coupling with surface-bound waves and to maxima location of the standing waves.

From this section and the pervious section, it was found that the S_{21} values were less sensitive for the case where the two antennas communicated around the sphere, whereas it has high sensitivity for the cases where the antennas communicated through and around the sphere.

4.3.5 Sensitivity of S_{21} to ε_r and σ

The electrical properties of the tissue may vary from person to person depending on age, gender or even race. In this section, the electrical properties were allowed to vary ±10 % around the electrical properties given in Fig. 4.2. The radius of the sphere and the distance of the antennas were kept constant. The S_{21} that corresponds to the electrical properties in Fig. 4.2 are referred to as the reference values. In Fig. 4.7, the ratio of the S_{21} values to the reference values at 1 GHz is shown, where the color is the scalar value of the ratio in dB.

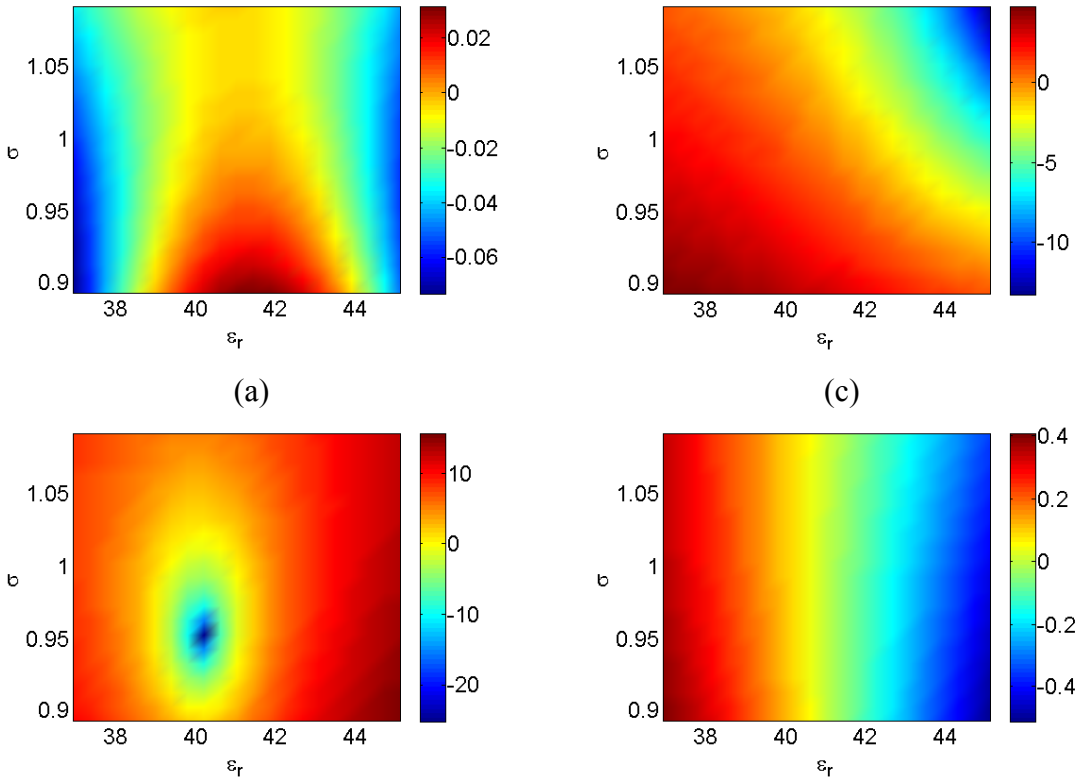

Fig. 4.7: The ratios of the S_{21} at 1 GHz for the EHDz (a), MHDz (b), EHDx (c) and MHDx (d).

The S_{21} of the EHDz antennas is almost insensitive to the changes in the electrical properties and the maximum change was observed at 2.45 GHz, where the change was 1.2 %, as seen in Tab. 4.1. The S_{21} for the MHDx was changed around 7.8 % at 400 MHz. Yet the changes were smaller than 10 %, which is the maximum change in the electrical properties. Large changes were observed for the EHDx and the MHDz, where the changes can be up to 498.6 % and 81.9 %, respectively. Therefore, such antennas have high sensitivity to the electrical properties of the head. For these antennas, the communication was through and around the head, except for the cases where the frequencies were 2.45 GHz. At this particular frequency the antennas exclusively communicate around the head. So when the communication takes place around the head, it becomes less sensitive to the small changes in the electrical properties. The results for the S_{21} at 400 MHz and 2.45 GHz are shown in appendix D.

Tab. 4.1: Differences in the S_{21}.

	$\lvert S_{21}\rvert$ %		
	400 MHz	1 GHz	2.45 GHz
EHDz	0.7	0.4	1.2
EHDx	70.8	498.6	8.4
MHDz	81.9	71.7	5.5
MHDx	7.8	4.8	1.3

4.4 Comparison of theory and measurement results

The path-loss is evaluated in a series of measurements. The antennas on both sides of the head are simultaneously moved away from the head in equally sized steps. The dipoles were kept tangential to the surface of the head at all times. S-parameters are obtained at each step, and the distance d between the antennas and the head is logged, as seen in Fig. 4.8. The path-loss measurements and the corresponding computed results are shown in Fig. 4.9, for the measurement and the computation series at the distance d. In regards to the computational model, the radius of the sphere is set to be 9.3 cm, where this value is the radius of a circle that has a half perimeter equal to l_{back}, which is defined in Fig. 4.8.

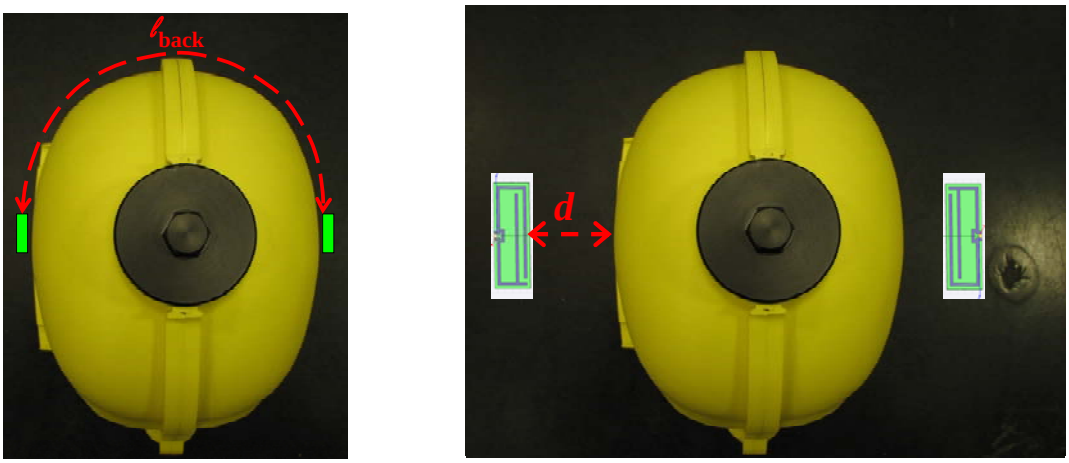

(a) (b)

Fig. 4.8: Top view of SAM head phantom.

The measured and the computed path-loss are determined for the frequencies 920 MHz, 1.5 GHz, 2.45 GHz and 3.227 GHz, as functions of the distance d. The blue lines in Fig. 4.9, are the computed values of the path-loss and the red lines are the measured values. At 920 MHz, the path-loss for short distances (d < 10 cm) is between -35 dB and -40 dB. The path-loss is between -45 dB to -50 dB at 1.5 GHz, -55 dB and -65 dB at 2.45 GHz, and -52 dB and -65 dB at 3.225. By taking the uncertainty of the measurements into account, the results of the measurements and the computations are relatively close to each other. Since the measurements took place inside a non-anechoic environment, there will be constructive and destructive interferences with reflected signals. Even after the use of time-gating method that removes the reflected signals from the walls, there are some objects located at short distances with respect to the head including the table that supports the head, the bars that hold the antennas, the cables and the ground plane, which have short time delays. These signals affect the measured S_{21} constructively or destructively. In addition to the reflections, the head is asymmetric relative to the antennas. From such measurements, it is difficult to decide the nature of the communication channel; whether it is inside or outside the head.

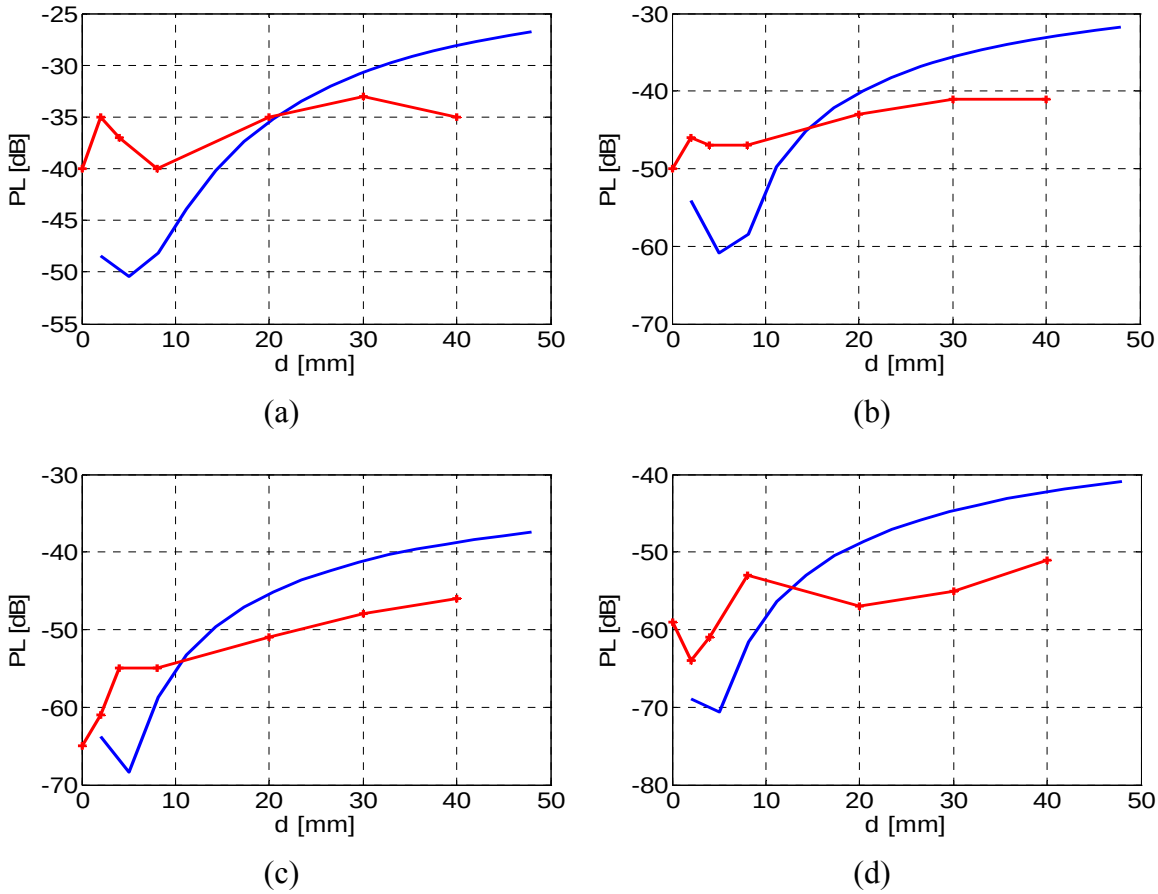

Fig. 4.9: Measured (red lines) and simulated (blue lines) path-loss at frequencies 920 MHz (a), 1.5 GHz (b), 2.45 GH (c) and 3.225 GHz (d) versus distances of the antennas.

4.5 Measurement campaign

Several measurements were obtained by different antennas. During those measurements, the antennas and the techniques were approved to obtain accurate results. In the beginning, some of the measurements were obtained without using baluns. It was expected that the leakage currents to radiate, but we expect their influence will be small in comparison with the radiation of the antenna. This was true in free-space case, where the cables were aligned in such way that minimizes the coupling of the leakage currents. In the section 3.2.1, the final antennas were shown, whereas the remaining antennas are not shown. But some the measurements that obtained by those antennas will be given in appendix F without discussions. In the beginning, some of the measurements were obtained without using baluns. Fig. 4.10 shows some of the measurements where Ant. 3 were used without baluns. The surface currents on the cable provide lower path-loss values in comparison with the path-loss at the resonant frequencies, which are around 2.45 GHz. To minimize the effect of the surface currents, the cables were oriented along the *z*-axis, as depicted in Fig. 4.10b, since it was expected the cables to perform as dipole antennas. Therefore in the free-space the path-loss of the surface currents is higher than the path-loss of the antenna. It is difficult to ensure that the measured path-loss at 2.45

GHz is the concrete value. Therefore, the antennas were mounted with the baluns to prevent the surface currents.

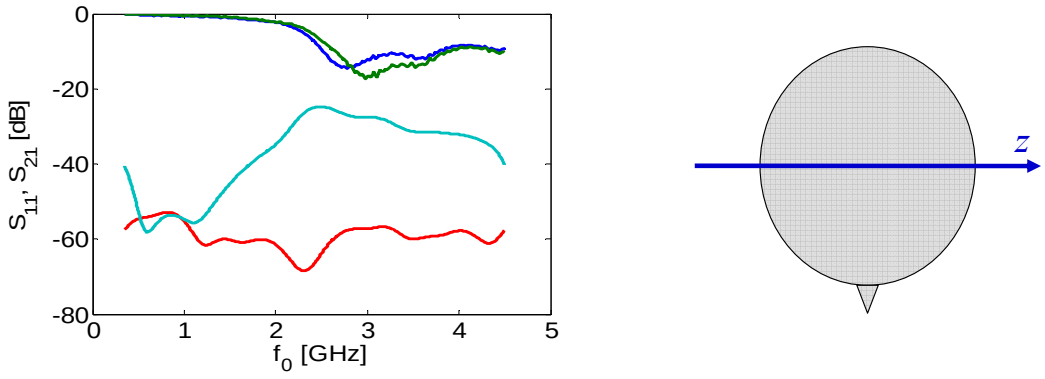

(a) (b)

Fig. 4.10: figure (a) shows the S_{11} and S_{21} of the Ant. 3 without baluns, where the blue and the green lines are the S_{11} of the antenna near SAM head phantom and in free-space respectively, while the red line is the S_{21} near SAM and the cyan line is S_{21} in free-space. Figure (b) shows the top view of the head.

The effect of the antennas angular position was also investigated. In the following measurements, the transmitting antenna has a fixed position while the receiving antenna moves in small steps on the head. Fig. 4.11 shows the measured path-loss as a function of the distances, which is measured from the transmitting antenna to the receiving antenna, as seen in Fig. 4.11d. The measurement were carried by the antennas; Ant. 1, Ant. 2 and Ant. 3. During the measurements the antennas were tangential to the head and had horizontal orientations with respect to the ground. The path-loss decreases as the distance increases at 920 MHz, as seen in Fig. 4.11a. The increase of the path-loss from the second measurement point can be described by a function of a distance from a reference point:

$$PL_1(l_{\text{back}}) = -32.55\text{dB} + 24\ln\frac{l_{\text{back}}/1\,\text{cm}}{25} \tag{4.2}$$

where the unit of l_{back} is cm. At 1.5 GHz, the path-loss increases as the as the distance increases, but the increase accompanies with oscillation because of the standing waves. The increase can be also described by a function of the distance:

$$PL_2(l_{\text{back}}) = -49\text{dB} - 22.9\ln\frac{l_{\text{back}}/1\,\text{cm}}{25} \tag{4.3}$$

The path-loss at 2.45 GHz increases as the distance increases, this increase accompanies with oscillations, which are the standing waves, and the increase will be described by the function:

$$PL_3(l_{\text{back}}) = -60\text{dB} - 17.8\ln\frac{l_{\text{back}}/1\,\text{cm}}{25} \tag{4.4}$$

The decrease of the path-loss at 920 MHz happens because the short distance between the antennas and so the increase will be small while the effect of the standing wave is

large, where the maximum is at the opposite side of the head with respect to the transmitting antenna.

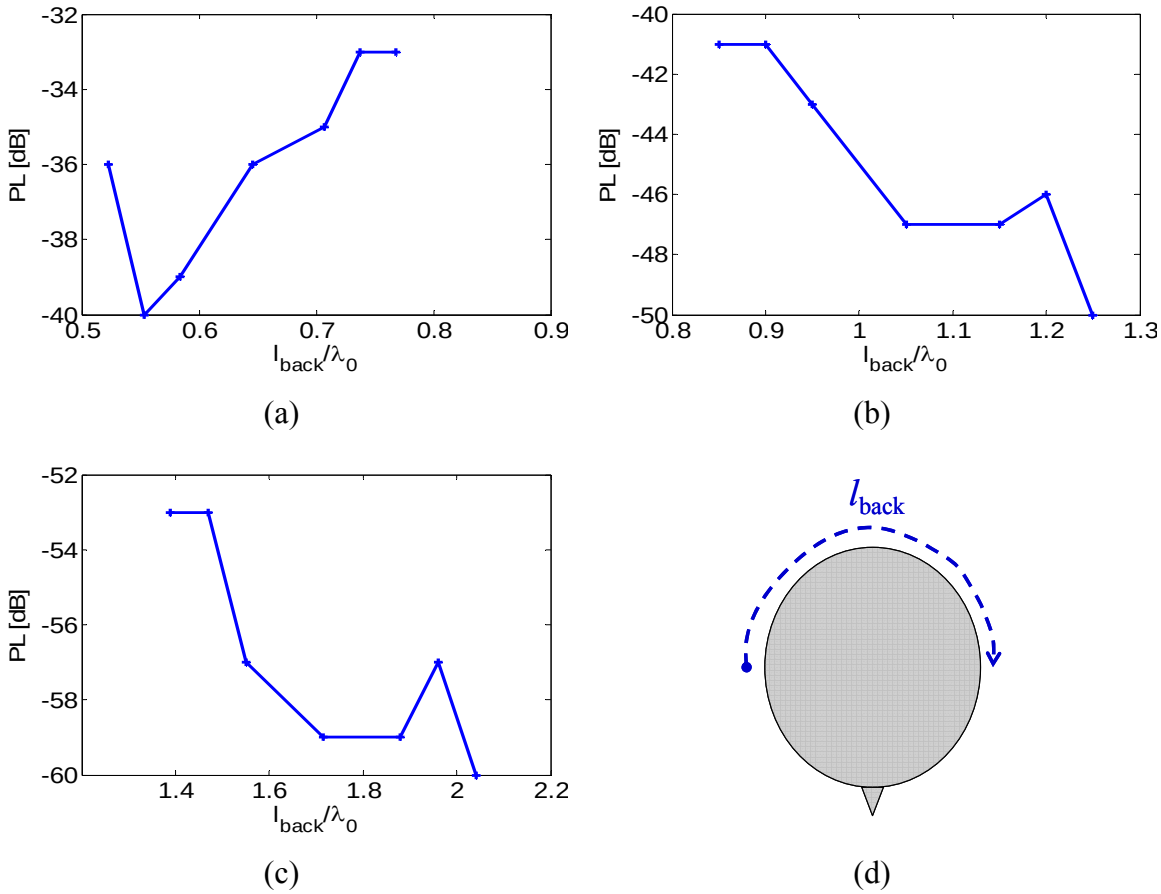

Fig. 4.11: Measured path-loss at frequencies 920 MHz (a), 1.5 GHz (b) and 2.45 GH (c) versus the distance l_{back} in wave-length. Figure (c) shows the top view of the head and the measured distance on back of the head.

4.5 Simulated results by HFSS

The measurements can provide the path-loss values, but in order to understand the involved mechanisms in the communication between the antennas, the field distribution must be computed inside and outside the head. The theoretical model gave some answers about the communication channels, but it remains an ideal model. Therefore, the measurement setup, including the antenna and the head phantom, was simulated in HFSS. In the numerical simulations, the details like the ground plane, the cable or the mechanical setup, were not included. The electrical properties of the numerical phantom head were specified by the electrical properties in Fig. 4.2. Measurement setup with two different antennas was simulated numerically by HFSS. One simulated the case where two Ant. 5 were located near the head, as seen in Fig. 4.12. The second simulated the case where two Ant. 1 were located near the head.

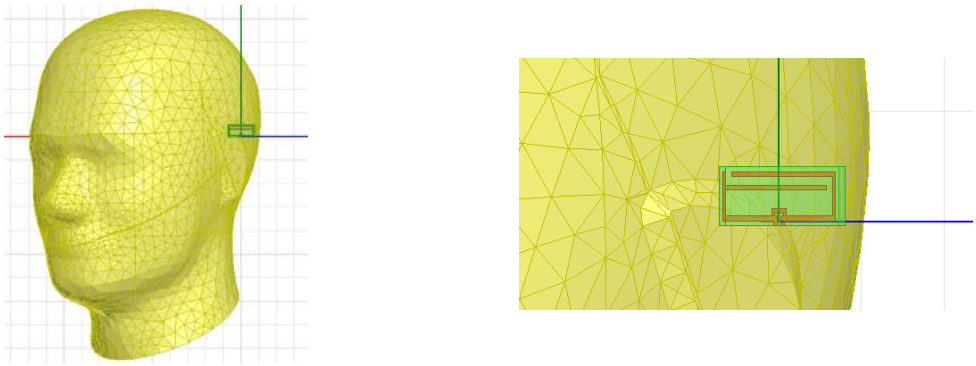

(a) (b)

Fig. 4.12: (a) A numerical phantom head used for the HFSS simulation and (b) Ant. 5.

The numerical simulation of the Ant. 5 shows the effect of the reflections from the surrounding environment and the dynamic range of the network analyzer on the measurements of S_{21}. The measured and the simulated values of S_{21} agree over a narrowband of frequencies, as seen in Fig. 4.13b, and then the measured S_{21} began to flatten. This occurs because the network analyzer can not measure values of S_{21} below ~ -75 dB.

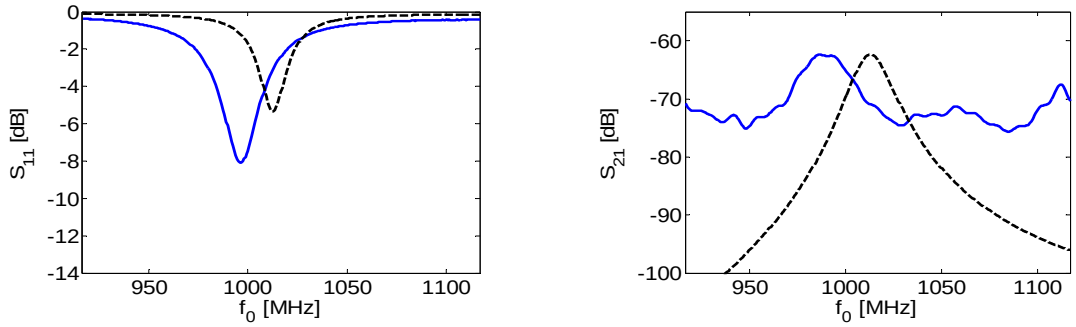

(a) (b)

Fig. 4.13: Measured and simulated *S*-parameters by Ant. 5.

The fields that were generated by Ant. 5 are shown in Fig. 4.14, where Fig. 4.14a shows the magnitudes of the electric field and Fig. 4.14b shows the magnitudes of the real values of the electric field. The transmitting antenna is located on the right side of the head and a receiving antenna on the left side.

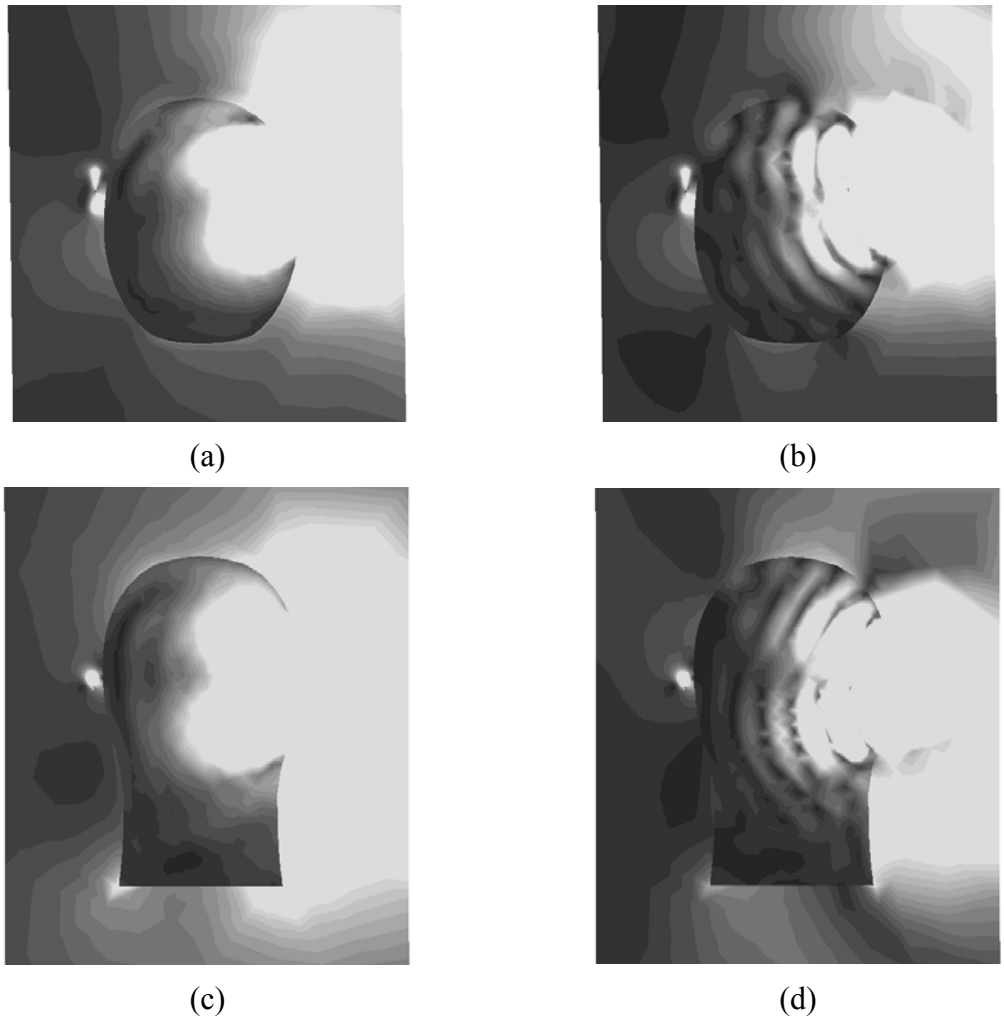

Fig. 4.14: Simulated magnitude of the complex (a) and (c), and the real (b) and (d), electric fields radiated by Ant. 5. The color scale ranges from 0 V/m (black) to 4 V/m (white) of the electric field. The plots (a) and (b) show top view, while (c) and (d) show the front view.

There are two channels for the ear-to-ear communication, one is inside and one is outside the head. Outside the head, the surface waves that propagate in clockwise and in counterclockwise directions result in constructive and destructive interference. This creates standing waves which appear clearly in Fig. 4.14a, where there are two minima regions and a maximum on the left side of the head. The real values of the field in Fig. 4.14b show the field waves propagate through and over the surface of the head. The waves that propagate through the head are less significant than the waves that propagate around the head, where the magnitude of the field experience higher attenuation inside the head than outside it. The attenuation appears because of the high conductivity of the head tissue and because the electrical path-length is larger inside the head than outside it.

The field distributions of Ant. 1, which are plotted in appendix F, show similar behaviors, where there exist two paths for the communication: one through the head and the second around the head. The high attenuation inside the head prevents these waves from attending the communication. The communication around the head takes place

through the surface-bound waves, where minima appears at $l_{back} \cong 3\lambda_0/4$ and $l_{back} \cong \lambda_0$, and one maximum at $l_{back} = l_{front}$.

As we notice here, the same behaviors have been observed as those in the theoretical investigations. This validates the qualitative results of the theoretical model.

5 Magneto-dielectric antenna

5.1 Introduction

Antenna miniaturization is essential for wireless communication in hearing aid systems since the mechanical as well as electrical size of the antenna must be small. There are several techniques for antenna miniaturization and recently there has emerged a significant interest in magneto-dielectric antennas. The magneto-dielectric materials facilitate miniaturization through a combination of magnetization and polarization, expressed in terms of the permeability and permittivity, yielding a smaller wavelength inside the material and thus allowing for mechanically smaller antenna structure compared to antennas without such materials. In contrast to purely dielectrically loaded antennas, the magneto-dielectric antennas can maintain an intrinsic impedance close to that of free space and may thus provide a better matching of the antenna at its input and output terminals as well as allowing larger bandwidth [47], [48] and [49].

It is difficult to find a material that has low loss of moderate permittivity and permeability values. Ferrite materials are highly lossy in the VHF range and up [48]. There are attempts to fabricate artificial magneto-dielectric materials [48]-[54]. In articles [48]-[50] the magneto-dielectric material was made by combining dielectric materials and ferrite materials. Others use the split-ring resonator, as in [51]-[54], to obtain the magneto-dielectric materials and that result in bulky substrates. The technique that was used in [48] to construct the magneto-dielectric material allows estimating the effective permittivity and permeability of the substrate, while there is not provide a pre-estimation of the effective constitutive parameters of the substrate in [49]. In [52] and [53] equivalent circuit models were provided to estimate the effective constitutive parameters. In [55] a technique was given to estimate the constitutive parameters, the technique is based on the *S*-parameters. This technique was also used in [52] and [53], where the unit cell was simulated using CST [56] and the results were compared to the analytical model. In [57] an experimental method was presented to estimate the effective constitutive parameters. The *S*-parameters were measured for two monopoles close to a unit cell which consists of a split ring resonator. From the S-parameters the constitutive parameters were estimated using the method in [55].

5.2 Material properties

5.2.1 Dielectric polarization and permittivity

Two opposite charges that have absolute values Q and are separated by a distance d form a dipole with a moment $\vec{p} = Q\vec{d}$. The dipole moment is directed from the negative to the positive charge. Average of the electric dipoles moment ($\vec{p}$) per volume (V) is the electric polarization vector ($\vec{P}$) [20, Eq. (2.3)];

$$\vec{P} = \lim_{\Delta V \to 0}\left[\frac{1}{\Delta V}\sum_{i=1}^{N}\vec{p}_i\right] \tag{5.1}$$

The units of the P are coulomb per meter (C/m). In a dielectric material, the electric flux density $\vec{D}$ is:

$$\vec{D} = \varepsilon_0 \vec{E} + \vec{P} \tag{5.2}$$

where $\vec{E}$ is the applied electric field. In a simple material there is proportionality between the polarization and the applied electric field, therefore (5.2) will be rewritten as following:

$$\vec{D} = \varepsilon_0 (1 + \chi_e) \vec{E} = \varepsilon_0 \varepsilon_r \vec{E} \tag{5.3}$$

where χ_e is electric susceptibility. There are three mechanisms that produce electric polarization for dielectric; dipole polarization, ionic polarization and electronic polarization. The materials, that have dipole (orientational) polarization, posse permanent dipole moments but in randomly orientation, thus the net result of the polarization is zero. However when an electric field applies, the dipoles tend to align with the applied field. Water has such polarization. The ionic (molecular) polarization appears in materials that consist of positive and negative ions such as sodium chloride (NaCl). Appling an electric field causes the charges to displace and that creates dipole moments. The electric polarization is evident in most materials, where the electrons in the atom / molecule can be modeled as negative charged cloud that surrounds a positive charge. When an electric field is applied, the cloud displaces from the center and that results in dipole moment [20, pp.46]. Fig. 5.1 shows the response of the electron cloud response to a time varying electric field.

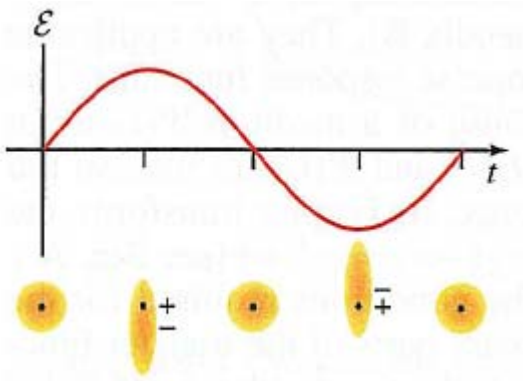

Fig. 5.1: Time varying electric field applied to an atom, inducing a time-varying dipole moment p that contributes to the overall polarization density P. The figure is copied from [58, Fig. 5.5-5].

5.2.2 Magnetization and permeability

Electric current flow always produces magnetic fields. Therefore atoms have magnetic dipole moments due to the motion of their electrons and due to the spin of the electrons. The average of the magnetic moments $\vec{m} = I\vec{S}$, where I is a current runs in a loop that has area S, per volume (V) is the magnetization ($\vec{M}$) [20, Eq. (2.17)];

$$\vec{M} = \lim_{\Delta V \to 0}\left[\frac{1}{\Delta V}\sum_{i=1}^{N}\vec{m}_i\right] \tag{5.4}$$

The unit of the magnetization in the m.k.s. units is ampere per meter (A/m) and in the c.g.s. units is emu per centimeters cubed (emu/cm^3) [59, pp. 10]. The magnetic flux density in a material is defined as;

$$\vec{B} = \mu_0\left(\vec{H} + \vec{M}\right) \tag{5.5}$$

where μ_0 is the free-space permeability $\vec{H}$ is the applied magnetic field. For simple materials (ferromagnetic materials excluded, $\vec{M}$ is linearly related to $\vec{H}$ and hence to $\vec{H}$ [21],

$$\vec{B} = \mu_0(1+\chi_m)\vec{H} = \mu_0\mu_r\vec{H} \tag{5.6}$$

where χ_m is the magnetic susceptibility. Materials fall into five groups; diamagnetic, paramagnetic, ferromagnetic, antiferromagnetic and ferrimagnetic, according to the behavior of their magnetic moments in an external magnetic field [20, pp. 57]. Diamagnetism arises from the orbital movement of the electrons. The orbital magnetic moments are opposite the direction of the applied magnetic field, thereby decreasing the field, and lead to negative magnetic susceptibility that result in values of relative permeability that are slightly less than unity. This effect occurs in all materials. Paramagnetism arises from the partial alignment of the electron spins in metals in the direction of the applied field. In paramagnetic materials the magnetic dipoles do not interact strongly with each other. The increase in the total magnetic field is therefore very small. Thus the magnetic susceptibility is slightly greater than unit. Ferromagnetism arises because of strong interaction between neighboring magnetic dipoles, a high degree of alignment occurs even in weak external magnetic dipoles, which causes a very large increase in the total field. Antiferromagnetism occurs when an ordered array of magnetic moments forms in which alternate moments have opposite polarizations. The result net magnetic moment is zero for the antiferromagnetic materials. The ferrimagnetism is a special case of the antiferrromagnetism whereas the alternate moments unequal in the absence of an applied magnetic field.

Ferromagnetic materials possess very high permeability and high conductivities; therefore there is minimum interaction between these materials and the electromagnetic waves [20]. Ferrites are made by sintering a mixture of metallic oxides and have a general chemical composition $A\mathrm{O}\cdot\mathrm{Fe_2O_3}$, where A is a divalent metal such as manganese, magnesium, iron, zinc, nickel, cadmium, etc. or a mixture of these [21, pp. 450] and [60, pp. 4]. Ferrites are ceramic-like materials with high specific resistivitis as much as 10^{14} greater than the metals and with dielectric constants around 10 to 15 or greater [21, pp. 450]. The high resistivity allows electromagnetic waves to penetrate them and therefore the ferrites are suitable for microwave applications (isolator, circulator, variable phase shifter, variable attenuators and switches) [21] and [60].

5.2 Theoretical approach

5.2.1 Antenna configuration

Antennas can have several configurations; linear wire antennas, loop antennas, helical antennas, microstrip antennas, etc. The microstrip antennas have low profile and they usually have light weights, simple and inexpensive to manufacture and many other benefits. For all these benefits, the patch antenna was chosen to study the effect of a magneto-dielectric substrate. The structure of the patch antenna that is depicted in Fig. 5.2 constitutes of a circular patch on top of a magneto-dielectric substrate of height h and an infinite ground plane. A coaxial cable feed the antenna through the ground plane at distance r_0 from the z-axis of the patch. The patch and the ground plane are made of conductors that have a finite conductivity σ. The magneto-dielectric substrate has both permittivity ε_r and permeability μ_r.

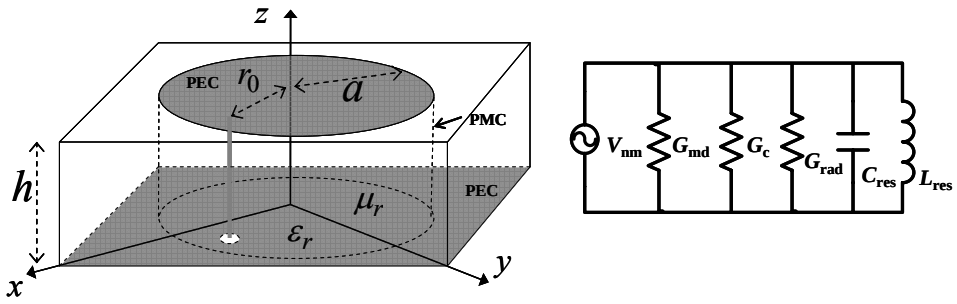

Fig. 5.2: The configuration of the circular patch antenna and its equivalent circuit.

Performance of an antenna can be described by many parameters, such as a bandwidth, radiation efficiency, size of the antenna, directivity, and etc. The study was limited on four parameters; which are the radiation efficiency, quality factor, bandwidth and the size of the antenna.

There are several techniques to analyze the patch antenna, including the cavity model [61]-[63] and the transmission line model [64]-[66]. The cavity model in [61] was expanded in this thesis to include the magneto-dielectric substrate. The patch antenna is modeled as a cylindrical cavity that is bounded with perfect electric conductors (PEC) on the top and on the bottom, and it is bounded by a perfect magnetic conductor (PMC) on the side wall, while the magneto-dielectric material fills the cylinder. The height of the substrate is very small in comparison with the radius a and the wave length λ inside the substrate. So the electric field is homogenous inside the substrate and it has a z-component,

$$E_z = CJ_n(kr)\cos n\phi \tag{5.7}$$

where C is a constant, J_n is the Bessel function of order n, and $k = \sqrt{\varepsilon_r \mu_r}\, k_0$ with k_0 is the free-space wave number. The magnetic field $\vec{H}$ can be calculated by using Maxwell's equation, and it becomes,

$$\vec{H} = -\frac{1}{j\omega\mu}\nabla \times \vec{E}$$

$$\vec{H} = -\hat{\phi}\frac{jCk}{k_0\eta_0\mu_r}J_n'(kr)\cos n\phi - \hat{r}\frac{jCk}{k_0\eta_0\mu_r r}J_n(kr)\sin n\phi \tag{5.8}$$

where $J_n'(kr) = dJ_n(kr)/d(kr)$. In order for the H_ϕ to vanish at the PMC wall the $J_n'(ka) = 0$. The roots χ_{nm} that satisfy this condition are given in [25, pp. 205]. So the antenna will be resonant at the frequency f_{nm} that is obtained by equating $\sqrt{\varepsilon_r\mu_r}k_0a_{nm}$ to χ_{nm}, where a_{nm} is the radius that satisfies the boundary condition;

$$f_{nm} = \frac{\chi_{nm}c}{2\pi a\sqrt{\mu_r\varepsilon_r}} \tag{5.9}$$

$$a_{nm} = \frac{\chi_{nm}}{k_0\sqrt{\mu_r\varepsilon_r}} \tag{5.10}$$

where c is the velocity of light in free-space. The electric field E_z on the PMC induces a surface magnetic current $\vec{M}^s = -2\hat{r}\times\hat{z}E_z = \hat{\phi}2E_z$ and this current is responsible for the radiation fields.

5.2.2 Efficiency calculation

The radiation efficiency ε_{rad} of the antenna is the ratio of the radiated power P_{rad} to the accepted power P_{acc}. The accepted power includes the radiated power, the lost power in the conducting disk and ground P_{C} and the lost power in the magneto-dielectric substrate P_{md}. So the efficiency is written as:

$$\varepsilon_{rad} = \frac{P_{\text{rad}}}{P_{\text{acc}}} = \frac{P_{\text{rad}}}{P_{\text{rad}} + P_{\text{C}} + P_{\text{md}}} \tag{5.11}$$

To calculate the far fields of the antenna, first the electric vector potential $\vec{F}$ can be calculated by using [39, eq. (3-28)] and then by applying [39, eq. (3-26)] and [39, (3-29)] the magnetic and the electric far fields can be found. Derneryd in [61] treats a microstrip disk antenna with dielectric substrate. He calculated the far fields, the conductance G_{rad} that will dissipate the same power as that radiated by the disk, the dielectric losses and the ohmic losses in the conductors as well the input impedance of the antenna. Similar approach will be used to find general expressions for the ohmic loss and for the magneto-dielectric loss for the magneto-dielectric microstrip disk antenna, while the radiated power will be calculated directly from G_{rad} since this value does not depend explicitly on constitutive parameters of the substrate. In reference to Fig. 5.2 the radiated power is calculated as:

$$P_{\text{rad}} = \tfrac{1}{2}G_{\text{rad}}\left|V_{nm}\right|^2 \tag{5.12}$$

$$V_{nm} = hE_z\big|_{r=a_{nm},\phi=0} = ChJ_n(ka_{nm}) \tag{5.13}$$

This is the radiated power for mode *nm*. The radiated power depends on the radius of the disk. So for a constant radius *a* the radiated power remains constant despite of values of the μ_r and ε_r as long as the product of them is constant.

The electric current density on the ground plane and on the disk, which have finite conductivities, are responsible for the ohmic losses. We assumed the electric and the magnetic loss tangents are small ($\mu_r'' << \mu_r'$ and $\varepsilon_r'' << \varepsilon_r'$), which minimizes the complexity of the calculations. This loss can be calculated as following:

$$P_{\mathrm{C}} = R_s \int_0^{2\pi}\int_0^{a} \left|\vec{J}^{\,s}\right|^2 \rho d\rho d\phi = R_s \int_0^{2\pi}\int_0^{a} \left(\left|J_\rho\right|^2 + \left|J_\phi\right|^2\right)\rho d\rho d\phi$$

$$P_{\mathrm{C}} \cong \frac{1}{2}\left|V_{nm}\right|^2 \frac{\pi R_s}{h^2 k_0^2 \eta_0^2 \mu_r'^2}\left(1+\delta_{0,n}\right)\left(\chi_{nm}^2 - n^2\right) = \frac{1}{2} G_{\mathrm{C}} \left|V_{nm}\right|^2 \tag{5.14}$$

where $\vec{J}^{\,s}$ is the electric surface current density on the ground plane and on the disk, R_s is the skin effect resistance and $\delta_{0,n}$ is the Kronecker delta and equals 1 for $n = 0$. Both the definition of R_s and the derivation of the ohmic power P_{C} are given in appendix III. Notice that the ohmic power is inverse proportional to the $\mu_n'^2$. So for constant radius the ohmic loss decreases as the value of μ_r increases.

The losses in the substrate can be divided to two losses, a magnetic loss and an electric loss. The sum of the magnetic and the electric losses in the substrate will be called as a magneto-dielectric loss. The magneto-dielectric loss power P_{md} will be calculated directly from eq. (5.7) and (5.8) by utilizing [25, pp.24] which yields;

$$P_{\mathrm{md}} = \frac{\omega \varepsilon_r'' \varepsilon_0}{2}\int_V \left|E_z\right|^2 dV + \frac{\omega \mu_r'' \mu_0}{2}\int_V \left|\vec{H}\right|^2 dV$$

$$P_{\mathrm{md}} \cong \frac{1}{2}\left|V_{nm}\right|^2 \left[\frac{\tan\delta_e}{\omega\mu_0} + \tan\delta_m\right]\frac{\pi(1+\delta_{0,n})}{2\mu_r' h}\left(\chi_{nm}^2 - n^2\right) = \frac{1}{2} G_{\mathrm{md}} \left|V_{nm}\right|^2 \tag{5.15}$$

where $\tan\delta_e = \varepsilon''/\varepsilon'$ and $\tan\delta_m = \mu''/\mu'$ are the electric and the magnetic loss tangents of the substrate, respectively. The derivation of the magneto-dielectric power is given in appendix III. The loss in the substrate is inverse proportional to μ_r'. The loss in the magneto-dielectric substrate is dominated by the magnetic loss, since the electric loss tangent is divided by $\omega\varepsilon_0$. For example, at a frequency of 100 MHz the $\omega\varepsilon_0$ is about ~ 800, so the first term in Eq. (5.15) becomes insignificantly small and thus it can be neglected from the equation. After we found all the necessary conductances, the radiation efficiency can be calculated in terms of the conductances. Because the voltage term is one for all the powers, therefore it will be canceled out and thus;

$$\varepsilon_{rad} = \frac{G_{\mathrm{rad}}}{G_{\mathrm{rad}} + G_{\mathrm{C}} + G_{\mathrm{md}}} \tag{5.16}$$

5.2.3 Quality factor and bandwidth calculations

The quality factor is defined as the ratio of the stored energy to the energy loss per cycle:

$$Q = \omega \frac{W_{\mathrm{e}} + W_{\mathrm{m}}}{P_{\mathrm{rad}} + P_{\mathrm{C}} + P_{\mathrm{md}}} \tag{5.17}$$

where ω is 2π times the operating frequency f, W_{e} and W_{m} are the stored electric and magnetic energies. At resonance the magnetic energy equals the electric energy, so the quality factor will be calculated in term of the electric energy:

$$Q = \frac{2\omega W_{\mathrm{e}}}{P_{\mathrm{rad}} + P_{\mathrm{C}} + P_{\mathrm{md}}} \tag{5.18}$$

The quality factor Q of an antenna is an important parameter specifying the antenna performance, in particular, a high value of Q means that large amounts of the reactive energy is stored in the near zone field, and this in turn implies large currents, high ohmic losses, narrow bandwidth, and large frequency sensitivity [67]. So it is preferred to reduce the Q value, but this value is physically limited and the lower bounds of Q for the first two modes are known as Chu lower bound which is given in [20]:

$$Q_{\mathrm{Chu},11} = \frac{1}{k_0 a} + \frac{1}{(k_0 a)^3} \tag{5.19a}$$

$$Q_{\mathrm{Chu},21} = \frac{3}{k_0 a} + \frac{6}{(k_0 a)^3} + \frac{18}{(k_0 a)^5} \tag{5.19b}$$

The Chu lower bound will be used to normalize the quality factor of the magneto-dielectric antenna. Another important parameter that specifies the antenna performance is the bandwidth BW of an antenna. The bandwidth relates to the quality factor Q of the antenna and from [39, eq. (14-88a)] it can be expressed as:

$$BW_{|\Gamma|} = \frac{2|\Gamma|}{Q\sqrt{1-|\Gamma|^2}} \tag{5.20}$$

where Γ is the maximum allowable input reflection coefficient. Most of the reactive energy of the patch antenna is stored inside the substrate while a small amount of the energy may stored outside the patch, this assumption is based on the condition that $h << a$. The total stored energy equals twice the stored electric energy at the resonance frequency. The stored electric energy can be calculated by utilizing [21, eq. (2.51a)]:

$$W_{\mathrm{e}} = \frac{1}{4}\int_V \varepsilon' \vec{E} \cdot \vec{E}^* dV \tag{5.21}$$

where $\varepsilon' = \mathrm{Re}\{\varepsilon_0 \varepsilon_r\}$ and V is the volume under the disk. By substituting eq. (5.7) in (5.21) the energy becomes as following:

$$W_{\mathrm{e}} = |C|^2 \frac{\pi \varepsilon_r' \varepsilon_0 h}{8k^2}\left(k^2 a_{nm}^2 - n^2\right) J_n^2(k a_{nm}) = |C|^2 h^2 J_n^2(\chi_{nm}) \frac{\pi \varepsilon_r' \varepsilon_0}{8k^2 h}\left(\chi_{nm}^2 - n^2\right)$$

$$W_{\mathrm{e}} = |V_{nm}|^2 \frac{\pi \varepsilon_r' \varepsilon_0}{8k^2 h}\left(\chi_{nm}^2 - n^2\right) \tag{5.22}$$

5.3 Numerical results

For this section in general, the substrate is taken to be lossless and the conductor is made of the copper. To understand the effect of the magneto-dielectric substrate on the performance of the patch, parameter studies will be carried where the frequency remains constant while the radius, μ_r and ε_r change.

5.3.1 Validation of the analytical formulas

The cavity can be modeled as a parallel resonator which is shown in Fig. 5.2. The input impedance of the antenna is given as:

$$Z_{in} = \frac{G - j\omega\left(C_{res} - \dfrac{1}{\omega^2 L_{res}}\right)}{G^2 + \omega^2\left(C_{res} - \dfrac{1}{\omega^2 L_{res}}\right)^2} \tag{5.23}$$

$$G = G_{rad} + G_C + G_{md}$$

The capacitance C_{res} and the inductance L_{res} can be calculated from the resonance frequency $f_0 = f_{nm}$ and the quality factor of the antenna Q:

$$L_{res} = \frac{1}{2\pi f_0 G Q} \tag{5.24a}$$

$$C_{res} = \frac{(2\pi f_0)^2}{L_{res}} \tag{5.24b}$$

By inserting L_{res} and C_{res} in eq. (5.23) we are able to find the real and the imaginary values of the input impedance Z_{in}.

The analytical solution was validated against numerical simulations by using HFSS. Three circular patch antennas that are resonant at 1 GHz and have radiuses a = 39.31 mm, are supported by three different substrates; one constitutes of a dielectric material, the second constitutes of magnetic materials and the third constitutes of magneto-dielectric materials. They have equal heights h = 1.5 mm, while the electrical properties were given in Tab 5.1. The structure of the circular patch antenna is depicted in Fig. 5.3.

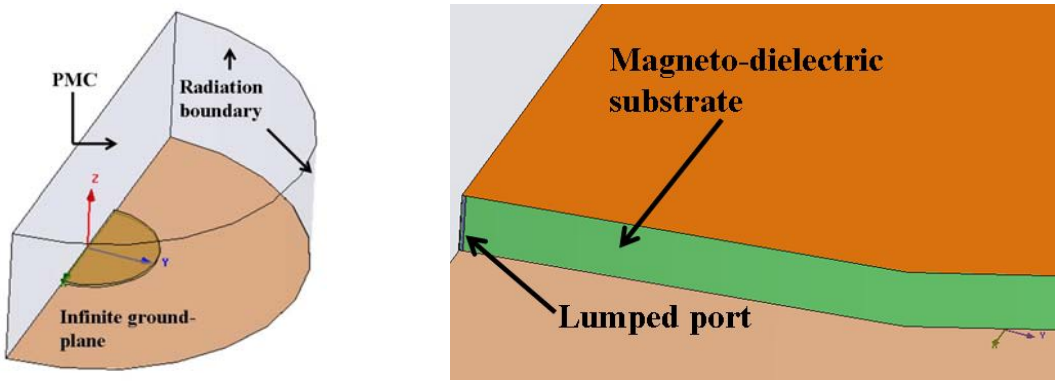

Fig. 5.3: The structure of the patch antenna in HFSS.

The antenna fed by a lumped source between the patch and the ground plane at *a*. Equation (5.10) was used to estimate the radius of the antennas which operate at the fundamental mode TM_{11}. The equation provides a good estimation about the radius, but in the simulation the resonance frequency is shifted a little bit to the right. Patch antennas usually have narrow bandwidth, so in the simulation the frequency swept between ±25 MHz around the resonant frequency.

Fig. 5.4, 5.5 and 5.6 show the real and the imaginary parts of the input impedance of the patch antennas. The blue lines represent the results of the analytical solutions while the red dashed lines represent the results of the simulations. The left graphs show the cases where the radiuses of both the analytical and simulated solutions are equals (a = 39.31 mm). In the right graphs, the radiuses of the analytical solutions were changed to shift the resonant frequencies toward the simulation results. There are good agreements between the simulations and the analytical solutions, where the differences between the impedances are small.

The calculation of the resonant frequency by eq. (5.9) does not take into account fringing effect. The fringing increases the dimension of the patch, so the resonant frequency shifts to the left. For dielectric substrates the actual radius a will be replaced by and an effective radius a_e which is given in [27, eq. (14-67)];

$$a_e = a\left\{1+\frac{2h}{\pi a\varepsilon_r}\left[\ln\left(\frac{\pi a}{2h}\right)+1.7726\right]\right\}^{1/2} \tag{5.25}$$

The shift of the resonant frequency for the dielectric substrate is not as large as the other cases, where the resonant shifts 2 % for the dielectric substrate, 2.5 % for the magneto-dielectric substrate and 5 % for the magnetic substrate. To shift the resonant frequencies toward the simulated results, the radius of the patch were changed to 38.5 mm, 37.5 mm and 38.2 mm for the antenna with dielectric, magnetic and magneto-dielectric substrates, respectively. Tab. 5.1 shows the values of the radiation efficiencies ε_{rad} and the bandwidths BW of the analytical and the simulated results. There are some differences between the analytical and the simulated results, but in general they seem to have close values. In order to design a circular patch antenna the analytical solution provides knowledge including the radius, the efficiency, the optimal location to match a feeding line and etc.

In addition to that, each simulation in HFSS requires at least 5 min which is the time to make the calculations, pre-preparations are required to make the simulation and that add extra time, while the analytical solution can perform hundreds of calculation in few seconds. Therefore, the parameter investigations were carried by the analytical model.

Tab. 5.1: Efficiency and bandwidth of magneto-dielectric antennas with different electrical properties

μ_r	ε_r	analytical		simulation	
		ε_{rad} %	$BW_{\text{-10dB}}$ %	ε_{rad} %	$BW_{\text{-10dB}}$ %
1	5	71.8	0.6	61.1	0.5
5	1	98.5	1.5	94.5	1.4
2.2361	2.2361	92.9	0.8	86.6	0.8

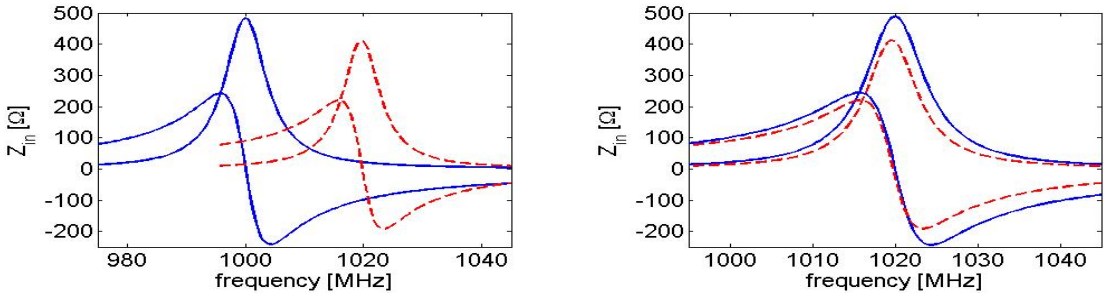

Fig. 5.4: The impedance of the patch antenna with a dielectric substrate ($\mu_r = 1$, $\varepsilon_r = 5$), where the blue lines represent the analytical results, while the red dashed lines represent the results of the simulation program HFSS.

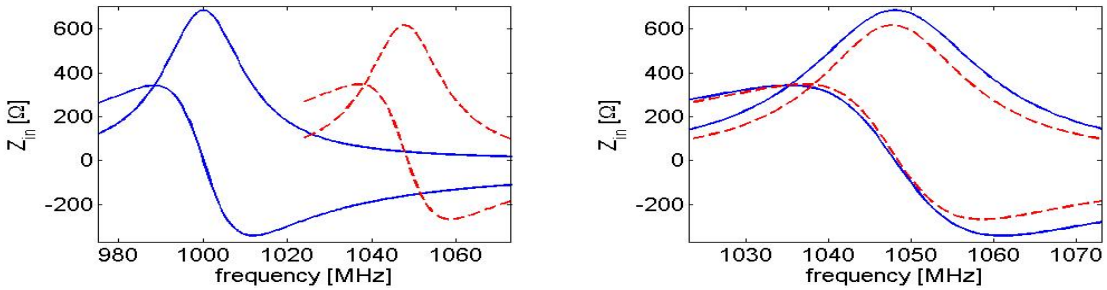

Fig. 5.5: The impedance of the patch antenna with a magnetic substrate ($\mu_r = 5$, $\varepsilon_r = 1$).

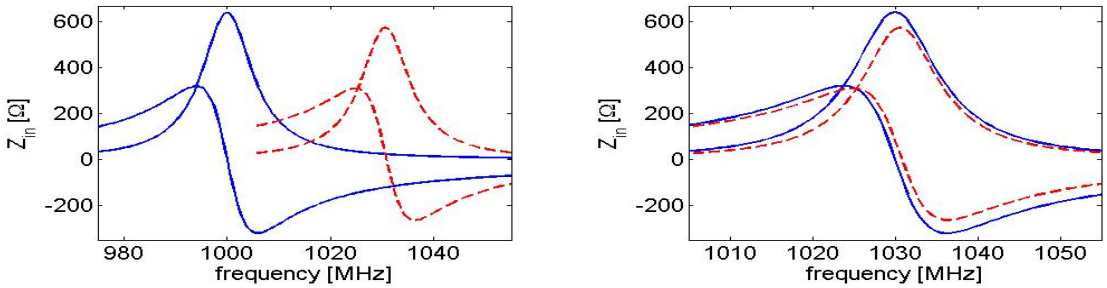

Fig. 5.6: The impedance of the patch antenna with a magneto-dielectric substrate ($\mu_r = \varepsilon_r = 2.2361$).

5.3.2 Effect of μ_r and ε_r on the efficiency

The efficiency is an important parameter that affects the link-budged of communication. Small antennas usually have poor efficiencies, small bandwidth, omni-directional pattern and very small input impedances. But the efficiency becomes a very important issue for a communication system that has limited power supply, such as hearing-aid devices, in/on body sensors or other small devices. Fig. 5.7 shows the efficiency in percent of the fundamental and the second modes (TM_{11} and TM_{21}), where the horizontal axis is values of μ_r, the vertical axis is the values of ε_r and the color is the scalar value of the efficiency. The dashed line represents the cases where the radius a was kept constant, while both μ_r and ε_r change according to eq. (5.10).

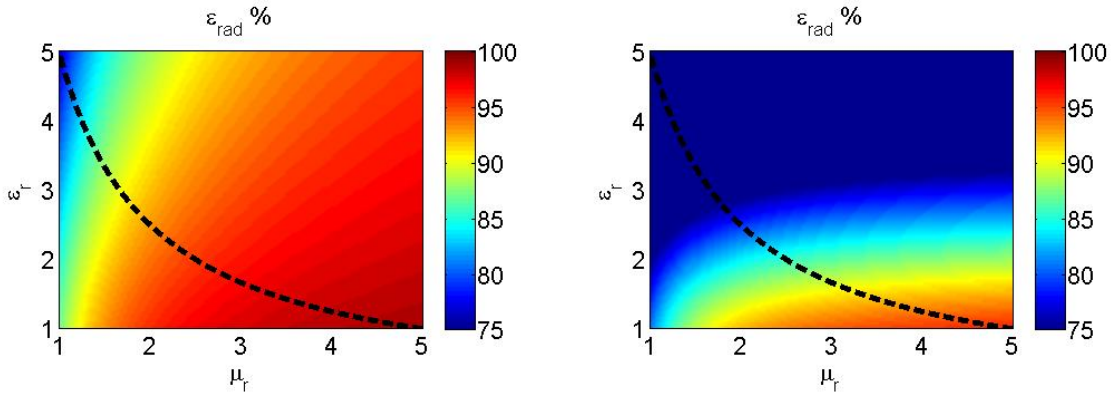

Fig. 5.7: Radiation efficiency of the TM_{11} (left) and TM_{21} (right).

By viewing the cases where a is constant we notice the following; a) the efficiency increases as μ_r increases for the TM_{11} and TM_{21}, b) for a constant ε_r the efficiency increases as μ_r increases until it saturates at certain values of μ_r for the second mode TM_{21} and c) we expect TM_{11} to have saturation but for higher values of ε_r than that for TM_{21}. The increment of the efficiency happen, because of the reduction in the electric currents on the patch and on the ground-plane, since the substrate was assumed to be lossless ($P_{md} = 0$) and the radiated power P_{rad} is constant, because it depends only on the radius a. So according to eq. (5.16) the denominator becomes small as μ_r increases, which leads to the conclusion that P_C becomes small as μ_r increases. This result had been found for a rectangular patch antenna numerically in [68].

5.3.3 Effect of μ_r and ε_r on the quality factor

The quality factors were also calculated for lossless substrates, where Fig. 5.8 shows the ratio of the quality factor Q to the Chu lower bounds $Q_{Chu,11}$ and $Q_{Chu,21}$ which are given by eq. (5.13a) and (5.13b), respectively. The Chu lower bounds depend only on the radius of the sphere that surrounds the antenna, so for the cases where the radiuses were kept constant the Chu lower bounds remain constants.

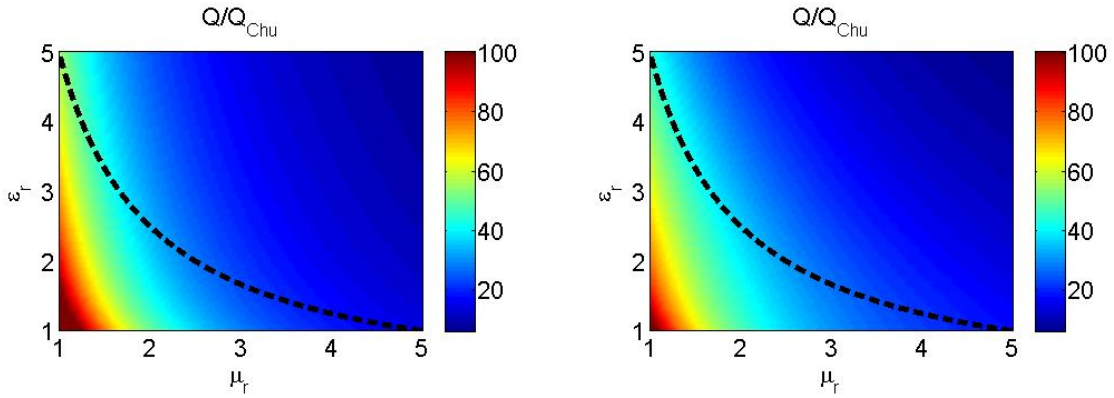

Fig. 5.8: Ratio of the quality factor to the Chu lower bound of the TM_{11} (left) and TM_{21} (right).

That ratios of the TM_{11} and TM_{21} are almost similar, as we follow the dashed line the ratio decreases as μ_r or ε_r increases but the reduction of the ratio is faster for the increase of μ_r than for the increase of ε_r. Since the Chu lower bounds are constants on the dashed lines, that means the reduction of the quality factor Q are faster than the reduction of the Chu lower bounds. The increment of ε_r results in high ohmic loss P_C which leads to a small Q, while the increment of μ_r results in small ohmic loss P_C which leads to a high Q. Since the Q decreases, so the increment of μ_r minimizes the total stored energy in the system. The minimum quality factor is almost 7 times the Chu lower bound, which is not a small value because the patch occupies a small fraction of the sphere that surrounds the antenna.

5.3.4 Effect of μ_r and ε_r on the bandwidth

Here we shall study the effect of the electrical properties of the magneto-dielectric substrates on the bandwidths of the antenna. The bandwidth increases as the μ_r increases for both of the modes, and decreases as the ε_r increases.

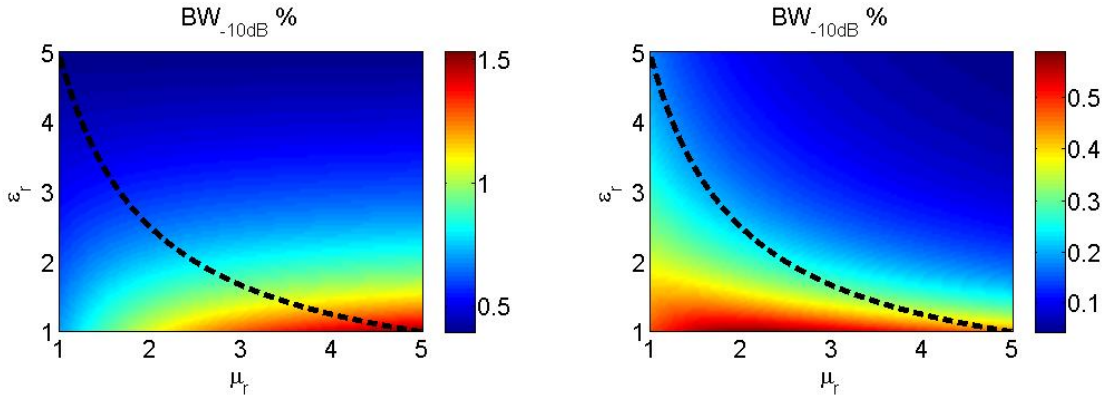

Fig. 5.9: Bandwidth of the TM_{11} (left) and TM_{21} (right).

We notice that the highest bandwidth is almost 1.5 % for the TM_{11} and smaller than 0.6 % for the TM_{21}. The pattern of the of the bandwidth for TM_{11} is different from the pattern of the TM_{21}, where for a constant ε_r the bandwidth increases as μ_r increases until BW saturates at certain μ_r for TM_{11}, while the bandwidth decreases as μ_r increases for TM_{21}. For the cases on the dashed lines, the bandwidth increases as μ_r increases for both TM_{11} and TM_{21}.

5.3.5 Lossy substrate

The magneto-dielectric substrate can have a high loss tangent [50] and [66]. It is possible to find dielectric substrates with high ε_r and small electrical loss tangents $\tan\delta_e$ around 0.001. We will compare the performances of a patch antenna with a lossy magneto-dielectric substrate to the performances of an antenna with a low loss dielectric substrate. The calculations are carried out with HFSS. The refractive index n of the magneto-dielectric and the dielectric substrate is kept equal, while the loss tangent is taken to reflect realistic values. Both antennas have the same dimensions and they are fed

through a lossless lumped component matching circuitry. A radiation boundary was used to calculate the efficiency of the antennas and the bandwidths were read from the S_{11} graphs.

Fig. 5.10 shows both the efficiency and the bandwidth results of the numerical solutions. The height of the antennas is kept constant h = 1.5 mm, and the radii are determined for an operation frequency of 1 GHz. Equation (5.7) can be used to estimate the radius of the antenna and during the simulation small adjustment on the radius is necessary to shift the resonant frequency toward 1 GHz. The ground plane and the patch are taken to be made of copper which reveals the advantage of using magneto-dielectric substrate. The black line is for a patch antenna with dielectric substrate. This antenna will be used as a reference for the comparison. The simulated antennas have dielectric substrate (ε_r=2, μ_r=1), magneto-dielectric substrates (ε_r=2, μ_r=2) and (ε_r=2, μ_r=4). The areas of these antennas compare with the reference antenna are 1:1, 1:2 and 1:4. The antennas with the magneto-dielectric substrates will be divided into two groups; a group with constant electrical loss tangent $\tan\delta_e$ = 0.001 while the magnetic loss tangent $\tan\delta_m$ varies, and a group with $\tan\delta_e = \tan\delta_m$. The antennas of the first group (the blue and the green lines) have higher efficiencies than the reference antenna (black line), while they have almost the same bandwidth. The antennas of the second group (the red and the cyan lines) have less or comparable efficiencies to the reference antenna and the bandwidth of these antennas are wider than the bandwidth of the reference antennas, especially for the high loss cases. This can be understood from equations (5.8) and (5.10), where the increase in P_{md} reduces the total quality factor and this leads to an increase in the bandwidth. The antennas of the first group are almost 10 % more efficient than the antennas of the second group. At low $\tan\delta_e$ the bandwidths of the two groups are almost comparable, while the bandwidth of the second group is almost 20 % wider than the bandwidth of the first group at high $\tan\delta_e$. For the same dielectric losses the efficiency of the antennas increases as the permeability μ_r increases, while the bandwidths are almost unchanged. This agrees with the analytical results of the fundamental mode (1,1).

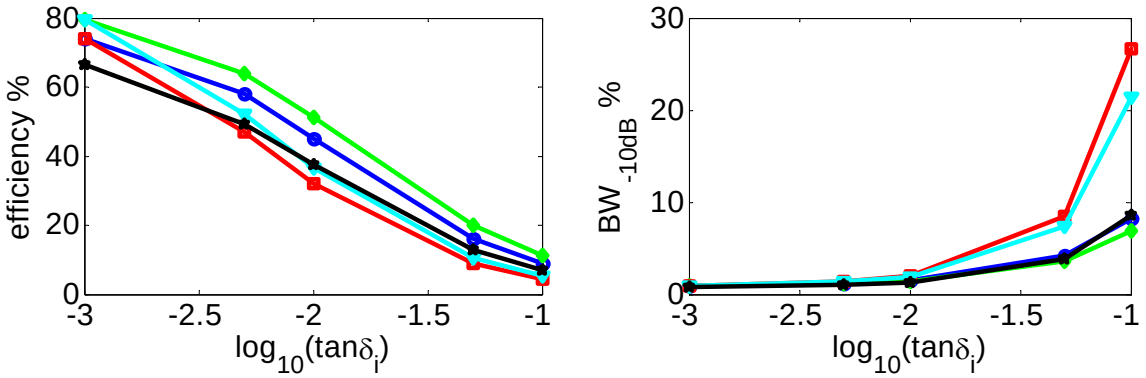

Fig. 5.10: The efficiency and the bandwidth for lossy magneto-dielectric antennas. All the antennas are supported by substrates that have ε_r = 2, while different μ_r and $\tan\delta_e$ have been taken. The index i = m for the magnetic loss tangent and i = e for the electric loss tangent. The blue and the green lines are related to substrates having constant $\tan\delta_e$ = 0.001, and μ_r = 2 and 4, respectively, while both the red and

the cyan lines are related to $\tan\delta_m = \tan\delta_e$ = [0.001, 0.005, 0.01, 0.05, 0.1], and μ_r = 2 and 4, respectively. The black line is related to dielectric substrates, which have ε_r = 2, μ_r = 1 and $\tan\delta_m$ = 0.

Since it is possible to find dielectric substrates with low $\tan\delta_e$, two other antennas have been also simulated, where the substrates have (ε_r=4, μ_r=1), (ε_r=8, μ_r=1) and $\tan\delta_e$ = 0.001. The efficiencies of these antennas are 56.5 % and 43.8 %, and the bandwidths are 0.7 % and 0.4 %. The sizes of these antennas are comparable to the sizes of the magneto-dielectric antennas with (ε_r=2, μ_r=2) and (ε_r=2, μ_r=4). Fig. 5.10 shows the differences between the efficiencies and the bandwidths of the antennas with the magneto-dielectric substrates and the antennas with the dielectric substrates of the same sizes. We see the same behavior here where the magneto-dielectric substrate with high μ_r and low losses provide good efficiency. As long the losses increase, which is the case for many ferrite composites, the efficiency degrades.

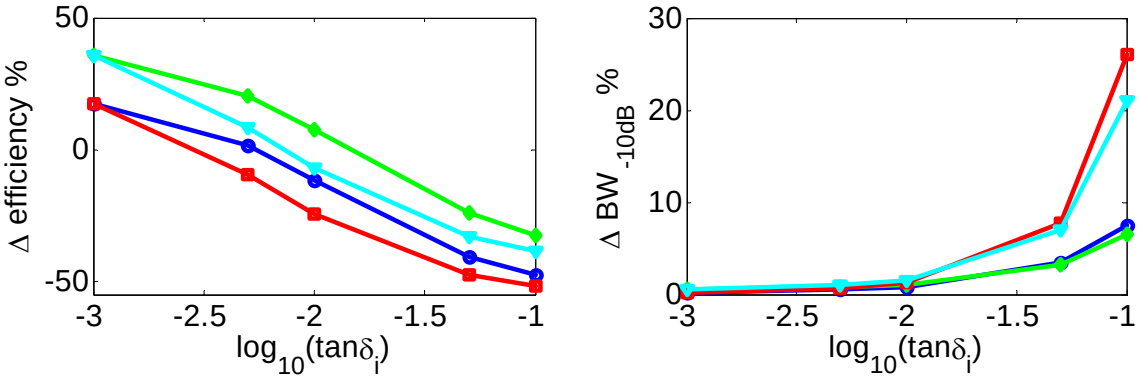

Fig. 5.11: The differences of the efficiencies and the bandwidth of the magneto-dielectric antennas in fig. 5 and antennas with dielectric substrates that have same sizes as the magneto-dielectric antennas.

6 Summary and conclusions

6.1 Ear-to-ear communication

The theoretical work focused on establishing a simple model for the communication between two antennas near a head. The model investigates the general nature of the communication in a qualitative way, whereas detailed and quantitative investigations require a more complicated model. Thus the head was modeled as a homogenous sphere and the antennas were modeled as electric/magnetic hertzian dipole antennas. The electromagnetic fields were expanded in terms of spherical vector wave functions. The dissipated and the radiated power were calculated, and the path-loss was defined in terms of the scattering coefficients for four cases; a *z*-oriented electric hertzian dipole antenna (EHDz), a *z*-oriented magnetic dipole antenna (MHDz), an *x*-oriented electric hertzian dipole antenna (EHDx) and an *x*-oriented magnetic hertzian dipole antenna (MHDx). The convergence of the solutions was tested and it was found that source and observation close to scatterer problem requires a large number of modes. The spherical model was used to generate 2D plots of the fields inside and outside the sphere. The plots provided information about the communication channels, such as the locations of the channels, the type of propagation and the polarization of the waves close to the sphere. The plots showed two channels; one is through the head and one is around it. The inside waves were subjected to high attenuation that makes the contribution of these waves in the communication insignificant. The outside communication channel used surface-bound waves to transmit signals between the antennas. It was found, at least for the studied frequencies, that the EHDz generated surface waves have orthogonal polarizations, while the EHDx and MHDz generated surface magnetic waves of mixed polarizations and the MHDx generated surface magnetic waves of tangential polarizations. The term “magnetic polarization” was used, because the transmitting and the receiving antennas were magnetic dipoles. The values of the path-loss for EHDz and MHDx were low (-10 dB for EHDx and -27 dB at 1 GHz), and high for the MHDz and EHDx (-65 dB for MHDz and -50 dB for EHDx at 1GHz). This is due to the coupling of the receiving antennas with the surface waves. The first two antennas had orientations that were parallel with the polarizations of the surface waves, while the latter two antennas had orientations that are almost orthogonal with the polarizations of the surface waves. So we came to the following conclusions:

1. Ear-to-ear wireless communications take place outside the head.
2. The communications take place through surface waves that run on the surface of the head.
3. Path-loss can be minimized by generating surface waves of polarizations that are parallel to the orientation of the receiving antenna.

In the second part of the study, experimental investigations were carried to measure the path-loss. A measurement setup consisting of a network analyzer, a set of antennas and a standard SAM phantom head, were arranged. Most of the designed antennas were dipoles, because they had been used to make comparisons with the theoretical results. Different baluns were designed to prevent the surface currents on the feed cables from corrupting the measurements. Performances of the antennas and the baluns were

characterized by measurements and simulations. The measurements of the path-loss took place near the head at different locations and frequencies and the path-losses of the head were found to be -40 dB at 920 MHz, -50 dB at 1.5 GHz, -65 dB at 2.45 GHz and -60 dB at 3.225 GHz. These values correspond to the antenna on the head. A comparison of the measurements and the theoretical computation shows good agreements between them.

The investigations show that the surface-bound waves are the main mechanism in the ear-to-ear wireless communication, and the path-loss values depend on the quality of the coupling between the polarizations of the surface-bound waves and the receiving antenna. Therefore, to minimize the path-loss, it is important to design antennas that generate surface-bound waves of polarizations that coincide with the polarization of the antennas. It is better to work in the frequency range between 1 GHz and 3 GHz, where the path-loss is smaller than -35 dB and the efficiency of the antennas are acceptable in this range.

In this subject, I suggest using of different orientations and other types of antennas, like loop antennas or monopoles. For future work, different orientations and different antenna types shall be considered, where loop antennas and monopoles can be use to measure the path-loss.

6.2 Magneto-dielectric antenna

For the magneto-dielectric antenna, an analytical method was used to study the effects of magneto-dielectric materials on the performances (the efficiency, the bandwidth and the quality factor) of an antenna. A circular patch antenna was chosen for the study. The antenna was modeled as a cylindrical cavity filled with the magneto-dielectric material. Analytical formulas for the efficiency, the bandwidth and the quality factor were derived, and they were validated against numerical simulations by HFSS. The analytical solution can handle low-loss substrates, while it can not treat high-losses cases. Parameter studies were carried to find the optimal performances of the antenna, where both μ_r and ε_r vary between 1 and 5. An increase of μ_r gives best performances, where the efficiency increase as well does the bandwidth which increases or at least remains constant while the size of the antenna reduces. An increase of μ_r results also in minimizing the stored energy, and that leads to minimize the quality factor. The increase of ε_r degrades the performances of the antenna, where the efficiency and the bandwidth decrease, as well does the quality factor which increases, and that results in increasing the stored energy. High loss tangent degrades the performances of the patch antennas.

It is possible to find substrates with high dielectric constant and yet with a small loss tangent, but it is difficult to find a magneto-dielectric substrate that has a small loss tangent. Both the quality factor and the bandwidth increase as the loss tangent increases, but the efficiency becomes small. The magneto-dielectric materials have potentials to replace the conventional dielectric materials, but they have problems which can be overcome with time.

This subject is not a new one, but it did not investigated as should be. The analytical model should be developed to include high-loss cases. Different antennas should be considered, like loop or helix antennas. In addition the theoretical investigation,

experimental works should use ferrite, but at low frequencies where the loss of the ferrite is small, or split ring resonators as magneto-dielectric materials.

References

[1] B. Edwards, "The Future of Hearing Aid Technology," *Trends in Amplification*, vol. 11, no. 1, pp. 31-45, Mar. 2007.

[2] Y. Zhao, Y. Hao, A. Alomainy, C. Parini, "UWB On-Body Radio Channel Modeling Using Ray Theory and Subband FDTD Method," *IEEE Trans. Microw. Theory Techniq.*, vol. 54, no. 4, pp. 1827-1835, Apr. 2006.

[3] A. Fort, J. Ryckaert, C. Desset, P. D. Doncker, P. Wambacq, L. V. Biesen, "Ultra-Wideband Channel Model for Communication Around the Human Body," *IEEE J. Selection Areas Comm.*, vol. 24, no. 4, pp. 927-933, Apr. 2006.

[4] P. S. Hall, Y. I. Nechayev, C. C. Constantinou, Y. Hao, A. Alomainy, R. Dubrovka, C. G. Parini, "Antennas and Propagation for On-Body Communication Systems," *Antennas Propag. M.*, vol. 49, issue 3, pp. 41-58, Jun. 2007.

[5] G. A. Conway, S. L. Cotton, W. G. Scanlon, "An Antennas and Propagation Approach to Improving Physical Layer Performance in Wireless Body Area Networking," *IEEE J. Selected Areas Comm.*, vol. 27, no. 1, pp. 27-36, Jan. 2009.

[6] S. L. Cotton, W. G. Scanlon, "Characterization and Modeling of On-Body Spatial Diversity within Indoor Environments at 868 MHz," *IEEE Trans. Wireless Comm.*, vol. 8, no. 1, pp. 176-185, Jan. 2009.

[7] S. L. Cotton, W. G. Scanlon, "Measurements, Modeling and Simulation of the Off-Body Radio Channel for the Implementation of Bodyworn Antenna Diversity at 868 MHz," *IEEE Trans. Antennas Propag.*, vol. 57, no. 12, pp. 3951-3961, Dec. 2009.

[8] P. S. Hall, Y, Hao, "Antennas and Propagation for Body Centric Communications," *Antenna Propag.*, 2006, EUCAP 2006, First EUCAP, Nice.

[9] H. N. Kritikos, H. O. Schwan, "The Distribution of Heating Potential Inside Lossy Spheres," *IEEE Tans. Biomed. Eng.*, vol. BME-22, no. 6, pp. 457-463, Nov. 1975.

[10] C. M. Well, "Absorption Characteristics of Multilayered Sphere Models Exposed to UHF/Microwave Radiation," *IEEE Trans. Biomed. Eng.*, vol. BME-22, no. 6, pp. 468-476, Nov. 1975.

[11] R. T. Cleveland, T. W. Athey, "Specific Absorption Rate (SAR) in Models of Human Head Exposed to Hand-Held UHF Portable Radios," *Bioelectromagnetics* 10, pp. 173-186, 1989.

[12] P. J. Dimbylow, O. O. Gandhi, "Finite-Difference Time-Domain Calculations of SAR in a Realistic Heterogeneous Model of the Head for Plane-Wave Exposure from 600 MHz to 3 GHz," *Phys. Med. Biol.*, vol. 36, no. 8, pp. 1075-1089, 1991.

[13] J. Kim, Y. Rahmat-Samii, "Implanted Antennas Inside a Human Body: Simulations, Designs, and Characterizations," *IEEE Trans. Microw. Theory Tech.*, vol. 52, no. 8, pp. 1934-1943, Aug. 2004.

[14] W. G. Whittow, C. J. Panagamuwa, R. M. Edwards, J. C. Vardaxoglou, "The Energy Absorbed in the Human Head Due to Ring-Type Jewelry and Face-Illuminating Mobile Phones Using a Dipole and a Realistic Source," *IEEE Trans. Antennas Propag.*, vol. 56, no. 12, pp. 3812-3817, Dec. 2008.

[15] www.ansoft.com.

[16] Schmid & Partner Engineering AG, www.speag.com.

[17] W. W. Hansen "A New Type of Expansion in Radiation Problems," *Phys. Rev.*, vol. 47, pp. 139-143, Jan. 1935.

[18] J. A. Stratton, *Electromagnetic Theory*, Donald, Ed. McGraw-Hill, 1941.
[19] J. E. Hansen, *Spherical Near-Field Antenna Measurements*, Peter Peregrinus Ltd. London, UK: Short Run Press Ltd., 1988.
[20] C. A. Balanis, *Advanced Engineering Electromagnetics*, New York: John Wiley and Sons INC., 1989.
[21] R. E. Collin, *Foundations for Microwave Engineering*, 2nd ed. New Jersey: Wiley, 2001.
[22] www.mathworks.se
[23] Y. Xu "Calculation of the Additional Coefficients in Electromagnetic Multisphere-Scattering theory," *J. Comput. Phys.*, vol. 127, pp. 285-298, 1996.
[24] Y. Xu "Fast Evaluation of the Gaunt Coefficients," *Math. Comput.*, vol. 65, no. 216, pp. 1601-1612, Oct. 1996.
[25] R. F. Harrington, *Time-Harmonic Electromagnetic Fields*, D. G. Dudley, New Jersy: Wiley, 2001.
[26] F. Meli, B. Fuchs, J. R. Mosig, A. K. Skrivervik, "The Effect of Insulating Layers on the Performance of Implanted Antennas," *IEEE Trans. Antennas Propag.*, vol. 59, no. 1, Jan. 2011.
[27] S. H. Kvist, J. Thaysen, K. B. Jakobsen, "The Effect of the Head Size on the Ear-to-Ear Radio-Propagation Channel for Body-Centric Wireless Networks," *2010 Laughborough Ant. Propag. Conference*, pp. 345-348, Nov. 2010.
[28] R. Zentner, M. Davic, Z. Spius, J. Bartolic, "Time Domain Analysis of Mutual Coupling Measurements between Stached Patches," *Appl. Electromag. Commun., 2003. ICECom 2003. 17th International Conference on*, pp. 370-373, 2003.
[29] W. L. Stutzman, G. A. Thiele, *Antenna Theory and Design*, John Wiley & Sons, 1998.
[30] C. A. Balanis, *Antenna Theory: Analysis and Design*, 2nd ed., New York: John Wiley and Sons INC., 1997.
[31] W. K. Roberts "A New Wide-Band Balun," *Proc. IRE*, vol. 45, pp. 1628-1631, Dec. 1957.
[32] R. Bawer, J. J. Wolfe, "A Printed Circuit Balun for Use with Spiral Antennas," *IRE Trans. Microw. Theory Tech.*, vol. 8, issue 3, pp. 319-325, May 1960.
[33] D. Kuylenstierna, P. Linner "Design of Broadband Lumped Element Baluns," in *IEEE MTT-S Int. Microwave Symp. Dig.*, pp. 899-902, 2004.
[34] D. Kuylenstierna, P. Linner "Design of Broad-Band Lumped Element Baluns With Inherent Impedance Transformation," *IEEE Trans. Microw. Theory Tech.*, vol. 52, no. 12, pp. 2739-2745, Dec. 2004.
[35] S. J. Parisi "180° Lumped Element Hybird," *IEEE MMT-S Int. Microwave Symp. Dig.*, pp. 1243-1246, 1989.
[36] D. M. Pozar, *Microwave Engineering*, New York: Addison-Wesley Publishing Company, 1993.
[37] R. Pallas-Areny, J. G. Webster, *Sensors and Signal Conditioning*, New York: John Wiley & Sons, Inc., 2001.
[38] http://www.dtu.dk/centre/ems/English/research/facilities.aspx.
[39] H. Cook "The Dielectric Behavior of Some Types of Human Tissues at Microwave Frequencies," *Brit. J. Appl. Phys.*, vol. 2, pp. 295-300, 1951.

[40] S. Roberts, A. V. Hippel "A New Method for Measuring Dielectric Constant and Loss in the Range of Centimeter Waves," *J. Appl. Phys.*, 17, pp. 610-616,1946.

[41] H. Cook "A Comparison of the Dielectric Behavior of Pure Water and Human Blood at Microwave Frequencies," *Brit. J. Appl. Phys.*, vol. 3, pp. 247-255, 1952.

[42] M. A. Stuchly, T. W. Athey, S. S. Stuchly, G. M. Samaras, G. Taylor "Dielectric Properties of Animal Tissues in Vivo at Frequencies 10 MHz – 1 GHz," *Bioelectromag.*, vol. 2, pp. 93-103, 1981.

[43] K. R. Foster, J. L. Schepps, R. D. Stoy, H. P. Schwan "Dielectric Properties of Brain Tissue between 0.01 and 10 GHz," *Phys. Med. Biol.*, vol. 24, no. 6, pp. 1177-1187, 1979.

[44] S. Gabriel, R. W. Lau, C. Gabriel "The Dielectric Properties of Biological Tissues: II. Measurements in the Frequency range 10 Hz to 20 GHz," *Phys. Med. Biol.*, 41, pp. 2251-2269, 1996.

[45] C. Gabriel, "Compilation of the Dielectric Properties of Body Tissues at RF and Microwave Frequencies," Phys. Dept., King's College London, London WC2R 2LS, UK, Rep. AL/OE-TR-1996-0004, Jan. 1996.

[46] K. S. Cole, R. H. Cole, "Dispersion and Absorption in Dielectrics: I. Alternating Current Characteristics," *J. Chem. Phys.*, vol. 9, pp. 341-351, Apr. 1941.

[47] R. C. Hansen and M. Burke "Antennas with Magneto-Dielectrics," *Microw. Opt. Technol. Lett.*, vol. 26, no. 2, pp. 27-78, Jul. 2000.

[48] H. Mosallaei, K. Sarabandi "Magneto-Dielectrics in Electromagnetics: Concept and Applications," *IEEE Trans. Antennas Propag*., vol. 52, no. 6, pp. 1558-1567, Jun. 2004.

[49] C. Morals, J. Dewdney, S. Pal, S. Skidmore, K. Stojak, H. Srikanth, T. Weller, and J. Wang "Tunable Magneto-Dielectric Polymer Nanocomposites for Microwave Applications," *IEEE Trans. Microw. Theory Tech*., vol. 59, no. 2, Feb. 2011.

[50] G. Le Fur, F. Grange, C. Delaveaud, D. Souriou, J. L. Mattei, P. Queffelec "Contribution on Notch Antenna Loaded by Magneto-Dielectric Material" presented at the *EUCAP 2011*, Rome, Italy, 11-15 Apr. 2011.

[51] A. N. Lagarkov, V. N. Semenenko, V. N. Kisel, and V. A. Chistyaev "Development and simulation of microwave artificial magnetic composites utilizing nonmagnetic inclusions" *J. Magnetism Magn. Mater.* 258-259 (2003), pp. 161-166.

[52] F. Bilotti, A. Toscano, and L. Vegni "Design of Spiral and Multiple Split-Ring Resonators for the Realization of Miniaturized Metamaterial Samples," *IEEE Trans. Antennas Propag.,* vol. 55, no. 8, Aug. 2007.

[53] F. Bilotti, A. Toscano, L. Vegni, K. Aydin, K. B. Alici, E. Ozbay "Equivalent-Circuit Models for the Design of Metamaterials Based on Artificial Magnetic Inclusions," *IEEE Trans. Microw. Theory Tech*., vol. 55, no. 12, Dec. 2007.

[54] X. M. Yang, Q. H. Sun, Y. Jing, Q. Cheng, X. Y. Zhou, H. W. Kong, and T. J. Cui "Increasing the Bandwidth of Microstrip Patch Antenna by Loading Compact Artificial Magneto-Dielectrics," *IEEE Trans. Antennas Propag*., vol. 59, no. 2, Feb. 2011.

[55] D. R. Smith, D. C. Vier, T. Koschny, and C. M. Soukoulis "Electromagnetic parameter retrieval from inhomogeneous metamaterials," *Phys. Rev. E* 71, 036617 (2005).

[56] Computer Simulation Technology "www.cst.com".
[57] K. Aydin, I. Bulu, K. Guven, M. Kafesaki, C. M. Soukoulis, and E. Ozbay "Investigation of magnetic resonances for different split-ring resonator parameters and designs" *New J. Phys.* 7 (2005) 168.
[58] B. E. A. Saleh, M. C. Teich, *Fundamentals of Photonics*, 2nd Ed., John Wiley & Sons, Inc., 2007.
[59] R. L. Comstock, *Introduction to Magnetism and Magnetic Recording*, New York: A Wiley-Interscience Publication, 1995.
[60] P. J. B. Clarricoats, H. M. Barlow, *Microwave Ferrites*, Belfast, Northern Ireland: Chapman & Hall, 1961.
[61] A. G. Derneryd "Analysis of the Microstrip Disk Antenna Element," *IEEE Trans. Antennas Porpag.*, vol. AP-27, no. 5, pp. 660-664, Sep. 1979.
[62] S. A. Long, L. C. Shen, M. D. Walton, M. R. Allering "Impedance of a Circular-Disc Printed-Circuit Antenna," Electron. Lett., vol. 14, no. 21, pp. 684-686, 12 Oct. 1978.
[63] L. C. Shen "Analysis of a Circular-Disc Printed-Circuit Antenna," *Proc. IEE*, vol. 126, no. 12, pp. 1220-1222, Dec. 1979.
[64] A. K. Bhattacharyya, R. Garg "Generalised Transmission Line Model for Microstrip Patches," *IEE Proc.*, vol. 132, no. 2, pp. 93-98, Apr. 1985.
[65] A. K. Bhattacharyya, R. Garg "Input Impedance of Annular Ring Microstrip Antenna Using Circuit Theory Approach," *IEEE Trans. Antennas Propag*., vol. AP-33, no. 4, pp. 369-374, Apr. 1985.
[66] B. Ke, A. A. Kishk "Analysis of Spherical Circular Microstrip Antennas," *IEE Proc*., vol. 138, no. 6, pp. 542-548, Dec. 1991.
[67] R. E. Collin, S. Rothschild "Evaluation of Antenna *Q*," *IEEE Trans. Antennas Propag.*, vol. 12, no. 1, pp. 23-27, Jun. 1964.
[68] P. Ikonen, S. Tretyakov "On the Advantages of Magnetic Materials in Microstrip Antenna Miniaturization," *Microw. Opt. Technol. Lett.*, vol. 50, no. 12, pp. 3131-3134, Dec. 2008.

A Spherical vector wave functions

General spherical wave functions

$$\vec{F}_{1nm}^{(c)}(r,\theta,\phi) = \frac{1}{\sqrt{2\pi}}\frac{1}{\sqrt{n(n+1)}}\left(-\frac{m}{|m|}\right)^m \cdot$$
$$R_{1n}^{(c)}(kr)\,\mathrm{e}^{im\phi}\left\{\hat{\theta}\frac{im\overline{P}_n^{|m|}(\cos\theta)}{\sin\theta} - \hat{\phi}\frac{\mathrm{d}\overline{P}_n^{|m|}(\cos\theta)}{\mathrm{d}\theta}\right\} \tag{A.1}$$

$$\vec{F}_{2nm}^{(c)}(r,\theta,\phi) = \frac{1}{\sqrt{2\pi}}\frac{1}{\sqrt{n(n+1)}}\left(-\frac{m}{|m|}\right)^m \mathrm{e}^{im\phi} \cdot$$
$$\left\{\hat{r}\frac{n(n+1)}{kr}R_{1n}^{(c)}(kr)\overline{P}_n^{|m|}(\cos\theta) + R_{2n}^{(c)}(kr)\left(\hat{\theta}\frac{\mathrm{d}\overline{P}_n^{|m|}(\cos\theta)}{\mathrm{d}\theta} + \hat{\phi}\frac{im\overline{P}_n^{|m|}(\cos\theta)}{\sin\theta}\right)\right\} \tag{A.2}$$

$$R_{sn}^{(c)}(kr) = \begin{cases} z_n^{(c)}(kr); & s=1 \\ \dfrac{1}{kr}\dfrac{\mathrm{d}}{\mathrm{d}(z_n^{(c)}(kr))}\left\{krz_n^{(c)}(kr)\right\}, & s=2 \end{cases} \tag{A.3}$$

Orthogonality of spherical wave functions

Vector product:

$$\int_0^{2\pi}\int_0^{\pi} \vec{F}_{smn}^{(c)} \times \vec{F}_{\sigma\mu\nu}^{(\gamma)*} \cdot \hat{r}\sin\theta\,\mathrm{d}\theta\,\mathrm{d}\phi = -\delta_{s,3-\sigma}\delta_{m,\mu}\delta_{n,\nu}(-1)^s R_{sn}^{(c)}(kr)R_{3-s,n}^{(\gamma)*}(kr) \tag{A.4}$$

Product of radial components:

$$\int_0^{2\pi}\int_0^{\pi} \left(\vec{F}_{smn}^{(c)} \cdot \hat{r}\right)\left(\vec{F}_{\sigma\mu\nu}^{(\gamma)*} \cdot \hat{r}\right)\sin\theta\,\mathrm{d}\theta\,\mathrm{d}\phi$$
$$= -\delta_{s,\sigma}\delta_{s,2}\delta_{m,-\mu}\delta_{n,\nu}(-1)^m n(n+1)\frac{R_{1n}^{(c)}(kr)}{kr}\frac{R_{1n}^{(\gamma)}(kr)}{kr} \tag{A.5}$$

Product of tangential components:

$$\int_0^{2\pi}\int_0^{\pi} \left[\left(\vec{F}_{smn}^{(c)} \cdot \hat{\theta}\right)\left(\vec{F}_{\sigma\mu\nu}^{(\gamma)*} \cdot \hat{\theta}\right) + \left(\vec{F}_{smn}^{(c)} \cdot \hat{\phi}\right)\left(\vec{F}_{\sigma\mu\nu}^{(\gamma)*} \cdot \hat{\phi}\right)\right]\sin\theta\,\mathrm{d}\theta\,\mathrm{d}\phi$$
$$= \delta_{s,\sigma}\delta_{m,-\mu}\delta_{n,\nu}(-1)^m R_{sn}^{(c)}(kr)R_{sn}^{(\gamma)}(kr) \tag{A.6}$$

Scalar product:

$$\int_0^{2\pi}\int_0^{\pi} \vec{F}_{smn}^{(c)} \cdot \vec{F}_{\sigma\mu\nu}^{(\gamma)} \sin\theta \, \mathrm{d}\theta \, \mathrm{d}\phi = \delta_{s,\sigma}\delta_{m,-\mu}\delta_{n,\nu}(-1)^m$$
$$\cdot \left[R_{sn}^{(c)}(kr) R_{s,n}^{(\gamma)}(kr) + \delta_{s,2} n(n+1) \frac{R_{1,n}^{(c)}(kr)}{kr} \frac{R_{1,n}^{(\gamma)}(kr)}{kr} \right] \tag{A.7}$$

B Sources coefficients

x-oriented electric dipoles

In the previous sections we used the reciprocity theorem to find the coefficients of the *z*-oriented electric and magnetic dipole. Another method can be used to find the coefficients by using the rotation and translation coefficients which are given in [3]. In this section and in the next section we will use this method to find the $Q_{smn}^{i(c)}$ coefficients of the *x*-oriented electric and magnetic dipoles.

An *x*-oriented electric dipole that is located at the origin of the coordinate system has the *Q* coefficients [3, eq. (2.124)]:

$$Q_{2,-1,1} = -Q_{211} = -d_e \frac{1}{\sqrt{12\pi}} \frac{k_0}{\sqrt{\eta_0}} \tag{B.1}$$

In [3, app. A3] there is a good explanation of how to apply the translation algorithm, so we don't need to repeat it again. The translation coefficients $C_{smn}^{21(c)}$ can be found by applying symmetry property [3, eq. (A3.10)] and special cases [3, eq. (A3.20)] and [3, eq. (A3.21)], and the *C* coefficients become:

$$C_{2,-1,n}^{21(c)}(k_0 r_0) = C_{21n}^{21(c)}(k_0 r_0) = (-1)^{n+1} \frac{\sqrt{3}}{2} \sqrt{2n+1} R_{2n}^{(c)}(k_0 r_0) \tag{B.2}$$

$$C_{1,-1,n}^{21(c)}(k_0 r_0) = -C_{11n}^{21(c)}(k_0 r_0) = j(-1)^n \frac{\sqrt{3}}{2} \sqrt{2n+1} R_{1n}^{(c)}(k_0 r_0) \tag{B.3}$$

where the radial function *R* is defined by eq. (A.3). So the $Q_{smn}^{i(c)}$ coefficients become:

$$Q_{2,-1,n}^{(c)} = -Q_{21n}^{(c)} = d_e \frac{k_0}{\sqrt{\eta_0}} (-1)^{n+1} \sqrt{\frac{2n+1}{16\pi}} R_{2n}^{(4-c)}(k_0 r_0) \tag{B.4}$$

$$Q_{1,-1,n}^{(c)} = Q_{11n}^{(c)} = d_e j \frac{k_0}{\sqrt{\eta_0}} (-1)^{n+1} \sqrt{\frac{2n+1}{16\pi}} R_{1n}^{(4-c)}(k_0 r_0) \tag{B.5}$$

We get the same *Q* coefficients by applying the reciprocity theorem.

x-oriented magnetic dipoles

The translation coefficients $C_{smn}^{21(c)}$ and the $Q_{smn}^{i(c)}$ coefficients of the *x*-oriented magnetic dipole are calculated using the rotation and translation method:

$$C_{2,-1,n}^{11(c)}(k_0 r_0) = -C_{21n}^{11(c)}(k_0 r_0) = j(-1)^n \frac{\sqrt{3}}{2} \sqrt{2n+1} R_{1n}^{(c)}(k_0 r_0) \tag{B.6}$$

$$C_{1,-1,n}^{11(c)}(k_0 r_0) = C_{11n}^{11(c)}(k_0 r_0) = (-1)^{n+1} \frac{\sqrt{3}}{2} \sqrt{2n+1} R_{2n}^{(c)}(k_0 r_0) \tag{B.7}$$

$$Q_{2,-1,n}^{(c)} = Q_{21n}^{(c)} = d_m k_0 \sqrt{\eta_0} (-1)^n \sqrt{\frac{2n+1}{16\pi}} R_{1n}^{(4-c)}(k_0 r_0) \tag{B.8}$$

$$Q_{1,-1,n}^{(c)} = -Q_{11n}^{(c)} = d_m jk_0\sqrt{\eta_0}(-1)^n\sqrt{\frac{2n+1}{16\pi}}R_{2n}^{(4-c)}(k_0 r_0) \tag{B.9}$$

z-oriented magnetic dipole

The coefficients of the scattered and the total are calculated to be:

$$Q_{10n}^{s} = Q_{10n}^{(1)}\frac{\eta_1 R_{1n}^{(1)}(k_0a)R_{2n}^{(1)}(k_1a) - \eta_0 R_{2n}^{(1)}(k_0a)R_{1n}^{(1)}(k_1a)}{\eta_0 R_{2n}^{(3)}(k_0a)R_{1n}^{(1)}(k_1a) - \eta_1 R_{1n}^{(3)}(k_0a)R_{2n}^{(1)}(k_1a)} \tag{B.10}$$

$$Q_{20n}^{t} = jQ_{10n}^{(1)}\frac{k_0}{k_1}\frac{1}{(k_0a)^2}\frac{\sqrt{\eta_0\eta_1}}{\eta_0 R_{2n}^{(3)}(k_0a)R_{1n}^{(1)}(k_1a) - \eta_1 R_{1n}^{(3)}(k_0a)R_{2n}^{(1)}(k_1a)} \tag{B.11}$$

x-oriented electric dipole

The coefficients of the scattered and the total are calculated to be:

$$Q_{1,-1,n}^{s} = Q_{11n}^{s} = Q_{11n}^{(1)}\frac{\eta_0 R_{2n}^{(1)}(k_0a)R_{1n}^{(1)}(k_1a) - \eta_1 R_{1n}^{(1)}(k_0a)R_{2n}^{(1)}(k_1a)}{\eta_1 R_{1n}^{(3)}(k_0a)R_{2n}^{(1)}(k_1a) - \eta_0 R_{2n}^{(3)}(k_0a)R_{1n}^{(1)}(k_1a)} \tag{B.12}$$

$$Q_{1,-1,n}^{t} = Q_{11n}^{t} = -jQ_{11n}^{(1)}\frac{k_0}{k_1}\frac{1}{(k_0a)^2}\frac{\sqrt{\eta_0\eta_1}}{\eta_1 R_{1n}^{(3)}(k_0a)R_{2n}^{(1)}(k_1a) - \eta_0 R_{2n}^{(3)}(k_0a)R_{1n}^{(1)}(k_1a)} \tag{B.13}$$

$$Q_{2,-1,n}^{s} = -Q_{21n}^{s} = -Q_{21n}^{(1)}\frac{\eta_0 R_{1n}^{(1)}(k_0a)R_{2n}^{(1)}(k_1a) - \eta_1 R_{2n}^{(1)}(k_0a)R_{1n}^{(1)}(k_1a)}{\eta_1 R_{2n}^{(3)}(k_0a)R_{1n}^{(1)}(k_1a) - \eta_0 R_{1n}^{(3)}(k_0a)R_{2n}^{(1)}(k_1a)} \tag{B.14}$$

$$Q_{2,-1,n}^{t} = -Q_{21n}^{t} = -jQ_{21n}^{(1)}\frac{k_0}{k_1}\frac{1}{(k_0a)^2}\frac{\sqrt{\eta_0\eta_1}}{\eta_1 R_{2n}^{(3)}(k_0a)R_{1n}^{(1)}(k_1a) - \eta_0 R_{1n}^{(3)}(k_0a)R_{2n}^{(1)}(k_1a)} \tag{B.15}$$

x-oriented magnetic dipole

The coefficients of the scattered and the total are calculated to be:

$$Q_{1,-1,n}^{s} = -Q_{11n}^{s} = -Q_{11n}^{(1)}\frac{\eta_0 R_{2n}^{(1)}(k_0a)R_{1n}^{(1)}(k_1a) - \eta_1 R_{1n}^{(1)}(k_0a)R_{2n}^{(1)}(k_1a)}{\eta_1 R_{1n}^{(3)}(k_0a)R_{2n}^{(1)}(k_1a) - \eta_0 R_{2n}^{(3)}(k_0a)R_{1n}^{(1)}(k_1a)} \tag{B.16}$$

$$Q_{1,-1,n}^{t} = -Q_{11n}^{t} = jQ_{11n}^{(1)}\frac{k_0}{k_1}\frac{1}{(k_0a)^2}\frac{\sqrt{\eta_0\eta_1}}{\eta_1 R_{1n}^{(3)}(k_0a)R_{2n}^{(1)}(k_1a) - \eta_0 R_{2n}^{(3)}(k_0a)R_{1n}^{(1)}(k_1a)} \tag{B.17}$$

$$Q_{2,-1,n}^{s} = Q_{21n}^{s} = Q_{21n}^{(1)}\frac{\eta_0 R_{1n}^{(1)}(k_0a)R_{2n}^{(1)}(k_1a) - \eta_1 R_{2n}^{(1)}(k_0a)R_{1n}^{(1)}(k_1a)}{\eta_1 R_{2n}^{(3)}(k_0a)R_{1n}^{(1)}(k_1a) - \eta_0 R_{1n}^{(3)}(k_0a)R_{2n}^{(1)}(k_1a)} \tag{B.18}$$

$$Q_{2,-1,n}^{t} = Q_{21n}^{t} = jQ_{21n}^{(1)}\frac{k_0}{k_1}\frac{1}{(k_0a)^2}\frac{\sqrt{\eta_0\eta_1}}{\eta_1 R_{2n}^{(3)}(k_0a)R_{1n}^{(1)}(k_1a) - \eta_0 R_{1n}^{(3)}(k_0a)R_{2n}^{(1)}(k_1a)} \tag{B.19}$$

Reproducing of Stratton's results

In this section, we will reproduce the results that are derived by Stratton for a plane wave scattered by a dielectric sphere. For this purpose, the variables were transformed to agree Stratton's notations,

$$N = \frac{k_1}{k_2} = \frac{k_1}{k_0} = \sqrt{\varepsilon_r \mu_r} \qquad \rho = k_0 a \qquad N\rho = k_1 a \tag{B.20}$$

we then replace the parameters in (2.38b) and (3.39b), and the coefficients becomes,

$$\alpha_{smn} = \frac{\sqrt{\varepsilon_0 \mu_r} R_{sn}^{(1)}(N\rho) R_{3-s,n}^{(1)}(\rho) - \sqrt{\varepsilon_0 \varepsilon_r} R_{3-s,n}^{(1)}(N\rho) R_{sn}^{(1)}(\rho)}{\sqrt{\varepsilon_0 \varepsilon_r} R_{3-s,n}^{(1)}(N\rho) R_{sn}^{(3)}(\rho) - \sqrt{\varepsilon_0 \mu_r} R_{sn}^{(1)}(N\rho) R_{3-s,n}^{(3)}(\rho)} \tag{B.21}$$

$$\beta_{smn} = (-1)^{s+1} \frac{1}{\rho^2} \frac{j}{\mu_r R_{sn}^{(1)}(N\rho) R_{3-s,n}^{(3)}(\rho) - \sqrt{\varepsilon_r \mu_r} R_{3-s,n}^{(1)}(N\rho) R_{sn}^{(3)}(\rho)} \tag{B.22}$$

For the TE mode (s = 1), the scattering coefficient becomes,

$$\alpha_{1mn} = \frac{\sqrt{\varepsilon_0 \mu_r} j_n(N\rho) \frac{1}{\rho} [\rho j_n(\rho)]' - \sqrt{\varepsilon_0 \varepsilon_r} \frac{1}{N\rho} [N\rho j_n(N\rho)]' j_n(\rho)}{\sqrt{\varepsilon_0 \varepsilon_r} \frac{1}{N\rho} [N\rho j_n(N\rho)]' h_n^{(1)}(\rho) - \sqrt{\varepsilon_0 \mu_r} j_n(N\rho) \frac{1}{\rho} [\rho h_n^{(1)}(\rho)]'}$$

,where $[f(N\rho)]' = \frac{d}{d(N\rho)} f(N\rho)$

$$\alpha_{1mn} = \frac{N\sqrt{\mu_r} j_n(N\rho) [\rho j_n(\rho)]' - N\sqrt{\varepsilon_r} \frac{1}{N} [N\rho j_n(N\rho)]' j_n(\rho)}{N\sqrt{\varepsilon_r} \frac{1}{N} [N\rho j_n(N\rho)]' h_n^{(1)}(\rho) - N\sqrt{\mu_r} j_n(N\rho) [\rho h_n^{(1)}(\rho)]'}$$

$$\alpha_{1mn} = -\frac{\mu_r j_n(N\rho) [\rho j_n(\rho)]' - [N\rho j_n(N\rho)]' j_n(\rho)}{\mu_r j_n(N\rho) [\rho h_n^{(1)}(\rho)]' - [N\rho j_n(N\rho)]' h_n^{(1)}(\rho)} \underset{\mu_2=1}{=} a_n^r \tag{B.23}$$

and for the TM mode (s = 2), eq. (B.21) becomes,

$$\alpha_{smn} = \frac{\sqrt{\varepsilon_0 \mu_r} R_{sn}^{(1)}(N\rho) R_{3-s,n}^{(1)}(\rho) - \sqrt{\varepsilon_0 \varepsilon_r} R_{3-s,n}^{(1)}(N\rho) R_{sn}^{(1)}(\rho)}{\sqrt{\varepsilon_0 \varepsilon_r} R_{3-s,n}^{(1)}(N\rho) R_{sn}^{(3)}(\rho) - \sqrt{\varepsilon_0 \mu_r} R_{sn}^{(1)}(N\rho) R_{3-s,n}^{(3)}(\rho)}$$

$$\alpha_{2mn} = \frac{\sqrt{\varepsilon_0 \mu_r} \frac{1}{N\rho} [N\rho j_n(N\rho)]' j_n(\rho) - \sqrt{\varepsilon_0 \varepsilon_r} j_n(N\rho) \frac{1}{\rho} [\rho j_n(\rho)]'}{\sqrt{\varepsilon_0 \varepsilon_r} j_n(N\rho) \frac{1}{\rho} [\rho h_n^{(1)}(\rho)]' - \sqrt{\varepsilon_0 \mu_r} \frac{1}{N\rho} [N\rho j_n(N\rho)]' h_n^{(1)}(\rho)}$$

$$\alpha_{2mn} = \frac{N\sqrt{\mu_r} \frac{1}{N} [N\rho j_n(N\rho)]' j_n(\rho) - N\sqrt{\varepsilon_r} j_n(N\rho) [\rho j_n(\rho)]'}{N\sqrt{\varepsilon_r} j_n(N\rho) [\rho h_n^{(1)}(\rho)]' - N\sqrt{\mu_r} \frac{1}{N} [N\rho j_n(N\rho)]' h_n^{(1)}(\rho)}$$

$$\alpha_{2mn} = -\frac{[N\rho j_n(N\rho)]' j_n(\rho) - \varepsilon_r j_n(N\rho) [\rho j_n(\rho)]'}{[N\rho j_n(N\rho)]' h_n^{(1)}(\rho) - \varepsilon_r j_n(N\rho) [\rho h_n^{(1)}(\rho)]'} \tag{B.24}$$

We re-write (II-14a) to agree with Stratton notations,

$$\alpha_{2mn} = -\frac{\mu_r j_n(\rho)\left[N\rho j_n(N\rho)\right]' - N^2 j_n(N\rho)\left[\rho j_n(\rho)\right]'}{\mu_r h_n^{(1)}(\rho)\left[N\rho j_n(N\rho)\right]' - N^2 j_n(N\rho)\left[\rho h_n^{(1)}(\rho)\right]'}\Bigg|_{\mu_2=1} = b_n^r \tag{B.25}$$

Both equations (B.23) and (B.25) agree with the results that had been found by Stratton.

C Closed forms of the sources

Here we shall derive the fields of the dipole antennas by using the closed form method. An infinitesimal dipole antenna is positioned at $z = -r_0$ has a current distribution:

$$\vec{J}_{e,m} = \hat{p} d_{e,m} \delta(\vec{r} - \vec{r}')$$

$$\vec{J}_{e,m} = \hat{p} d_{e,m} \frac{\delta(r - r_0)\delta(\theta - \pi)}{r^2 \sin\theta} \tag{C.1}$$

The definition of the delta function $\delta(\vec{r} - \vec{r}')$ is given in [32, eq. (14-167)], where $\hat{p}$ is a unit vector for the orientation of the dipole, $d_{e,m}$ is the dipole moment, the index e represents the electric dipole, m represents the magnetic dipole and δ is the Dirac delta function. The time factor $\exp(j\omega t)$ is used to derive the closed form equations.The electric vector potential $\vec{A}$ becomes:

$$\vec{A}(R) = \hat{z} d_e \varepsilon \frac{e^{-jkR}}{4\pi R} \tag{C.2}$$

Then the magnetic and the electric fields of the dipole can be calculated using Maxwell's equations and the formula in [26, eq. (3-29)]:

$$\vec{H}_A = \frac{1}{\mu} \nabla \times \vec{A} \tag{C.3}$$

$$\vec{E}_A = \frac{1}{j\omega\varepsilon} \nabla \times \vec{H}_A \tag{C.4}$$

By inserting eq. (C.2) in (C.3) and (C.4), we found the electric and the magnetic fields of the electric dipole which is oriented in the z-direction:

$$\vec{E}_e^z = \vec{E}_A = d_e \frac{1}{j\omega\mu} \frac{e^{-jkR}}{4\pi R^3} \left\{ -\hat{r} \left[-2\cos\theta(1 + jkR) + r r_0 \sin^2\theta \frac{3 - k^2R^2 + 3jkR}{R^2} \right] \right.$$
$$\left. + \hat{\theta} \sin\theta \left[-2(1 + jkR) + r(r - r_0\cos\theta) \frac{3 - k^2R^2 + 3jkR}{R^2} \right] \right\} \tag{C.5}$$

$$\vec{H}_e^z = \vec{H}_A = \hat{\phi} d_e \sin\theta \frac{e^{-jkR}}{4\pi R^3} r(1 + jkR) \tag{C.6}$$

$$H_{e,r}^z = H_{e,\theta}^z = E_{e,\phi}^z = 0 \tag{C.7}$$

The electric vector potential $\vec{F}$ is related to the magnetic vector potential $\vec{A}$ by the following relation:

$$\vec{A} = \frac{d_e}{d_m} \frac{\mu}{\varepsilon} \vec{F} \tag{C.8}$$

To calculate the electric and the magnetic fields from the electric vector potential we use the following relations:

$$\vec{E}_F = -\frac{1}{\varepsilon}\nabla \times \vec{F} \tag{C.9}$$

$$\vec{H}_F = -\frac{1}{j\omega\mu}\nabla \times \vec{E}_F \tag{C.10}$$

By inserting (C.8) in (C.9) and using (C.5), we found the following relations between fields of the magnetic and the electric dipoles:

$$\vec{E}_m^z = \vec{E}_F = -\frac{1}{\varepsilon}\nabla \times \left(\vec{F}\right) = -\frac{d_m}{d_e}\frac{1}{\mu}\nabla \times \vec{A} = -\frac{d_m}{d_e}\vec{H}_A \tag{C.11}$$

$$\vec{H}_F = -\frac{1}{j\omega\mu}\nabla \times \vec{E}_F = -\frac{1}{j\omega\mu}\nabla \times \left(-\frac{1}{\varepsilon}\nabla \times \vec{F}\right) = \frac{1}{j\omega\mu\varepsilon}\nabla \times \nabla \times \vec{F}$$

$$\vec{H}_F = \frac{1}{j\omega\mu\varepsilon}\nabla \times \nabla \times \frac{\varepsilon}{\mu}\frac{d_m}{d_e}\vec{A} = \frac{d_m}{d_e}\frac{1}{j\omega\mu}\nabla \times \frac{1}{\mu}\nabla \times \vec{A} = \frac{d_m}{d_e}\frac{1}{j\omega\mu}\nabla \times \vec{H}_A$$

$$\vec{H}_m^z = \vec{H}_F = \frac{d_m}{d_e}\frac{\varepsilon}{\mu}\vec{E}_A \tag{C.12}$$

Eq. (C.11) and (C.12) are general relations and they are independent of the directions. So we will use the equations also with the *x*-oriented dipoles.

D Fields distributions

In this appendix, the plots of the fields distributions are given for the *z*-oriented magnetic dipole antenna (MHDz), *x*-oriented electric dipole antenna (EHDx) and *z*-oriented magnetic dipole antenna (MHDz). The electrical property effects on the S21 will be also given. All the plots were generated by the theoretical model.

MHDz

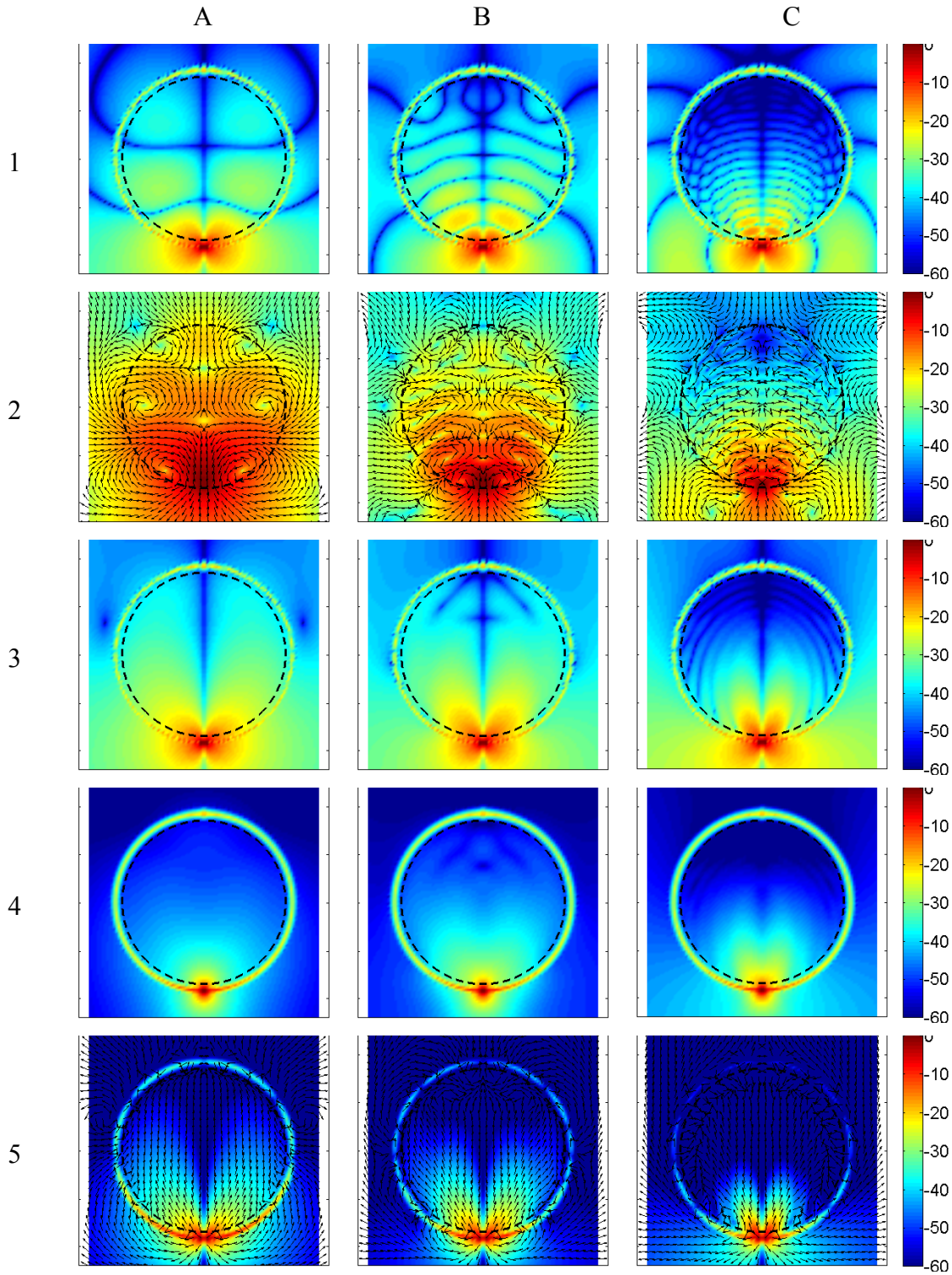

Fig. D.1: The results for a *z*-oriented magnetic dipole near a dielectric sphere. Amplitude in dB. The horizontal axis is the *x*-axis and the vertical axis is the *z*-axis.

EHDx (E-plane)

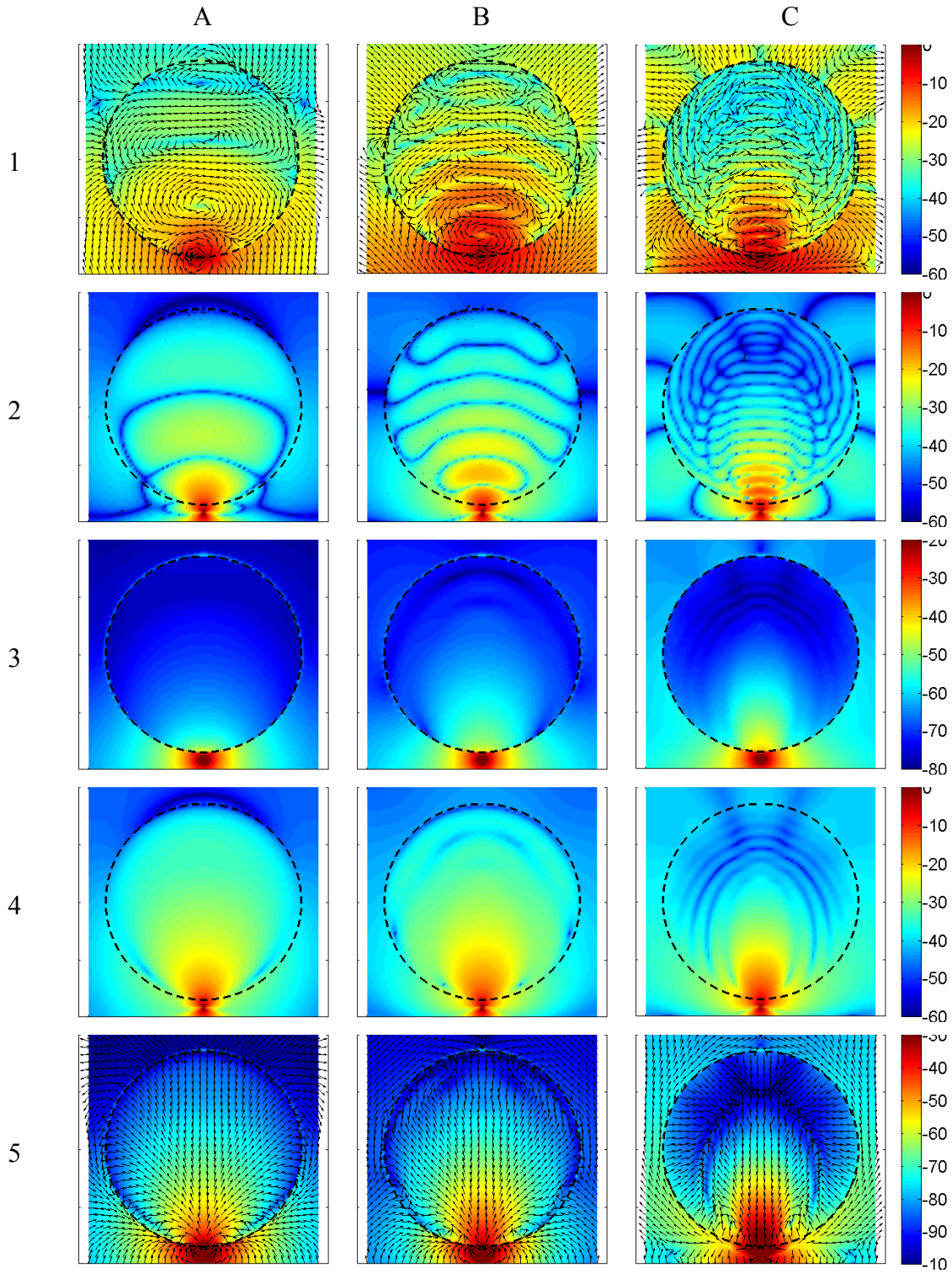

Fig. D.2: Amplitude in dB for the electric and the magnetic fields of the *x*-oriented electric dipole near the dielectric sphere. The horizontal axis is the *x*-axis and the vertical axis is the *z*-axis.

EHDx (H-plane)

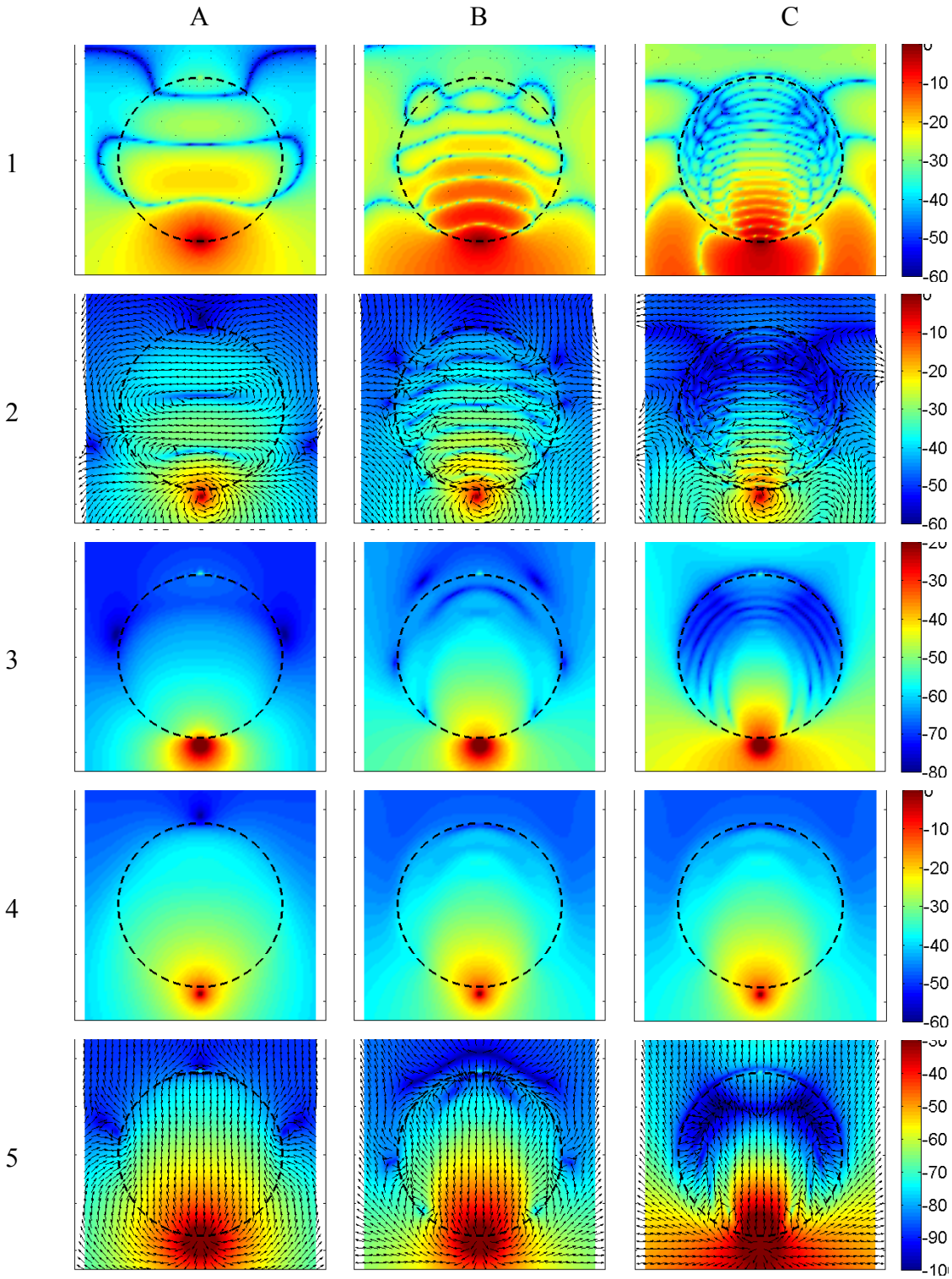

Fig. D.3: Amplitude in dB for the electric and the magnetic fields of the *x*-oriented electric dipole near the dielectric sphere. The horizontal axis is the *y*-axis and the vertical axis is the *z*-axis.

MHDx (H-plane)

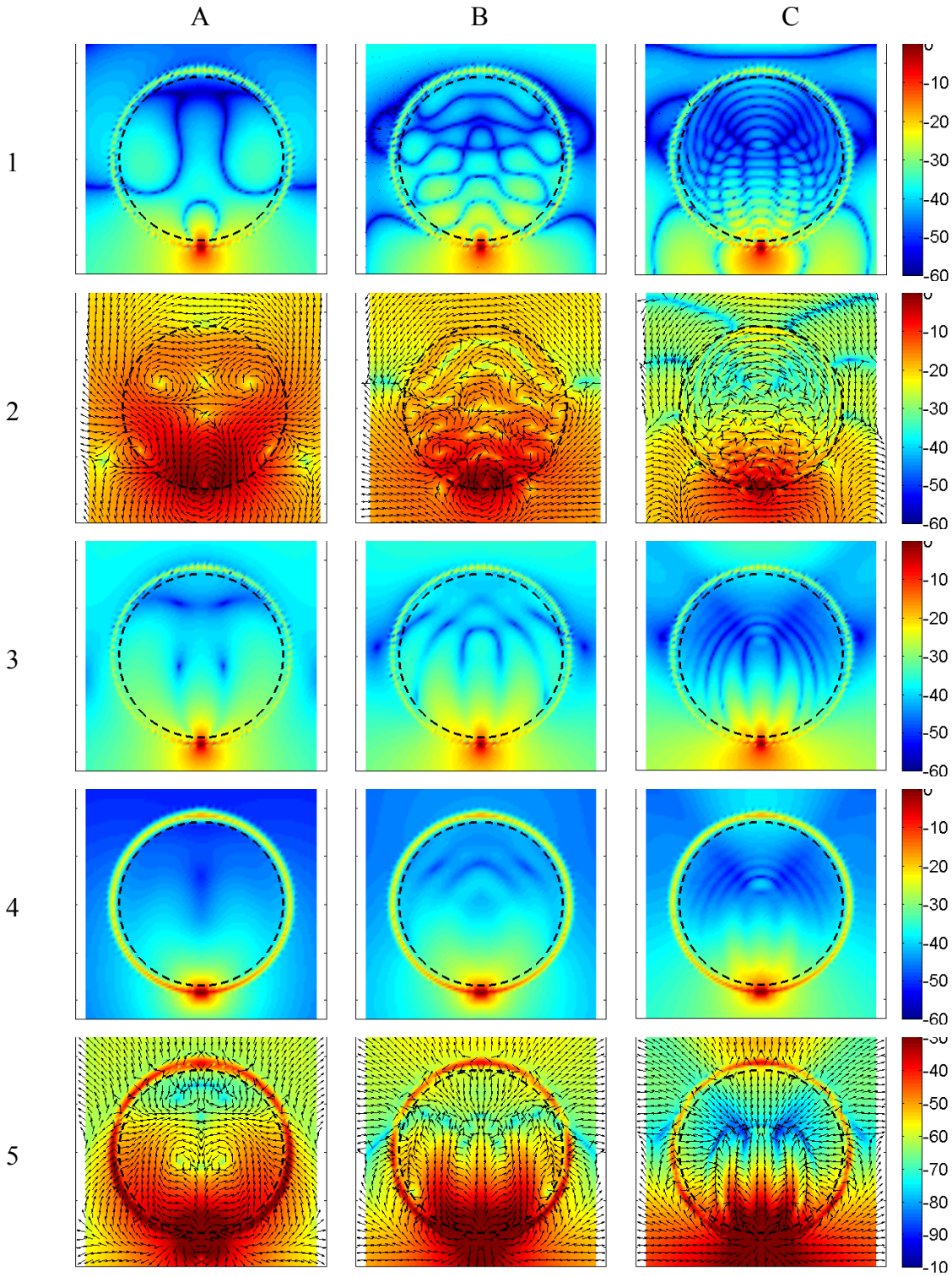

Fig. D.4: Amplitude in dB for the electric and the magnetic fields of the *x*-oriented magnetic dipole near the dielectric sphere. The horizontal axis is the *x*-axis and the vertical axis is the *z*-axis.

MHDx (E-plane)

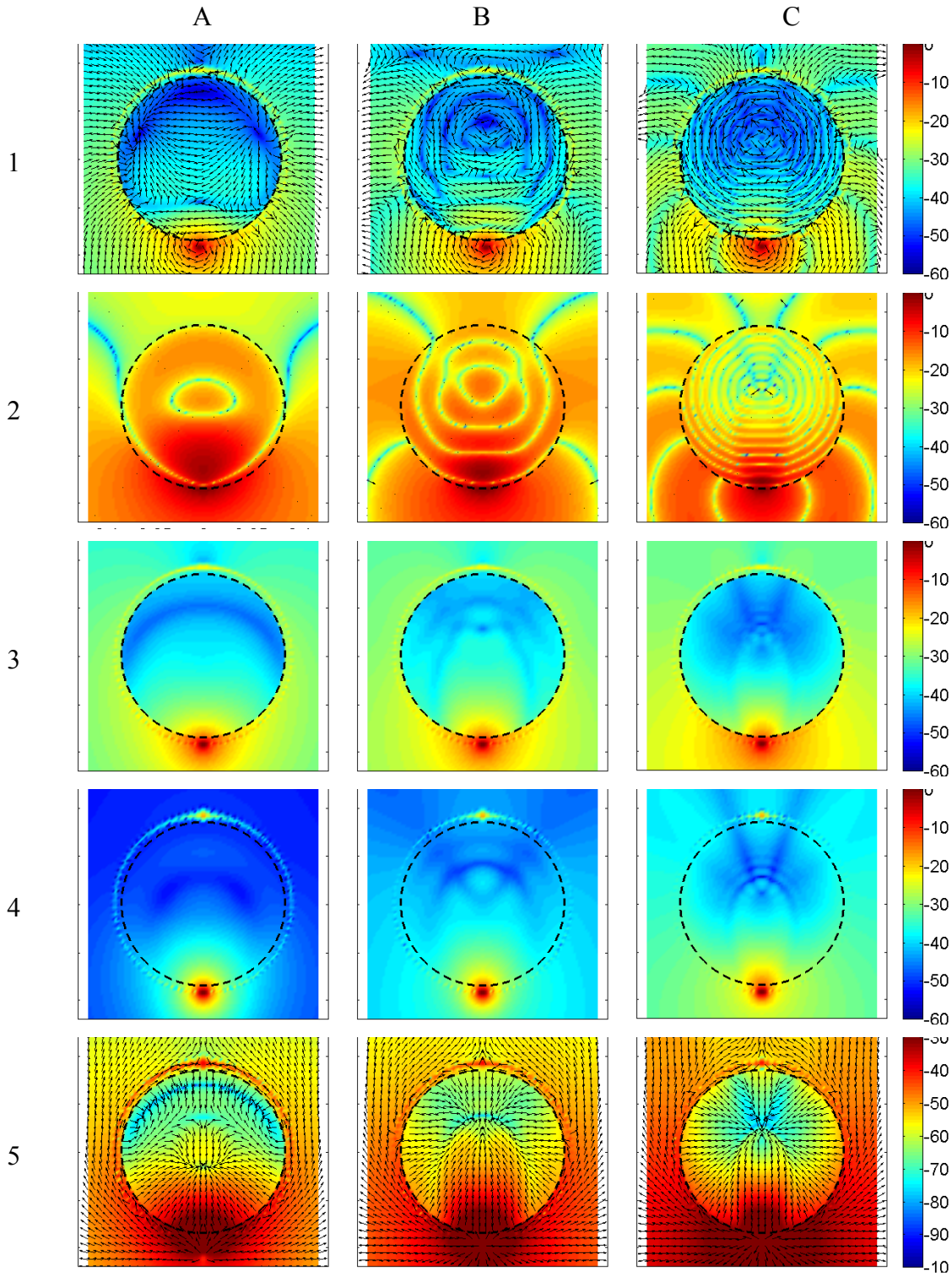

Fig. D.5: Amplitude in dB for the electric and the magnetic fields of the *x*-oriented magnetic dipole near the dielectric sphere. The horizontal axis is the *y*-axis and the vertical axis is the *z*-axis.

Electrical properties effects

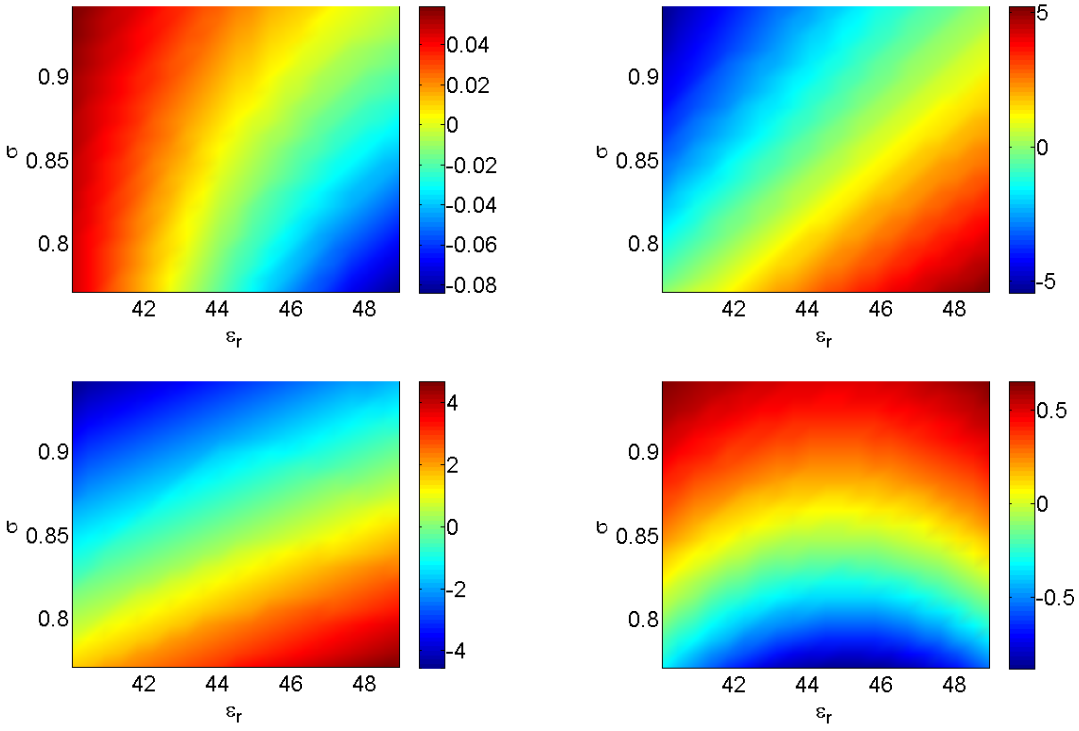

Fig. D.6: The normalized S_{21} at 400 MHz.

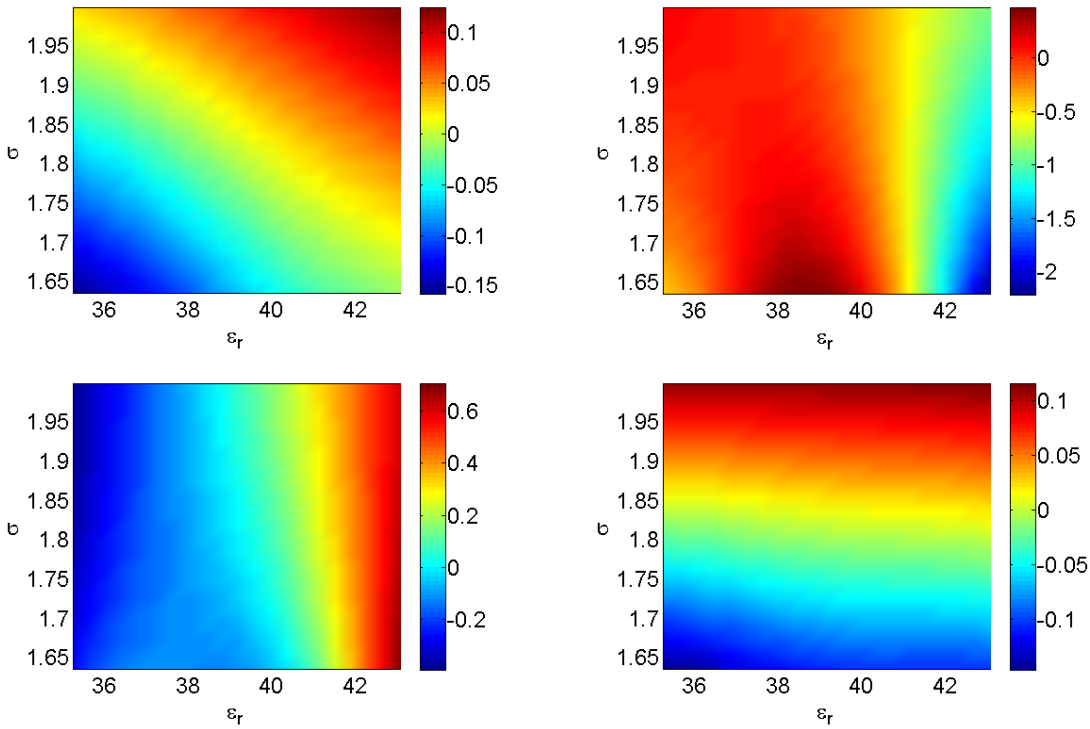

Fig. D.7: The normalized S_{21} at 2.45 GHz.

E Power calculations of the magneto-dielectric antenna

Ohmic power P_C

The fields under the microstrip disk are given by eq. (4.1) and (4.2). The electric surface current on conductors leads to the ohmic loss, similar to [21, pp. 498-499] the ohmic power P_C can be found as:

$$P_C = R_s \int_0^{2\pi}\int_0^a \left|\vec{J}^s\right|^2 \rho d\rho d\phi = R_s \int_0^{2\pi}\int_0^a \left(\left|J_\rho\right|^2 + \left|J_\phi\right|^2\right)\rho d\rho d\phi$$

$$R_s = \sqrt{\frac{\omega\mu_0}{2\sigma}}$$

$$P_C = R_s \int_0^{2\pi}\int_0^a \left(\left|H_\rho\right|^2 + \left|H_\phi\right|^2\right)\rho d\rho d\phi \tag{E.1}$$

where R_s is skin effect resistance and σ is the conductivity of the ground plane and the disk. Since the electric current density is $\hat{z}\times\vec{H}$ on the ground plane and $-\hat{z}\times\vec{H}$ on the disk. After substituting from eq. (4.2) the general expression of the ohmic power for any mode becomes:

$$P_C = \left|C\right|^2 \frac{\pi R_s}{k_0^2\eta_0^2\mu_r'^2}\begin{cases}\displaystyle\int_0^a\left[k^2 J_n'^2(k\rho)+\frac{n^2}{\rho^2}J_n^2(k\rho)\right]\rho d\rho & ,n\neq 0\\ \displaystyle\int_0^a 2k^2 J_n'^2(k\rho)\rho d\rho & ,n=0\end{cases}$$

Since we assume the loss tangent is very small ($\mu_r'' << \mu_r'$ and $\varepsilon_r'' << \varepsilon_r'$), and to minimize the complexity of the calculations we assume the wave number $k \cong k_0\sqrt{\mu_r'\varepsilon_r'}$. Integration by parts the first term gives the following:

$$\int_0^a k^2 J_n'^2(k\rho)\rho d\rho = \int_0^a \frac{dJ_n(k\rho)}{d\rho}\frac{dJ_n(k\rho)}{d\rho}\rho d\rho$$

$$= aJ_n(ka)\underbrace{J_n'(ka)}_{0 \text{ from B.C.}} - \int_0^a J_n(k\rho)\frac{d}{d\rho}\left(\rho\frac{dJ_n(k\rho)}{d\rho}\right)d\rho \tag{E.2}$$

where B.C. is an short form of boundary condition. Reference to [1, eq. (6.5.4)] the differential equation in the integral term is:

$$\frac{d}{d\rho}\rho\frac{dJ_n}{d\rho}+\left(k^2\rho-\frac{n^2}{\rho}\right)J_n = 0 \tag{E.3}$$

So the integration becomes:

$$\int_0^a \left[k^2 \rho J_n'^2(k\rho) + \frac{n^2}{\rho} J_n^2(k\rho) \right] d\rho = \int_0^a \left[k^2 \rho J_n^2(k\rho) - \frac{n^2}{\rho} J_n^2(k\rho) + \frac{n^2}{\rho} J_n^2(k\rho) \right] d\rho$$

$$= \int_0^a k^2 \rho J_n^2(k\rho) d\rho$$

$$= \frac{1}{2}\left(k^2 a^2 - n^2\right) J_n^2(ka) \tag{E.4}$$

The ohmic power for mode *n* becomes:

$$P_C = \left|C\right|^2 J_n^2(ka) \frac{\pi R_s}{2k_0^2 \eta_0^2 \mu_r'^2} \left(1 + \delta_{0,n}\right)\left(k^2 a^2 - n^2\right) \tag{E.5}$$

$$P_C = h^2 \left|C\right|^2 J_n^2(ka) \frac{\pi R_s}{2h^2 k_0^2 \eta_0^2 \mu_r'^2} \left(1 + \delta_{0,n}\right)\left(k^2 a^2 - n^2\right)$$

$$P_C = \left|V_{nm}\right|^2 \frac{\pi R_s}{2h^2 k_0^2 \eta_0^2 \mu_r'^2} \left(1 + \delta_{0,n}\right)\left(\chi_{nm}^2 - n^2\right) \tag{E.6}$$

$$\delta_{0,n} = \begin{cases} 1, & n = 0 \\ 0, & n \neq 0 \end{cases}$$

Magneto-dielectric power P_{md}

While the power loss in the substrate which is the magneto-dielectric power will be calculated as two separate losses, a loss because of the imaginary part of the dielectric constant and a loss because of the imaginary part of the permeability. The sum of these losses, precisely the loss of the dielectric constant and the loss of the magnetic constant, will give the loss of the magneto-dielectric substrate:

$$P_{\text{md}} = \frac{\omega \varepsilon_r'' \varepsilon_0}{2} \int_V \left|E_z\right|^2 dV + \frac{\omega \mu_r'' \mu_0}{2} \int_V \left|\vec{H}\right|^2 dV \tag{E.7}$$

By substituting eq. (4.1) and (4.2) in (E.6) we get the following:

$$P_{\text{md}} = \left|C\right|^2 \frac{\omega \varepsilon_r'' \varepsilon_0}{2} h \int_0^a \int_0^{2\pi} J_n^2(k\rho) \cos^2 n\phi \rho d\phi d\rho + \frac{\omega \mu_r'' \mu_0}{2} h \int_0^a \int_0^{2\pi} \left(\left|H_\rho\right|^2 + \left|H_\phi\right|^2\right) \rho d\phi d\rho \tag{E.8}$$

The second term in eq. (E.7) can be treated as eq. (E.1), while the integration of the first term is a straightforward integration. So the magneto-dielectric power becomes:

$$P_{\text{md}} = h\left|C\right|^2 J_n^2(ka) \left[\frac{\omega \varepsilon_r'' \varepsilon_0 \pi}{4k^2} + \frac{\omega \mu_r'' \mu_0 \pi}{4k_0 \eta_0 \mu_r'^2} \right] (1 + \delta_{0,n})\left(k^2 a^2 - n^2\right) \tag{E.9}$$

$$P_{\text{md}} = \frac{1}{2} h\left|C\right|^2 J_n^2(ka) \left[\frac{\varepsilon_r''}{\omega \mu_0 \mu_r' \varepsilon_r'} + \frac{\mu_r''}{\mu_r'^2} \right] \frac{\pi(1 + \delta_{0,n})}{2} \left(k^2 a^2 - n^2\right)$$

$$P_{\text{md}} = \frac{1}{2} h \left|C\right|^2 J_n^2(ka) \left[\frac{\tan\delta_e}{\omega\mu_0\mu_r'} + \frac{\tan\delta_m}{\mu_r'} \right] \frac{\pi(1+\delta_{0,n})}{2} \left(k^2 a^2 - n^2\right)$$

$$P_{\text{md}} = \frac{1}{2} \left|V_{nm}\right|^2 \left[\frac{\tan\delta_e}{\omega\mu_0\mu_r' h} + \frac{\tan\delta_m}{\mu_r' h} \right] \frac{\pi(1+\delta_{0,n})}{2} \left(\chi_{nm}^2 - n^2\right) \tag{E.10}$$

$$P_{\text{md}} \cong \frac{1}{2} \left|V_{nm}\right|^2 \frac{\tan\delta_m}{\mu_r' h} \frac{\pi(1+\delta_{0,n})}{2} \left(\chi_{nm}^2 - n^2\right) \tag{E.11}$$

where $\tan\delta_e = \dfrac{\varepsilon''}{\varepsilon'}$ and $\tan\delta_m = \dfrac{\mu''}{\mu'}$.

F HFSS simulation and measurement results

The plots of the fields distributions for the Ant. 1 near SAM phantom head. The fields were generated by HFSS.

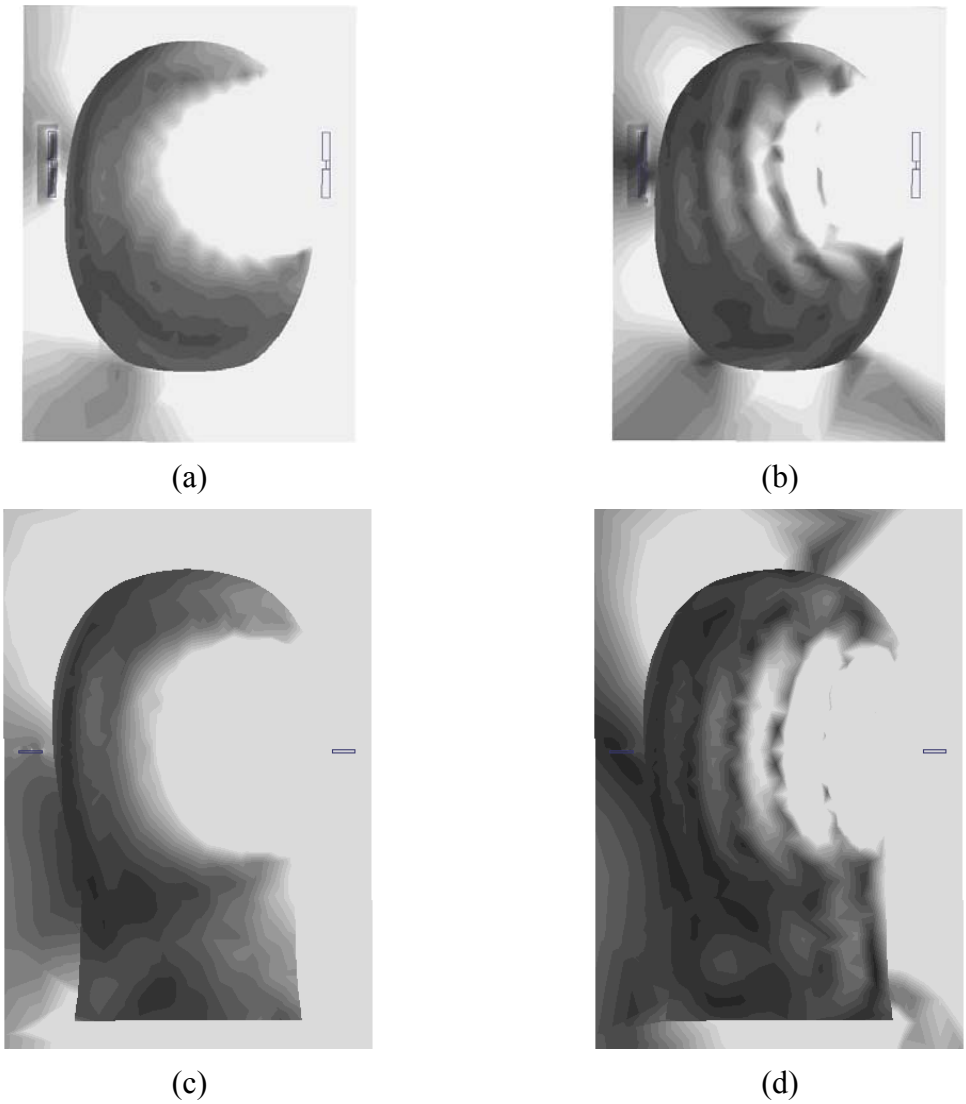

(a) (b)

(c) (d)

Fig. F.1: Simulated magnitude of the complex (a) and (c), and the real (b) and (d), electric fields that radiated by Ant. 1. The color scale ranges from 0 V/m (black) to 1 V/m (white) of the electric field. The plots (a) and (b) show top view, while (c) and (d) show the front view.

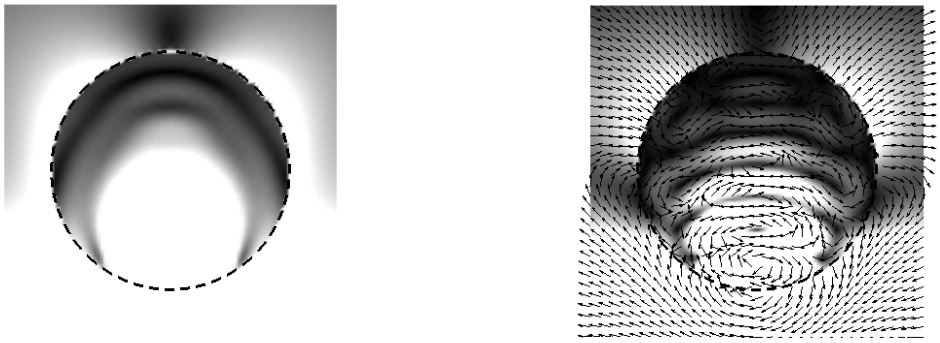

(a) (b)

Fig. F.2: Computed magnitude of the complex (a) and the real (b) electric fields that radiated by a tangential electric dipole, where it radiate 0.5 W. The color scale ranges from 0 (black) to 5 V/m (white) of the electric field. The antenna is 1 cm away from the surface of the sphere which has a radius a = 9.3 cm.

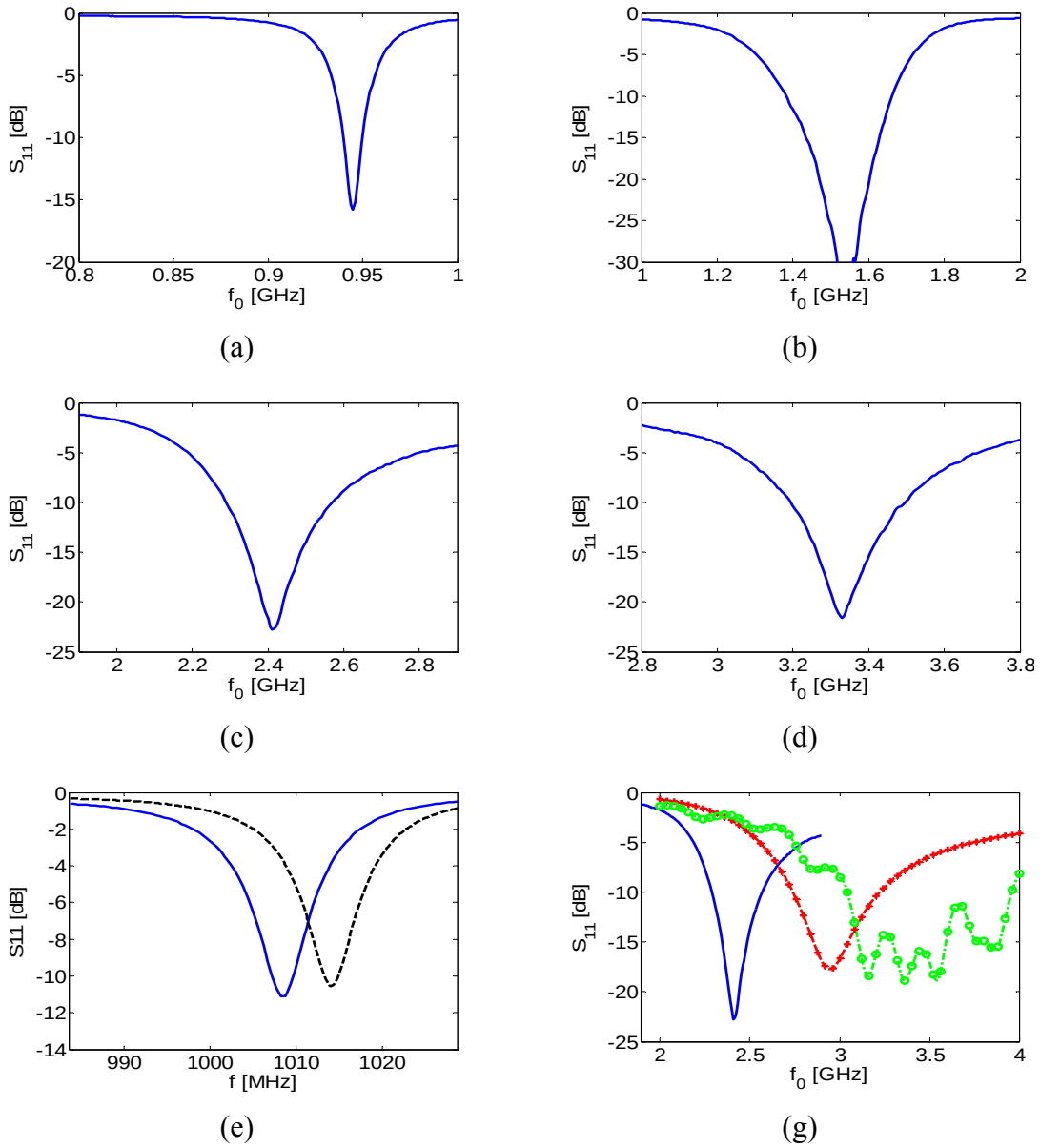

Fig. F.3: The measured reflection coefficient S_{11} of (a) Ant. 1, (b) Ant. 2, (c) Ant. 3 and (d) Ant. 4, while (e) and (g) show the measured and the simulated S_{11} of Ant. 5 and Ant. 3, respectively. The dashed line is the simulated S_{11} for the antenna fed without a cable, while the doted line corresponds to the antenna fed by a cable.

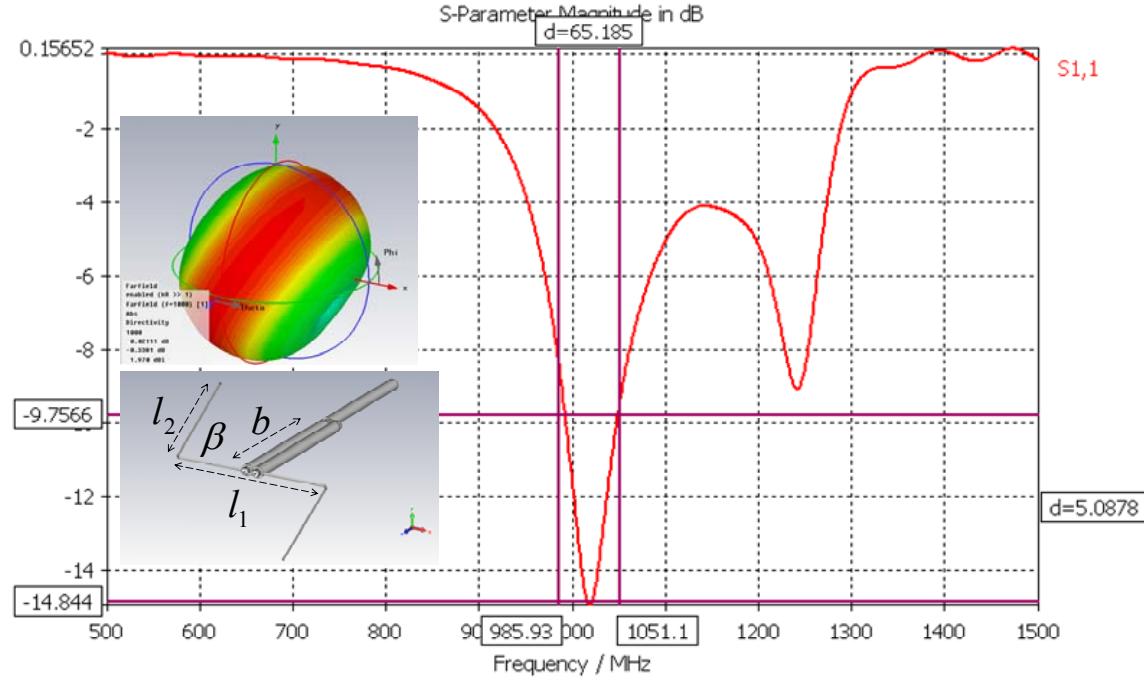

(a)

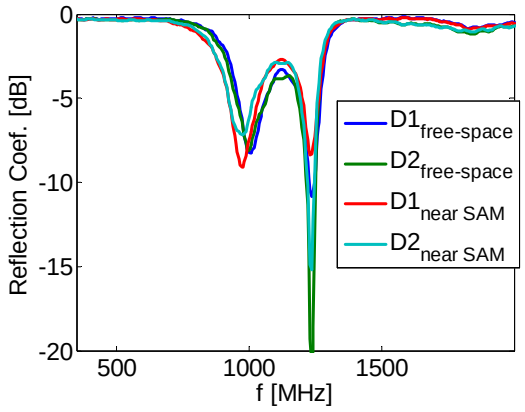

(b)

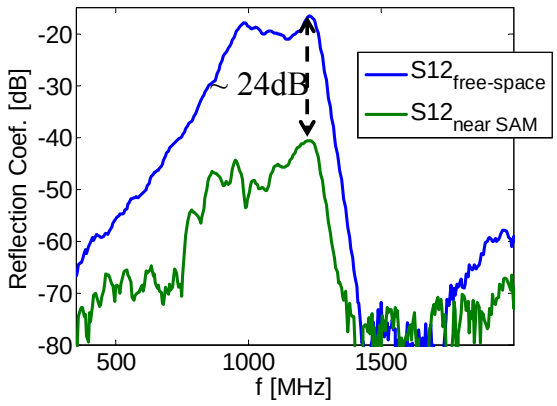

(c)

Fig. F.4: Simulation (a) of a Z-dipole antenna mounted with wideband coaxial balun, whereas figure (b) and (c) shows the measured S_{11} and S_{21} in free-space and near SAM phantom head. The simulation was carried by CST [56]. The dimensions of the antenna are: l_1 = 6 cm, l_2 = 4 cm, b = 6.25 cm and β = 60 deg.

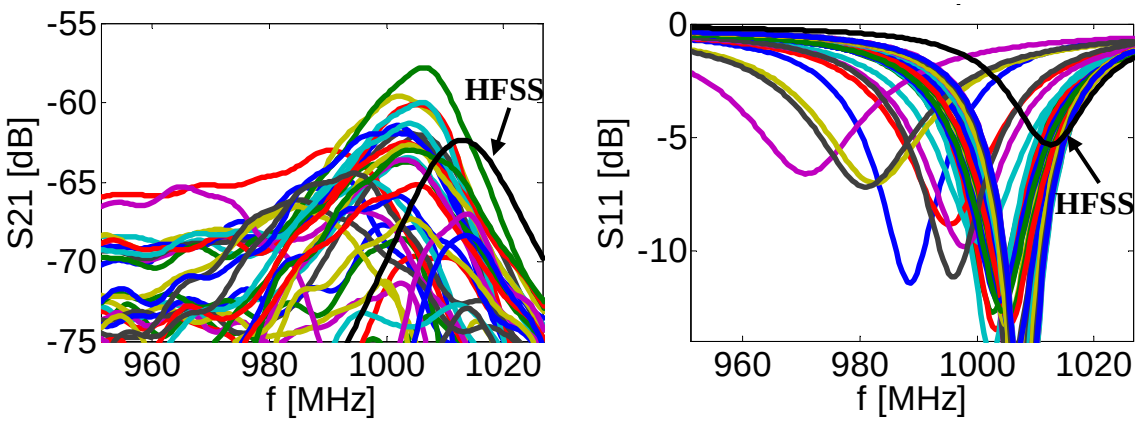

(a) (b)

Fig. F.5: The measured and the simulated S_{21} (a) and S_{11} (b) for Ant. 5, where as figure (c) shows the path-loss for frequency range from 941 MHz to 1027 MHz.

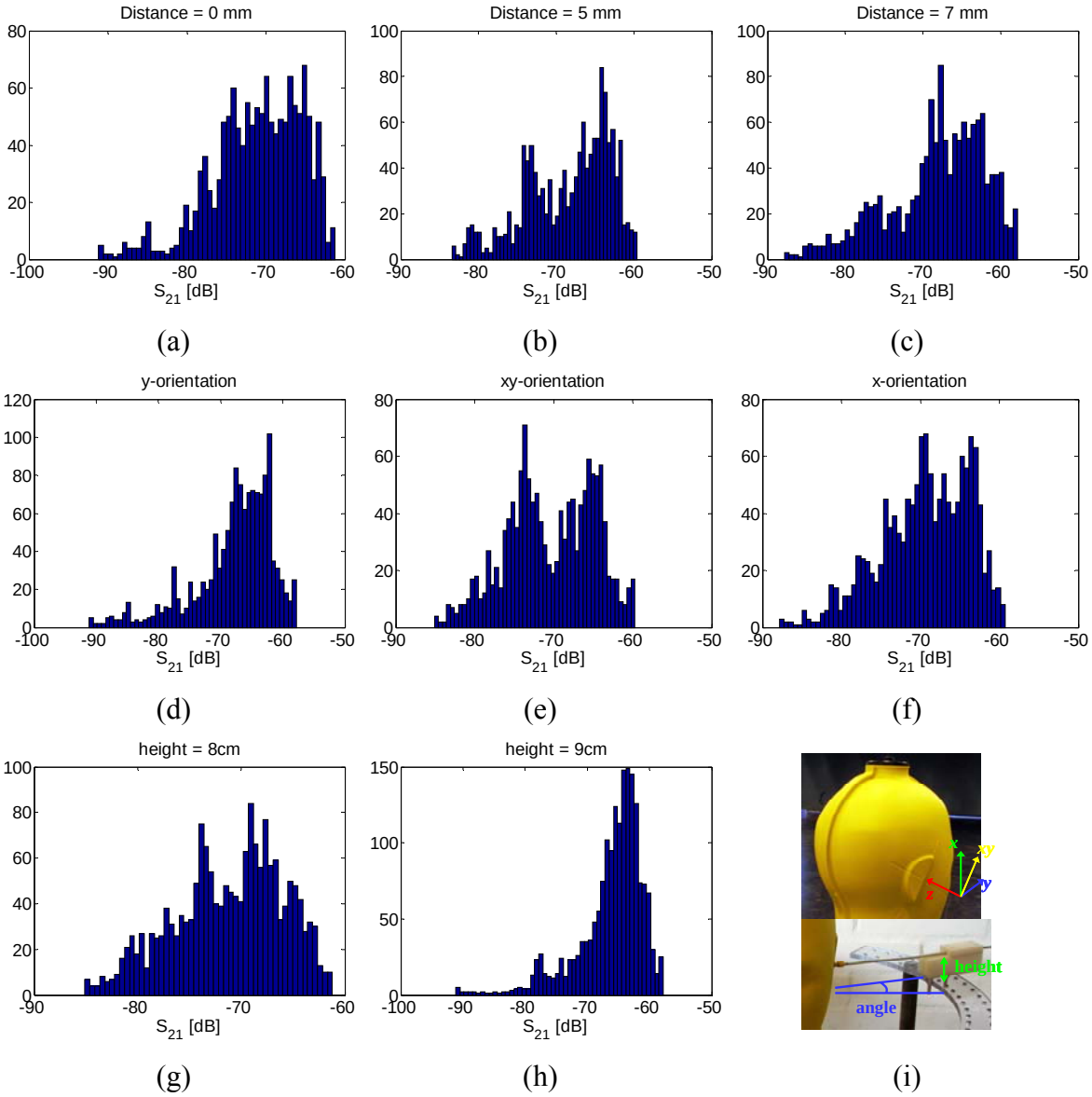

Fig. F.6: Measured S_{21} between 990 and 1016 MHz for Ant. 5. The vertical axes are the sample number and the horizontal axes are the S_{21}. Figures (a), (b) and (c) correspond to the distance from the head, while (d) to (f) correspond to the orientation of the antenna with respect to the head. The last two figures (g) and (h) correspond to the height. All the parameters are defined in figure (i).

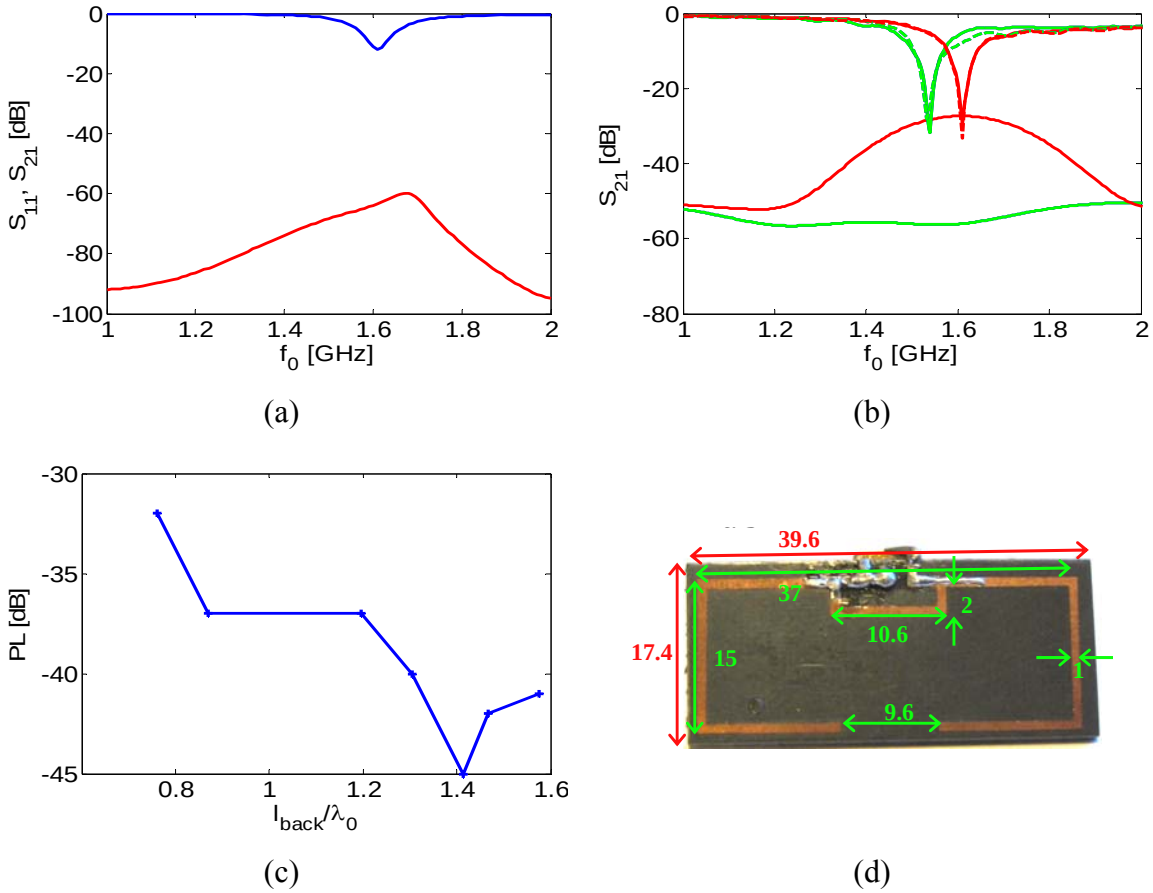

Fig. F.7: Simulated (a) and measured (b) S_{11} and S_{21} of the antenna in (d), where figure (c) shows the measured *PL* as function of the l_{back}. The green lines in figure (b) are the S-parameters near SAM phantom head and the red lines are the S-parameters in free-space.

G Matlab scripts

In this section all the used Matlab scripts that are used in this thesis will be given. The programs are given as scripts with numbers start from 1 to 16:

- Script 1 is an algorithm that calculates the spherical function that is defined by eq. (A.3).
- Scripts 2 and 3 are algorithms that calculate the theta and the phi components of the spherical wave function which are defined by eq. (A.1).
- Scripts 4, 5 and 6 are algorithms that calculate the radial, the theta and the phi components of the spherical wave function which are defined by eq. (A.2).
- Script 7 is an algorithm that calculates the rotation coefficient which is defined by eq. (2.42).
- Script 8 is an algorithm that calculates the translation coefficient.
- Scripts 9 to 12 are algorithms that calculate the electric, the magnetic and the power density of EHDz, EHDx, MHDz and MHDx near a dielectric sphere.
- Script 13 is an algorithm that calculates the electric and the magnetic fields for EHDz after translation and rotation of the coordinate system. This script uses scripts 14 to 16.
- Scripts 14 to 16 are algorithms that calculate the spherical wave function components which are defined by eq. (A.1) and (A.2).

Script 1

This script calculates the spherical functions $R_{sn}^{(c)}(kr)$ [19, eq. (A1.6)].

```
%%%%%%%%%%%%%%%%%%%%%%%%%%%%%%%%%%%%%%%%%%%%%%%%%%%%%%%%%%%%%%%%%%%%%%%%%%%%
% Input:                                                                      %
%       s    : is the type of mode which can be 1 or 2.                       %
%       c    : takes values 1 to 4 to describe the type of the wave.          %
%       n    : is the mode number which is different from zero.               %
%       kr   : is the product of wave-number and the translation distance.    %
%                                                                             %
% Output:                                                                     %
%       R    : is the spherical coefficient.                                  %
%%%%%%%%%%%%%%%%%%%%%%%%%%%%%%%%%%%%%%%%%%%%%%%%%%%%%%%%%%%%%%%%%%%%%%%%%%%%

function R=Rfunc(s,c,n,kr)
if(s==1)
    R=sbessel(c,n,kr);
else
    R=sbessel(c,n,kr)./kr + dbessel(c,n,kr);
end

function zn=sbesself(c,n,kr)
if(c==1)
    zn=sqrt(pi./(2.*kr)).*besselj(n+.5,kr);
end
if(c==2)
    zn=sqrt(pi./(2.*kr)).*bessely(n+.5,kr);
end


function zn=sbessel(c,n,kr)
if(c==1)
    zn=sbesself(c,n,kr);
end
if(c==2)
    zn=sbesself(c,n,kr);
end
if(c==3)
    zn=sbesself(1,n,kr)+j*sbesself(2,n,kr);
end
if(c==4)
    zn=sbesself(1,n,kr)-j*sbesself(2,n,kr);
end

function db=dbessel(c,n,kr)
db = (n)./kr.*sbessel(c,n,kr) - sbessel(c,n+1,kr);
```

Script 2

The first function (F1n_theta) is the main function while the remain functions are sub-function which are used by the main function. This program calculates $\vec{F}_{1mn}^{(c)}(r,\theta,\phi)\cdot\hat{\theta}$, [19, eq. (A1.45)].

```
%%%%%%%%%%%%%%%%%%%%%%%%%%%%%%%%%%%%%%%%%%%%%%%%%%%%%%%%%%%%%%%%%%%%%%%%
% Input:                                                                  %
%       c    : takes values 1 to 4 to describe the type of the wave.      %
%       n    : is the mode number which is different from zero.           %
%       m    : is the mode number which is |m| ≤ n .                      %
%       kr   : is the product of wave-number and the radial distance.     %
%       theta: is the position angle (radian).                            %
%       phi  : is the position angle (radian).                            %
%                                                                         %
% Output:                                                                 %
%       F1n  :This is the theta component of the wave function where s = 1. %
%%%%%%%%%%%%%%%%%%%%%%%%%%%%%%%%%%%%%%%%%%%%%%%%%%%%%%%%%%%%%%%%%%%%%%%%

function F1n=F1n_theta(c,m,n,kr,theta,phi)

F1n = mFun(m)*1/sqrt(2*pi)*sqrt(1/(n*(n+1)))*NormLegCoef(n,m)*...

sbessel(c,n,kr).*j.*m.*legendre_(n,m,cos(theta))./sin(theta).*exp(j*m*p
hi);

function mm=mFun(m)
if(m==0)
    mm=1;
else
    mm=(-m/abs(m))^(m);
end

function zn=sbesself(c,n,kr)
if(c==1)
    zn=sqrt(pi./(2.*kr)).*besselj(n+.5,kr);
end
if(c==2)
    zn=sqrt(pi./(2.*kr)).*bessely(n+.5,kr);
end


function zn=sbessel(c,n,kr)
if(c==1)
    zn=sbesself(c,n,kr);
end
if(c==2)
    zn=sbesself(c,n,kr);
end
if(c==3)
```

```
    zn=sbesself(1,n,kr)+j*sbesself(2,n,kr);
end
if(c==4)
    zn=sbesself(1,n,kr)-j*sbesself(2,n,kr);
end

function P=legendre_(n,m,x)
n=abs(n);
m=abs(m);
if(n>=abs(m))
P=(-1)^m*legendre(n,x);
P=P(m+1,:);
else
    P=zeros(size(x));
end

function nL=NormLegCoef(n,m)
m=abs(m);
nL=sqrt((2*n+1)/2*factorial(n-m)/factorial(n+m));
```

Script 3

This program calculates $\vec{F}_{1mn}^{(c)}(r,\theta,\phi)\cdot\hat{\phi}$, [19, eq. (A1.45)].

```
%%%%%%%%%%%%%%%%%%%%%%%%%%%%%%%%%%%%%%%%%%%%%%%%%%%%%%%%%%%%%%%%%%%%%%%%%%%%%%%%
% Input:                                                                          %
%       c    : takes values 1 to 4 to describe the type of the wave.              %
%       n    : is the mode number which is different from zero.                   %
%       m    : is the mode number which is |m| ≤ n .                              %
%       kr   : is the product of wave-number and the radial distance.             %
%       theta: is the position angle (radian).                                    %
%       phi  : is the position angle (radian).                                    %
%                                                                                 %
% Output:                                                                         %
%       F1n  :This is the phi component of the wave function where s = 1.         %
%%%%%%%%%%%%%%%%%%%%%%%%%%%%%%%%%%%%%%%%%%%%%%%%%%%%%%%%%%%%%%%%%%%%%%%%%%%%%%%%

function F1n=F1n_phi(c,m,n,kr,theta,phi)


F1n = -mFun(m)*1/sqrt(2*pi)*sqrt(1/(n*(n+1)))*NormLegCoef(n,m)*...
    sbessel(c,n,kr).*dlegendre(n,m,cos(theta)).*exp(j*m*phi);

function mm=mFun(m)
if(m==0)
    mm=1;
else
    mm=(-m/abs(m))^(m);
end

function zn=sbesself(c,n,kr)
if(c==1)
    zn=sqrt(pi./(2.*kr)).*besselj(n+.5,kr);
end
if(c==2)
    zn=sqrt(pi./(2.*kr)).*bessely(n+.5,kr);
end


function zn=sbessel(c,n,kr)
if(c==1)
    zn=sbesself(c,n,kr);
end
if(c==2)
    zn=sbesself(c,n,kr);
end
if(c==3)
    zn=sbesself(1,n,kr)+j*sbesself(2,n,kr);
end
if(c==4)
    zn=sbesself(1,n,kr)-j*sbesself(2,n,kr);
end
```

```
function P=legendre_(n,m,x)
n=abs(n);
m=abs(m);
if(n>=abs(m))
P=(-1)^m*legendre(n,x);
P=P(m+1,:);
else
    P=zeros(size(x));
end

function dP=dlegendre(n,m,x)
n=abs(n);
m=abs(m);
if(m==0)
    dP=-legendre_(n,1,x);
else
    dP=1/2*((n-m+1)*(n+m)*legendre_(n,m-1,x)-legendre_(n,m+1,x));
end

function nL=NormLegCoef(n,m)
m=abs(m);
nL=sqrt((2*n+1)/2*factorial(n-m)/factorial(n+m));
```

Script 4

This program calculates $\vec{F}_{2mn}^{(c)}(r,\theta,\phi)\cdot\hat{r}$, [19, eq. (A1.46)].

```
%%%%%%%%%%%%%%%%%%%%%%%%%%%%%%%%%%%%%%%%%%%%%%%%%%%%%%%%%%%%%%%%%%%%%%%%
%  Input:                                                                  %
%       c    : takes values 1 to 4 to describe the type of the wave.       %
%       n    : is the mode number which is different from zero.            %
%       m    : is the mode number which is |m| ≤ n .                       %
%       kr   : is the product of wave-number and the radial distance.      %
%       theta: is the position angle (radian).                             %
%       phi  : is the position angle (radian).                             %
%                                                                          %
% Output:                                                                  %
%       F2n  :This is the radial component of the wave function where s = 2.%
%%%%%%%%%%%%%%%%%%%%%%%%%%%%%%%%%%%%%%%%%%%%%%%%%%%%%%%%%%%%%%%%%%%%%%%%

function F2n=F2n_r(c,m,n,kr,theta,phi)

F2n = mFun(m)*1/sqrt(2*pi)*sqrt(1/(n*(n+1)))*NormLegCoef(n,m)*...

n*(n+1)./kr.*sbessel(c,n,kr).*legendre_(n,m,cos(theta)).*exp(j*m*phi);

function mm=mFun(m)
if(m==0)
    mm=1;
else
    mm=(-m/abs(m))^(m);
end

function zn=sbesself(c,n,kr)
if(c==1)
    zn=sqrt(pi./(2.*kr)).*besselj(n+.5,kr);
end
if(c==2)
    zn=sqrt(pi./(2.*kr)).*bessely(n+.5,kr);
end


function zn=sbessel(c,n,kr)
if(c==1)
    zn=sbesself(c,n,kr);
end
if(c==2)
    zn=sbesself(c,n,kr);
end
if(c==3)
    zn=sbesself(1,n,kr)+j*sbesself(2,n,kr);
end
if(c==4)
    zn=sbesself(1,n,kr)-j*sbesself(2,n,kr);
end
```

```
function P=legendre_(n,m,x)
n=abs(n);
m=abs(m);
if(n>=abs(m))
P=(-1)^m*legendre(n,x);
P=P(m+1,:);
else
    P=zeros(size(x));
end

function nL=NormLegCoef(n,m)
m=abs(m);
nL=sqrt((2*n+1)/2*factorial(n-m)/factorial(n+m));
```

Script 5

This program calculates $\vec{F}_{2mn}^{(c)}(r,\theta,\phi)\cdot\hat{\theta}$, [19, eq. (A1.46)].

```
%%%%%%%%%%%%%%%%%%%%%%%%%%%%%%%%%%%%%%%%%%%%%%%%%%%%%%%%%%%%%%%%%%%%%%%%
% Input:                                                                  %
%       c    : takes values 1 to 4 to describe the type of the wave.      %
%       n    : is the mode number which is different from zero.           %
%       m    : is the mode number which is |m| ≤ n .                      %
%       kr   : is the product of wave-number and the radial distance.     %
%       theta: is the position angle (radian).                            %
%       phi  : is the position angle (radian).                            %
%                                                                         %
% Output:                                                                 %
%       F2n  :This is the theta component of the wave function where s = 2. %
%%%%%%%%%%%%%%%%%%%%%%%%%%%%%%%%%%%%%%%%%%%%%%%%%%%%%%%%%%%%%%%%%%%%%%%%

function F2n=F2n_theta(c,m,n,kr,theta,phi)


F2n = mFun(m)*1/sqrt(2*pi)*sqrt(1/(n*(n+1)))*NormLegCoef(n,m)*...
    (sbessel(c,n,kr)./kr + dbessel(c,n,kr)).*...
    dlegendre(n,m,cos(theta)).*exp(j*m*phi);


function mm=mFun(m)
if(m==0)
    mm=1;
else
    mm=(-m/abs(m))^(m);
end

function zn=sbesself(c,n,kr)
if(c==1)
    zn=sqrt(pi./(2.*kr)).*besselj(n+.5,kr);
end
if(c==2)
    zn=sqrt(pi./(2.*kr)).*bessely(n+.5,kr);
end


function zn=sbessel(c,n,kr)
if(c==1)
    zn=sbesself(c,n,kr);
end
if(c==2)
    zn=sbesself(c,n,kr);
end
if(c==3)
    zn=sbesself(1,n,kr)+j*sbesself(2,n,kr);
end
if(c==4)
```

```
    zn=sbesself(1,n,kr)-j*sbesself(2,n,kr);
end

function P=legendre_(n,m,x)
n=abs(n);
m=abs(m);
if(n>=abs(m))
P=(-1)^m*legendre(n,x);
P=P(m+1,:);
else
    P=zeros(size(x));
end

function db=dbessel(c,n,kr)
db = (n)./kr.*sbessel(c,n,kr) - sbessel(c,n+1,kr);

function dP=dlegendre(n,m,x)
n=abs(n);
m=abs(m);
if(m==0)
    dP=-legendre_(n,1,x);
else
    dP=1/2*((n-m+1)*(n+m)*legendre_(n,m-1,x)-legendre_(n,m+1,x));
end

function nL=NormLegCoef(n,m)
m=abs(m);
nL=sqrt((2*n+1)/2*factorial(n-m)/factorial(n+m));
```

Script 6

This program calculates $\vec{F}_{2mn}^{(c)}(r,\theta,\phi)\cdot\hat{\phi}$, [19, eq. (A1.46)].

```
%%%%%%%%%%%%%%%%%%%%%%%%%%%%%%%%%%%%%%%%%%%%%%%%%%%%%%%%%%%%%%%%%%%%%%%%
% Input:                                                                  %
%       c    : takes values 1 to 4 to describe the type of the wave.      %
%       n    : is the mode number which is different from zero.           %
%       m    : is the mode number which is |m| ≤ n .                      %
%       kr   : is the product of wave-number and the radial distance.     %
%       theta: is the position angle (radian).                            %
%       phi  : is the position angle (radian).                            %
%                                                                         %
% Output:                                                                 %
%       F2n  :This is the phi component of the wave function where s = 2. %
%%%%%%%%%%%%%%%%%%%%%%%%%%%%%%%%%%%%%%%%%%%%%%%%%%%%%%%%%%%%%%%%%%%%%%%%

function F2n=F2n_phi(c,m,n,kr,theta,phi)


F2n = mFun(m)*1/sqrt(2*pi)*sqrt(1/(n*(n+1)))*NormLegCoef(n,m)*...
    (sbessel(c,n,kr)./kr + dbessel(c,n,kr)).*...
    j.*m.*legendre_(n,1,cos(theta))./sin(theta).*exp(j*m*phi);

function mm=mFun(m)
if(m==0)
    mm=1;
else
    mm=(-m/abs(m))^(m);
end


function zn=sbesself(c,n,kr)
if(c==1)
    zn=sqrt(pi./(2.*kr)).*besselj(n+.5,kr);
end
if(c==2)
    zn=sqrt(pi./(2.*kr)).*bessely(n+.5,kr);
end


function zn=sbessel(c,n,kr)
if(c==1)
    zn=sbesself(c,n,kr);
end
if(c==2)
    zn=sbesself(c,n,kr);
end
if(c==3)
    zn=sbesself(1,n,kr)+j*sbesself(2,n,kr);
end
if(c==4)
```

```
    zn=sbesself(1,n,kr)-j*sbesself(2,n,kr);
end

function P=legendre_(n,m,x)
n=abs(n);
m=abs(m);
if(n>=abs(m))
P=(-1)^m*legendre(n,x);
P=P(m+1,:);
else
    P=zeros(size(x));
end

function db=dbessel(c,n,kr)
db = (n)./kr.*sbessel(c,n,kr) - sbessel(c,n+1,kr);

function nL=NormLegCoef(n,m)
m=abs(m);
nL=sqrt((2*n+1)/2*factorial(n-m)/factorial(n+m));
```

Script 7

This script calculates the rotation coefficients $d^{n}_{\mu m}(\theta_0)$, [19, eq. (A2.3)].

```
%%%%%%%%%%%%%%%%%%%%%%%%%%%%%%%%%%%%%%%%%%%%%%%%%%%%%%%%%%%%%%%%%%%%%%%%
% Input:                                                                  %
%       n    : is the mode number which is different from zero.           %
%       m    : is the mode number which is |m| ≤ n .                      %
%       theta: is the rotation angle (radian) θ0.                         %
%                                                                         %
% Output:                                                                 %
%       d_a2 : is the rotation coefficients, which run from μ = –n to n.  %
%%%%%%%%%%%%%%%%%%%%%%%%%%%%%%%%%%%%%%%%%%%%%%%%%%%%%%%%%%%%%%%%%%%%%%%%

function d_a2=rotationCoef(n,m,theta)
% Calculate the rotation coefficients using (A2.3)

mu=-n:n;

for k=1:2*n+1
sigma=max(0,-mu(k)-m):min(n-m,n-mu(k));

d_a2(k,1)=sqrt(factorial(n+mu(k)).*factorial(n-
mu(k))./(factorial(n+m).*factorial(n-m))).*...
    sum(comp(n+m,n-mu(k)-sigma).*comp(n-m,sigma).*(-1).^(n-mu(k)-
sigma).*(cos(theta/2)).^(2*sigma+mu(k)+m).*...
    (sin(theta/2)).^(2*n-2*sigma-mu(k)-m));
end

function P=comp(n,k)
P=factorial(n)./(factorial(k).*factorial(n-k));
```

Script 8

This script calculates the translation coefficient $C_{\sigma\mu\nu}^{sn(c)}(kA)$, [19, eq. (A.3.3)].

```
%%%%%%%%%%%%%%%%%%%%%%%%%%%%%%%%%%%%%%%%%%%%%%%%%%%%%%%%%%%%%%%%%%%%%%%%
% Input:                                                                  %
%       c    : takes values 1 to 4 to describe the type of the wave.      %
%       s    : is the type of mode which can be 1 or 2.                   %
%       sigma: is the σ in the translation coefficient.                   %
%       n    : is the mode number which is different from zero.           %
%       mu   : is the μ in the translation coefficient.                   %
%       nu   : is the ν in the translation coefficient.                   %
%       kA   : is the product of wave-number and the translation distance.%
%                                                                         %
% Output:                                                                 %
%       C    : is the translation coefficient.                            %
%%%%%%%%%%%%%%%%%%%%%%%%%%%%%%%%%%%%%%%%%%%%%%%%%%%%%%%%%%%%%%%%%%%%%%%%

function C=translationCoef(c,s,sigma,n,mu,nu,kA)
[a_q,p]=GauntCoefs(mu,n,-mu,nu);
C=sqrt((2*n+1)*(2*nu+1)/(n*(n+1)*nu*(nu+1)))*...
    sqrt(factorial(nu+mu)*factorial(n-mu)/(factorial(nu-
mu)*factorial(n+mu))).*...
    (-1)^mu*1/2*j^(n-nu)*sum(j.^(-
p).*(deltaFun(s,sigma).*(n.*(n+1)+nu*(nu+1)-p.*(p+1))+...
    deltaFun(3-s,sigma)*2*j*mu*kA).*a_q.*sbessel(c,p,kA));

function d=deltaFun(s,sigma)
if(s==sigma)
    d=1;
else
    d=0;
end

function zn=sbesself(c,n,kr)
if(c==1)
    zn=sqrt(pi./(2.*kr)).*besselj(n+.5,kr);
end
if(c==2)
    zn=sqrt(pi./(2.*kr)).*bessely(n+.5,kr);
end


function zn=sbessel(c,n,kr)
if(c==1)
    zn=sbesself(c,n,kr);
end
if(c==2)
    zn=sbesself(c,n,kr);
end
if(c==3)
    zn=sbesself(1,n,kr)-j*sbesself(2,n,kr);
end
```

```
if(c==4)
    zn=sbesself(1,n,kr)+j*sbesself(2,n,kr);
end


function [a_q,p_]=GauntCoefs(m,n,mu,nu)

q_max=qmax(m,mu,n,nu);
q=2;
p=n+nu-2*q;
p_=[n+nu;n+nu-2];
n4=n+nu-m-mu;

a_q(1,1)=1;  % a_0
a_q(2,1)=(2*n+2*nu-3)/2*(1-(2*n+2*nu-1)/(n4*(n4-1))*...
    ((m-n)*(m-n+1)/(2*n-1)+(mu-nu)*(mu-nu+1)/(2*nu-1)));  % a_1

while(q<=q_max)
    while(Afunc(p+4,m,mu,n,nu)~=0 && q<=q_max)

a_q(q+1,1)=(cfunc1(p,m,mu,n,nu)*a_q(q,1)+cfunc2(p,m,mu,n,nu)*a_q(q-
1,1))/cfunc0(p,m,mu,n,nu);
        p_(q+1,1)=p;
        q=q+1;
        p=n+nu-2*q;
    end

    while(Afunc(p+4,m,mu,n,nu)==0 && Afunc(p+6,m,mu,n,nu)==0 &&
q<=q_max)
        p1=p-m-mu;
        p2=p+m+mu;

a_q(q+1,1)=(p+1)*(p2+2)*Alfafunc(p+2,n,nu)*a_q(q,1)/((p+2)*(p1+1)*Alfaf
unc(p+1,n,nu));
        p_(q+1,1)=p;
        q=q+1;
        p=n+nu-2*q;
    end

    while(Afunc(p+4,m,mu,n,nu)==0 && Afunc(p+6,m,mu,n,nu)~=0 &&
q<=q_max)
        p1=p-m-mu;
        p2=p+m+mu;
        a(2,1)=(2*n+2*nu-1)*(2*n+2*nu-7)/4*((2*n+2*nu-3)/(n4*(n4-
1))*((2*n+2*nu-5)/(2*(n4-2)*(n4-3))*...
            ((m-n)*(m-n+1)*(m-n+2)*(m-n+3)/((2*n-1)*(2*n-3))+2*(m-
n)*(m-n+1)*(mu-nu)*(mu-nu+1)/((2*n-1)*(2*nu-1))+...
            (mu-nu)*(mu-nu+1)*(mu-nu+2)*(mu-nu+3)/((2*nu-1)*(2*nu-3)))-
(m-n)*(m-n+1)/(2*n-1)-...
            (mu-nu)*(mu-nu+1)/(2*nu-1))+1/2);


a_q(q+1,1)=(cfunc12(p,m,mu,n,nu)*a_q(q,1)+cfunc22(p,m,mu,n,nu)*a_q(q-
1,1)+...
            cfunc32(p,m,mu,n,nu)*a_q(q-2,1))/cfunc02(p,m,mu,n,nu);
```

```
        if(q==2)
            p_(3,1)=n+nu-2*q;
        end
        p_(q+1,1)=p;
        q=q+1;
        p=n+nu-2*q;
    end
end
a_q=Astart(m,mu,n,nu)*a_q;


function q=qmax(m,mu,n,nu)
q1=min(nu,floor((n+nu-abs(m+mu))/2));
q=min(n,q1);
function A=Afunc(p,m,mu,n,nu)
A=p*(p-1)*(m-mu)-(m+mu)*(n-nu)*(n+nu+1);
function c0=cfunc0(p,m,mu,n,nu)
p1=p-m-mu;
p2=p+m+mu;
c0=(p+2)*(p+3)*(p1+1)*(p1+2)*Afunc(p+4,m,mu,n,nu)*Alfafunc(p+1,n,nu);
function c1=cfunc1(p,m,mu,n,nu)
p1=p-m-mu;
p2=p+m+mu;
c1=Afunc(p+2,m,mu,n,nu)*Afunc(p+3,m,mu,n,nu)*Afunc(p+4,m,mu,n,nu)+...

(p+1)*(p+3)*(p1+2)*(p2+2)*Afunc(p+4,m,mu,n,nu)*Alfafunc(p+2,n,nu)+...
    (p+2)*(p+4)*(p1+3)*(p2+3)*Afunc(p+2,m,mu,n,nu)*Alfafunc(p+3,n,nu);
function c2=cfunc2(p,m,mu,n,nu)
p1=p-m-mu;
p2=p+m+mu;
c2=-(p+2)*(p+3)*(p2+3)*(p2+4)*Afunc(p+2,m,mu,n,nu)*Alfafunc(p+4,n,nu);
function a=Alfafunc(p,n,nu)
a=(p^2-(n+nu+1)^2)*(p^2-(n-nu)^2)/(4*p^2-1);
function c0=cfunc02(p,m,mu,n,nu)
p1=p-m-mu;
p2=p+m+mu;
c0=(p+2)*(p+3)*(p+5)*(p1+1)*(p1+2)*(p1+4)*Afunc(p+6,m,mu,n,nu)*Alfafunc
(p+1,n,nu);
function c1=cfunc12(p,m,mu,n,nu)
p1=p-m-mu;
p2=p+m+mu;
c1=(p+5)*(p1+4)*Afunc(p+6,m,mu,n,nu)*(Afunc(p+2,m,mu,n,nu)*Afunc(p+3,m,
mu,n,nu)+...
    (p+1)*(p+3)*(p1+2)*(p2+2)*Alfafunc(p+2,n,nu));
function c2=cfunc22(p,m,mu,n,nu)
p1=p-m-mu;
p2=p+m+mu;
c2=(p+2)*(p2+3)*Afunc(p+2,m,mu,n,nu)*(Afunc(p+5,m,mu,n,nu)*Afunc(p+6,m,
mu,n,nu)+...
    (p+4)*(p+6)*(p1+5)*(p2+5)*Alfafunc(p+5,n,nu));
function c3=cfunc32(p,m,mu,n,nu)
p1=p-m-mu;
p2=p+m+mu;
c3=-
(p+2)*(p+4)*(p+5)*(p2+3)*(p2+5)*(p2+6)*Afunc(p+2,m,mu,n,nu)*Alfafunc(p+
6,n,nu);
```

```
function a0=Astart(m,mu,n,nu)
a0=upfactorial(n+1,n)*upfactorial(nu+1,nu)/upfactorial(n+nu+1,n+nu)*...
    factorial(n+nu-m-mu)/(factorial(n-m)*factorial(nu-mu));
function n=upfactorial(n,v)
N=cumprod(n+(0:v-1));
n=N(end);
```

Script 9

This script calculates electric and the magnetic fields as well as the power density inside and outside a dielectric sphere of radius a and the transmitting antenna is z-oriented electric dipole antenna EHDz and has r_0 distance from the origin. This script is not a function, therefore it is necessary to put all the functions (scripts 1 to 8) in the same directory as this script. There are several parameters that need to be assigned before running the script.

```
%%%%%%%%%%%%%%%%%%%%%%%%%%%%%%%%%%%%%%%%%%%%%%%%%%%%%%%%%%%%%%%%%%%%%%%%%%%%
% Input:                                                                      %
%       a    : the radius of the sphere.                                      %
%       r0   : the position distance of the transmitting antenna.             %
%       f0   : the operating frequency.                                       %
%       N1   : the number of modes.                                           %
%       N    : number of points that are used to calculate the fields on.     %
%       x    : the limit of the region where the fields are calculated on the x-axis.  %
%       z    : the limit of the region where the fields are calculated on the z-axis.  %
%                                                                             %
% Output:                                                                     %
%       Electric field, magnetic field and power density.                     %
%%%%%%%%%%%%%%%%%%%%%%%%%%%%%%%%%%%%%%%%%%%%%%%%%%%%%%%%%%%%%%%%%%%%%%%%%%%%
```

```
% Validation of the fields of z-oriented electric fields scattered by a
% dielectric sphere.

%-----------------------------------------------------------
% The parameters of the system
% clear all
e0=8.854e-12; % permittivity of the free-space.  [F/m]
u0=4*pi*1e-7; % permeability of the free-space.  [H/m]
n0=1/376.7;     % impedance of the free-space.  [Ohom]
c=2.998e8;    % velocity of light in free-space. [m/s]
r0=.093;      % location of the dipole. [m]
a=.085;       % radius of the sphere
f0=1e9;       % operating frequency. [Hz]
w=2*pi*f0;    % angular frequency.   [radian/s]
k0=w/c;       % wave length in free-space. [1/m]
er=41.0 +j*17.8;        % relative permittivity of the sphere
ur=1;         % relative permeability of the sphere
n1=n0*sqrt(er./ur); % the impedance of the sphere [Ohom]
k1=k0.*sqrt(ur.*er); % the wave number inside the sphere
N1=80; % number of the modes

N=100; % number of the points
x=linspace(-.13,.13,N);
z=linspace(-.13,.13,N);
[X,Z]=meshgrid(x,z);
Y=0*ones(N);
[phi,theta,r]=cart2sph(X,Y,Z);
theta=pi/2-theta;
```

```
r=reshape(r,1,N*N);
theta=reshape(theta,1,N*N);
phi=reshape(phi,1,N*N);


%-------------------------------------------------------------------------
% interpolation of the data of the head
p1 = 3.2404e-048;
p2 = -5.057e-038;
p3 = 2.5808e-028;
p4 = -3.6429e-019;
p5 = 4.1155e-010;
p6 = 0.73379;
sigmaFun= @(x) p1*x.^5 + p2*x.^4 +p3*x.^3 + p4*x.^2 +p5*x + p6; % sigma
p1 = 2.6703e-075;
p2 = -7.7329e-065;
p3 = 9.3934e-055;
p4 = -6.2078e-045;
p5 = 2.4204e-035;
p6 = -5.6427e-026;
p7 = 7.5919e-017;
p8 = -5.4572e-008;
p9 = 57.247;
epsilonFun = @(x) p1*x.^8 + p2*x.^7 +p3*x.^6 + p4*x.^5 +p5*x.^4 +
p6*x.^3 +p7*x.^2 + p8*x + p9; % mu_r

sigma=sigmaFun(f0);
epsilon=epsilonFun(f0);

er = conj(epsilon-j*sigma./(w*e0));
n1=n0*sqrt(er./ur); % the impedance of the sphere [Ohom]
k1=k0.*sqrt(ur.*er); % the wave number inside the sphere
%-------------------------------------------------------------------------

n=(1:N1)';

Q20i1=k0./sqrt(n0).*(-
1).^n.*sqrt(n.*(n+1).*(2*n+1)/(4*pi)).*Rfunc(1,3,n,k0.*r0)./(k0.*r0);
Q20i3=k0./sqrt(n0).*(-
1).^n.*sqrt(n.*(n+1).*(2*n+1)/(4*pi)).*Rfunc(1,1,n,k0.*r0)./(k0.*r0);


              % Rfunc(s,c,n,kr)
Q20s1=Q20i1.*(sqrt(n1/n0).*Rfunc(2,1,n,k0.*a).*Rfunc(1,1,n,k1.*a)...
    -sqrt(n0/n1).*Rfunc(1,1,n,k0.*a).*Rfunc(2,1,n,k1.*a))./...
    (sqrt(n0/n1).*Rfunc(1,3,n,k0.*a).*Rfunc(2,1,n,k1.*a)...
    -sqrt(n1/n0).*Rfunc(2,3,n,k0.*a).*Rfunc(1,1,n,k1.*a));
Q20t1=Q20i1.*k0./k1.*-j./((k0.*a).^2)./...
    (sqrt(n0/n1).*Rfunc(1,3,n,k0.*a).*Rfunc(2,1,n,k1.*a)...
    -sqrt(n1/n0).*Rfunc(2,3,n,k0.*a).*Rfunc(1,1,n,k1.*a));


for n=1:N1
    % z-orientation
    F1i1pz(:,n)=transpose(F1n_phi(1,0,n,k0.*r,theta,phi));
```

```
    F1i3pz(:,n)=transpose(F1n_phi(3,0,n,k0.*r,theta,phi));
    F2i1rz(:,n)=transpose(F2n_r(1,0,n,k0.*r,theta,phi));
    F2i3rz(:,n)=transpose(F2n_r(3,0,n,k0.*r,theta,phi));
    F2i1thz(:,n)=transpose(F2n_theta(1,0,n,k0.*r,theta,phi));
    F2i3thz(:,n)=transpose(F2n_theta(3,0,n,k0.*r,theta,phi));

    F1t1pz(:,n)=transpose(F1n_phi(1,0,n,k1.*r,theta,phi));
    F2t1rz(:,n)=transpose(F2n_r(1,0,n,k1.*r,theta,phi));
    F2t1thz(:,n)=transpose(F2n_theta(1,0,n,k1.*r,theta,phi));
end
% z-orientation
F1s3pz=F1i3pz;
F2s3rz=F2i3rz;
F2s3thz=F2i3thz;

F1t1pz(r>a,:)=0;
F2t1rz(r>a,:)=0;
F2t1thz(r>a,:)=0;
F1s3pz(r<=a,:)=0;
F2s3rz(r<=a,:)=0;
F2s3thz(r<=a,:)=0;

F1i1pz(r>r0,:)=0;
F2i1rz(r>r0,:)=0;
F2i1thz(r>r0,:)=0;
F1i3pz(r<=r0,:)=0;
F2i3rz(r<=r0,:)=0;
F2i3thz(r<=r0,:)=0;
F1i1pz(r<=a,:)=0;
F2i1rz(r<=a,:)=0;
F2i1thz(r<=a,:)=0;

Hipz=-j*k0.*sqrt(n0).*(F1i1pz*Q20i1+F1i3pz*Q20i3);
Eirz=k0./sqrt(n0).*(F2i1rz*Q20i1+F2i3rz*Q20i3);
Eithz=k0./sqrt(n0).*(F2i1thz*Q20i1+F2i3thz*Q20i3);

Hspz=-j*k0.*sqrt(n0).*(F1s3pz*Q20s1);
Esrz=k0./sqrt(n0).*(F2s3rz*Q20s1);
Esthz=k0./sqrt(n0).*(F2s3thz*Q20s1);

Htpz=-j*k1.*sqrt(n1).*(F1t1pz*Q20t1);
Etrz=k1./sqrt(n1).*(F2t1rz*Q20t1);
Etthz=k1./sqrt(n1).*(F2t1thz*Q20t1);


% The analytical equation of z-oriented magnetic dipole:
% These equations are varified and they show similarity between them
% and the SVWE which are the correct behavior as we expect.

r0=-r0;
R=sqrt(r.^2+r0^2-2*r.*r0.*cos(theta));
H_pz=exp(-j*k0.*R)./(4*pi*R).*sin(theta).*r.*(1+j*k0.*R)./(R.^2);
E_rz=-1./(j*w.*e0).*exp(-j*k0.*R)./(4*pi*R).*(-
2*cos(theta).*(1+j*k0.*R)./(R.^2)+...
    r.*r0.*(sin(theta)).^2.*((j*k0.*R).^2+3*j*k0.*R+3)./(R.^4));
```

```
E_thz=1./(j*w.*e0).*exp(-j*k0.*R)./(4*pi*R).*sin(theta).*...
    (-2*(1+j*k0.*R)./(R.^2)+...
    r.*(r-r0.*cos(theta)).*((j*k0.*R).^2+3*j*k0.*R+3)./(R.^4));

H_pz=conj(H_pz);
E_rz=conj(E_rz);
E_thz=conj(E_thz);
%-------------------------------------------------------------------------
----

Hpz=Hipz+Hspz+Htpz;
Erz=Eirz+Esrz+Etrz;
Ethz=Eithz+Esthz+Etthz;


% Reform the fields from the colum matrix to (NxN) matrix form
H_pz=reshape(H_pz,N,N);
E_thz=reshape(E_thz,N,N);
E_rz=reshape(E_rz,N,N);

Hpz=reshape(Hpz,N,N);
Ethz=reshape(Ethz,N,N);
Erz=reshape(Erz,N,N);


r=reshape(r,N,N);
theta=reshape(theta,N,N);
phi=reshape(phi,N,N);

% Convert from sphrical to cartisian components
Emagz=sqrt((real(Erz)).^2+(real(Ethz)).^2);
Exz=Erz.*sin(theta).*cos(phi)+Ethz.*cos(theta).*cos(phi);
Eyz=Erz.*sin(theta).*sin(phi)+Ethz.*cos(theta).*sin(phi);
Ezz=Erz.*cos(theta)-Ethz.*sin(theta);
Hmagz=sqrt((real(Hpz)).^2);
Hxz=-Hpz.*sin(phi);
Hyz=Hpz.*cos(phi);
Hzz=zeros(N);
Eabs=sqrt((abs(Erz)).^2+(abs(Ethz)).^2);
Habs=abs(Hpz);

E_magz=sqrt((real(E_rz)).^2+(real(E_thz)).^2);
E_xz=E_rz.*sin(theta).*cos(phi)+E_thz.*cos(theta).*cos(phi);
E_yz=E_rz.*sin(theta).*sin(phi)+E_thz.*cos(theta).*sin(phi);
E_zz=E_rz.*cos(theta)-E_thz.*sin(theta);
H_magz=sqrt((real(H_pz)).^2);
H_xz=-H_pz.*sin(phi);
H_yz=H_pz.*cos(phi);
H_zz=zeros(N);



% Poynting vector S (radiating power)
Sxz=1/2*real(-Ezz.*conj(Hyz));
```

```
Syz=1/2*real(Ezz.*conj(Hxz));
Szz=1/2*real(Exz.*conj(Hyz)-Eyz.*conj(Hxz));
Smagz=sqrt((real(Sxz)).^2+(real(Syz)).^2+(real(Szz)).^2);



m=3;
figure(1)
axes('fontsize',18)
pcolor(X,Z,20*log10(abs(Emagz)/max(max(abs(Emagz)))))
shading interp
colorbar('fontsize',18)
hold on
h=quiver(X(1:m:N,1:m:N),Z(1:m:N,1:m:N),...
    real(Exz(1:m:N,1:m:N))./Emagz(1:m:N,1:m:N),...
    real(Ezz(1:m:N,1:m:N))./Emagz(1:m:N,1:m:N));
set(h,'color','k')
xlabel('x [m]')
ylabel('z [m]')
title('|Re\{E^z\}| [dB]')%title('E^z svwe method [V/m]')
axis([x(1) x(N) z(1) z(N)]);
hold off
axis('equal')
x1=linspace(0,2*pi);hold on; plot(a*sin(x1),a*cos(x1),'k--
','linewidth',2);hold off;


figure(2)
axes('fontsize',18)
pcolor(X,Z,20*log10(abs(Hmagz)/max(max(abs(Hmagz)))))
shading interp
colorbar('fontsize',18)
% hold on
% h=quiver(X(1:m:N,1:m:N),Z(1:m:N,1:m:N),...
%     real(Hxz(1:m:N,1:m:N))./Hmagz(1:m:N,1:m:N),...
%     real(Hzz(1:m:N,1:m:N))./Hmagz(1:m:N,1:m:N));
% set(h,'color','k')
xlabel('x [m]')
ylabel('z [m]')
title('|Re\{H^z\}| [dB]')%title('H^z svwe method [A/m]')
axis([x(1) x(N) z(1) z(N)]);
% hold off
axis('equal')
x1=linspace(0,2*pi);hold on; plot(a*sin(x1),a*cos(x1),'k--
','linewidth',2);hold off;


figure(3)
axes('fontsize',18)
pcolor(X,Z,10*log10(abs(Smagz)/max(max(abs(Smagz)))))
shading interp
colorbar('fontsize',18)
hold on
h=quiver(X(1:m:N,1:m:N),Z(1:m:N,1:m:N),...
    real(Sxz(1:m:N,1:m:N))./Smagz(1:m:N,1:m:N),...
```

```
    real(Szz(1:m:N,1:m:N))./Smagz(1:m:N,1:m:N));
set(h,'color','k')
xlabel('x [m]')
ylabel('z [m]')
title('|S^z| [dB]')
axis([x(1) x(N) z(1) z(N)]);
hold off
axis('equal')
x1=linspace(0,2*pi);hold on; plot(a*sin(x1),a*cos(x1),'k--
','linewidth',2);hold off;
```

Script 10

This script calculates electric and the magnetic fields as well as the power density inside and outside a dielectric sphere of radius a and the transmitting antenna is x-oriented electric dipole antenna EHDx and has r_0 distance from the origin. This script is not a function, therefore it is necessary to put all the functions (scripts 1 to 8) in the same directory as this script. There are several parameters that need to be assigned before running the script.

```
%%%%%%%%%%%%%%%%%%%%%%%%%%%%%%%%%%%%%%%%%%%%%%%%%%%%%%%%%%%%%%%%%%%%%%%%%%%%
% Input:                                                                      %
%       a    : the radius of the sphere.                                      %
%       r0   : the position distance of the transmitting antenna.             %
%       f0   : the operating frequency.                                       %
%       N1   : the number of modes.                                           %
%       N    : number of points that are used to calculate the fields on.     %
%       x    : the limit of the region where the fields are calculated on the x-axis.  %
%       z    : the limit of the region where the fields are calculated on the z-axis.  %
%                                                                             %
% Output:                                                                     %
%       Electric field, magnetic field and power density.                     %
%%%%%%%%%%%%%%%%%%%%%%%%%%%%%%%%%%%%%%%%%%%%%%%%%%%%%%%%%%%%%%%%%%%%%%%%%%%%
```

```
% The parameters of the system
clear all
e0=8.854e-12; % permittivity of the free-space.  [F/m]
u0=4*pi*1e-7; % permeability of the free-space.  [H/m]
n0=1/376.7;     % impedance of the free-space.  [Ohom]
c=2.998e8;    % velocity of light in free-space. [m/s]
r0=.103;      % location of the dipole. [m]
a=.093;       % radius of the sphere
f0=.912e9;       % operating frequency. [Hz]
w=2*pi*f0;    % angular frequency.   [radian/s]
k0=w/c;       % wave length in free-space. [1/m]
er=41.0279 +j*17.8281;        % relative permittivity of the sphere
ur=1;         % relative permeability of the sphere
n1=n0*sqrt(er./ur); % the impedance of the sphere [Ohom]
k1=k0.*sqrt(ur.*er); % the wave number inside the sphere
N1=50; % number of the modes

N=100; % number of the points
x=linspace(-.13,.13,N);
z=linspace(-.13,.13,N);
[X,Z]=meshgrid(x,z);
Y=0*ones(N);
[phi,theta,r]=cart2sph(X,Y,Z);
theta=pi/2-theta;

r=reshape(r,1,N*N);
theta=reshape(theta,1,N*N);
phi=reshape(phi,1,N*N);
```

```
%-------------------------------------------------------------------------
----
% interpolation of the data of the head
p1 = 3.2404e-048;
p2 = -5.057e-038;
p3 = 2.5808e-028;
p4 = -3.6429e-019;
p5 = 4.1155e-010;
p6 = 0.73379;
sigmaFun= @(x) p1*x.^5 + p2*x.^4 +p3*x.^3 + p4*x.^2 +p5*x + p6; % sigma
p1 = 2.6703e-075;
p2 = -7.7329e-065;
p3 = 9.3934e-055;
p4 = -6.2078e-045;
p5 = 2.4204e-035;
p6 = -5.6427e-026;
p7 = 7.5919e-017;
p8 = -5.4572e-008;
p9 = 57.247;
epsilonFun = @(x) p1*x.^8 + p2*x.^7 +p3*x.^6 + p4*x.^5 +p5*x.^4 +
p6*x.^3 +p7*x.^2 + p8*x + p9; % mu_r

sigma=sigmaFun(f0);
epsilon=epsilonFun(f0);

er = conj(epsilon-j*sigma./(w*e0));
n1=n0*sqrt(er./ur); % the impedance of the sphere [Ohom]
k1=k0.*sqrt(ur.*er); % the wave number inside the sphere
%-------------------------------------------------------------------------
----


n=(1:N1)'; %Rfunc(s,c,n,kr)
Q11i1=j*k0./sqrt(n0).*(-
1).^(n+1).*1/4.*sqrt((2*n+1)/pi).*Rfunc(1,3,n,k0.*r0);   %  r <= r0
Q11i3=j*k0./sqrt(n0).*(-
1).^(n+1).*1/4.*sqrt((2*n+1)/pi).*Rfunc(1,1,n,k0.*r0);   %  r > r0
Q21i1=k0./sqrt(n0).*(-
1).^(n+1).*1/4.*sqrt((2*n+1)/pi).*Rfunc(2,3,n,k0.*r0);   %  r <= r0
Q21i3=k0./sqrt(n0).*(-
1).^(n+1).*1/4.*sqrt((2*n+1)/pi).*Rfunc(2,1,n,k0.*r0);   %  r > r0

Q11s3=Q11i1.*(-sqrt(n0/n1).*Rfunc(2,1,n,k0*a).*Rfunc(1,1,n,k1*a)+...
    sqrt(n1/n0).*Rfunc(1,1,n,k0*a).*Rfunc(2,1,n,k1*a))./...
    (sqrt(n0/n1).*Rfunc(1,1,n,k1*a).*Rfunc(2,3,n,k0*a)-...
    sqrt(n1/n0).*Rfunc(2,1,n,k1*a).*Rfunc(1,3,n,k0*a));
Q21s3=Q21i1.*(sqrt(n0/n1).*Rfunc(2,1,n,k1*a).*Rfunc(1,1,n,k0*a)-...
    sqrt(n1/n0).*Rfunc(1,1,n,k1*a).*Rfunc(2,1,n,k0*a))./...
    (sqrt(n1/n0).*Rfunc(1,1,n,k1*a).*Rfunc(2,3,n,k0*a)-...
    sqrt(n0/n1).*Rfunc(2,1,n,k1*a).*Rfunc(1,3,n,k0*a));

Q11t1=Q11i1.*k0./k1.*(j./((k0*a).^2))./...
    (sqrt(n0/n1).*Rfunc(1,1,n,k1*a).*Rfunc(2,3,n,k0*a)-...
```

```
    sqrt(n1/n0).*Rfunc(2,1,n,k1*a).*Rfunc(1,3,n,k0*a));
Q21t1=Q21i1.*k0./k1.*(j./((k0*a).^2))./...
    (sqrt(n1/n0).*Rfunc(1,1,n,k1*a).*Rfunc(2,3,n,k0*a)-...
    sqrt(n0/n1).*Rfunc(2,1,n,k1*a).*Rfunc(1,3,n,k0*a));


for n=1:N1
    % x-orientation

    F1i1px1(:,n)=transpose(F1n_phi(1,1,n,k0*r,theta,phi)); % m=1
    F1i3px1(:,n)=transpose(F1n_phi(3,1,n,k0*r,theta,phi)); % m=1
    F1i1px2(:,n)=transpose(F1n_phi(1,-1,n,k0*r,theta,phi)); % m=-1
    F1i3px2(:,n)=transpose(F1n_phi(3,-1,n,k0*r,theta,phi)); % m=-1

    F1i1thx1(:,n)=transpose(F1n_theta(1,1,n,k0*r,theta,phi)); % m=1
    F1i3thx1(:,n)=transpose(F1n_theta(3,1,n,k0*r,theta,phi)); % m=1
    F1i1thx2(:,n)=transpose(F1n_theta(1,-1,n,k0*r,theta,phi)); % m=-1
    F1i3thx2(:,n)=transpose(F1n_theta(3,-1,n,k0*r,theta,phi)); % m=1

    F2i1px1(:,n)=transpose(F2n_phi(1,1,n,k0*r,theta,phi)); % m=1
    F2i3px1(:,n)=transpose(F2n_phi(3,1,n,k0*r,theta,phi)); % m=1
    F2i1px2(:,n)=transpose(F2n_phi(1,-1,n,k0*r,theta,phi)); % m=-1
    F2i3px2(:,n)=transpose(F2n_phi(3,-1,n,k0*r,theta,phi)); % m=-1

    F2i1thx1(:,n)=transpose(F2n_theta(1,1,n,k0*r,theta,phi)); % m=1
    F2i3thx1(:,n)=transpose(F2n_theta(3,1,n,k0*r,theta,phi)); % m=1
    F2i1thx2(:,n)=transpose(F2n_theta(1,-1,n,k0*r,theta,phi)); % m=-1
    F2i3thx2(:,n)=transpose(F2n_theta(3,-1,n,k0*r,theta,phi)); % m=-1

    F2i1rx1(:,n)=transpose(F2n_r(1,1,n,k0*r,theta,phi)); % m=1
    F2i3rx1(:,n)=transpose(F2n_r(3,1,n,k0*r,theta,phi)); % m=1
    F2i1rx2(:,n)=transpose(F2n_r(1,-1,n,k0*r,theta,phi)); % m=-1
    F2i3rx2(:,n)=transpose(F2n_r(3,-1,n,k0*r,theta,phi)); % m=-1


    %   total fields
    F1t1px1(:,n)=transpose(F1n_phi(1,1,n,k1*r,theta,phi)); % m=1
    F1t1px2(:,n)=transpose(F1n_phi(1,-1,n,k1*r,theta,phi)); % m=-1

    F1t1thx1(:,n)=transpose(F1n_theta(1,1,n,k1*r,theta,phi)); % m=1
    F1t1thx2(:,n)=transpose(F1n_theta(1,-1,n,k1*r,theta,phi)); % m=-1

    F2t1px1(:,n)=transpose(F2n_phi(1,1,n,k1*r,theta,phi)); % m=1
    F2t1px2(:,n)=transpose(F2n_phi(1,-1,n,k1*r,theta,phi)); % m=-1

    F2t1thx1(:,n)=transpose(F2n_theta(1,1,n,k1*r,theta,phi)); % m=1
    F2t1thx2(:,n)=transpose(F2n_theta(1,-1,n,k1*r,theta,phi)); % m=-1

    F2t1rx1(:,n)=transpose(F2n_r(1,1,n,k1*r,theta,phi)); % m=1
    F2t1rx2(:,n)=transpose(F2n_r(1,-1,n,k1*r,theta,phi)); % m=-1
  end
% x-orientation

% scattered fields
```

```
F1s3px1=F1i3px1;
F1s3thx1=F1i3thx1;
F1s3px2=F1i3px2;
F1s3thx2=F1i3thx2;

F2s3px1=F2i3px1;
F2s3thx1=F2i3thx1;
F2s3rx1=F2i3rx1;
F2s3px2=F2i3px2;
F2s3thx2=F2i3thx2;
F2s3rx2=F2i3rx2;

F1s3px1(r<=a,:)=0;
F1s3thx1(r<=a,:)=0;
F1s3px2(r<=a,:)=0;
F1s3thx2(r<=a,:)=0;

F2s3px1(r<=a,:)=0;
F2s3thx1(r<=a,:)=0;
F2s3rx1(r<=a,:)=0;
F2s3px2(r<=a,:)=0;
F2s3thx2(r<=a,:)=0;
F2s3rx2(r<=a,:)=0;

% incident fields
F1i1px1(r>r0,:)=0;
F1i1thx1(r>r0,:)=0;
F1i1px2(r>r0,:)=0;
F1i1thx2(r>r0,:)=0;

F1i1px1(r<=a,:)=0;
F1i1thx1(r<=a,:)=0;
F1i1px2(r<=a,:)=0;
F1i1thx2(r<=a,:)=0;

F1i3px1(r<=r0,:)=0;
F1i3thx1(r<=r0,:)=0;
F1i3px2(r<=r0,:)=0;
F1i3thx2(r<=r0,:)=0;

F2i1px1(r>r0,:)=0;
F2i1thx1(r>r0,:)=0;
F2i1rx1(r>r0,:)=0;
F2i1px2(r>r0,:)=0;
F2i1thx2(r>r0,:)=0;
F2i1rx2(r>r0,:)=0;

F2i1px1(r<=a,:)=0;
F2i1thx1(r<=a,:)=0;
F2i1rx1(r<=a,:)=0;
F2i1px2(r<=a,:)=0;
F2i1thx2(r<=a,:)=0;
F2i1rx2(r<=a,:)=0;

F2i3px1(r<=r0,:)=0;
```

```
F2i3thx1(r<=r0,:)=0;
F2i3rx1(r<=r0,:)=0;
F2i3px2(r<=r0,:)=0;
F2i3thx2(r<=r0,:)=0;
F2i3rx2(r<=r0,:)=0;

% total field
F1t1px1(r>a,:)=0;
F1t1thx1(r>a,:)=0;
F1t1px2(r>a,:)=0;
F1t1thx2(r>a,:)=0;

F2t1px1(r>a,:)=0;
F2t1thx1(r>a,:)=0;
F2t1rx1(r>a,:)=0;
F2t1px2(r>a,:)=0;
F2t1thx2(r>a,:)=0;
F2t1rx2(r>a,:)=0;

% incident fields
Eipx=k0./sqrt(n0).*((F1i1px1+F1i1px2)*Q11i1+(F1i3px1+F1i3px2)*Q11i3...
    +(F2i1px1-F2i1px2)*Q21i1+(F2i3px1-F2i3px2)*Q21i3);
Eithx=k0./sqrt(n0).*((F1i1thx1+F1i1thx2)*Q11i1+(F1i3thx1+F1i3thx2)*Q11i
3...
    +(F2i1thx1-F2i1thx2)*Q21i1+(F2i3thx1-F2i3thx2)*Q21i3);
Eirx=k0./sqrt(n0).*((F2i1rx1-F2i1rx2)*Q21i1+(F2i3rx1-F2i3rx2)*Q21i3);
Hipx=-
j*k0.*sqrt(n0).*((F2i1px1+F2i1px2)*Q11i1+(F2i3px1+F2i3px2)*Q11i3...
    +(F1i1px1-F1i1px2)*Q21i1+(F1i3px1-F1i3px2)*Q21i3);
Hithx=-
j*k0.*sqrt(n0).*((F2i1thx1+F2i1thx2)*Q11i1+(F2i3thx1+F2i3thx2)*Q11i3...
    +(F1i1thx1-F1i1thx2)*Q21i1+(F1i3thx1-F1i3thx2)*Q21i3);
Hirx=-
j*k0.*sqrt(n0).*((F2i1rx1+F2i1rx2)*Q11i1+(F2i3rx1+F2i3rx2)*Q11i3);

% scattered fields
Espx=k0./sqrt(n0).*((F1s3px1+F1s3px2)*Q11s3...
    +(F2s3px1-F2s3px2)*Q21s3);
Esthx=k0./sqrt(n0).*((F1s3thx1+F1s3thx2)*Q11s3...
    +(F2s3thx1-F2s3thx2)*Q21s3);
Esrx=k0./sqrt(n0).*((F2s3rx1-F2s3rx2)*Q21s3);
Hspx=-j*k0.*sqrt(n0).*((F2s3px1+F2s3px2)*Q11s3...
    +(F1s3px1-F1s3px2)*Q21s3);
Hsthx=-j*k0.*sqrt(n0).*((F2s3thx1+F2s3thx2)*Q11s3...
    +(F1s3thx1-F1s3thx2)*Q21s3);
Hsrx=-j*k0.*sqrt(n0).*((F2s3rx1+F2s3rx2)*Q11s3);

% total fields
Etpx=k1./sqrt(n1).*((F1t1px1+F1t1px2)*Q11t1...
    +(F2t1px1-F2t1px2)*Q21t1);
Etthx=k1./sqrt(n1).*((F1t1thx1+F1t1thx2)*Q11t1...
    +(F2t1thx1-F2t1thx2)*Q21t1);
Etrx=k1./sqrt(n1).*((F2t1rx1-F2t1rx2)*Q21t1);
Htpx=-j*k1.*sqrt(n1).*((F2t1px1+F2t1px2)*Q11t1...
    +(F1t1px1-F1t1px2)*Q21t1);
Htthx=-j.*k1.*sqrt(n1).*((F2t1thx1+F2t1thx2)*Q11t1...
```

```
    +(F1t1thx1-F1t1thx2)*Q21t1);
Htrx=-j*k1.*sqrt(n1).*((F2t1rx1+F2t1rx2)*Q11t1);


%-------------------------------------------------------------------------
----
% The analytical equation of x-oriented magnetic dipole:
%  These equations are varified and they show similarity between them
and
%  the SVWE which are the correct behavior as we expect.
%  The equations of the closed-form and the SVWE are varified in the
%  m-file "ValidationOf_x_Scattering.m"

r0=-r0;
R=sqrt(r.^2+r0^2-2*r.*r0.*cos(theta));
H_rx=exp(-
j*k0.*R)./(4*pi*R).*sin(theta).*sin(phi).*r0.*(1+j*k0.*R)./(R.^2);
H_thx=-exp(-j*k0.*R)./(4*pi*R).*sin(phi).*(r-
r0.*cos(theta)).*(1+j*k0.*R)./(R.^2);
H_px=-exp(-j*k0.*R)./(4*pi*R).*cos(phi).*(r.*cos(theta)-
r0).*(1+j*k0.*R)./(R.^2);
E_rx=-j*w.*u0.*exp(-j*k0.*R)./(4*pi*R).*sin(theta).*cos(phi).*...
    (1-(1+j*k0.*R)./((k0.*R).^2)+...
    r.*(r-r0.*cos(theta)).*((-j*k0.*R).^2+3*j*k0.*R+3)./(k0.^2.*R.^4));
E_thx=-j*w.*u0.*exp(-j*k0.*R)./(4*pi*R).*cos(theta).*cos(phi).*...
    (1-(1+j*k0.*R)./((k0.*R).^2)+...
    r.*r0.*(sin(theta)).^2.*((-
j*k0.*R).^2+3*j*k0.*R+3)./(k0.^2.*R.^4.*cos(theta)));
E_px=j*w.*u0.*exp(-j*k0.*R)./(4*pi*R).*sin(phi).*(1-
(1+j*k0.*R)./(k0.^2.*R.^2));

E_rx=transpose(conj(E_rx));
E_thx=transpose(conj(E_thx));
E_px=transpose(conj(E_px));
H_rx=transpose(conj(H_rx));
H_thx=transpose(conj(H_thx));
H_px=transpose(conj(H_px));
E_rx(r<=a,:)=0;
E_thx(r<=a,:)=0;
E_px(r<=a,:)=0;
H_rx(r<=a,:)=0;
H_thx(r<=a,:)=0;
H_px(r<=a,:)=0;
%-------------------------------------------------------------------------
----

% Calculating the fields
Epx=E_px+Espx+Etpx;
Ethx=E_thx+Esthx+Etthx;
Erx=E_rx+Esrx+Etrx;
Hpx=H_px+Hspx+Htpx;
Hthx=H_thx+Hsthx+Htthx;
Hrx=H_rx+Hsrx+Htrx;

% Reform the fields from the colum matrix to (NxN) matrix form
E_px=reshape(E_px,N,N);
```

```
E_thx=reshape(E_thx,N,N);
E_rx=reshape(E_rx,N,N);
H_px=reshape(H_px,N,N);
H_thx=reshape(H_thx,N,N);
H_rx=reshape(H_rx,N,N);

Epx=reshape(Epx,N,N);
Ethx=reshape(Ethx,N,N);
Erx=reshape(Erx,N,N);
Hpx=reshape(Hpx,N,N);
Hthx=reshape(Hthx,N,N);
Hrx=reshape(Hrx,N,N);


r=reshape(r,N,N);
theta=reshape(theta,N,N);
phi=reshape(phi,N,N);

% Convert from sphrical to cartisian components
Hmagx=sqrt((real(Hrx)).^2+(real(Hthx)).^2+(real(Hpx)).^2);
Hxx=Hrx.*sin(theta).*cos(phi)+Hthx.*cos(theta).*cos(phi)-Hpx.*sin(phi);
Hyx=Hrx.*sin(theta).*sin(phi)+Hthx.*cos(theta).*sin(phi)+Hpx.*cos(phi);
Hzx=Hrx.*cos(theta)-Hthx.*sin(theta);
Emagx=sqrt((real(Erx)).^2+(real(Ethx)).^2+(real(Epx)).^2);
Exx=Erx.*sin(theta).*cos(phi)+Ethx.*cos(theta).*cos(phi)-Epx.*sin(phi);
Eyx=Erx.*sin(theta).*sin(phi)+Ethx.*cos(theta).*sin(phi)+Epx.*cos(phi);
Ezx=Erx.*cos(theta)-Ethx.*sin(theta);
Eabs=sqrt((abs(Erx)).^2+(abs(Ethx)).^2+(abs(Epx)).^2);
Habs=sqrt((abs(Hrx)).^2+(abs(Hthx)).^2+(abs(Hpx)).^2);

H_magx=sqrt((real(H_rx)).^2+(real(H_thx)).^2+(real(H_px)).^2);
H_xx=H_rx.*sin(theta).*cos(phi)+H_thx.*cos(theta).*cos(phi)-
H_px.*sin(phi);
H_zx=H_rx.*cos(theta)-H_thx.*sin(theta);
E_magx=sqrt((real(E_rx)).^2+(real(E_thx)).^2+(real(E_px)).^2);
E_xx=E_rx.*sin(theta).*cos(phi)+E_thx.*cos(theta).*cos(phi)-
E_px.*sin(phi);
E_zx=E_rx.*cos(theta)-E_thx.*sin(theta);


% Poynting vector S (radiating power)
Sxx=1/2*real(Eyx.*conj(Hzx)-Ezx.*conj(Hyx));
Syx=1/2*real(Ezx.*conj(Hxx)-Exx.*conj(Hzx));
Szx=1/2*real(Exx.*conj(Hyx)-Eyx.*conj(Hxx));
Smagx=sqrt((real(Sxx)).^2+(real(Syx)).^2+(real(Szx)).^2);


m=3;
figure(1)
axes('fontsize',18)
pcolor(X,Z,20*log10(Hmagx/max(max(Hmagx))))
shading interp
colorbar('fontsize',18)
hold on
h=quiver(X(1:m:N,1:m:N),Z(1:m:N,1:m:N),...
```

```
    real(Hxx(1:m:N,1:m:N))./Hmagx(1:m:N,1:m:N),...
    real(Hzx(1:m:N,1:m:N))./Hmagx(1:m:N,1:m:N));
set(h,'color','k')
xlabel('x [m]')
ylabel('z [m]')
title('H^x [dB]')
axis([x(1) x(N) z(1) z(N)]);
hold off
x1=linspace(0,2*pi);hold on; plot(a*sin(x1),a*cos(x1),'k--
','linewidth',2);hold off;
axis('equal')

figure(2)
axes('fontsize',18)
pcolor(X,Z,20*log10(Emagx/max(max(Emagx))))
shading interp
colorbar('fontsize',18)
hold on
h=quiver(X(1:m:N,1:m:N),Z(1:m:N,1:m:N),...
    real(Exx(1:m:N,1:m:N))./Emagx(1:m:N,1:m:N),...
    real(Ezx(1:m:N,1:m:N))./Emagx(1:m:N,1:m:N));
set(h,'color','k')
xlabel('x [m]')
ylabel('z [m]')
title('E^x [dB]')
axis([x(1) x(N) z(1) z(N)]);
hold off
x1=linspace(0,2*pi);hold on; plot(a*sin(x1),a*cos(x1),'k--
','linewidth',2);hold off;
axis('equal')

figure(3)
axes('fontsize',18)
pcolor(X,Z,10*log10(Smagx/max(max(Smagx))))
shading interp
colorbar('fontsize',18)
hold on
h=quiver(X(1:m:N,1:m:N),Z(1:m:N,1:m:N),...
    real(Sxx(1:m:N,1:m:N))./Smagx(1:m:N,1:m:N),...
    real(Szx(1:m:N,1:m:N))./Smagx(1:m:N,1:m:N));
set(h,'color','k')
xlabel('x [m]')
ylabel('z [m]')
title('S^x [W/m^2]')
axis([x(1) x(N) z(1) z(N)]);
hold off
x1=linspace(0,2*pi);hold on; plot(a*sin(x1),a*cos(x1),'k--
','linewidth',2);hold off;
axis('equal')
```

Script 11

This script calculates electric and the magnetic fields as well as the power density inside and outside a dielectric sphere of radius a and the transmitting antenna is z-oriented magnetic dipole antenna MHDz and has r_0 distance from the origin. This script is not a function, therefore it is necessary to put all the functions (scripts 1 to 8) in the same directory as this script. There are several parameters that need to be assigned before running the script.

```
%%%%%%%%%%%%%%%%%%%%%%%%%%%%%%%%%%%%%%%%%%%%%%%%%%%%%%%%%%%%%%%%%%%%%%%%%%%%
% Input:                                                                      %
%       a    : the radius of the sphere.                                      %
%       r0   : the position distance of the transmitting antenna.             %
%       f0   : the operating frequency.                                       %
%       N1   : the number of modes.                                           %
%       N    : number of points that are used to calculate the fields on.     %
%       x    : the limit of the region where the fields are calculated on the x-axis.  %
%       z    : the limit of the region where the fields are calculated on the z-axis.  %
%                                                                             %
% Output:                                                                     %
%       Electric field, magnetic field and power density.                     %
%%%%%%%%%%%%%%%%%%%%%%%%%%%%%%%%%%%%%%%%%%%%%%%%%%%%%%%%%%%%%%%%%%%%%%%%%%%%
```

```
% The parameters of the system
clear all
e0=8.854e-12; % permittivity of the free-space.  [F/m]
u0=4*pi*1e-7; % permeability of the free-space.  [H/m]
n0=1/376.7;     % impedance of the free-space.  [Ohom]
c=2.998e8;    % velocity of light in free-space. [m/s]
r0=.092;      % location of the dipole. [m]
a=.085;       % radius of the sphere
f0=2.45e9;       % operating frequency. [Hz]
w=2*pi*f0;    % angular frequency.   [radian/s]
k0=w/c;       % wave length in free-space. [1/m]
er=39.1568 +j*13.3150;        % relative permittivity of the sphere
ur=1;         % relative permeability of the sphere
n1=n0*sqrt(er./ur); % the impedance of the sphere [Ohom]
k1=k0.*sqrt(ur.*er); % the wave number inside the sphere
N1=100; % number of the modes

N=100; % number of the points
x=linspace(-.12,.12,N);
z=linspace(-.12,.12,N);
[X,Z]=meshgrid(x,z);
Y=0*ones(N);
[phi,theta,r]=cart2sph(X,Y,Z);
theta=pi/2-theta;

r=reshape(r,1,N*N);
theta=reshape(theta,1,N*N);
phi=reshape(phi,1,N*N);
```

```
%-------------------------------------------------------------------------
----
n=(1:N1)';

Q10i1=j*k0.*sqrt(n0).*(-
1).^n.*sqrt(n.*(n+1).*(2*n+1)/(4*pi)).*Rfunc(1,3,n,k0.*r0)./(k0.*r0);
Q10i3=j*k0.*sqrt(n0).*(-
1).^n.*sqrt(n.*(n+1).*(2*n+1)/(4*pi)).*Rfunc(1,1,n,k0.*r0)./(k0.*r0);


              % Rfunc(s,c,n,kr)
Q10s1=-Q10i1.*(sqrt(n1/n0).*Rfunc(1,1,n,k0.*a).*Rfunc(2,1,n,k1.*a)...
    -sqrt(n0/n1).*Rfunc(2,1,n,k0.*a).*Rfunc(1,1,n,k1.*a))./...
    (sqrt(n1/n0).*Rfunc(1,3,n,k0.*a).*Rfunc(2,1,n,k1.*a)...
    -sqrt(n0/n1).*Rfunc(2,3,n,k0.*a).*Rfunc(1,1,n,k1.*a));
Q10t1=Q10i1.*k0./k1.*-j./((k0.*a).^2)./...
    (sqrt(n1/n0).*Rfunc(1,3,n,k0.*a).*Rfunc(2,1,n,k1.*a)...
    -sqrt(n0/n1).*Rfunc(2,3,n,k0.*a).*Rfunc(1,1,n,k1.*a));


for n=1:N1
    % z-orientation
    F1i1pz(:,n)=transpose(F1n_phi(1,0,n,k0.*r,theta,phi));
    F1i3pz(:,n)=transpose(F1n_phi(3,0,n,k0.*r,theta,phi));
    F2i1rz(:,n)=transpose(F2n_r(1,0,n,k0.*r,theta,phi));
    F2i3rz(:,n)=transpose(F2n_r(3,0,n,k0.*r,theta,phi));
    F2i1thz(:,n)=transpose(F2n_theta(1,0,n,k0.*r,theta,phi));
    F2i3thz(:,n)=transpose(F2n_theta(3,0,n,k0.*r,theta,phi));

    F1t1pz(:,n)=transpose(F1n_phi(1,0,n,k1.*r,theta,phi));
    F2t1rz(:,n)=transpose(F2n_r(1,0,n,k1.*r,theta,phi));
    F2t1thz(:,n)=transpose(F2n_theta(1,0,n,k1.*r,theta,phi));
end
% z-orientation
F1s3pz=F1i3pz;
F2s3rz=F2i3rz;
F2s3thz=F2i3thz;

F1t1pz(r>a,:)=0;
F2t1rz(r>a,:)=0;
F2t1thz(r>a,:)=0;
F1s3pz(r<=a,:)=0;
F2s3rz(r<=a,:)=0;
F2s3thz(r<=a,:)=0;

F1i1pz(r>r0,:)=0;
F2i1rz(r>r0,:)=0;
F2i1thz(r>r0,:)=0;
F1i3pz(r<=r0,:)=0;
F2i3rz(r<=r0,:)=0;
F2i3thz(r<=r0,:)=0;
F1i1pz(r<=a,:)=0;
F2i1rz(r<=a,:)=0;
F2i1thz(r<=a,:)=0;
```

```
Eipz=k0./sqrt(n0).*(F1i1pz*Q10i1+F1i3pz*Q10i3);
Hirz=-j*k0.*sqrt(n0).*(F2i1rz*Q10i1+F2i3rz*Q10i3);
Hithz=-j*k0.*sqrt(n0).*(F2i1thz*Q10i1+F2i3thz*Q10i3);

Espz=k0./sqrt(n0).*(F1s3pz*Q10s1);
Hsrz=-j*k0.*sqrt(n0).*(F2s3rz*Q10s1);
Hsthz=-j*k0.*sqrt(n0).*(F2s3thz*Q10s1);

Etpz=k1./sqrt(n1).*(F1t1pz*Q10t1);
Htrz=-j*k1.*sqrt(n1).*(F2t1rz*Q10t1);
Htthz=-j*k1.*sqrt(n1).*(F2t1thz*Q10t1);


% The analytical equation of z-oriented magnetic dipole:
%  These equations are varified and they show similarity between them
and
%  the SVWE which are the correct behavior as we expect.

r0=-r0;
R=sqrt(r.^2+r0^2-2*r.*r0.*cos(theta));
E_pz=-exp(-j*k0.*R)./(4*pi*R).*sin(theta).*r.*(1+j*k0.*R)./(R.^2);
H_rz=-1./(j*w.*u0).*exp(-j*k0.*R)./(4*pi*R).*(-
2*cos(theta).*(1+j*k0.*R)./(R.^2)+...
    r.*r0.*(sin(theta)).^2.*((j*k0.*R).^2+3*j*k0.*R+3)./(R.^4));
H_thz=1./(j*w.*u0).*exp(-j*k0.*R)./(4*pi*R).*sin(theta).*...
    (-2*(1+j*k0.*R)./(R.^2)+...
    r.*(r-r0.*cos(theta)).*((j*k0.*R).^2+3*j*k0.*R+3)./(R.^4));

E_pz=conj(E_pz);
H_rz=conj(H_rz);
H_thz=conj(H_thz);

Epz=Eipz+Espz+Etpz;
Hrz=Hirz+Hsrz+Htrz;
Hthz=Hithz+Hsthz+Htthz;


% Reform the fields from the colum matrix to (NxN) matrix form
E_pz=reshape(E_pz,N,N);
H_thz=reshape(H_thz,N,N);
H_rz=reshape(H_rz,N,N);

Epz=reshape(Epz,N,N);
Hthz=reshape(Hthz,N,N);
Hrz=reshape(Hrz,N,N);


r=reshape(r,N,N);
theta=reshape(theta,N,N);
phi=reshape(phi,N,N);

% Convert from sphrical to cartisian components
Hmagz=sqrt((real(Hrz)).^2+(real(Hthz)).^2);
Hxz=Hrz.*sin(theta).*cos(phi)+Hthz.*cos(theta).*cos(phi);
```

```
Hyz=Hrz.*sin(theta).*sin(phi)+Hthz.*cos(theta).*sin(phi);
Hzz=Hrz.*cos(theta)-Hthz.*sin(theta);
Emagz=sqrt((real(Epz)).^2);
Exz=-Epz.*sin(phi);
Eyz=Epz.*cos(phi);
Ezz=zeros(N);
Habs=sqrt((abs(Hrz)).^2+(abs(Hthz)).^2);
Eabs=abs(Epz);

H_magz=sqrt((real(H_rz)).^2+(real(H_thz)).^2);
H_xz=H_rz.*sin(theta).*cos(phi)+H_thz.*cos(theta).*cos(phi);
H_yz=H_rz.*sin(theta).*sin(phi)+H_thz.*cos(theta).*sin(phi);
H_zz=H_rz.*cos(theta)-H_thz.*sin(theta);
E_magz=sqrt((real(E_pz)).^2);
E_xz=-E_pz.*sin(phi);
E_yz=E_pz.*cos(phi);
E_zz=zeros(N);

% Poynting vector S (radiating power)
Sxz=1/2*real(Eyz.*conj(Hzz));
Syz=1/2*real(-Exz.*conj(Hzz));
Szz=1/2*real(Exz.*conj(Hyz)-Eyz.*conj(Hxz));
Smagz=sqrt((real(Sxz)).^2+(real(Syz)).^2+(real(Szz)).^2);



m=3;
figure(1)
axes('fontsize',18)
pcolor(X,Z,20*log10(abs(Hmagz)/max(max(abs(Hmagz)))))
shading interp
colorbar('fontsize',18);
hold on
h=quiver(X(1:m:N,1:m:N),Z(1:m:N,1:m:N),...
    real(Hxz(1:m:N,1:m:N))./Hmagz(1:m:N,1:m:N),...
    real(Hzz(1:m:N,1:m:N))./Hmagz(1:m:N,1:m:N));
set(h,'color','k')
xlabel('x [m]')
ylabel('z [m]')
title('|Re\{H^z\}| [dB]')%title('H^z svwe method [A/m]')
axis([x(1) x(N) z(1) z(N)]);
axis('equal')
hold off
x1=linspace(0,2*pi);hold on; plot(a*sin(x1),a*cos(x1),'k--
','linewidth',2);hold off;


figure(2)
axes('fontsize',18)
pcolor(X,Z,20*log10(abs(Emagz)/max(max(abs(Emagz)))))
shading interp
colorbar('fontsize',18);
% hold on
% h=quiver(X(1:m:N,1:m:N),Z(1:m:N,1:m:N),...
%     real(Exz(1:m:N,1:m:N))./Emagz(1:m:N,1:m:N),...
%     real(Ezz(1:m:N,1:m:N))./Emagz(1:m:N,1:m:N));
```

```
% set(h,'color','k')
xlabel('x [m]')
ylabel('z [m]')
title('|Re\{E^z\}| [dB]')%title('E^z svwe method [V/m]')
axis([x(1) x(N) z(1) z(N)]);
axis('equal')
% hold off
x1=linspace(0,2*pi);hold on; plot(a*sin(x1),a*cos(x1),'k--
','linewidth',2);hold off;


figure(3)
axes('fontsize',18)
pcolor(X,Z,10*log10(abs(Smagz)/max(max(abs(Smagz)))))
shading interp
colorbar('fontsize',18);
hold on
h=quiver(X(1:m:N,1:m:N),Z(1:m:N,1:m:N),...
    real(Sxz(1:m:N,1:m:N))./Smagz(1:m:N,1:m:N),...
    real(Szz(1:m:N,1:m:N))./Smagz(1:m:N,1:m:N));
set(h,'color','k')
xlabel('x [m]')
ylabel('z [m]')
title('|S^z| [dB]')
axis([x(1) x(N) z(1) z(N)]);
hold off
axis('equal')
x1=linspace(0,2*pi);hold on; plot(a*sin(x1),a*cos(x1),'k--
','linewidth',2);hold off;
```

Script 12

This script calculates electric and the magnetic fields as well as the power density inside and outside a dielectric sphere of radius a and the transmitting antenna is x-oriented magnetic dipole antenna MHDz and has r_0 distance from the origin. This script is not a function, therefore it is necessary to put all the functions (scripts 1 to 8) in the same directory as this script. There are several parameters that need to be assigned before running the script.

```
%%%%%%%%%%%%%%%%%%%%%%%%%%%%%%%%%%%%%%%%%%%%%%%%%%%%%%%%%%%%%%%%%%%%%%%%%%%%
% Input:                                                                      %
%       a    : the radius of the sphere.                                      %
%       r0   : the position distance of the transmitting antenna.             %
%       f0   : the operating frequency.                                       %
%       N1   : the number of modes.                                           %
%       N    : number of points that are used to calculate the fields on.     %
%       x    : the limit of the region where the fields are calculated on the x-axis.  %
%       z    : the limit of the region where the fields are calculated on the z-axis.  %
%                                                                             %
% Output:                                                                     %
%       Electric field, magnetic field and power density.                     %
%%%%%%%%%%%%%%%%%%%%%%%%%%%%%%%%%%%%%%%%%%%%%%%%%%%%%%%%%%%%%%%%%%%%%%%%%%%%
```

```
% The parameters of the system
clear all
e0=8.854e-12; % permittivity of the free-space.  [F/m]
u0=4*pi*1e-7; % permeability of the free-space.  [H/m]
n0=1/376.7;     % impedance of the free-space.  [Ohom]
c=2.998e8;    % velocity of light in free-space. [m/s]
r0=.092;      % location of the dipole. [m]
a=.085;       % radius of the sphere
f0=1e9;       % operating frequency. [Hz]
w=2*pi*f0;    % angular frequency.   [radian/s]
k0=w/c;       % wave length in free-space. [1/m]
er=41.0279 +j*17.8281;        % relative permittivity of the sphere
ur=1;         % relative permeability of the sphere
n1=n0*sqrt(er./ur); % the impedance of the sphere [Ohom]
k1=k0.*sqrt(ur.*er); % the wave number inside the sphere
N1=80; % number of the modes

N=100; % number of the points
x=linspace(-.12,.12,N);
z=linspace(-.12,.12,N);
[X,Z]=meshgrid(x,z);
Y=0*ones(N);
[phi,theta,r]=cart2sph(X,Y,Z);
theta=pi/2-theta;

r=reshape(r,1,N*N);
theta=reshape(theta,1,N*N);
phi=reshape(phi,1,N*N);
```

```
n=(1:N1)'; %Rfunc(s,c,n,kr)
Q11i1=j*k0.*sqrt(n0).*(-
1).^(n+1).*1/4.*sqrt((2*n+1)/pi).*Rfunc(2,3,n,k0.*r0);   %  r <= r0
Q11i3=j*k0.*sqrt(n0).*(-
1).^(n+1).*1/4.*sqrt((2*n+1)/pi).*Rfunc(2,1,n,k0.*r0);   %  r > r0
Q21i1=k0.*sqrt(n0).*(-
1).^(n).*1/4.*sqrt((2*n+1)/pi).*Rfunc(1,3,n,k0.*r0);   %  r <= r0
Q21i3=k0.*sqrt(n0).*(-
1).^(n).*1/4.*sqrt((2*n+1)/pi).*Rfunc(1,1,n,k0.*r0);   %  r > r0

Q11s3=Q11i1.*(sqrt(n0/n1).*Rfunc(2,1,n,k0*a).*Rfunc(1,1,n,k1*a)-...
    sqrt(n1/n0).*Rfunc(1,1,n,k0*a).*Rfunc(2,1,n,k1*a))./...
    (sqrt(n1/n0).*Rfunc(1,3,n,k0*a).*Rfunc(2,1,n,k1*a)-...
    sqrt(n0/n1).*Rfunc(2,3,n,k0*a).*Rfunc(1,1,n,k1*a));
Q21s3=Q21i1.*(sqrt(n0/n1).*Rfunc(1,1,n,k0*a).*Rfunc(2,1,n,k1*a)-...
    sqrt(n1/n0).*Rfunc(2,1,n,k0*a).*Rfunc(1,1,n,k1*a))./...
    (sqrt(n1/n0).*Rfunc(2,3,n,k0*a).*Rfunc(1,1,n,k1*a)-...
    sqrt(n0/n1).*Rfunc(1,3,n,k0*a).*Rfunc(2,1,n,k1*a));

Q11t1=Q11i1.*k0./k1.*(-j./((k0*a).^2))./...
    (sqrt(n1/n0).*Rfunc(1,3,n,k0*a).*Rfunc(2,1,n,k1*a)-...
    sqrt(n0/n1).*Rfunc(2,3,n,k0*a).*Rfunc(1,1,n,k1*a));
Q21t1=Q21i1.*k0./k1.*(j./((k0*a).^2))./...
    (sqrt(n1/n0).*Rfunc(2,3,n,k0*a).*Rfunc(1,1,n,k1*a)-...
    sqrt(n0/n1).*Rfunc(1,3,n,k0*a).*Rfunc(2,1,n,k1*a));


for n=1:N1
    % x-orientation
    sL=j*Lfunc(1,1,n,theta)./sin(theta);
    dL=Lfunc(2,1,n,theta);
    L=-legendre(n,cos(theta));

    F1i1px1(:,n)=transpose(F1n_phi(1,1,n,k0*r,theta,phi)); % m=1
    F1i3px1(:,n)=transpose(F1n_phi(3,1,n,k0*r,theta,phi)); % m=1
    F1i1px2(:,n)=transpose(F1n_phi(1,-1,n,k0*r,theta,phi)); % m=-1
    F1i3px2(:,n)=transpose(F1n_phi(3,-1,n,k0*r,theta,phi)); % m=-1

    F1i1thx1(:,n)=transpose(F1n_theta(1,1,n,k0*r,theta,phi)); % m=1
    F1i3thx1(:,n)=transpose(F1n_theta(3,1,n,k0*r,theta,phi)); % m=1
    F1i1thx2(:,n)=transpose(F1n_theta(1,-1,n,k0*r,theta,phi)); % m=-1
    F1i3thx2(:,n)=transpose(F1n_theta(3,-1,n,k0*r,theta,phi)); % m=1

    F2i1px1(:,n)=transpose(F2n_phi(1,1,n,k0*r,theta,phi)); % m=1
    F2i3px1(:,n)=transpose(F2n_phi(3,1,n,k0*r,theta,phi)); % m=1
    F2i1px2(:,n)=transpose(F2n_phi(1,-1,n,k0*r,theta,phi)); % m=-1
    F2i3px2(:,n)=transpose(F2n_phi(3,-1,n,k0*r,theta,phi)); % m=-1

    F2i1thx1(:,n)=transpose(F2n_theta(1,1,n,k0*r,theta,phi)); % m=1
    F2i3thx1(:,n)=transpose(F2n_theta(3,1,n,k0*r,theta,phi)); % m=1
    F2i1thx2(:,n)=transpose(F2n_theta(1,-1,n,k0*r,theta,phi)); % m=-1
    F2i3thx2(:,n)=transpose(F2n_theta(3,-1,n,k0*r,theta,phi)); % m=-1

    F2i1rx1(:,n)=transpose(F2n_r(1,1,n,k0*r,theta,phi)); % m=1
    F2i3rx1(:,n)=transpose(F2n_r(3,1,n,k0*r,theta,phi)); % m=1
```

```
    F2i1rx2(:,n)=transpose(F2n_r(1,-1,n,k0*r,theta,phi)); % m=-1
    F2i3rx2(:,n)=transpose(F2n_r(3,-1,n,k0*r,theta,phi)); % m=-1


    %   total fields
    F1t1px1(:,n)=transpose(F1n_phi(1,1,n,k1*r,theta,phi)); % m=1
    F1t1px2(:,n)=transpose(F1n_phi(1,-1,n,k1*r,theta,phi)); % m=-1

    F1t1thx1(:,n)=transpose(F1n_theta(1,1,n,k1*r,theta,phi)); % m=1
    F1t1thx2(:,n)=transpose(F1n_theta(1,-1,n,k1*r,theta,phi)); % m=-1

    F2t1px1(:,n)=transpose(F2n_phi(1,1,n,k1*r,theta,phi)); % m=1
    F2t1px2(:,n)=transpose(F2n_phi(1,-1,n,k1*r,theta,phi)); % m=-1

    F2t1thx1(:,n)=transpose(F2n_theta(1,1,n,k1*r,theta,phi)); % m=1
    F2t1thx2(:,n)=transpose(F2n_theta(1,-1,n,k1*r,theta,phi)); % m=-1

    F2t1rx1(:,n)=transpose(F2n_r(1,1,n,k1*r,theta,phi)); % m=1
    F2t1rx2(:,n)=transpose(F2n_r(1,-1,n,k1*r,theta,phi)); % m=-1
  end
% x-orientation

% scattered fields
F1s3px1=F1i3px1;
F1s3thx1=F1i3thx1;
F1s3px2=F1i3px2;
F1s3thx2=F1i3thx2;

F2s3px1=F2i3px1;
F2s3thx1=F2i3thx1;
F2s3rx1=F2i3rx1;
F2s3px2=F2i3px2;
F2s3thx2=F2i3thx2;
F2s3rx2=F2i3rx2;

F1s3px1(r<=a,:)=0;
F1s3thx1(r<=a,:)=0;
F1s3px2(r<=a,:)=0;
F1s3thx2(r<=a,:)=0;

F2s3px1(r<=a,:)=0;
F2s3thx1(r<=a,:)=0;
F2s3rx1(r<=a,:)=0;
F2s3px2(r<=a,:)=0;
F2s3thx2(r<=a,:)=0;
F2s3rx2(r<=a,:)=0;

% incident fields
F1i1px1(r>r0,:)=0;
F1i1thx1(r>r0,:)=0;
F1i1px2(r>r0,:)=0;
F1i1thx2(r>r0,:)=0;

F1i1px1(r<=a,:)=0;
```

```
F1i1thx1(r<=a,:)=0;
F1i1px2(r<=a,:)=0;
F1i1thx2(r<=a,:)=0;

F1i3px1(r<=r0,:)=0;
F1i3thx1(r<=r0,:)=0;
F1i3px2(r<=r0,:)=0;
F1i3thx2(r<=r0,:)=0;

F2i1px1(r>r0,:)=0;
F2i1thx1(r>r0,:)=0;
F2i1rx1(r>r0,:)=0;
F2i1px2(r>r0,:)=0;
F2i1thx2(r>r0,:)=0;
F2i1rx2(r>r0,:)=0;

F2i1px1(r<=a,:)=0;
F2i1thx1(r<=a,:)=0;
F2i1rx1(r<=a,:)=0;
F2i1px2(r<=a,:)=0;
F2i1thx2(r<=a,:)=0;
F2i1rx2(r<=a,:)=0;

F2i3px1(r<=r0,:)=0;
F2i3thx1(r<=r0,:)=0;
F2i3rx1(r<=r0,:)=0;
F2i3px2(r<=r0,:)=0;
F2i3thx2(r<=r0,:)=0;
F2i3rx2(r<=r0,:)=0;

% total field
F1t1px1(r>a,:)=0;
F1t1thx1(r>a,:)=0;
F1t1px2(r>a,:)=0;
F1t1thx2(r>a,:)=0;

F2t1px1(r>a,:)=0;
F2t1thx1(r>a,:)=0;
F2t1rx1(r>a,:)=0;
F2t1px2(r>a,:)=0;
F2t1thx2(r>a,:)=0;
F2t1rx2(r>a,:)=0;

% incident fields
Eipx=k0./sqrt(n0).*((F1i1px1-F1i1px2)*Q11i1+(F1i3px1-F1i3px2)*Q11i3...
    +(F2i1px1+F2i1px2)*Q21i1+(F2i3px1+F2i3px2)*Q21i3);
Eithx=k0./sqrt(n0).*((F1i1thx1-F1i1thx2)*Q11i1+(F1i3thx1-
F1i3thx2)*Q11i3...
    +(F2i1thx1+F2i1thx2)*Q21i1+(F2i3thx1+F2i3thx2)*Q21i3);
Eirx=k0./sqrt(n0).*((F2i1rx1+F2i1rx2)*Q21i1+(F2i3rx1+F2i3rx2)*Q21i3);
Hipx=-j*k0.*sqrt(n0).*((F2i1px1-F2i1px2)*Q11i1+(F2i3px1-
F2i3px2)*Q11i3...
    +(F1i1px1+F1i1px2)*Q21i1+(F1i3px1+F1i3px2)*Q21i3);
Hithx=-j*k0.*sqrt(n0).*((F2i1thx1-F2i1thx2)*Q11i1+(F2i3thx1-
F2i3thx2)*Q11i3...
```

```
    +(F1i1thx1+F1i1thx2)*Q21i1+(F1i3thx1+F1i3thx2)*Q21i3);
Hirx=-j*k0.*sqrt(n0).*((F2i1rx1-F2i1rx2)*Q11i1+(F2i3rx1-
F2i3rx2)*Q11i3);

% scattered fields
Espx=k0./sqrt(n0).*((F1s3px1-F1s3px2)*Q11s3...
    +(F2s3px1+F2s3px2)*Q21s3);
Esthx=k0./sqrt(n0).*((F1s3thx1-F1s3thx2)*Q11s3...
    +(F2s3thx1+F2s3thx2)*Q21s3);
Esrx=k0./sqrt(n0).*((F2s3rx1+F2s3rx2)*Q21s3);
Hspx=-j*k0.*sqrt(n0).*((F2s3px1-F2s3px2)*Q11s3...
    +(F1s3px1+F1s3px2)*Q21s3);
Hsthx=-j*k0.*sqrt(n0).*((F2s3thx1-F2s3thx2)*Q11s3...
    +(F1s3thx1+F1s3thx2)*Q21s3);
Hsrx=-j*k0.*sqrt(n0).*((F2s3rx1-F2s3rx2)*Q11s3);

% total fields
Etpx=k1./sqrt(n1).*((F1t1px1-F1t1px2)*Q11t1...
    +(F2t1px1+F2t1px2)*Q21t1);
Etthx=k1./sqrt(n1).*((F1t1thx1-F1t1thx2)*Q11t1...
    +(F2t1thx1+F2t1thx2)*Q21t1);
Etrx=k1./sqrt(n1).*((F2t1rx1+F2t1rx2)*Q21t1);
Htpx=-j*k1.*sqrt(n1).*((F2t1px1-F2t1px2)*Q11t1...
    +(F1t1px1+F1t1px2)*Q21t1);
Htthx=-j.*k1.*sqrt(n1).*((F2t1thx1-F2t1thx2)*Q11t1...
    +(F1t1thx1+F1t1thx2)*Q21t1);
Htrx=-j*k1.*sqrt(n1).*((F2t1rx1-F2t1rx2)*Q11t1);



%-------------------------------------------------------------------------
----
% The analytical equation of x-oriented magnetic dipole:
%  These equations are varified and they show similarity between them
and
%  the SVWE which are the correct behavior as we expect.
%  The equations of the closed-form and the SVWE are varified in the
%  m-file "ValidationOf_x_Scattering.m"

r0=-r0;
R=sqrt(r.^2+r0^2-2*r.*r0.*cos(theta));
E_rx=-exp(-
j*k0.*R)./(4*pi*R).*sin(theta).*sin(phi).*r0.*(1+j*k0.*R)./(R.^2);
E_thx=exp(-j*k0.*R)./(4*pi*R).*sin(phi).*(r-
r0.*cos(theta)).*(1+j*k0.*R)./(R.^2);
E_px=exp(-j*k0.*R)./(4*pi*R).*cos(phi).*(r.*cos(theta)-
r0).*(1+j*k0.*R)./(R.^2);
H_rx=-j*w.*e0.*exp(-j*k0.*R)./(4*pi*R).*sin(theta).*cos(phi).*...
    (1-(1+j*k0.*R)./((k0.*R).^2)+...
    r.*(r-r0.*cos(theta)).*((-j*k0.*R).^2+3*j*k0.*R+3)./(k0.^2.*R.^4));
H_thx=-j*w.*e0.*exp(-j*k0.*R)./(4*pi*R).*cos(theta).*cos(phi).*...
    (1-(1+j*k0.*R)./((k0.*R).^2)+...
    r.*r0.*(sin(theta)).^2.*((-
j*k0.*R).^2+3*j*k0.*R+3)./(k0.^2.*R.^4.*cos(theta)));
H_px=j*w.*e0.*exp(-j*k0.*R)./(4*pi*R).*sin(phi).*(1-
(1+j*k0.*R)./(k0.^2.*R.^2));
```

```
E_rx=conj(E_rx);
E_thx=conj(E_thx);
E_px=conj(E_px);
H_rx=conj(H_rx);
H_thx=conj(H_thx);
H_px=conj(H_px);
%-------------------------------------------------------------------------
----

% Calculating the fields
Epx=Eipx+Espx+Etpx;
Ethx=Eithx+Esthx+Etthx;
Erx=Eirx+Esrx+Etrx;
Hpx=Hipx+Hspx+Htpx;
Hthx=Hithx+Hsthx+Htthx;
Hrx=Hirx+Hsrx+Htrx;

% Reform the fields from the colum matrix to (NxN) matrix form
E_px=reshape(E_px,N,N);
E_thx=reshape(E_thx,N,N);
E_rx=reshape(E_rx,N,N);
H_px=reshape(H_px,N,N);
H_thx=reshape(H_thx,N,N);
H_rx=reshape(H_rx,N,N);

Epx=reshape(Epx,N,N);
Ethx=reshape(Ethx,N,N);
Erx=reshape(Erx,N,N);
Hpx=reshape(Hpx,N,N);
Hthx=reshape(Hthx,N,N);
Hrx=reshape(Hrx,N,N);


r=reshape(r,N,N);
theta=reshape(theta,N,N);
phi=reshape(phi,N,N);

% Convert from sphrical to cartisian components
Hmagx=sqrt((real(Hrx)).^2+(real(Hthx)).^2+(real(Hpx)).^2);
Hxx=Hrx.*sin(theta).*cos(phi)+Hthx.*cos(theta).*cos(phi)-Hpx.*sin(phi);
Hyx=Hrx.*sin(theta).*sin(phi)+Hthx.*cos(theta).*sin(phi)+Hpx.*cos(phi);
Hzx=Hrx.*cos(theta)-Hthx.*sin(theta);
Emagx=sqrt((real(Erx)).^2+(real(Ethx)).^2+(real(Epx)).^2);
Exx=Erx.*sin(theta).*cos(phi)+Ethx.*cos(theta).*cos(phi)-Epx.*sin(phi);
Eyx=Erx.*sin(theta).*sin(phi)+Ethx.*cos(theta).*sin(phi)+Epx.*cos(phi);
Ezx=Erx.*cos(theta)-Ethx.*sin(theta);
Eabs=sqrt((abs(Erx)).^2+(abs(Ethx)).^2+(abs(Epx)).^2);
Habs=sqrt((abs(Hrx)).^2+(abs(Hthx)).^2+(abs(Hpx)).^2);

H_magx=sqrt((real(H_rx)).^2+(real(H_thx)).^2+(real(H_px)).^2);
H_xx=H_rx.*sin(theta).*cos(phi)+H_thx.*cos(theta).*cos(phi)-
H_px.*sin(phi);
H_zx=H_rx.*cos(theta)-H_thx.*sin(theta);
E_magx=sqrt((real(E_rx)).^2+(real(E_thx)).^2+(real(E_px)).^2);
```

```
E_xx=E_rx.*sin(theta).*cos(phi)+E_thx.*cos(theta).*cos(phi)-
E_px.*sin(phi);
E_zx=E_rx.*cos(theta)-E_thx.*sin(theta);


% Poynting vector S (radiating power)
Sxx=1/2*real(Eyx.*conj(Hzx)-Ezx.*conj(Hyx));
Syx=1/2*real(Ezx.*conj(Hxx)-Exx.*conj(Hzx));
Szx=1/2*real(Exx.*conj(Hyx)-Eyx.*conj(Hxx));
Smagx=sqrt((real(Sxx)).^2+(real(Syx)).^2+(real(Szx)).^2);



m=3;
figure(1)
axes('fontsize',18)
pcolor(X,Z,20*log10(Hmagx/max(max(Hmagx))))
shading interp
colorbar('fontsize',18)
hold on
h=quiver(X(1:m:N,1:m:N),Z(1:m:N,1:m:N),...
    real(Hxx(1:m:N,1:m:N))./Hmagx(1:m:N,1:m:N),...
    real(Hzx(1:m:N,1:m:N))./Hmagx(1:m:N,1:m:N));
set(h,'color','k')
xlabel('x [m]')
ylabel('z [m]')
title('H^x [dB]')
axis([x(1) x(N) z(1) z(N)]);
hold off
x1=linspace(0,2*pi);hold on; plot(a*sin(x1),a*cos(x1),'k--
','linewidth',2);hold off;
axis('equal')


figure(2)
axes('fontsize',18)
pcolor(X,Z,20*log10(Emagx/max(max(Emagx))))
shading interp
colorbar('fontsize',18)
hold on
h=quiver(X(1:m:N,1:m:N),Z(1:m:N,1:m:N),...
    real(Exx(1:m:N,1:m:N))./Emagx(1:m:N,1:m:N),...
    real(Ezx(1:m:N,1:m:N))./Emagx(1:m:N,1:m:N));
set(h,'color','k')
xlabel('x [m]')
ylabel('z [m]')
title('E^x [dB]')
axis([x(1) x(N) z(1) z(N)]);
hold off
x1=linspace(0,2*pi);hold on; plot(a*sin(x1),a*cos(x1),'k--
','linewidth',2);hold off;
axis('equal')


figure(3)
```

```
axes('fontsize',18)
pcolor(X,Z,10*log10(Smagx/max(max(Smagx))))
shading interp
colorbar('fontsize',18)
hold on
h=quiver(X(1:m:N,1:m:N),Z(1:m:N,1:m:N),...
    real(Sxx(1:m:N,1:m:N))./Smagx(1:m:N,1:m:N),...
    real(Szx(1:m:N,1:m:N))./Smagx(1:m:N,1:m:N));
set(h,'color','k')
xlabel('x [m]')
ylabel('z [m]')
title('S^x [W/m^2]')
axis([x(1) x(N) z(1) z(N)]);
hold off
x1=linspace(0,2*pi);hold on; plot(a*sin(x1),a*cos(x1),'k--
','linewidth',2);hold off;
axis('equal')
```

Script 13

This script calculates and plots electric and the magnetic fields for a *z*-oriented electric hertzian dipole EHDz in free space after translation and rotation of the antenna. This script uses spherical wave functions that are programmed in scripts 14 to 16.

```
%%%%%%%%%%%%%%%%%%%%%%%%%%%%%%%%%%%%%%%%%%%%%%%%%%%%%%%%%%%%%%%%%%%%%%%%
%  Input:                                                                   %
%       a    : the radius of the sphere.                                   %
%       r0   : the position distance of the transmitting antenna.          %
%       f0   : the operating frequency.                                    %
%       N1   : the number of modes.                                        %
%       N    : number of points that are used to calculate the fields on.  %
%       x    : the limit of the region where the fields are calculated on the x-axis.  %
%       z    : the limit of the region where the fields are calculated on the z-axis.  %
%       theta: the rotation angle (radian).                                %
%                                                                          %
% Output:                                                                  %
%       Electric field, magnetic field and power density.                  %
%%%%%%%%%%%%%%%%%%%%%%%%%%%%%%%%%%%%%%%%%%%%%%%%%%%%%%%%%%%%%%%%%%%%%%%%
```

```
% The parameters of the system
clear all
e0=8.854e-12; % permittivity of the free-space.  [F/m]
u0=4*pi*1e-7; % permeability of the free-space.  [H/m]
n0=1/376.7;     % impedance of the free-space.  [Ohom]
c=2.998e8;    % velocity of light in free-space. [m/s]
r0=10e-2;      % location of the dipole. [m]
a=.07;       % radius of the sphere
f0=1e9;       % operating frequency. [Hz]
w=2*pi*f0;    % angular frequency.   [radian/s]
k0=w/c;       % wave length in free-space. [1/m]
er=1;        % relative permittivity of the sphere
ur=1;         % relative permeability of the sphere
n1=n0*sqrt(er./ur); % the impedance of the sphere [Ohom]
k1=k0.*sqrt(ur.*er); % the wave number inside the sphere
theta1=45*pi/180; % the rotation angle
chi1=0*pi/180; % the rotation angle
phi1=0*pi/180; % the rotation angle
N1=15; % number of the modes
J=2*N1*(N1+2); % number of the total modes

N=80; % number of the points
x=linspace(-.25,.25,N);
z=linspace(-.25,.25,N);
[X,Z]=meshgrid(x,z);
Y=0*ones(N);
[phi,theta,r]=cart2sph(X,Y,Z);
theta=pi/2-theta;

r=reshape(r,1,N*N);
theta=reshape(theta,1,N*N);
phi=reshape(phi,1,N*N);
```

```
F1ip=zeros(N*N,J);
F3ip=zeros(N*N,J);
F1ith=zeros(N*N,J);
F3ith=zeros(N*N,J);
F1ir=zeros(N*N,J);
F3ir=zeros(N*N,J);
Q1=zeros(J,1);
Q1m=zeros(J,1); % for the magnetic fields
Q3=zeros(J,1);
Q3m=zeros(J,1); % for the magnetic fields
Q201=-1/sqrt(6*pi)*k0/sqrt(n0);
% Calculating the coefficients

for sigma=1:2
    s2=3-sigma;
    s=2;
    for n=1:N1
        d_a2=rotationCoef(n,0,theta1);    % rotationCoef(n,m,theta)
        d_a2=flipud(d_a2); % to start from -n:n
        C1=translationCoef(3,2,sigma,1,0,n,k0.*r0);% translation
coefficient
        C3=translationCoef(1,2,sigma,1,0,n,k0.*r0);%
translationCoef(c,s,sigma,n,mu,nu,kA)
        for m=1:2*n+1 % because of the rotation
            m1=m-n-1;%  to insure that  m=-n:n
            j1=2*(n*(n+1)+m1-1)+sigma; % the index for the electric
fields
            j2=2*(n*(n+1)+m1-1)+s2; % the index for the magnetic fields
            Q1(j1,1)=d_a2(m)*C1; % is used because we just need s=2
            Q3(j1,1)=d_a2(m)*C3; % is used because we just need s=2
            Q1m(j2,1)=Q1(j1,1); % for the magnetic fields
            Q3m(j2,1)=Q3(j1,1); % for the magnetic fields
        end
    end
end

% calculating the modes
for n=1:N1
    for m=1:2*n+1 % because of the rotation
        for s=1:2
            m1=m-n-1;%  to insure that  m=-n:n
            j1=2*(n*(n+1)+m1-1)+s; % the index for the electric fields
            % z-orientation
            F1ir(:,j1)=transpose(F_r(s,1,m1,n,k0.*r,theta,phi));
            F3ir(:,j1)=transpose(F_r(s,3,m1,n,k0.*r,theta,phi));
            F1ith(:,j1)=transpose(F_theta(s,1,m1,n,k0.*r,theta,phi));
            F3ith(:,j1)=transpose(F_theta(s,3,m1,n,k0.*r,theta,phi));
            F1ip(:,j1)=transpose(F_phi(s,1,m1,n,k0.*r,theta,phi));
            F3ip(:,j1)=transpose(F_phi(s,3,m1,n,k0.*r,theta,phi));
        end
    end
end

% z-orientation
F1ir(r>r0,:)=0;
```

```
F1ith(r>r0,:)=0;
F1ip(r>r0,:)=0;
F3ir(r<=r0,:)=0;
F3ith(r<=r0,:)=0;
F3ip(r<=r0,:)=0;

Hpz=-j*k0.*sqrt(n0).*Q201.*(F1ip*Q1m+F3ip*Q3m);
Erz=k0./sqrt(n0).*Q201.*(F1ir*Q1+F3ir*Q3);
Ethz=k0./sqrt(n0).*Q201.*(F1ith*Q1+F3ith*Q3);


%-------------------------------------------------------------------------
% The analytical equation of z-oriented magnetic dipole:
%  These equations are varified and they show similarity between them
and
%  the SVWE which are the correct behavior as we expect.

r0=-r0;
R=sqrt(r.^2+r0^2-2*r.*r0.*cos(theta));
H_pz=exp(-j*k0.*R)./(4*pi*R).*sin(theta).*r.*(1+j*k0.*R)./(R.^2);
E_rz=-1./(j*w.*e0).*exp(-j*k0.*R)./(4*pi*R).*(-
2*cos(theta).*(1+j*k0.*R)./(R.^2)+...
    r.*r0.*(sin(theta)).^2.*((j*k0.*R).^2+3*j*k0.*R+3)./(R.^4));
E_thz=1./(j*w.*e0).*exp(-j*k0.*R)./(4*pi*R).*sin(theta).*...
    (-2*(1+j*k0.*R)./(R.^2)+...
    r.*(r-r0.*cos(theta)).*((j*k0.*R).^2+3*j*k0.*R+3)./(R.^4));

H_pz=conj(H_pz);
E_rz=conj(E_rz);
E_thz=conj(E_thz);
%-------------------------------------------------------------------------
----


% Reform the fields from the colum matrix to (NxN) matrix form
H_pz=reshape(H_pz,N,N);
E_thz=reshape(E_thz,N,N);
E_rz=reshape(E_rz,N,N);

Hpz=reshape(Hpz,N,N);
Ethz=reshape(Ethz,N,N);
Erz=reshape(Erz,N,N);


r=reshape(r,N,N);
theta=reshape(theta,N,N);
phi=reshape(phi,N,N);

% Convert from sphrical to cartisian components
Emagz=sqrt((real(Erz)).^2+(real(Ethz)).^2);
Exz=Erz.*sin(theta).*cos(phi)+Ethz.*cos(theta).*cos(phi);
Eyz=Erz.*sin(theta).*sin(phi)+Ethz.*cos(theta).*sin(phi);
Ezz=Erz.*cos(theta)-Ethz.*sin(theta);
Hmagz=sqrt((real(Hpz)).^2);
Hxz=-Hpz.*sin(phi);
```

```
Hyz=Hpz.*cos(phi);
Hzz=zeros(N);


E_magz=sqrt((real(E_rz)).^2+(real(E_thz)).^2);
E_xz=E_rz.*sin(theta).*cos(phi)+E_thz.*cos(theta).*cos(phi);
E_yz=E_rz.*sin(theta).*sin(phi)+E_thz.*cos(theta).*sin(phi);
E_zz=E_rz.*cos(theta)-E_thz.*sin(theta);
H_magz=sqrt((real(H_pz)).^2);
H_xz=-H_pz.*sin(phi);
H_yz=H_pz.*cos(phi);
H_zz=zeros(N);


m=5;
figure(1)
pcolor(X,Z,Emagz)
shading interp
colorbar
hold on
h=quiver(X(1:m:N,1:m:N),Z(1:m:N,1:m:N),...
    real(Exz(1:m:N,1:m:N))./Emagz(1:m:N,1:m:N),...
    real(Ezz(1:m:N,1:m:N))./Emagz(1:m:N,1:m:N));
set(h,'color','k')
xlabel('x [m]')
ylabel('z [m]')
title('E^z svwe method [V/m]')
axis([x(1) x(N) z(1) z(N)]);
hold off


figure(2)
pcolor(X,Z,E_magz)
shading interp
colorbar
hold on
h=quiver(X(1:m:N,1:m:N),Z(1:m:N,1:m:N),...
    real(E_xz(1:m:N,1:m:N))./E_magz(1:m:N,1:m:N),...
    real(E_zz(1:m:N,1:m:N))./E_magz(1:m:N,1:m:N));
set(h,'color','k')
xlabel('x [m]')
ylabel('z [m]')
title('E^z closed-form [V/m]')
axis([x(1) x(N) z(1) z(N)]);
hold off


figure(3)
pcolor(X,Z,Hmagz)
shading interp
colorbar
hold on
h=quiver(X(1:m:N,1:m:N),Z(1:m:N,1:m:N),...
    real(Hxz(1:m:N,1:m:N))./Hmagz(1:m:N,1:m:N),...
    real(Hzz(1:m:N,1:m:N))./Hmagz(1:m:N,1:m:N));
```

```
set(h,'color','k')
xlabel('x [m]')
ylabel('z [m]')
title('H^z svwe method [A/m]')
axis([x(1) x(N) z(1) z(N)]);
hold off

figure(4)
pcolor(X,Z,H_magz)
shading interp
colorbar
hold on
h=quiver(X(1:m:N,1:m:N),Z(1:m:N,1:m:N),...
    real(H_xz(1:m:N,1:m:N))./H_magz(1:m:N,1:m:N),...
    real(H_zz(1:m:N,1:m:N))./H_magz(1:m:N,1:m:N));
set(h,'color','k')
xlabel('x [m]')
ylabel('z [m]')
title('H^z [A/m]')
axis([x(1) x(N) z(1) z(N)]);
hold off
```

Script 14

```
%%%%%%%%%%%%%%%%%%%%%%%%%%%%%%%%%%%%%%%%%%%%%%%%
%  Input:                                                                    %
%        s    : the type of wave, it takes 1 or 2.                           %
%        c    : takes values 1 to 4 to describe the type of the wave.        %
%        n    : the mode number which is different from zero.                %
%        m    : the mode number which is |m| ≤ n .                           %
%        kr   : the product of wave-number and the radial distance.          %
%        theta: the position angle (radian).                                 %
%        phi  : the position angle (radian).                                 %
%                                                                            %
% Output:                                                                    %
%        Fn  :This is the radial component of the spherical wave function.   %
%%%%%%%%%%%%%%%%%%%%%%%%%%%%%%%%%%%%%%%%%%%%%%%%

function Fn=F_r(s,c,m,n,kr,theta,phi)

if(s==2)
    Fn=F2n_r(c,m,n,kr,theta,phi);
end
if(s==1)
    N1=max(length(kr),length(theta));
    N2=max(N1,length(phi));

    Fn=zeros(1,N2);
end


function F2n=F2n_r(c,m,n,kr,theta,phi)

F2n = mFun(m)*1/sqrt(2*pi)*sqrt(1/(n*(n+1)))*NormLegCoef(n,m)*...

n*(n+1)./kr.*sbessel(c,n,kr).*legendre_(n,m,cos(theta)).*exp(j*m*phi);

function mm=mFun(m)
if(m==0)
    mm=1;
else
    mm=(-m/abs(m))^(m);
end

function zn=sbessel(c,n,kr)
if(c==1)
    zn=sqrt(pi./(2.*kr)).*besselj(n+.5,kr);
end
if(c==2)
    zn=sqrt(pi./(2.*kr)).*bessely(n+.5,kr);
end
if(c==3)
    zn=sqrt(pi./(2.*kr)).*besselh(n+.5,1,kr);
```

```
end
if(c==4)
    zn=sqrt(pi./(2.*kr)).*besselh(n+.5,2,kr);
end

function P=legendre_(n,m,x)
n=abs(n);
m=abs(m);
if(n>=abs(m))
P=(-1)^m*legendre(n,x);
P=P(m+1,:);
else
    P=zeros(size(x));
end

function nL=NormLegCoef(n,m)
m=abs(m);
nL=sqrt((2*n+1)/2*factorial(n-m)/factorial(n+m));
```

Script 15

```
%%%%%%%%%%%%%%%%%%%%%%%%%%%%%%%%%%%%%%%%%%%%%%%%
%  Input:                                                                        %
%       s     : the type of wave, it takes 1 or 2.                               %
%       c     : takes values 1 to 4 to describe the type of the wave.            %
%       n     : the mode number which is different from zero.                    %
%       m     : the mode number which is |m| ≤ n .                               %
%       kr    : the product of wave-number and the radial distance.              %
%       theta: the position angle (radian).                                      %
%       phi   : the position angle (radian).                                     %
%                                                                                %
% Output:                                                                        %
%       Fn  :This is the theta component of the spherical wave function.         %
%%%%%%%%%%%%%%%%%%%%%%%%%%%%%%%%%%%%%%%%%%%%%%%%

function Fn=F_theta(s,c,m,n,kr,theta,phi)

if(s==1)
    Fn=F1n_theta(c,m,n,kr,theta,phi);
end
if(s==2)
    Fn=F2n_theta(c,m,n,kr,theta,phi);
end

function F1n=F1n_theta(c,m,n,kr,theta,phi)

F1n = mFun(m)*1/sqrt(2*pi)*sqrt(1/(n*(n+1)))*NormLegCoef(n,m)*...

sbessel(c,n,kr).*j.*m.*legendre_(n,m,cos(theta))./sin(theta).*exp(j*m*p
hi);

function F2n=F2n_theta(c,m,n,kr,theta,phi)

F2n = mFun(m)*1/sqrt(2*pi)*sqrt(1/(n*(n+1)))*NormLegCoef(n,m)*...
    (sbessel(c,n,kr)./kr + dbessel(c,n,kr)).*...
    dlegendre(n,m,cos(theta)).*exp(j*m*phi);

function mm=mFun(m)
if(m==0)
    mm=1;
else
    mm=(-m/abs(m))^(m);
end

function zn=sbessel(c,n,kr)
if(c==1)
    zn=sqrt(pi./(2.*kr)).*besselj(n+.5,kr);
end
if(c==2)
    zn=sqrt(pi./(2.*kr)).*bessely(n+.5,kr);
```

```
end
if(c==3)
    zn=sqrt(pi./(2.*kr)).*besselh(n+.5,1,kr);
end
if(c==4)
    zn=sqrt(pi./(2.*kr)).*besselh(n+.5,2,kr);
end

function P=legendre_(n,m,x)
n=abs(n);
m=abs(m);
if(n>=abs(m))
P=(-1)^m*legendre(n,x);
P=P(m+1,:);
else
    P=zeros(size(x));
end

function db=dbessel(c,n,kr)
db = (n)./kr.*sbessel(c,n,kr) - sbessel(c,n+1,kr);

function dP=dlegendre(n,m,x)
n=abs(n);
m=abs(m);
if(m==0)
    dP=-legendre_(n,1,x);
else
    dP=1/2*((n-m+1)*(n+m)*legendre_(n,m-1,x)-legendre_(n,m+1,x));
end

function nL=NormLegCoef(n,m)
m=abs(m);
nL=sqrt((2*n+1)/2*factorial(n-m)/factorial(n+m));
```

Script 16

```
%%%%%%%%%%%%%%%%%%%%%%%%%%%%%%%%%%%%%%%%%%%%%%%
%  Input:                                                                   %
%       s    : the type of wave, it takes 1 or 2.                           %
%       c    : takes values 1 to 4 to describe the type of the wave.        %
%       n    : the mode number which is different from zero.                %
%       m    : the mode number which is |m| ≤ n .                           %
%       kr   : the product of wave-number and the radial distance.          %
%       theta: the position angle (radian).                                 %
%       phi  : the position angle (radian).                                 %
%                                                                           %
% Output:                                                                   %
%       Fn  :This is the phi component of the spherical wave function.      %
%%%%%%%%%%%%%%%%%%%%%%%%%%%%%%%%%%%%%%%%%%%%%%%

function Fn=F_phi(s,c,m,n,kr,theta,phi)

if(s==1)
    Fn=F1n_phi(c,m,n,kr,theta,phi);
end
if(s==2)
    Fn=F2n_phi(c,m,n,kr,theta,phi);
end


function F1n=F1n_phi(c,m,n,kr,theta,phi)

F1n = -mFun(m)*1/sqrt(2*pi)*sqrt(1/(n*(n+1)))*NormLegCoef(n,m)*...
    sbessel(c,n,kr).*dlegendre(n,m,cos(theta)).*exp(j*m*phi);

function F2n=F2n_phi(c,m,n,kr,theta,phi)

F2n = mFun(m)*1/sqrt(2*pi)*sqrt(1/(n*(n+1)))*NormLegCoef(n,m)*...
    (sbessel(c,n,kr)./kr + dbessel(c,n,kr)).*...
    j.*m.*legendre_(n,1,cos(theta))./sin(theta).*exp(j*m*phi);

function mm=mFun(m)
if(m==0)
    mm=1;
else
    mm=(-m/abs(m))^(m);
end

function zn=sbessel(c,n,kr)
if(c==1)
    zn=sqrt(pi./(2.*kr)).*besselj(n+.5,kr);
end
if(c==2)
    zn=sqrt(pi./(2.*kr)).*bessely(n+.5,kr);
end
```

```
if(c==3)
    zn=sqrt(pi./(2.*kr)).*besselh(n+.5,1,kr);
end
if(c==4)
    zn=sqrt(pi./(2.*kr)).*besselh(n+.5,2,kr);
end

function P=legendre_(n,m,x)
n=abs(n);
m=abs(m);
if(n>=abs(m))
P=(-1)^m*legendre(n,x);
P=P(m+1,:);
else
    P=zeros(size(x));
end

function dP=dlegendre(n,m,x)
n=abs(n);
m=abs(m);
if(m==0)
    dP=-legendre_(n,1,x);
else
    dP=1/2*((n-m+1)*(n+m)*legendre_(n,m-1,x)-legendre_(n,m+1,x));
end

function db=dbessel(c,n,kr)
db = (n)./kr.*sbessel(c,n,kr) - sbessel(c,n+1,kr);

function nL=NormLegCoef(n,m)
m=abs(m);
nL=sqrt((2*n+1)/2*factorial(n-m)/factorial(n+m));
```

Paper [1]

Investigation of Bandwidth, Efficiency, and Quality Factor for Circular Patch Antennas with Magneto-Dielectric Substrate

Baqer Nour[1] Olav Breinbjerg[2]

Abstract – **This article documents an investigation of the effect of a magneto-dielectric substrate on the performance of a circular patch antenna; in particular, the radiation efficiency, the quality factor, and the bandwidth. Both analytical and numerical methods have been used to model the patch antenna. The numerical method is used for lossy substrates, while the analytical method is used for lossless substrates.**

1 Introduction

Wireless communication becomes pervasive in daily life and there are demands to miniaturize devices which make small antenna important. A small antenna in general has narrow bandwidth, low efficiency, and it needs a matching circuit which adds extra losses to the antenna [1]. Patch antennas have the advantage of low profile and their ability to be integrated within the wireless device.

Antennas with a magneto-dielectric substrate have been investigated and the focus was on the bandwidth and the size [2]-[4]. A magneto-dielectric substrate can offer high refractive index $n = \sqrt{\mu_r \varepsilon_r}$ and intrinsic impedance $\eta = \eta_0 \sqrt{\mu_r / \varepsilon_r}$ close to the free-space impedance η_0 for $\mu_r \cong \varepsilon_r$ [2]-[4].

The present work is based on analytical and numerical models to study the effect of a magneto-dielectric substrate on the performances of a circular patch antenna. The analytical model treats the patch antenna as a cavity that is loaded with the magneto-dielectric substrate. The electric field of the cavity will be used to calculate an equivalent surface magnetic current which is used to determine the radiation fields. The magnetic field of the cavity will be used to find the losses in the patch antenna conductors that have finite conductivity. The cavity is modelled as a parallel resonator. Fig. 1 shows the structure of the patch antenna and its equivalent circuit. The analytical method can not handle a high-loss substrate, but it gives good results for a lossless substrate. For lossy substrates the commercial simulation program HFSS [5] was used to calculate the bandwidth and the efficiency. The analytical model provides a good understanding of the physics that affect the performances and it is much faster than the numerical model. The antenna is circular with radius a and height h. The patch lays on a substrate that has relative permittivity ε_r and relative permeability μ_r. The antenna is fed by a coaxial cable at a distance r_0 from the centre of the patch. The side wall of the antenna is modelled as a perfect magnetic conductor (PMC) while the top and the ground planes are modelled as perfect electric conductors (PEC). The loss in the conductors is represented by the ohmic loss in a layer with thickness equals to the skin depth. Losses that correspond to the radiation, ohmic losses, and the losses inside the magneto-dielectric substrate are represented by conductances G_{rad}, G_{c}, and G_{md}, respectively. V_{nm} is the voltage of the source for cavity mode (n, m). Explicit expressions for the equivalent circuit components exist but are not included here.

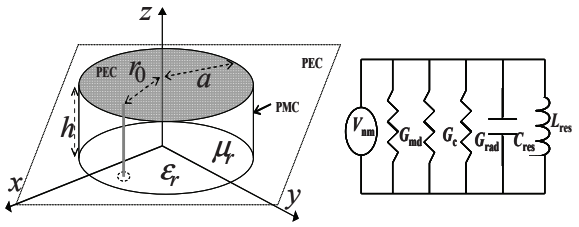

Fig.1: The patch antenna on infinite ground plane and its equivalent circuit.

2 Efficiency of the antenna

The efficiency of the antenna e_{rad} is the ratio of the radiation conductance G_{rad} to the total conductance $G_{\text{rad}} + G_{\text{c}} + G_{\text{md}}$ of the antenna. Fig. 2 shows the radiation efficiency of the patch antenna for modes (1,1) and (2,1) which are the 1st and 2nd mode. The conductors are taken to be copper and the substrate is assumed to be lossless. The horizontal axis is the relative permeability μ_r and the vertical axis is the relative permittivity ε_r of the substrate.

Department of Electrical Engineering, Electromagnetic Systems, Technical University of Denmark, Ørsteds Plads, building 348, DK-2800 Kgs. Lyngby, Denmark,
[1] e-mail: bn@elektro.dtu.dk, tel.: +45 4525 3815.
[2] e-mail: ob@elektro.dtu.dk, tel.: +45 4525 3814.

978-1-61284-978-2/11/$26.00 ©2011

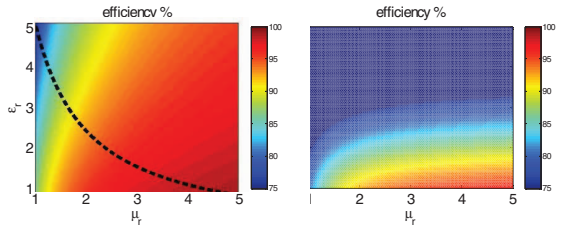

Fig. 2: The efficiency of the modes (1,1) and (2,1).

The operating frequency and the height h of the antenna are kept constant, while the radius a varies according to the resonance condition for the (n, m) mode:

$$a = \frac{\chi_{nm}}{k_0 \sqrt{\mu_r \varepsilon_r}} \tag{1}$$

where k_0 is the wave number of the free-space and χ_{nm} is either $\chi_{11} = 1.841$ or $\chi_{21} = 3.054$ [6, pp. 205]. The behaviour of the efficiency depends on the loading materials. An increase of the permittivity ε_r leads to a decrease of the efficiency, whereas the efficiency increases as the permeability μ_r increases. This increase depends on the value of the permittivity ε_r. The efficiency of mode (2,1) saturates at a certain ε_r which is almost independent of the permeability μ_r increase. This phenomenon appears also for mode (1,1), but outside the range of the plot in Fig. 2.

The ohmic and radiation conductances are the only losses that affect the efficiency since we assumed the substrate is lossless. The increase in efficiency is related to either an increase of the radiation conductance or/and a decrease in the ohmic conductivity. The dashed line in Fig. 2 represents antennas that have constant radius. Since the radiation conductance is constant for a constant radius, thus the only change appears for the ohmic conductance which decreases as the μ_r increases. Filling the antenna with a magnetic material decreases the magnetic field and hence the surface current on the conducting parts and that leads to an increase of the radiation efficiency of the antenna.

3 Quality factor of the antenna

Most of the reactive energy of the patch antenna is assumed to be stored inside the substrate since $h << a$. So the total stored energy equals the stored energy inside the substrate.
At resonance the magnetic energy W_m equals the electric energy W_e, so the total energy equals $2W_e$. The quality factor of the antenna Q_t can thus be calculated as:

$$Q_t = \frac{2\omega W_e}{P_{rad} + P_c + P_{md}} \tag{2}$$

where P_{rad}, P_c and P_{md} are the radiated power, the ohmic power dissipated in the conductors, and the power dissipated in the substrate, respectively. The quality factor will be normalized to the Chu lower bound, which is given in [7]:

$$Q_{Chu} = \frac{1}{(k_0 a)^3} + \frac{1}{k_0 a} \tag{3}$$

Fig. 3 shows the normalized Q_t for modes (1,1) and (2,1). The minimum Q_t of the mode (1,1) is $7.45Q_{Chu}$ and that for $\mu_r = \varepsilon_r = 5$. This quality factor is not close to the Chu lower bound, because the patch antenna fills only a small part of the sphere that surrounds the antenna. The Chu lower bound increases as the size of the antenna decreases. The same behaviour is expected when the antenna is loaded with a magneto-dielectric material, where the quality factor of the antenna increases. But the normalized quality factor decreases as the size decreases. This indicates that the increase of the quality factor by loading the antenna with magneto-dielectric material is lower than the increase of the Chu limit. For the fundamental mode (1,1) the decrease of the normalized quality factor is faster for increasing μ_r than for increasing ε_r.

Eq. (1) shows that the radius a is inverse proportional to the refractive index n and the electric energy W_e is proportional to the ε_r. For a constant refraction index the stored energy decreases by increase μ_r.

The mode (2,1) has a complicated normalized quality factor behaviour with respect to the constitutive parameters. The normalized quality factor increases as ε_r increase and it decreases as μ_r increases. But this mode has very high quality factor compared to the Chu lower bound.

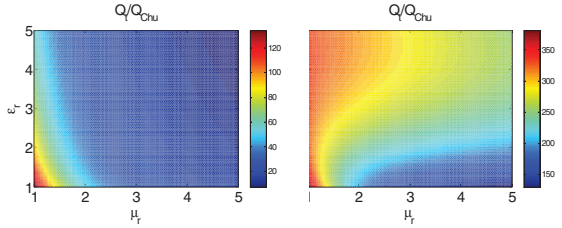

Fig. 3: The normalized quality factor of the modes (1,1) and (2,1).

4 Bandwidth of the antenna

The bandwidth is related to the total quality factor of the antenna and from [8, eq. (14-88a)] it can be expressed as:

$$BW = \frac{2|\Gamma|}{Q_t\sqrt{1-|\Gamma|^2}} \qquad (4)$$

where Γ is the maximum allowable input reflection coefficient. Fig. 4 shows the bandwidth $BW_{\text{-10dB}}$ of the antenna. The bandwidth of mode (1,1) increases as the μ_r increases and it decreases as ε_r increases. The permittivity ε_r limits the bandwidth of the antenna. So for a constant ε_r the radius of the antenna a can be reduced by increasing the μ_r while the bandwidth will remain unchanged. This figure shows that the widest bandwidth can be achieved for a substrate that has permittivity $\varepsilon_r = 1$. It is well-known that the bandwidth of the patch antenna reduces by loading it with a dielectric material and that is clear in Fig. 4. But it is unusual to decrease the size of the antenna and at same time increase the bandwidth. The bandwidth of an antenna that is filled with air is 0.71%, while it becomes 1.53% for antenna that is filled by magnetic substrate $\mu_r = 5$. The bandwidth is almost doubled for the magnetic substrate while the size of the antenna is 1/5 of the antenna area with the air substrate.

Mode (2,1) has a smaller bandwidth compared to mode (1,1). For this mode the bandwidth depends on both μ_r and ε_r, where the bandwidth decreases whenever μ_r or ε_r increases.

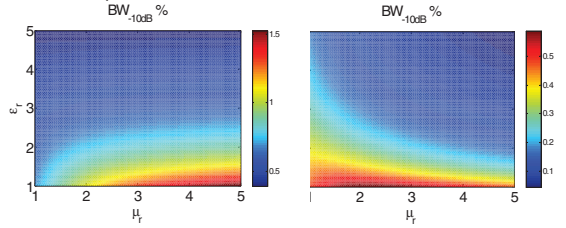

Fig. 4: The bandwidth of the modes (1, 1) and (2, 1).

5 Lossy substrate

The magneto-dielectric substrate can have a high loss tangent [4] and [9]. It is possible to find dielectric substrates with high ε_r and small electrical loss tangents $\tan\delta_e$ around 0.001. We will compare the performances of a patch antenna with a lossy magneto-dielectric substrate to the performances of an antenna with a low loss dielectric substrate. The calculations are carried out with HFSS. The refractive index n of the magneto-dielectric and the dielectric substrate is kept equal, while the loss tangent is taken to reflect realistic values. Both antennas have the same dimensions and they are fed through a lossless lumped component matching circuitry. A radiation boundary was used to calculate the efficiency of the antennas and the bandwidths were read from the S_{11} graphs.

Fig. 5 shows both the efficiency and the bandwidth results of the numerical solutions. The height of the antennas is kept constant h = 1.5 mm, and the radii are determined for an operation frequency of 1 GHz. Equation (1) can be used to estimate the radius of the antenna and during the simulation small adjustment on the radius is necessary to shift the resonant frequency toward 1 GHz. The ground plane and the patch are taken to be made of copper which reveals the advantage of using magneto-dielectric substrate. The black line is for a patch antenna with dielectric substrate. This antenna will be used as a reference for the comparison. The simulated antennas have dielectric substrate (ε_r=2, μ_r=1), magneto-dielectric substrates (ε_r=2, μ_r=2) and (ε_r=2, μ_r=4). The areas of these antennas compare with the reference antenna are 1:1, 1:2 and 1:4. The antennas with the magneto-dielectric substrates will be divided into two groups; a group with constant electrical loss tangent $\tan\delta_e$ = 0.001 while the magnetic loss tangent $\tan\delta_m$ varies, and a group with $\tan\delta_e = \tan\delta_m$. The antennas of the first group (the blue and the green lines) have higher efficiencies than the reference antenna (black line), while they have almost the same bandwidth. The antennas of the second group (the red and the cyan lines) have less or comparable efficiencies to the reference antenna and the bandwidth of these antennas are wider than the bandwidth of the reference antennas, especially for the high loss cases. This can be understood from equations (2) and (4), where the increase in P_{md} reduces the total quality factor and this leads to an increase in the bandwidth. The antennas of the first group are almost 10 % more efficient than the antennas of the second group. At low $\tan\delta_e$ the bandwidths of the two groups are almost comparable, while the bandwidth of the second group is almost 20 % wider than the bandwidth of the first group at high $\tan\delta_e$. For the same dielectric losses the efficiency of the antennas increases as the permeability μ_r increases, while the bandwidths are almost unchanged. This agrees with the analytical results of the fundamental mode (1,1).

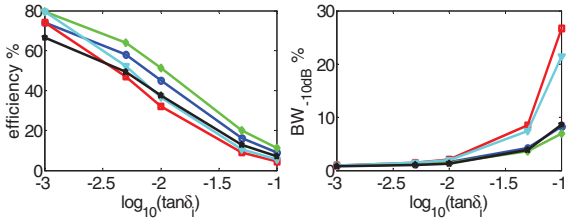

Fig. 5: The efficiency and the bandwidth for lossy magneto-dielectric antennas. All the antennas are supported by substrates that have ε_r = 2, while different μ_r and $\tan\delta_e$ are investigated. The index i = m

for the magnetic loss tangent and i = e for the electric loss tangent. The blue and the green lines are related to substrates having constant $\tan\delta_e$ = 0.001, and μ_r = 2 and 4, respectively, while both the red and the cyan lines are related to $\tan\delta_m = \tan\delta_e$ = [0.001, 0.005, 0.01, 0.05, 0.1], and μ_r = 2 and 4, respectively. The black line is related to dielectric substrates with ε_r = 2, μ_r = 1 and $\tan\delta_m$ = 0.

Since it is possible to find dielectric substrates with low $\tan\delta_e$, two other antennas have been also simulated, where the substrates have (ε_r=4, μ_r=1), (ε_r=8, μ_r=1) and $\tan\delta_e$ = 0.001. The efficiencies of these antennas are 56.5 % and 43.8 %, and the bandwidths are 0.7 % and 0.4 %. The sizes of these antennas are comparable to the sizes of the magneto-dielectric antennas with (ε_r=2, μ_r=2) and (ε_r=2, μ_r=4). Fig. 6 shows the differences between the efficiencies and the bandwidths of the antennas with the magneto-dielectric substrates and the antennas with the dielectric substrates of the same sizes. We see the same behaviour here where the magneto-dielectric substrate with high μ_r and low losses provide good efficiency. As long as the losses increase, which is the case for many ferrite composites, the efficiency degrades.

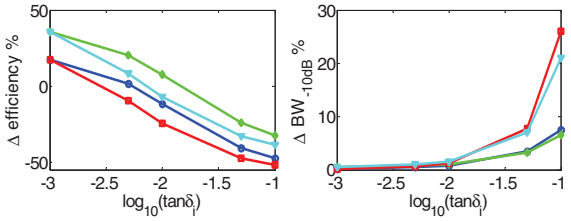

Fig. 6: The differences of the efficiencies and the bandwidth of the magneto-dielectric antennas in fig. 5 and antennas with dielectric substrates that have same sizes as the magneto-dielectric antennas.

6 Conclusions

The analytical method with a single mode is simple and it provides good results for the low loss cases.

Lossless (low losses) magneto-dielectric substrate provides a more efficient antenna than the antenna with dielectric substrate. The efficiency depends on both μ_r and ε_r. At moderate values of ε_r the efficiency increases as μ_r increases, while at a certain ε_r the efficiency saturates

The increase of μ_r minimizes the stored energy faster than the increase of ε_r.

The bandwidth improves as μ_r increases. The bandwidth has similar a behaviour as the efficiency, it saturates at certain values of ε_r regardless of μ_r. However this provides good performance where the antenna can be miniaturized while its bandwidth remains constant, at least for $\mu_r \leq 5$.

High loss tangent degrades the performances of the patch antennas. It is possible to find substrates with high dielectric constant and yet with a small loss tangent, but it is at prsent difficult to find a magneto-dielectric substrate that has a small loss tangent.

References

[1] H. A. Wheeler "Fundamental Limitations of Small Antennas," *Proc. IRE.*, vol. 35, pp. 1479–1484, Dec. 1947.

[2] R. C. Hansen and M. Burke "Antennas with Magneto-Dielectrics," *Microw. and Opt. Technol. Lett.*, vol. 26, no. 2, pp. 75-78, Jul. 2000.

[3] H. Mosallaei, K. Sarabandi "Magneto-Dielectrics in Electromagnetics: Concept and Applications," *IEEE Trans. Antennas Propag.*, vol. 52, no. 6, pp. 1558-1567, Jun. 2004.

[4] P. M. T. Ikonen, K. N. Rozanov, A. V. Osipov, P. Alitalo, and S. A. Tretyakov "Magnetodielectric Substrates in Antenna Miniaturization: Potential and Limitations," *IEEE Trans. Antennas Propag.*, vol. 54, no. 11, Nov. 2006.

[5] High Frequency Structure Simulator "www.ansoft.com".

[6] R. F. Harrington, *Time-Harmonic Electromagnetic Fields*, New York: Wiley-IEEE Press, 2001.

[7] R. E. Collin, S. Rothschild "Evaluation of Antenna *Q*," *IEEE Trans. Antennas Propag.*, vol. 12, no. 1, pp. 23-27, Jun. 1964.

[8] C. A. Balanis, *Antenna Theory: Analysis and Design*, 2nd ed., New York: John Wiley and Sons INC., 1997.

[9] G. Le Fur, F. Grange, C. Delaveaud, D. Souriou, J. L. Mattei, P. Queffelec "Contribution on Notch Antenna Loaded by Magneto-Dielectric Material" presented at the *EUCAP 2011*, Rome, Italy, 11-15 Apr. 2011.

Paper [2]

Measurement and Characterization of the Path Loss for Ear-to-Ear Wireless Communication

Baqer Nour[1], Olav Breinbjerg[2]
Department of Electrical Engineering, Electromagnetic Systems, Technical University of Denmark
Ørsteds Plads, building 348, DK-2800 Kgs. Lyngby, Denmark
[1]bn@elektro.dtu.dk, [2]ob@elektro.dtu.dk.

1. Introduction: Application of wireless technology have found place in many areas. One of the promising applications is the wireless body area network (WBAN). WBAN is used for monitoring the health of a person without limiting his/her movement. Recently, the industry of hearing aids has begun to investigate the use of wireless communication between the hearing aids to improve the quality of the hearing [1]. Such devices are small and the power supply is limited. So it is important to determine the path loss of the communication channel. There are many experimental works investigating the path loss around the human body; we just mention a few of them [2] and [3], where the transmitting antenna is located on the stomach of the person while the receiving antenna is located on the body at certain locations. The measurements were done at 2.45 GHz and at range 3-9 GHz for [2] and on the range 3-6 GHz for [3]. However these works do not characterize the communication channel around the head. In [4] the ear-to-ear path loss is evaluated with UWB antennas. It was found that communications take place around the head rather than through it. [5] investigates the 2.45 GHz path loss between monopole antennas that are placed orthogonal to the human head. It was found that the ear-to-ear path loss can vary by 10 dB, depending on the features of the head.

The purpose of this work is to perform an experimental determination of the path loss between two antennas located close to either side of a human head. These measurements are done with small antennas (both physical and electrical dimension) that operate at 1GHz, 1.6 GHz, 2.6 GHz and 3.6 GHz.

2. Experiment setup: The setup of the measurements near a head model (SAM) is shown in figure 1.

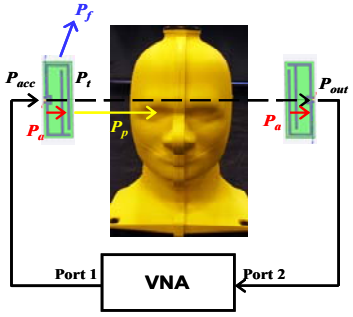

Fig. 1: The setup of the measurements

The head model is filled with a broadband solid material that is compatible with IEC 62209 and CTIA Test Plan for Mobile Station Over Air Performance, Revisions 3.0 standards [6]. An HP8753D vector network analyzer (VNA) measures the S_{21} parameter between two antennas near the head. To minimize the impact of the supporting tool, which holds the antennas, the cables and the head, this is made of low-loss materials. The supporting tool allows movements in three directions with good accuracy. The measurements are made inside two environments; anechoic and non-anechoic environments.

3. Antennas used in the measurements: We designed different antennas that have different sizes and different operating frequencies. Some of the antennas are re-scaled versions of the loop antennas in [7]. Common features for all the antennas are that the length and the width of the antennas are smaller than 4 cm and 1.8 cm, respectively, and they are printed on Rogers RT / duroid 5870 (TM). Figure 2 shows the details of the antennas designs and configurations.

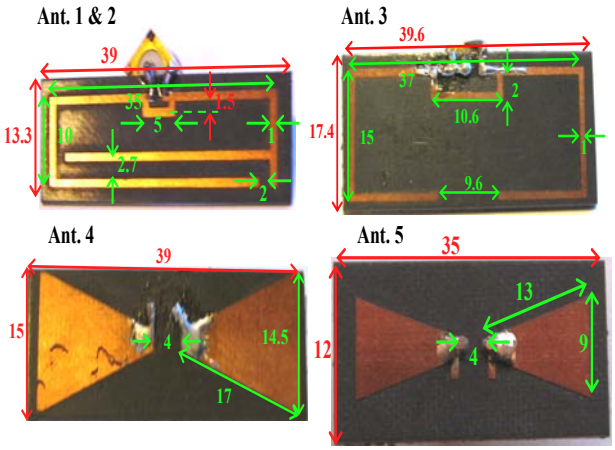

Fig. 2: The configurations and the dimensions of the antennas that have been used in the measurements. All the dimensions are given in mm and the height of the substrates is 1.5 mm.

Figure 3 shows the reflection coefficients of the antennas that appear in figure 2. The number of the line corresponds to the number of the antenna in figure 2. Line 1 corresponds to antenna 1, where its magnetic dipole moment is parallel to the surface of the head, line

2 corresponds to the same loop antenna but the magnetic dipole moment is perpendicular to the surface of the head, line 3 corresponds to antenna 3 where its magnetic dipole moment is perpendicular to the surface of head, lines 4 and 5 correspond to the bowtie antennas 4 and 5 which are parallel to the surface of the head. All the reflection coefficients are measured near the head.

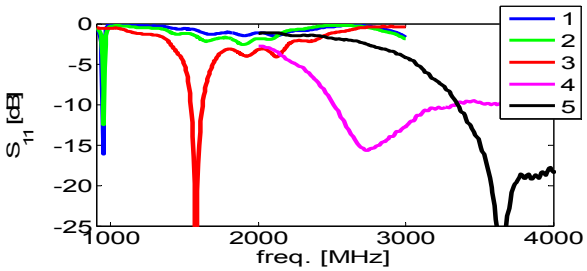

Fig. 3: The S_{11} of the antennas near the head.

Antennas 1 and 2 are narrow-band antennas since the dimensions of the antennas are very small (< 0.13λ). The efficiencies (in free space) of the antennas are calculated numerically. Antennas 1 and 2 have 10% (-10 dB) efficiency, antenna 3 has 92.6 % (-0.33 dB) efficiency, and antennas 4 and 5 have efficiencies almost equal to 100 % (0 dB). The efficiencies are calculated at the resonance frequencies of the antennas. The small efficiencies in antenna 1 and 2 due to the lose in the conductors.

4. Measurement accuracy: The measurements are repeated different days, where the setups had been preserved as much as possible. The accuracy of the measurements can be affected by several sources: 1) the environment surrounding the measurement setup, 2) the dynamic range of the VNA, 3) the mechanical alignment of the antennas with respect to the head. For the mechanical alignment there are several parameters that can affect the accuracy; a) the distance d to the head (which can be measured with an accuracy of ±1 mm), b) the angle ϕ of the antenna with the head (±1 degree), c) the alignment of the two antenna with each other (±2 degrees), and d) the height h of the antenna with respect to a reference plane (±1 mm).

The uncertainty in the measurements will be expressed by $Z_{90\%}$, where the Z can be the S-parameters, the resonance frequencies or any other variable. Figure 2 shows the definition of the uncertainty $Z_{90\%}$, where 90% of the measurements fall inside the shaded area. For a normal distribution $Z_{90\%}$ equals 1.645 times the standard deviation.

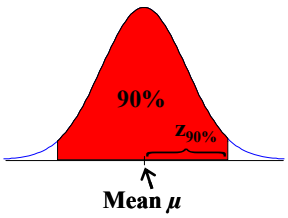

Fig. 4: Measurement accuracy.

The uncertainties of the measurements are shown in Table 1:

	$Z_{90\%}$
S_{11}	1.8 dB
S_{22}	2.0 dB
S_{12}	6.0 dB
PL	5.0 dB
$f_{0,1}$	4.4 MHz
$f_{0,2}$	4.9 MHz

Table1: the accuracy of the measurements

5. Measurement Results and Analysis: Figure 1 shows the types of losses which are included in the measurements of S_{21}. Some of the power accepted by the transmitting antenna P_{acc} will be dissipated as loss inside the antenna (P_a) and the remains will radiate. Part of the radiated power is lost inside the head (P_p) and as a far-field radiation (P_f), while the remaining part couples to the receiver antenna. Some of the losses are irrelevant to the path loss, such as the power that is dissipated in the antennas. Different antennas can have different losses, so it is important to eliminate this loss from the path loss. The path loss PL (in dB) will thus be defined as:

$$PL = 10\log_{10}\frac{|S_{21}|^2}{1-|S_{11}|^2} - 2\times 10\log_{10}\varepsilon_{ant} \qquad (2)$$

where ε_{ant} is the efficiency of each antenna. At high efficiency the second part of equation (2) can be neglected. And for good matching, the path loss can be approximated by S_{21}.

The results will be classified on the basis of the following procedure; we change one parameter at a time and keep the other parameters unchanged. The measured parameters are: 1) the distance d of the antenna from the head, 2) the orientations of the antennas with respect to the head, 3) the locations of the antennas on an arc in the horizontal plane where the location will be characterized by an angle ϕ, 4) the height of the antenna h, and 5) the environment. Figure 5 shows the parameters of the measurements.

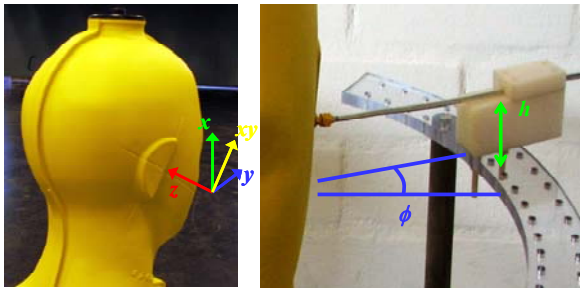

Fig. 5: Measurements parameters.

Since the measured values of S_{21} are very small with typical values approximately -60 dBm, the noise will disturb the measurements. After we make the measurements, the noise will be suppressed by using a low pass filter that filters the measurements of the S_{21} at the dBm scale. Figure 6 shows some of the measurements around 1 GHz together with a simulation graph that was calculated by HFSS [8]. The dashed line shows the limitation of the measurements. After calibration of the VNA, we attached wide-loads to the cables of the VNA, and the S_{21} was approximately -76 dBm. Since the uncertainty of S_{21} is 6 dB, so we will reject any measurement of S_{21} that is smaller than -70 dBm.

Figure 7 shows the distribution of the measurements of the path loss, as it defined by equation (2), for all parameter values in a narrow-band of frequencies around 1 GHz. The efficiency of the antenna is estimated numerically (HFSS) to be around 10 %. The path loss $|PL|$ has a mean value of 45.9 dB. These measurements are done inside a small area near the ears.

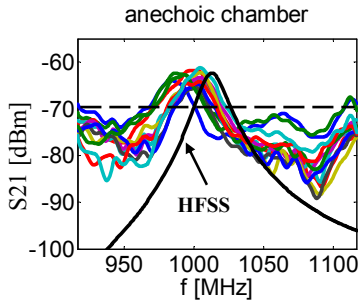

Fig. 6: Measurement of S_{21} near the head.

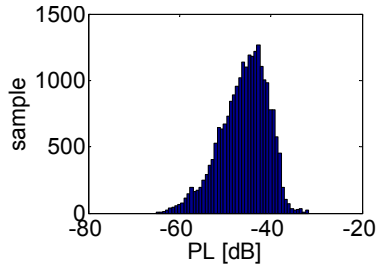

Fig. 7: Measurements that are made by antenna 2 of PL for all the parameter values, which are the distance d, the orientation and the height h. The mean value of the path loss is around PL = 45.9 dB.

The path loss $|PL|$ for the distances d = 0 mm, 3.5 mm and 5.5mm are 47.0 dB, 46.3 dB and 46.2 dB, respectively. The path loss $|PL|$ for the orientations of the antennas varies between 44.5 dB, 47.9 dB and 48.1 dB, and for the height h the path losses are 43.7 dB and 47.9 dB. In the case of the anechoic and non-anechoic chamber the path losses $|PL|$ are 44.9 dB and 46.4 dB. As we notice all these values are close to the mean value. And the differences between these values are smaller than the uncertainty value for the path loss 5.0 dB.

Since we do not see differences (larger than the uncertainty value) at small distances, the distances are chosen to be d = 5 mm and 14 mm. The difference between the new distances is larger than the distances, which were used in the uncertainty measurements. The orientation is measured just for one antenna and the height h is kept constant for all the measurements, since the height had a small effect on the PL. The measurements take place inside an anechoic chamber. After the reduction in the number of the parameter, the total number of combinations for each antenna is 5 and the number of antennas is 5.

Figure 8 shows the probability distribution of the S_{21} for the antennas 1 to 5. These values are measured for the frequencies where S_{11} < -10 dB. Figures 8(1) and 8(2) show few samples because the loop antenna is small compared to the wavelength (< λ / 10). The mean values of the S_{21} for the different antennas, which correspond to the figures 8(1) to 8(5), are -53, -65, -62, -56 and -65 dB, which correspond to $|PL|$ around 33 dB, 45 dB, 62 dB, 56 dB and 65 dB, respectively. These values correspond to a narrow bandwidth around the frequencies 1 GHz, 1.6 GHz, 2.6 GHz and 3.6 GHz, where the first two path losses are measured at 1 GHz.

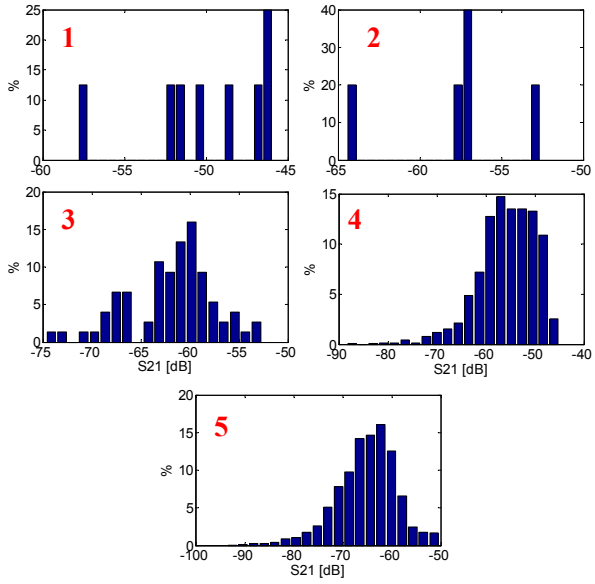

Fig. 8: Distribution of the S_{21} for antennas 1-5.

We observe that the path loss increases as the frequency increases for antenna 2 and 3, as for antennas 4 and 5. But the path loss measured by antenna 3 is higher than the path loss that measured by antenna 4 though antenna 4 operates at frequencies higher than antenna 3. The measurement setups for the antennas 2, 3 and 4 have been simulated numerically and the following path losses $|PL|$ have been estimated: 41 dB, 60 dB and 73 dB, respectively. The measurements of antenna 2 and 3 have acceptable similarity to the simulations, while the measurements of antenna 4 show approximately 18 dB difference to the value of the simulation. Both the loop antenna and the bowtie antenna have balanced feeding and the cables that connect the antennas to the VNA are coaxial cables (unbalanced). So there may be leakage currents that run on the outer surface of the cables, which will radiate. For the cases of antennas 1, 2 and 3 the leakage currents have small effects on the measurements of the S_{21}, while for the antennas 4 and 5 (we expect antenna 5 having the same problem) the leakage currents have significant affects on the S_{21}. Though the cables are aligned in a way that reduced the coupling between the cables, but we still see this effect on the measurements. We can't use the ferrite-cores to suppress the leakage current because they produce high losses at frequencies higher than around 1 GHz. So to account for the leakage currents, we will add 18 dB (which is estimated from the simulation results) to the path losses that have been measured by antennas 4 and 5.

Table 2 includes the mean values of the path loss $|PL|$ for the antennas 1 to 5 for different distances (d) and angles (ϕ). Small variations in the distance near the head have negligible effects on the path loss, as table 2 showing, since all the measured values are within the uncertainty value (5 dB).

The orientation of the magnetic dipole (in the case of the loop antennas) has a clear effect on the $|PL|$ as the mean values "33" (which is calculated as: (32dB + 35dB + 34dB + 34dB + 32dB)/5, the values are taken from table 2) and "45" dB show. The path loss for the case of the tangential magnetic dipole antenna is smaller than the path loss of the perpendicular magnetic dipole antenna. This phenomenon has also been seen in [9] but for electric dipoles, where the head was modeled as a dielectric sphere and the antennas were modeled by electrical hertzian dipoles that can be oriented tangential or orthogonal to the sphere. The path loss of the orthogonal dipoles was smaller than the path loss of the tangential dipoles, where most of the radiated power for the first orientation flows around the sphere, while the tangential dipoles force the power to flow inside the sphere. Image theory gives better explanation for both the magnetic and the dielectric dipoles. According to the image theory the surface of the head acts as an electric ground plane. Figure 9 shows the principle of the image theory. The ground plane supports the radiation of the tangential magnetic dipole and the orthogonal electric dipole.

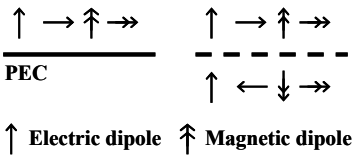

Fig. 9: Image theory

Ant.	d = 5 mm	d = 14 mm	ϕ = 0 deg.	ϕ = 10 deg.	ϕ = 20 deg.
1	32	35	34	34	32
2	44	45	43	46	46
3	62	62	60	64	62
4	73	74	74	75	72
5	83	83	83	84	81

Table 2: The mean path loss $|PL|$ in dB

6. Summary and Conclusions: The path loss of the ear-to-ear wireless communication channel has been measured for the frequencies 1 GHz, 1.6 GHz, 2.6 GHz and 3.6 GHz. The accuracy of the PL measurements was estimated to be 5 dB. Several parameters that could affect the path loss have been investigated. The parameters were chosen to cover all the possible locations and orientations of the antennas near the head. We came to the conclusion that small variations in the locations of the antennas do not affect the path loss of the ear-to-ear channel while the operating frequencies have a large impact on the path loss. The path loss increases as the frequency increases. We measured the path loss $|PL|$ at 1 GHz to approximately 33 dB for the tangential magnetic dipole and 45 dB for the normal magnetic dipole. These measurements show the importance of the orientation with respect to the surface of the head. We were able to gain 12 dB for the same antenna just by choosing different orientation. The significance of the feeding cables was demonstrated in the measurements with bow-tie dipoles (ant. 4 and 5), where the measurements show smaller path loss than for the low frequency cases. By using numerical simulations we were able to estimate the cable effect on the measurements.

REFERENCES

[1] Jeff Solum "Hearing Aids: Cutting Edge Technology, In An Ultra Constrained Environment" IEEE P802.15 Working Group for Wireless Personal Area Networks (WPANs), doc.: IEEE 802. 15-08-0365-01-0006, May 2008.

[2] Peter S. Hall, Yuriy I. Nechayev, Costas C. Constantinou, Yang Hao, Akram Alomainy, Rostyslav Dubrovka, and Clive G. Parini "Antennas and Propagation for On-Body Communication Systems" Antennas and Propagation Magazine, Vol. 49, pp. 41-58, June 2007.

[3] Andrew Fort, Julien Rychaert, Claude Desset, Philippe De Doncker, Piet Wambacq and Leo Van Biesen "Ultra-Wideband Channel Model for Communication Around the Human Body"

IEEE Jounal on Selected Areas in Communications, Vol. 24, No. 4, April 2006.

[4] T. Zasowski, G. Meyer, F. Althaus, and A. Wittneben "UWB Signal Propagation at the Human Head" IEEE Trans. Microwave Theory Tech., Vol. 54, No. 4, pp. 1836-1845, April 2006.

[5] Søren H. Kvist, Jesper Thaysen, and Kaj B. Jakobsen "The Effect of the Head Size on the Ear-to-Ear Radio-Propagation Channel for Body-Centric Wireless Networks" Antennas and Propagation Conference 2010, Loughborough, UK, 8-9 Nov. 2010.

[6] Schmid & Partner Engineering AG "www.speag.com".

[7] Jiaying Zhang and Olav Breinbjerg "Self-Resonant Electrically small Loop Antennas for Hearing-Aids Application" European Conference on Antennas and Propagation *EUCAP 2010*, Barcelona , 12-16 April 2010.

[8] "www.ansoft.com".

[9] Baqer Nour and Olav Breinbjerg " Electromagnetic power flow between opposite sides of a lossy dielectric sphere using spherical vector wave expansion" European Conference on Antennas and Propagation *EUCAP 2010*, Barcelona , 12-16 April 2010.

Paper [3]

Electromagnetic power flow between opposite sides of a lossy dielectric sphere using spherical vector wave expansion

Baqer Nour*, Olav Breinbjerg+

Department of Electrical Engineering, Electromagnetic Systems, Technical University of Denmark
Ørsteds Plads, building 348, DK-2800 Kgs. Lyngby, Denmark
**bn@elektro.dtu.dk, +ob@elektro.dtu.dk.*

***Abstract*— This article addresses the problem of communication in near field region. The proposed example is the communication between two small antennas, which are modelled as an electric dipole antenna (transmitter) and a small box (receiver), near a sphere that models a head. Spherical vector wave expansion SVWE is used to calculate the response of the model and to investigate propagation of power. Influence of the orientation of the antennas on the propagation is studied. The effect of location of the receiving antenna on the amount of the received power is investigated too.**

I. INTRODUCTION

Applications of wireless technology have found place in many areas. Recently they have been used in wireless sensors placed on a person, either for monitoring health information, [1] and [2], or for communication between hearing aids devices. Such devices are small in size and the power supply is limited. The impact of the environment is important in designing the antenna and deciding the working frequency. Communication channel of such an environment is not fully characterized, and the mechanisms of coupling are not clear. The example of hearing aids is taken, where two small antennas communicate to each other in presence of the head. The antennas are taken to be operating at wave lengths comparable to or larger than the diameter of the head.

A simple model is used to investigate the coupling. The head is modelled as a sphere, which represents the brain. The necessarily parameters are the conductivity and the permittivity of the brain, [3]. The transmitting antenna is modelled as electric dipoles.

The traditional free-space / plane wave propagation link-model is inapplicable for the configuration of two antennas on opposite sides of a head. Indeed, for this unusual radio communication link it is necessary to determine the coupling mechanisms; i.e. how power flows from one antenna to the other. For a hertzian z-polarized the electric dipole has components depend on $1/kr$, $1/(kr)^2$ and $1/(kr)^3$. Usually we ignore $1/(kr)^2$ and $1/(kr)^3$ at certain distance form the antenna. But these parts become significant at small distance, which is the case for hearing aids communications.

The sphere model is used to compute the electric and magnetic fields, at the same time it is used to compute the power intensity induced by electric dipole near the head. The fields are calculated using spherical wave expansions.

The article is organized to section II, which describes the geometry of the problem and the selected solution. Coefficients of the incident, scattered and total fields are mentioned. The powers dissipate in the dielectric sphere and the radiation power are given in term of the coefficients of the fields. Section III includes numerical results of the powers as a function of frequencies, and 2D plots of the power density for different frequencies and different orientations of the transmitting antenna. Transmission efficiency concept will be defined for communication between a transmitting antenna and receiving model of an antenna. Conclusions are given in section IV.

II. ANALYTICAL FORMULATION

The model consists of a hertzian dipole of *p*-polarization located on the z-axis at distance r' and a sphere that has the same parameters as the brain tissue and has radius r_{sph}, see Figure 1. The properties of the brain are taken from [3]. Two polarizations are considered, *x* and *z*. The sphere is centred at the origin of the coordinate system. The dipoles are shown as vectors. A receiving antenna, to collect the power on the other side of the sphere, is modelled as box located at same distance as the dipole at angle θ_{rec} with the z-axis. It is orthogonal to the sphere for the *z*-oriented dipole, and it is tangential for the *x*-oriented dipole.

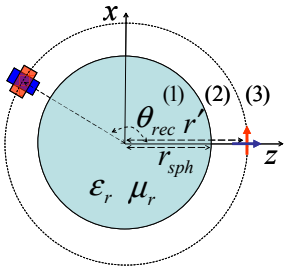

Fig. 1 The configuration of the model, which consists of a hertzian dipole of *p*-polarization (the red and blue arrows), and a sphere that has permittivity ε_r and conductivity σ_r. The sphere has radius r_{sph} and the dipole is located at distance r'. A receiver antenna (the red and the blue boxes) is located at distance r' and angle θ_{rec}.

The space is divided into three regions. Region 1 ($r < r_{sph}$) is the sphere, region 2 ($r_{sph} < r < r'$) is the free-space between

the sphere and the dipole and region 3 ($r > r'$) is the free-space outside the dipole. The incident field $\boldsymbol{E}^i$ of the dipole induces a scattering field $\boldsymbol{E}^s$ outside the sphere and a total field $\boldsymbol{E}^t$ inside the sphere.

The field intensities in each region are written as spherical vector wave expansions SVWE, [4], [5], [6] and [7]. The idea is to find coefficients that weight the spherical modes in the expansion. The coefficients are calculated for each mode using the boundary conditions at the interface of the regions. Electric and magnetic fields in a source-free region are given as, [5, A1.1 and A1.2]:

$$\vec{E}(r,\theta,\phi) = \frac{k}{\sqrt{\eta}} \sum_{csmn} Q_{smn}^{(c)} \vec{F}_{smn}^{(c)}(r,\theta,\phi) \tag{1a}$$

$$\vec{H}(r,\theta,\phi) = -ik\sqrt{\eta} \sum_{csmn} Q_{smn}^{(c)} \vec{F}_{3-s,mn}^{(c)}(r,\theta,\phi) \tag{1b}$$

$$\eta = \sqrt{\frac{\varepsilon}{\mu}} \qquad k = \omega\sqrt{\mu\varepsilon}$$

Time factor exp(-$i\omega t$) is used through this article. The spherical vector wave functions $\overline{F}_{smn}^{(c)}$ are defined in [5, A1.45 and A1.46].

A. Excitation and incident field

An electric hertzian dipole source is used to excite the model. Electric moment d_e of the dipole is taken to be constant. Two basic orientations of the dipole are used, x-oriented dipole (tangential to the sphere) and z-oriented dipole (orthogonal to the sphere). Any orientation can be realized by vector addition. The current density of the dipoles is $\boldsymbol{J} = \boldsymbol{p}\cdot d_e\cdot\ \delta(x)\ \delta(y)\delta(z-z')$, where $\boldsymbol{p}$ can be along x-direction or z-direction, $z' = r'$ and δ is the Dirac delta function.

The coefficients for the incident field are calculated using the reciprocity theorem, [5, A1.77 – A1.81]. The coefficients will be used to calculate the scattering field and the total field coefficients. SVWE model treats the space outside the dipole as two regions; inside and outside region. If we consider the problem of Figure 1 in absence of the sphere, the inside region is region 2 and the outside region is 3.

The coefficients of the x-oriented dipole are calculated to be:

$$Q_{11n}^{(c)i} = -id_e \frac{k_0}{\sqrt{\eta_0}} \frac{1}{4} \sqrt{\frac{2n+1}{\pi}} z_n^{(4-c)}(k_0 r') \tag{2}$$

$$Q_{1,-1,n}^{(c)i} = Q_{11n}^{(c)i} \tag{3}$$

$$Q_{21n}^{(c)i} = d_e \frac{k_0}{\sqrt{\eta_0}} \frac{1}{4} \sqrt{\frac{2n+1}{\pi}} \frac{1}{k_0 r'} \frac{d}{d(k_0 r')} \left\{ k_0 r' z_n^{(4-c)}(k_0 r') \right\} \tag{4}$$

$$Q_{2,-1,n}^{(c)i} = -Q_{21n}^{(c)i} \tag{5}$$

where $c = 1$ for $r < r'$ and $c = 3$ for $r > r'$ and k_0 and η_0 are the wave number and the intrinsic admittance of the free-space respectively. The function $z_n^{(c)}$ is the spherical Bessel function ($c = 1$), spherical Neumann function ($c = 2$), spherical Hankel function of the first kind ($c = 3$) or spherical Hankel function of the second kind ($c = 4$). The remaining coefficients are zero.

By same method the coefficients of the z-oriented dipole are calculated, all the coefficients are zero except for the following coefficients:

$$Q_{20n}^{(c)i} = -d_e \frac{k_0}{\sqrt{\eta_0}} \sqrt{\frac{n(n+1)(2n+1)}{4\pi}} \frac{z_n^{(4-c)}(k_0 r')}{k_0 r'} \tag{6}$$

B. Scattering by dielectric sphere

The incident field will be spherical Bessel functions ($c = 1$). The tangential components of the electric and the magnetic fields are continuous at the sphere surface:

$$\begin{aligned} \hat{r}\times\left(\vec{E}^i + \vec{E}^s\right) &= \hat{r}\times\vec{E}^t \\ \hat{r}\times\left(\vec{H}^i + \vec{H}^s\right) &= \hat{r}\times\vec{H}^t \end{aligned} \tag{7}$$

The coefficients of the scattered and the total fields are calculated using the orthogonality property of SVWE [5, A1.69]. For an x-polarized dipole, the coefficients are:

$$Q_{11n}^{s} = Q_{11n}^{(1)i} \cdot \frac{\sqrt{\frac{\eta_0}{\eta_1}} R_{1n}^{(1)}(k_0 r_{sph}) R_{2n}^{(1)}(k_0 r_{sph}) - \sqrt{\frac{\eta_1}{\eta_0}} R_{2n}^{(1)}(k_1 r_{sph}) R_{1n}^{(1)}(k_0 r_{sph})}{\sqrt{\frac{\eta_1}{\eta_0}} R_{2n}^{(1)}(k_1 r_{sph}) R_{1n}^{(3)}(k_0 r_{sph}) - \sqrt{\frac{\eta_0}{\eta_1}} R_{1n}^{(1)}(k_1 r_{sph}) R_{2n}^{(3)}(k_0 r_{sph})} \tag{8}$$

$$Q_{21n}^{s} = Q_{21n}^{(1)i} \cdot \frac{\sqrt{\frac{\eta_0}{\eta_1}} R_{2n}^{(1)}(k_1 r_{sph}) R_{1n}^{(1)}(k_0 r_{sph}) - \sqrt{\frac{\eta_1}{\eta_0}} R_{1n}^{(1)}(k_1 r_{sph}) R_{2n}^{(1)}(k_0 r_{sph})}{\sqrt{\frac{\eta_0}{\eta_1}} R_{1n}^{(1)}(k_1 r_{sph}) R_{2n}^{(3)}(k_0 r_{sph}) - \sqrt{\frac{\eta_1}{\eta_0}} R_{2n}^{(1)}(k_1 r_{sph}) R_{1n}^{(3)}(k_0 r_{sph})} \tag{9}$$

$$Q_{11n}^{t} = Q_{11n}^{(1)i} \frac{k_0}{k_1} \cdot \frac{R_{1n}^{(1)}(k_0 r_{sph}) R_{2n}^{(3)}(k_0 r_{sph}) - R_{2n}^{(1)}(k_0 r_{sph}) R_{1n}^{(3)}(k_0 r_{sph})}{\sqrt{\frac{\eta_0}{\eta_1}} R_{1n}^{(1)}(k_1 r_{sph}) R_{2n}^{(3)}(k_0 r_{sph}) - \sqrt{\frac{\eta_1}{\eta_0}} R_{2n}^{(1)}(k_1 r_{sph}) R_{1n}^{(3)}(k_0 r_{sph})} \tag{10}$$

$$Q_{21n}^{t} = Q_{21n}^{(1)i} \frac{k_0}{k_1} \cdot \frac{R_{2n}^{(1)}(k_0 r_{sph}) R_{1n}^{(3)}(k_0 r_{sph}) - R_{1n}^{(1)}(k_0 r_{sph}) R_{2n}^{(3)}(k_0 r_{sph})}{\sqrt{\frac{\eta_0}{\eta_1}} R_{2n}^{(1)}(k_1 r_{sph}) R_{1n}^{(3)}(k_0 r_{sph}) - \sqrt{\frac{\eta_1}{\eta_0}} R_{1n}^{(1)}(k_1 r_{sph}) R_{2n}^{(3)}(k_0 r_{sph})} \tag{11}$$

$$\begin{aligned} Q_{1,-1,n}^{s} &= Q_{11n}^{s}, \quad Q_{2,-1,n}^{s} = -Q_{21n}^{s} \\ Q_{1,-1,n}^{t} &= Q_{11n}^{t}, \quad Q_{2,-1,n}^{t} = -Q_{21n}^{t} \end{aligned} \tag{12}$$

$$R_{sn}^{(c)}(kr) = \begin{cases} z_n^{(c)}(kr) & s = 1 \\ \dfrac{1}{kr} \dfrac{d}{d(kr)} \left\{ kr z_n^{(c)}(kr) \right\} & s = 2 \end{cases} \tag{13}$$

k_1 and η_1 are the wave-number and the intrinsic admittance of the sphere ($r < r_{sph}$) respectively. For a z-polarized dipole the coefficients become:

$$Q_{20n}^{s} = Q_{20n}^{(1)i} \cdot \frac{\sqrt{\frac{\eta_1}{\eta_0}} R_{2n}^{(1)}(k_0 r_{sph}) R_{1n}^{(1)}(k_1 r_{sph}) - \sqrt{\frac{\eta_0}{\eta_1}} R_{1n}^{(1)}(k_0 r_{sph}) R_{2n}^{(1)}(k_1 r_{sph})}{\sqrt{\frac{\eta_0}{\eta_1}} R_{1n}^{(3)}(k_0 r_{sph}) R_{2n}^{(1)}(k_1 r_{sph}) - \sqrt{\frac{\eta_1}{\eta_0}} R_{2n}^{(3)}(k_3 r_{sph}) R_{1n}^{(1)}(k_1 r_{sph})} \tag{14}$$

$$Q_{20n}^{t} = Q_{20n}^{(1)i} \frac{k_0}{k_1} \cdot \frac{R_{1n}^{(3)}(k_0 r_{sph}) R_{2n}^{(1)}(k_0 r_{sph}) - R_{2n}^{(3)}(k_0 r_{sph}) R_{1n}^{(1)}(k_0 r_{sph})}{\sqrt{\frac{\eta_0}{\eta_1}} R_{1n}^{(3)}(k_0 r_{sph}) R_{2n}^{(1)}(k_1 r_{sph}) - \sqrt{\frac{\eta_1}{\eta_0}} R_{2n}^{(3)}(k_3 r_{sph}) R_{1n}^{(1)}(k_1 r_{sph})} \tag{15}$$

C. Power calculations

The power delivered by the dipole P_{del} is the sum of the power dissipated in the sphere P_{dis} and the far-field radiated power P_{rad}. It is noted that the delivered power P_{del} varies with the parameters of the sphere and it is different from the well-known power by a dipole in free space ($\omega\mu_0 k_0 d_e^2/12\pi$). The dissipated power and the radiated power will be calculated using the poynting vector:

$$P_{dis} = -\mathrm{Re}\left\{\frac{1}{2}\oint_{S_1} \vec{E}^{t} \times \vec{H}^{t*} \cdot d\vec{S}\right\} \tag{16}$$

$$P_{rad} = \mathrm{Re}\left\{\frac{1}{2}\oint_{S_2} (\vec{E}^{i} + \vec{E}^{s}) \times (\vec{H}^{i} + \vec{H}^{s})^{*} \cdot d\vec{S}\right\} \tag{17}$$

$$P_{del}^{x} = P_{dis}^{x} + P_{rad}^{x} \tag{18}$$

Here S_1 is the surface of the sphere and S_2 is a far-field sphere. The powers for the x-oriented dipole are:

$$P_{dis}^{x} = -\mathrm{Re}\left\{ir^2|k_1|^2 \frac{(\sqrt{\eta_1})^*}{\sqrt{\eta_1}} \sum_{n=1}^{N} \left[\left|Q_{11n}^{t}\right|^2 R_{1n}^{(1)} R_{2n}^{(1)*} - \left|Q_{21n}^{t}\right|^2 R_{2n}^{(1)} R_{1n}^{(1)*}\right]\right\} \tag{19}$$

$$P_{rad}^{x} = 2\,\mathrm{Re}\left\{\sum_{n=1}^{N}\left[\left|Q_{11n}^{(3)i} + Q_{11n}^{s}\right|^2 + \left|Q_{21n}^{(3)i} + Q_{21n}^{s}\right|^2\right]\right\} \tag{20}$$

$$R_{sn}^{(1)} = R_{sn}^{(1)}(k_1 r_{sph})$$

The powers for the z-oriented dipole are:

$$P_{dis}^{z} = \mathrm{Re}\left\{i\frac{1}{2}r^2|k_1|^2 \frac{(\sqrt{\eta_1})^*}{\sqrt{\eta_1}} \sum_{n=1}^{N}\left[R_{1n}^{(1)} R_{2n}^{(1)*}\left|Q_{20n}^{t}\right|^2\right]\right\} \tag{21}$$

$$P_{rad}^{z} = \mathrm{Re}\left\{\sum_{n=1}^{N}\left|Q_{20n}^{(3)i} + Q_{20n}^{s}\right|^2\right\} \tag{22}$$

III. Results and Discussion

The power flow is investigated in different ways: 1) inspection of the 2D plot of the magnitude and direction of the power flow density and 2) the power entering the surfaces of the receiving antenna.

Figure 2 shows, at frequencies 400 MHz and 4 GHz, the normalized wave impedances of the total field (sum of the incident and the scattered fields outside the sphere) and normalized wave impedances of the incident field. The normalized wave impedance is the ratio of the magnitude of electric and magnetic fields, normalized to the intrinsic impedance of the medium.

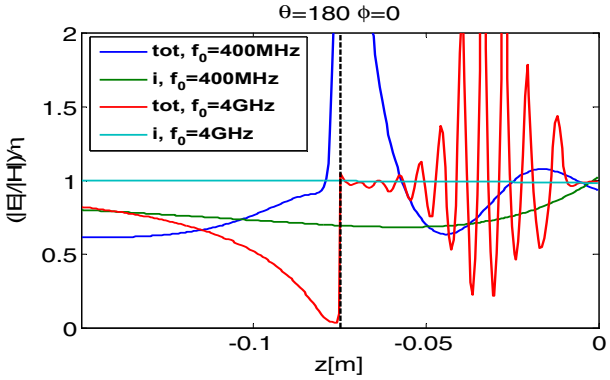

Fig. 2 Normalized wave impedances of the total fields at frequencies 400 MHz (blue line) and 4 GHz (red line), and the incident fields at 400 MHz (green line) and 4GHz (cyan line). η is the intrinsic impedance of the free-space for the incident fields, while for the total field it is the intrinsic impedance of the sphere and the free-space for observation points inside and outside the sphere respectively. The dashed line is the surface of the sphere.

At 400 MHz the normalized wave impedance of the total field varies around one inside the sphere (z > -0.075m), and it is high at the surface of the sphere and less than 1 outside the surface. Both inside and outside the sphere, the normalized wave impedance of the total field oscillates around the normalized wave impedance of incident field. At 4 GHz the normalized impedance of total field oscillates more rapidly with distance, and it converges to 1 near the inside surface and it less than 1 outside the surface.

For plane wave propagation the normalized wave impedance equals 1. Thus Figure 2 clearly shows that the field inside and outside the sphere is far more complicated than a plane wave. This is the case for the incident field of 400 MHz because we are in the near-field of the dipole, while the incident field for 4 GHz shows plane wave property. For both frequencies the total field, inside and outside the sphere, deviates significantly from a plane wave.

The radiated and dissipated powers are frequency dependent. In Figure 3 the radiated and dissipated power are calculated for different frequencies and different orientations of the dipole. The vertical axis shows the radiated and dissipated power normalized to the delivered power of the dipole, which can be oriented in x or z directions, and the horizontal axis is the operation frequency in MHz. The dissipation is larger at the low frequencies, while at high frequencies the radiation becomes dominant. The normalized radiated power is higher for the z-oriented dipole than the x-oriented dipole. While for the z-oriented dipole the

normalized dissipated power is smaller than the x-oriented dipole.

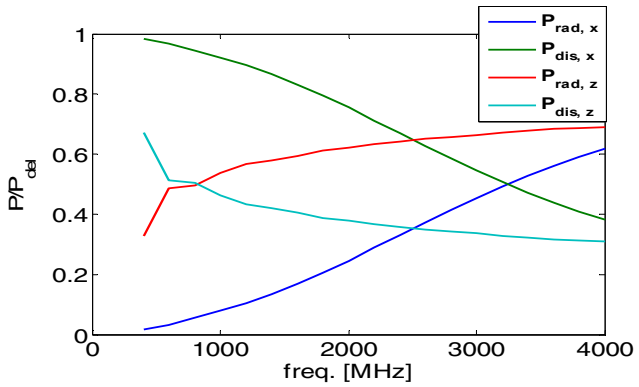

Fig. 3 Dissipated power P_{dis} and radiated power P_{rad} normalized to delivered power P_{del} vs. frequency for *x*- and *z*-oriented dipoles.

The decrease of the dissipated power can be explained in two ways; 1) as the frequency increases the ratio of the conductivity to the frequency decrease, so the attenuation becomes smaller. The loss tangent of the sphere at 400 MHz and 4 GHz are $\mathrm{Im}\{\varepsilon\}/\mathrm{Re}\{\varepsilon\} = 0.755$ and 0.285 respectively, and 2) a small amount of the delivered power penetrates the sphere while most of the power reflects back from the sphere. The reflection coefficients at 400 MHz and 4 GHz are 0.79 and 0.86 respectively.

The presence of the sphere near the dipole redistributes the power flow density. Figures 4 and 5 show the power flow density at 400 MHz for *x*- and *z*-polarized dipoles respectively, where the power density is normalized to the delivered power.

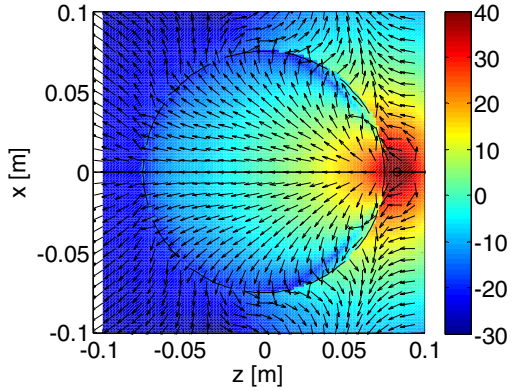

Fig. 4 Normalized power density for the sphere and an *x*-oriented hertzian dipole works at 400 MHz. The colour is the magnitude (dB/m^2) and the directions are indicated by arrows. The location of the hertzian dipole is shown as a small black circle in the right side.

The colours are the magnitude (dB/m^2) of the normalized power flow density and the direction of the power flow density is indicated by arrows. In both orientations the power flows inside and outside the sphere. A large magnitude of power density is concentrated in a small area near the antenna. This area will be called hot spot, which is characterized by a dark red colour.

The *x*-oriented dipole has a large hot spot. The inside power propagates through the sphere in almost radial lines from the area close to the dipole. The power decreases very rapidly as it propagates through the sphere. There is a jump in power density between the inside and the outside regions near the surface of the sphere since the tangential component is not necessarily continuous. At left side of the sphere the power flows out of the sphere.

The *z*-oriented dipole has a small hot spot. The inside power flow density propagates toward the poles region. The magnitude of the inside power flow density declines as it propagates and it is null along the *z*-axis, which is expected for the *z*-oriented dipole. The magnitude of the power density jumps at the surface of the sphere. The outside power flows along the surface of the sphere to the poles, and then it flows in the negative *z*-direction. The magnitude of the power flow density, that bounds the sphere, is larger than the case of the *x*-oriented dipole.

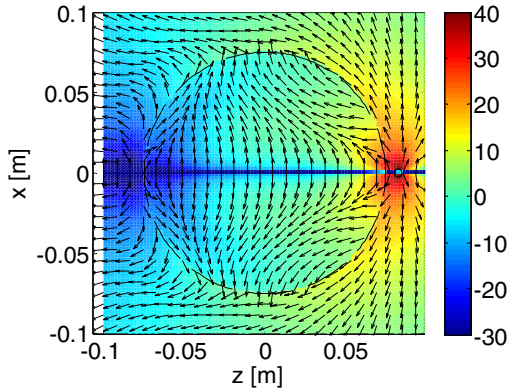

Fig. 5 Normalized power density for a *z*-oriented hertzian dipole works at 400 MHz.

Since the dipole is close to the sphere, the surface of the sphere acts as a ground plane to the dipole. So the image theory can be applied here. The image of the *x*-oriented dipole has destructive effect on the radiated power. Most of the power is concentrated inside the region between the dipole and its image, at same time the decreasing of the power becomes faster with the distance. While the image of the *z*-oriented dipoles has a constructive effect on the radiation of the dipole, so there is small hot spot around the dipole.

The jump in power density, at the surface of the sphere, supports the idea that power flows inside and along the surface. Since the normal power flow has to be continues through the surface of the sphere, the extra power at the outside surface is the power that flows along the surface of the sphere; the directions of arrows shows this phenomenon in all figures of the normalized power density.

Figure 6 and 7 shows the normalized power density of an *x*- and *z*-oriented dipoles operate at 4 GHz. The inside power flow density is focused in narrow beam and less amount of power flow density propagates inside the sphere than the case of 400 MHz. At same time magnitude of the power density bounding the sphere becomes larger, and the sphere reflects back more power toward the antenna as the arrows show.

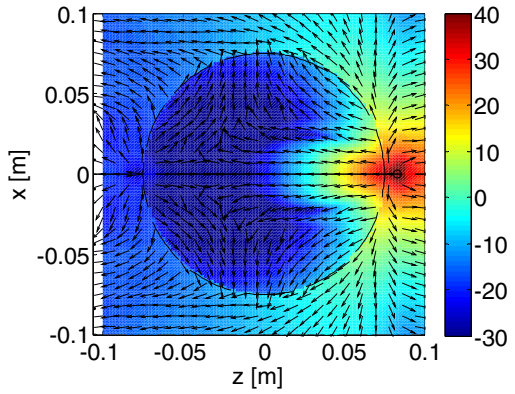

Fig. 6 The normalized power density for an *x*-oriented hertzian dipole works at 4 GHz.

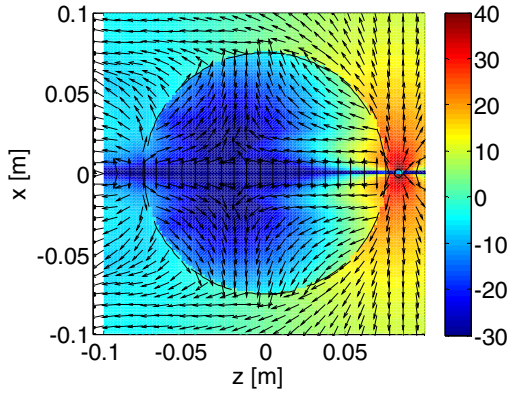

Fig. 7 The normalized power density for a *z*-oriented hertzian dipole works at 4 GHz.

The receiver antenna model is a rectangular box and has the following dimensions 1.5 cm x 0.5 cm x 0.5 cm. The antenna receives a power P_{rec}, which is calculated by integrating the power density that enters the surfaces over the surfaces of the box. The ratio of the received power to the delivered power will be called the transmission efficiency. Figure 8 shows the transmission efficiency, as a function of the location angle θ_{rec}, for the *x*- and *z*-oriented dipoles.

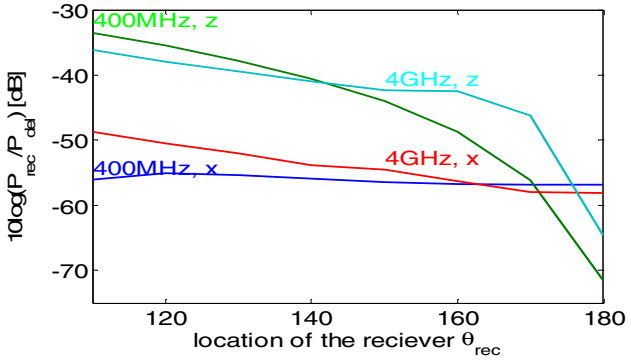

Fig. 8 The power received by a box, with dimensions 1.5cm x0.5cm x 0.5 cm, at frequencies 400 MHz and 4 GHz as a function of the location angle θ_{rec}. The distance form the sphere model to the center of the sphere and the box is 0.75 cm. Letters *x* and *z* stand for *x*- and *z*-orientation of the dipole.

The transmission efficiency of the *z*-oriented dipole is more sensitive to the location angle θ_{rec} than the *x*-oriented dipole. The *z*-oriented dipole has higher transmission efficiencies in general than the *x*-oriented dipole. This effect can also be seen from the power flow density Figures 4 to 7.

IV. Conclusions

The power flow is investigated near a lossy dielectric sphere. The analysis is based on the spherical vector wave expansion. Two orientations are studied, *x*-and *z*-oriented hertzian dipoles. The normalized wave impedances show the complex nature of the propagation near the sphere. The propagation is far from being a plane wave.

The dissipated and radiated powers are frequency related. The dissipation is large at low frequencies and becomes smaller at high frequencies. While the radiated power increases with increasing the frequency. The z-oriented dipole causes less dissipation in the sphere and higher radiation than the *x*-oriented dipole.

The sphere acts as ground for the dipole. So hot spot region is located between the dipole and the sphere. The size of the hot spot area depends on the orientation and the frequency of the dipole.

The transmission efficiency, between the dipole and the receiving box, is investigated vs. location angle, orientation and frequency. The z-oriented dipole gives higher transmission efficiency values in general, except for location angles close to 180 degree. The transmission efficiency becomes high as the receiving model displaces from the *z*-axis.

References

[1] T. Zasowski, G. Mayer, F. Althaus, A. Wittneben, "UWB Signal Propagation at the Human Head," *IEEE Trans on Microwave Theory and Techniqes* ., vol. 54, No. 4, pp. 1836–1844, April 2006.

[2] A. Fort, C. Desset, J. Rychaert, P. D. Doncker, L. V. Biesen, S. Donnay, "Ultra Wide-band Area Channel Model," IEEE International Conference on Communicatios *ICC 2005*, Seoul, 16-20 May 2005, pp. 2840-2844.

[3] P. J. Dimbylow, O. P. Gandhi, "Finite-difference time-domain calculations of SAR in a realistic heterogeneous model of the head for plane-wave exposure from 600 MHz to 3," *Phys. Med. Biol.*., vol. 36, No. 8, pp. 1075–1089.

[4] Arthur L. Aden, Milton Kerker, "Scattering of Electromagnetic Waves from Two Concentric Spheres," *Journal of Applied Phyics.*, vol. 22, No. 10, pp. 1242-1246, Oct. 1951.

[5] J. E. Hansen, *Spherical Near-Field Antenna Measurements*, Peter Peregrinus Ltd. London, United Kingdom: Short Run Press Ltd., 1988.

[6] J. A. Stratton, *Electomagnetic Theory*, Donald G Dudley, Series Editor, The IEEE Press Series on Electromagnetic Wave Theory.

[7] John H. Bruning, Yuen T. Lo, "Multiple Scattering of EM Waves by Spheres: Part I –Multipole Expansion and Ray-Optical Solutions," *IEEE Trans on Antennas and Propagation Propagation* ., vol. AP-19, No. 3, pp. 378–390, May 1971.